Computational Study and Analysis of Structural Imperfections in 1D and 2D Photonic Crystals

by

Karlene Rosera Maskaly

Bachelor of Science, Physics
Massachusetts Institute of Technology, 2000

Submitted to the Department of Materials Science and Engineering in Partial Fulfillment of the Requirements for the Degree of

Doctor of Philosophy in Materials Science and Engineering

at the

MASSACHUSETTS INTITUTE OF TECHNOLOGY

JUNE 2005

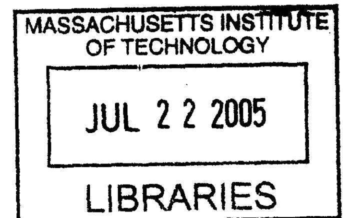

© 2005 Massachusetts Institute of Technology. All Rights Reserved.

Signature of Author...
Department of Materials Science and Engineering
May 25, 2005

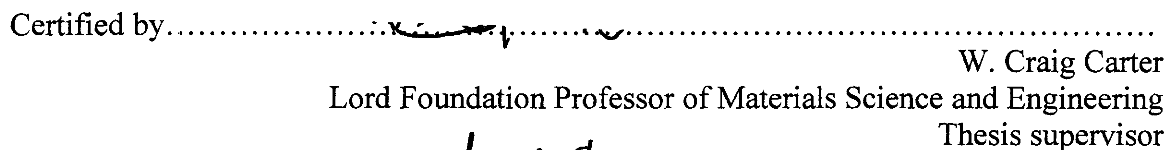

Certified by..
W. Craig Carter
Lord Foundation Professor of Materials Science and Engineering
Thesis supervisor

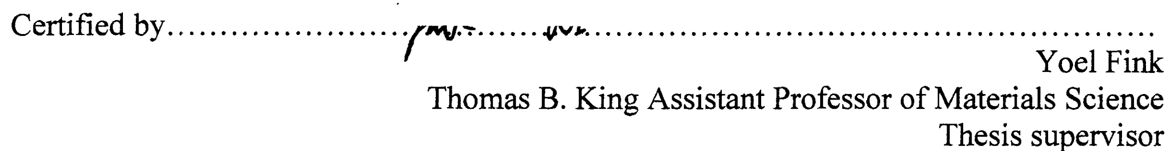

Certified by..
Yoel Fink
Thomas B. King Assistant Professor of Materials Science
Thesis supervisor

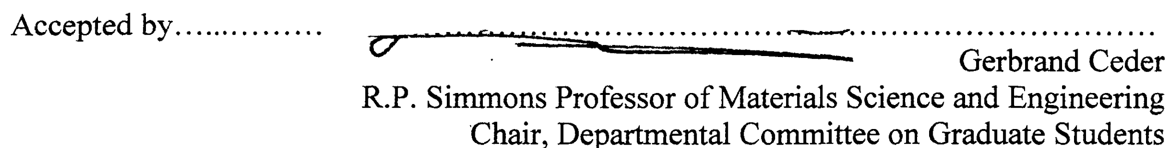

Accepted by..
Gerbrand Ceder
R.P. Simmons Professor of Materials Science and Engineering
Chair, Departmental Committee on Graduate Students

ARCHIVES

Computational Study and Analysis of Structural Imperfections in 1D and 2D Photonic Crystals

By

Karlene Rosera Maskaly

Submitted to the Department of Materials Science and Engineering
on May 25th, 2005 in partial fulfillment of the
requirements for the degree of
Doctor of Philosophy in Materials Science

Abstract

Dielectric reflectors that are periodic in one or two dimensions, also known as 1D and 2D photonic crystals, have been widely studied for many potential applications due to the presence of wavelength-tunable photonic bandgaps. However, the unique optical behavior of photonic crystals is based on theoretical models of perfect analogues. Little is known about the practical effects of dielectric imperfections on their technologically useful optical properties. In order to address this issue, a finite-difference time-domain (FDTD) code is employed to study the effect of three specific dielectric imperfections in 1D and 2D photonic crystals. The first imperfection investigated is dielectric interfacial roughness in quarter-wave tuned 1D photonic crystals at normal incidence. This study reveals that the reflectivity of some roughened photonic crystal configurations can change up to 50% at the center of the bandgap for RMS roughness values around 20% of the characteristic periodicity of the crystal. However, this reflectivity change can be mitigated by increasing the index contrast and/or the number of bilayers in the crystal. In order to explain these results, the homogenization approximation, which is usually applied to single rough surfaces, is applied to the quarter-wave stacks. The results of the homogenization approximation match the FDTD results extremely well, suggesting that the main role of the roughness features is to grade the refractive index profile of the interfaces in the photonic crystal rather than diffusely scatter the incoming light. This result also implies that the amount of incoherent reflection from the roughened quarter-wave stacks is extremely small. This is confirmed through direct extraction of the amount of incoherent power from the FDTD calculations. Further FDTD studies are done on the entire normal incidence bandgap of roughened 1D photonic crystals. These results reveal a narrowing and red-shifting of the normal incidence bandgap with increasing RMS roughness. Again, the homogenization approximation is able to predict these results. The problem of surface scratches on 1D photonic crystals is also addressed. Although the reflectivity decreases are lower in this study, up to a 15% change in reflectivity is observed in certain scratched photonic crystal structures. However, this reflectivity change can be significantly decreased by adding a low index protective coating to the surface of the photonic crystal. Again, application of homogenization theory to these structures confirms its predictive power for this type of imperfection as well. Additionally, the problem of acircular pores in 2D photonic crystals is investigated,

showing that almost a 50% change in reflectivity can occur for some structures. Furthermore, this study reveals trends that are consistent with the 1D simulations: parameter changes that increase the absolute reflectivity of the photonic crystal will also increase its tolerance to structural imperfections. Finally, experimental reflectance spectra from roughened 1D photonic crystals are compared to the results predicted computationally in this thesis. Both the computed and experimental spectra correlate favorably, validating the findings presented herein.

Keywords: Photonic Crystals, Bragg Mirror, Roughness, Imperfections, FDTD

Thesis Supervisor: W. Craig Carter
Title: Lord Foundation Professor of Materials Science and Engineering

Thesis Supervisor: Yoel Fink
Title: Thomas B. King Assistant Professor of Materials Science

Acknowledgements

The Lord is my strength and my shield;
My heart trusts in Him, and I am helped;
Therefore my heart exults,
And with my song I shall thank Him.
(Psalm 28:7 NASB)

There are so many people that have helped me through these past several years. But first and foremost, I would like to acknowledge the one who has played the most critical role in bringing me to this point: my Lord and Savior Jesus Christ. It is through Him that I had the strength, patience, courage, wisdom, and faith to persevere through the most difficult times during graduate school. Indeed, when I first began my studies at MIT, I did not know God. I relied on myself for earthly gains and was often disappointed when I fell short. For some reason, I began attending bible studies during my second year of graduate school. Looking back, I cannot remember any logical reason why I began doing this. But it was during these bible study sessions that I grew in knowledge, and therefore love, of God. And *this* is by far the most valuable thing I have gained from my time in graduate school. In the words of Paul:

...I count all things to be loss in view of the surpassing value of knowing Christ Jesus my Lord ... and count them but rubbish so that I may gain Christ, and may be found in Him, not having a righteousness of my own derived from the Law, but that which is through faith in Christ ... that I may know Him and the power of His resurrection ... in order that I may attain to the resurrection from the dead. (Philippians 2:10-11 NASB)

In addition to the promise of eternal salvation, love and trust in God also brings with it a promise for our life here on earth:

And we know that God causes all things to work together for good to those who love God, to those who are called according to His purpose. (Romans 8:28 NASB)

It was the knowledge of this truth that carried me through one of the most difficult times in my life.

But I would be amiss if I did not also acknowledge the people that God put into my life to help me through these times. First, I would like to thank my husband, Garry. Some people may think that seeing your husband almost every hour of the day both at work and at home would become unbearable. But I truly count that as one of the most special blessings that God gave me during graduate school. I would often trot down to his floor when I was troubled, or bored, or just wanted to get a snack – and being near him would always bring joy to my heart and could easily turn a bad day into a good one. Not only was Garry always there to emotionally help me through difficult times, he also had the knowledge to advise me through those times as well. This also made him one of the most intellectually influential people in my life during my graduate studies.

I would also like to thank the members of the Thursday night GCF bible study and Praisedance, who supported me through their endless prayers and words of encouragement. Indeed, their efforts helped me to focus on that which is most important. I would especially like to thank Shandon Hart, who first introduced me to the bible study and helped both me and Garry grow immensely in our faith. I really want to thank him

for the love, guidance, and fellowship he gave to us, which made graduate school a truly joyful time in my life. He taught us what it means to be a true follower of Christ, and I have yet to meet another person as kind, loving, compassionate, thoughtful, and wise as him and his wife Colleen. Knowing them has been a real blessing.

I would also like to thank my advisor, Prof. Craig Carter. From the beginning, he has been an extraordinary advisor. Two and a half years ago, I came to him with a research idea but, of course, no funding. And even though the research was not in his area of interest, he used money that he could have done anything else with to fund my idea. This was a genuinely magnanimous gesture that I will never forget. Furthermore, he gave me freedom in my research for which I am very grateful. And finally, he and Marty have been extremely kind to me, allowing me to intrude on their home while I was preparing for my preliminary defense. Having an advisor like Craig is extremely rare, and I want to thank him for taking me in as a student even when there wasn't really any room in his group.

I also want to thank all the members of Prof. Carter's group. They all put up with me using basically any CPU in the group I could get my hands on to do my simulations. Rick and Colin were especially patient with me when I had computer problems. Rick spent so much time setting up the machines and trying to install random 3D graphics packages for me that never ended up working. Colin toiled away at ensuring that the machines were secure and, of course, rebooting my computer at MIT when it crashed while I was working at LANL. But I can't forget Ming's late hours that comforted me when I wasn't the only one working late, and also saved me when I needed a computer to be rebooted on Christmas Eve. And of course, there's Ellen. Her unique personality really helped me to laugh and have a life outside of research (e.g. the walk for hunger). She has been a really great friend and I already miss her.

Cody and Kristy Friesen have also been very good friends to Garry and I throughout graduate school. They helped us relax by joining us on trips to Canada and North Carolina, as well as numerous skiing trips. And we had countless hours of fun just going out to dinner or movies or candlepin bowling. Additionally, Cody helped me a lot with some of my initial research, for which I am also grateful.

Even though Prof. Yet-Ming Chiang was not one of my advisors, I want to acknowledge the kindness he and his group showed me during graduate school. Initially, my research involved experiments. However, because Prof. Carter only does computational work, I had no labs in which to do the experiments. So Prof. Chiang allowed me to crowd into his space and use his equipment (at no cost). In addition, the members of his group were very nice to me and treated me like I was also a member of the group. I especially want to thank Steven who was a very good friend to both Garry and me.

I also want to acknowledge the help that Prof. Yoel Fink and his group gave me. Yoel helped me to think more critically about some of the most difficult problems in my thesis. In addition, the members of his group, especially Ofer and Shandon, were kind enough to set aside some of their time to help me with various aspects of my research.

While I was working at LANL, Rick Averitt and James Maxwell served as mentors to me. It is truly amazing how God looked after me for this portion of my research. For here too, I was blessed with two remarkable mentors who spent money to fund me on a project that was outside their field of interest and gave me the freedom to

do the research I needed to finish my thesis. This allowed Garry and me to stay together during his internship and subsequent postdoc appointment at LANL, while still making progress on my thesis.

At Los Alamos, I was also blessed with many friends that prayed for me and helped me through the most difficult part of my thesis – the writing and defense. I especially want to thank Doug and Marci, Kate and Neil, and Jennifer and Neil for their support and prayers.

Lastly, I would like to thank both my parents and Garry's parents for the support they have given me. In their own quiet way, my parents stood by me through both the triumphs and the struggles in my life. Whatever happened, I knew they would always be proud of me. They never pushed me to be something I didn't want to be, and they never expected more from me than what I could do while still being happy. As for Garry's parents, from the first time I met them, they have treated me like I was their own daughter. The love and support they have given me is remarkable, and I am so thankful that they are part of my life.

The research in this thesis was supported by the MIT-Singapore Alliance, the Los Alamos National Laboratory Directed Research and Development Program, and the U.S. Army through the Institute for Soldier Nanotechnologies under contract DAAD-19-02-D-0002 with the U.S. Army Research Office. The content does not necessarily reflect the position of U.S. government, and no official endorsement should be inferred.

Scripture quotations taken from the New American Standard Bible®,
Copyright © 1960, 1962, 1963, 1968, 1971, 1972, 1973,
1975, 1977, 1995 by The Lockman Foundation
Used by permission. (www.Lockman.org)

Table of Contents

List of Figures 11
Glossary of Symbols 19
Chapter 1: Introduction 23
Chapter 2: An Introduction to Electromagnetism and Photonic Crystals 29
2.1 The Maxwell Equations and the Helmholtz Wave Equation 30
2.2 The Behavior of Light at Boundaries 34
2.3 Systems with Multiple Interfaces 42
2.4 Photonic Crystals 46
2.5 Mie Scattering Theory 51
Chapter 3: Methods for Simulating Electromagnetic Responses 57
3.1 1D Transfer Matrix Method 58
3.2 Frequency Domain Method 60
3.3 Finite Difference Time Domain (FDTD) Method 61
Chapter 4: Interfacial Roughness in 1D Photonic Crystals: An FDTD Study 69
4.1 Interfacial Roughness Parameters 72
4.2 Generation of the Roughened Structures 73
4.3 Simulation and Analysis Method 76
4.4 TE Polarization Reflectivity Results 80
4.5 TM Polarization Reflectivity Results 86
4.6 Conclusions 88
Chapter 5: A Scattering Model of Interfacial Roughness 91
5.1 Scattering Model 93
5.2 Implementation of the Model 97
5.3 Results of the Model 100
5.4 Conclusions 104
Chapter 6: Homogenization and Kirchhoff Approximations for Interfacial Roughness 107
6.1 The Homogenization Approximation 108
6.2 The Kirchhoff Approximation 109
6.3 Implementation of the Homogenization Approximation 111
6.4 Implementation of the Kirchhoff Approximation 113
6.5 Results of the Applied Approximations 114
6.6 Conclusions 120
Chapter 7: Calculation of the Scattered Power from Interfacial Roughness 123
7.1 General Form of the Reflected Wave 124
7.2 Calculation of the Scattered Power 126
7.3 Results for the Simulated Structures 130
7.4 Conclusions 136
Chapter 8: Effect of Interfacial Roughness on the Normal Incidence Band Gap 139
8.1 FDTD Reflectivity Results 140
8.2 Homogenization Approximation Reflectivity Results 144
8.3 Conclusions 152

Chapter 9: Surface Scratches on 1D Photonic Crystals 153
9.1 Surface Scratch Parameter 154
9.2 Generation of the Scratched Structures 155
9.3 FDTD Reflectivity Results 157
9.4 Homogenization Approximation Reflectivity Results 163
9.5 Conclusions 163
Chapter 10: Acircular Pores in 2D Photonic Crystals 169
10.1 Determination of Simulation Conditions 172
10.2 Porous Acircularity Parameter 173
10.3 Generation of the Acircular Structures 174
10.4 Simulation Equilibration 177
10.5 Porous Alumina Reflectivity Results 178
10.6 Porous Silicon Reflectivity Results 180
10.7 Conclusions 184
Chapter 11: Experimental Corroboration 187
11.1 Calculated Reflectance Spectra for Two Rough Structures 189
11.2 Proposed Experiments 193
Chapter 12: Conclusions and Future Work 199
Appendix A: Code for the Simulation of Actual Roughened Structures 205
Bibliography 227

List of Figures

Figure 2.1 Reflection and transmission at a plane boundary from a TE polarized incident plane wave. 35

Figure 2.2 TE and TM reflection off a plane boundary with $\mu_i=\mu_t=1.0$, $\varepsilon_i=1.0$, and $\varepsilon_t=4.0$. The Brewster angle, where the TM reflectivity goes to zero, is clear. 41

Figure 2.3 A structure consisting of n interfaces, with the position of each interface given by $z = -d_l$. 42

Figure 2.4 Possible photonic crystal architectures. The dielectric periodicity can occur in one dimension, two dimensions, or three dimensions [Joannopoulos (1995), reprinted with permission from Princeton University Press]. 47

Figure 2.5 Plot of the reflectivity versus wavelength and incident angle for three different photonic crystal structures. The red region in each plot indicates a high reflectivity, while the blue region corresponds to a low reflectivity. All three systems have 4 bilayers with n_1=2.25 and n_2=1.5. However, the volume fraction of the constituent materials changes, as indicated by the t_1 and t_2 values. The center plot corresponds to a quarter-wave stack configuration. 48

Figure 2.6 Plot of the reflectivity versus wavelength and incident angle for three quarter-wave stack structures that all have 4 bilayers and n_1/n_2 = 1.5. As the average refractive index of the structure increases, the width of the bandgap also increases. 49

Figure 2.7 Plot of the reflectivity versus wavelength and incident angle for three quarter-wave stacks that all have 4 bilayers and average refractive indices of 1.875. As the index contrast of the photonic crystal increases, the absolute reflectivity in the bandgap also increases. 50

Figure 2.8 Plot of the reflectivity versus wavelength and incident angle for three quarter-wave stacks with various bilayers. All structures have n_1=2.25 and n_2=1.5. As the number of bilayers increases, the absolute reflectivity in the bandgap also increases. 50

Figure 2.9 Band diagram for a 2D hexagonal lattice (shown in the inset) where the pores/rods have a refractive index of 1.0 and the matrix has a refractive index of 3.5. Also shown is the Brillouin zone with the irreducible section shaded in yellow. The photonic bandgap, where no eigenmodes exist for any wave vector, is shown in yellow.51

Figure 2.10 Angle-dependent scattering intensity as a function of scatterer radius from perpendicularly polarized incident light at wavelength λ_0. As the radius (indicated on top

of each plot) increases, the magnitude of the scattered intensity also increases. The index contrast between the scatterer and the ambient was 1.5 in all cases. 53

Figure 2.11 Angle-dependent scattering intensity as a function of index contrast from perpendicularly polarized incident light at wavelength λ_0. As the index contrast increases, the amount of scattered intensity also increases at every angle. The radius of the scatterer here is $0.10\lambda_0$. 54

Figure 3.1 Schematic of the simulation domain illustrating the unidirectional source that allows separation of the total field and the reflected field. 64

Figure 4.1 One example of a "real world" structure with a large amount of interfacial roughness. This particular structure is a liquid crystal multilayer fabricated by K. Hsiao, et al. [Hsiao (2004), reprinted with permission]. The micrograph on the left is the actual structure, while the schematic on the right is the idealized structure on which the theoretical optical response of the device is based. 70

Figure 4.2 A micrograph of a porous silicon multilayer structure fabricated by Agarwal, et al. (reprinted with permission from V. Agarwal and J. A. del Río, *Applied Physics Letters*, 82, 1512 (2003), copyright 2003, American Institute of Physics). Although this structure does not deviate from its ideal as much as the structure in Fig. 4.1, some amount of interfacial roughness is still evident. 71

Figure 4.3 Schematic of the rough interfaces in the simulated structures illustrating the two parameters that were used to characterize each roughened structure: RMS roughness and RMS wavelength. Also shown is the characteristic periodicity (a) of the photonic crystal. 72

Figure 4.4 Close up of a roughened interface illustrating the process used to create the roughness features. 75

Figure 4.5 Simulation results showing that the size of the domain between periodic walls was sufficiently large. The distance between periodic walls is given by the parameter n_x. An n_x value of 450 was used for all the FDTD simulations presented in this thesis. 77

Figure 4.6 The equilibration of three simulated bilayer systems. The pink region corresponds to the time steps over which the time average was taken in Eq. 4.9. 78

Figure 4.7 The calculated percent change in the TE-polarized normal incidence reflectivity for roughened 4-bilayer quarter-wave stacks with n_1=2.25 and n_2=1.5. Also shown are four example structures for four particular simulations. 81

Figure 4.8 The calculated percent change in reflectivity for several 4-bilayer quarter-wave stack configurations. Empirical fits to the data, with index contrast and number of bilayers as the only parameters, are also shown. 82

Figure 4.9 The calculated percent change in reflectivity for several n_1=2.25, n_2=1.5 quarter-wave stack configurations with varying bilayer numbers. Again, empirical fits to the data, with index contrast and number of bilayers as the only parameters, are also shown. 84

Figure 4.10 The calculated percent change in the TM-polarized normal incidence reflectivity for roughened 4-bilayer quarter-wave stacks with n_1=2.25 and n_2=1.5. 87

Figure 4.11 Comparison of the TE and TM polarization reflectivity results........ 88

Figure 5.1 Schematic illustrating the idea of mimicking the change in reflection and transmission due to the roughness features by replacing the rough surface with a smooth surface and correspondingly modifying its refractive index........ 93

Figure 5.2 Transmissivity vs. the transmitting medium's refractive index (n_t) for an incident medium with refractive index n_i=1.5. Notice that for a given transmissivity (t) there are two possibilities for n_t, one larger than n_i and one smaller. 95

Figure 5.3 Illustration of the four distinct interfaces in the simulated quarter-wave stacks. Each interface results in a different amount of scattering........ 97

Figure 5.4 Schematic illustrating that the incident wavelength for each interface depends on the refractive index of the preceding layer, while the scatterer size remains the same. 99

Figure 5.5 The index modification process applied to a 4-bilayer structure with n_1=2.25, n_2=1.5, and R_{RMS} = 0.1a. 101

Figure 5.6 Index modification results for the same 4-bilayer systems presented in chapter 4. The scatterer sizes reported on the plot have been scaled to the equivalent RMS roughness value. The trends predicted with this model agree with the FDTD results. . 102

Figure 5.7 Index modification results for the same n_1=2.25, n_2=1.5 bilayer systems presented in chapter 4. The scatterer sizes above have been scaled to their equivalent R_{RMS} value. Again, the trends are consistent with those seen from the FDTD results... 103

Figure 5.8 Comparison of the results from the FDTD calculations and the index modification model for the 4-bilayer n_1=2.25, n_2=1.5 system. Although the index modification model correctly predicts the trends seen with the FDTD calculations, it fails to reproduce the actual magnitude and curve shape of the FDTD data. 104

Figure 6.1 Schematic depicting the homogenization approximation for a single rough interface. The dielectric constant in the region of the rough interface is average to produce a smoothed dielectric constant function. The smooth dielectric constant is then approximated with a series of layers........ 109

Figure 6.2 Schematic depicting the Kirchhoff approximation for a single rough interface. The reflectivity of the roughened surface is estimated by averaging the reflection coefficients from several smooth surfaces with varying heights. The height distribution of the smooth structures is equal to the height distribution of the rough interface......... 110

Figure 6.3 Application of the homogenization approximation to the roughened quarter-wave stacks. The dielectric constant is averaged across each row of the input structure. The smooth profile is then converted into a series of layers... 111

Figure 6.4 The averaged refractive index profiles for four R_{RMS} values in the 4-bilayer, n_1=2.25, n_2=1.5 system. For the R_{RMS} values of 0.1453a and 0.1759a, the index of refraction in the approximated structure never reaches the extreme values of 2.25 and 1.5. 112

Figure 6.5 Application of the Kirchhoff approximation to the roughened quarter-wave stacks. The structure is broken up into many structures by taking each column of the rough structure as a separate 1D structure. The reflection coefficients for each structure are calculated and averaged to give the estimated reflectivity of the roughened structure. 113

Figure 6.6 Comparison of the FDTD results with the results of both the homogenization and Kirchhoff approximations for the same 4-bilayer systems presented in chapter 4. The Kirchhoff approximation does a poor job at reproducing the data, but the homogenization approximation matches the FDTD results very well. 115

Figure 6.7 Explanation for why the Kirchhoff approximation under-estimates in some cases and over-estimates in others. The pink region is the quarter-wave tuned wavelength. The dashed line is the FDTD result and the dotted line is the Kirchhoff result.. 117

Figure 6.8 Comparison of the FDTD results with the results of both the homogenization and Kirchhoff approximations for the n_1=2.25, n_2=1.5 systems presented in chapter 4. Again, the Kirchhoff approximation does not predict the FDTD results, while the homogenization approximation matches them very well. 119

Figure 7.1 The simulated reflected wave for one of the roughened structure. As shown, the photonic crystal is positioned behind the wave. Thus, the direction of propagation is out of the page. The periodic boundaries of the domain are located along the yz planes. 127

Figure 7.2 The residual of the fit to the reflected wave. The orientation of the photonic crystal is the same as that in Fig. 7.1. The second order Floquet mode (evanescent) and the incoherent field are apparent.. 128

Figure 7.3 Incoherent power from the 4-bilayer n_1=2.25, n_2=1.5 system. Note that the largest amount of incoherent power is only about 10^{-3} for an incident wave power of 1.0. 130

Figure 7.4 The power in the propagating Floquet mode for the 4-bilayer, n_1=2.25, n_2=1.5 system. Again, note that the maximum power is only 10^{-2} for an incident wave power of 1.0..................... 131

Figure 7.5 The incoherent power from two 4-bilayer systems presented in chapter 4: n_1=2.25, n_2=1.5, and n_1=3.0, n_2=1.5. The higher index contrast system shows slightly more incoherent power, but the magnitude is still extremely small (< 10^{-3}). 132

Figure 7.6 The power in the propagating Floquet mode from the same two 4-bilayer systems shown in Fig. 7.6. Again, the magnitude of the power in both systems is extremely small (< 10^{-2})..................... 133

Figure 7.7 Mie theory prediction of the amount of scattered power from the high-to-low index interfaces in the n_1=2.25, n_2=1.5 and n_1=3.0, n_2=1.5 structures. Notice that both the curve shape and the trend predicted here are consistent with the incoherent power calculation from the FDTD data of the same systems. 134

Figure 7.8 The percentage of reflected power that is carried by scattered light (incoherent plus Floquet mode) for the n_1=2.25, n_2=1.5 and n_1=3.0, n_2=1.5 systems. In the worst case, only 4.5% of the reflected power is carried by scattered light..................... 135

Figure 8.1 The simulated normal incidence reflectance spectra corresponding to several 4-bilayer systems. In all systems, a narrowing and red-shifting of the normal incidence bandgap is apparent..................... 142

Figure 8.2 The percent change in reflectivity (Δr) across the entire normal incidence bandgap for several 4-bilayer systems. The shading indicates the region where the reflectivity of the bandgap is within 10% of its maximum value. Again, the red-shift is apparent in all systems. 143

Figure 8.3 The simulated normal incidence reflectance spectra corresponding to several bilayer systems with n_1=2.25 and n_2=1.5. Again, a narrowing and red-shifting of the bandgap is evident in all systems..................... 145

Figure 8.4 The percent change in reflectivity (Δr) across the entire normal incidence bandgap for several bilayer systems with n_1=2.25 and n_2=1.5. 146

Figure 8.5 The results of the homogenization approximation applied to the 4-bilayer structures presented in Fig. 8.1. Comparison of the two figures shows that the homogenization approximation is in good agreement with the FDTD results. 148

Figure 8.6 The results of the homogenization approximation applied to the 4-bilayer structures presented in Fig. 8.2. 149

Figure 8.7 The results of the homogenization approximation applied to the bilayer systems shown in Fig. 8.3. Again, comparison of the two figures shows that the homogenization approximation is in good agreement with the FDTD results. 150

Figure 8.8 The results of the homogenization approximation applied to the bilayer structures presented in Fig. 8.4. 151

Figure 9.1 The percent change in reflectivity (Δr) for several 4-bilayer quarter-wave stacks with different constituent refractive index values. In addition to structures without protective coatings, structures with coatings were also tested in all of the systems. The coatings had refractive index values of 1.5, 2.0, and 2.5. 158

Figure 9.2 The normal incidence bandgap for a unscratched 4-bilayer n_1=2.25, n_2=1.5 structure with (top) and without (bottom) a protective coating. The coating used for the bottom structure had a refractive index of 1.5 (beneficial coating). 160

Figure 9.3 The effect of surface scratches on the normal incidence bandgap for two 4-bilayer n_1=2.25, n_2=1.5 structures. The top structure has no protective coating, while the bottom structure has an n_c=1.5 coating (beneficial coating). 161

Figure 9.4 Percent change in reflectivity (Δr) for two 4-bilayer structures with n_1=2.25 and n_2=1.5. The top structure has no protective coating, while the bottom structure has an n_c=1.5 coating (beneficial coating). 162

Figure 9.5 The results of the homogenization approximation for the 4-bilayer n_1=2.25, n_2=1.5 structures presented in Fig. 9.1. As with the other studies, the homogenization approximation correctly predicts the FDTD results for the scratched structures. 164

Figure 9.6 The homogenization approximation results for the 4-bilayer, n_1=2.25, n_2=1.5 systems across the entire normal incidence bandgap. The benefit of an $n_c/n_1 < 1.0$ coating is correctly predicted with the approximation. 165

Figure 10.1 Two micrographs of porous alumina. The structure in the left micrograph was produced under controlled anodization conditions, while the structure on the right was fabricated with poor control over the anodization process. 170

Figure 10.2 A micrograph of porous indium phosphide [Carstensen (2005), Christophersen (2005), reprinted with permission]. Although this structure does not deviate from its ideal as much as the porous alumina in Fig. 10.1, some amount of pore acircularity is still evident. 171

Figure 10.3 Schematic of the hexagonal lattice used in the simulations. The Brillouin zone, with the irreducible section shaded, is also shown superimposed on the lattice. The

direction of the incident wave vector is coincident with the M-point of the irreducible Brillouin zone.... 172

Figure 10.4 The TE bandgap in porous alumina, and the TE and TM bandgaps in porous silicon are shown as a function of the pore radius (r) normalized to the center-to-center distance between pores (a). These maps were calculated for the perfect structures using the MPB frequency domain code [Johnson (2001), Johnson (2005)]. 173

Figure 10.5 Schematic illustrating the range of curvature radii that characterize an acircular pore. The RMS acircularity (A_{RMS}) is defined as the RMS radius of curvature deviation from the mean radius of the pore r_0. 174

Figure 10.6 Schematic of the simulated hexagonal lattice illustrating the relevant parameters.... 175

Figure 10.7 Results of the equilibration run for both the 8 row and 12 row structures. The initial large transient behavior is gone by about the 20,000th step in both cases. The shaded region indicated the time steps over which the time-averaging was done in the reflectivity calculation. 179

Figure 10.8 The percent change in the TE polarized reflectivity (Δr) for 8 and 12 row structures of porous alumina. Also shown are two example structures corresponding to the most extreme structural deviations tested in this study.... 180

Figure 10.9 The percent change in the TM polarized reflectivity (Δr) for 8 and 12 row structures of porous silicon. Again, two example structures are shown that corresponding to the most extreme structural deviations tested in this study. The architectural deviations in these structures are much more severe than those in the porous alumina study.... 181

Figure 10.10 The percent change in the TE polarized reflectivity (Δr) for 8 and 12 row structures of porous silicon. Two example structures with much lower A_{RMS} values are shown for comparison with those in Figs. 10.8 and 10.9. 182

Figure 10.11 The percent change in the TM polarized reflectivity from the porous silicon system for A_{RMS} values less than $0.04r_0$.... 183

Figure 10.12 The percent change in the TE polarized reflectivity from the porous silicon system for A_{RMS} values less than $0.04r_0$.... 184

Figure 11.1 One of the “real-world” roughened structures analyzed with the homogenization approximation [Hsiao (2005), reprinted with permission].... 189

Figure 11.2 Experimental reflectance spectrum for the structure shown in Fig. 11.1 [Hsiao (2005), reprinted with permission].... 190

Figure 11.3 Results of the homogenization approximation applied to the structure shown in Fig. 11.1. 191

Figure 11.4 The second roughened structure analyzed with the homogenization approximation [Hsiao (2005), reprinted with permission]. Although it is not apparent to the eye, there are three periodicities built into the structure. 192

Figure 11.5 Experimental reflectance spectrum for the structure shown in Fig. 11.4 [Hsiao (2005), reprinted with permission]. Notice the three distinct reflectivity peaks. 193

Figure 11.6 Results of the homogenization approximation applied to the structure shown in Fig. 11.4. Again, note the three distinct reflectivity peaks. 194

Glossary of Symbols

A_l Field amplitude of the positive z propagating waves in the l layer
A_{RMS} RMS pore acircularity
$\mathbf{B}$ Magnetic flux density vector
B_l Field amplitude of the negative z propagating waves in the l layer
$C_{ang,||}$ Angular cross section of scattered light polarized parallel to the scattering plane
$\mathbf{D}$ Electric displacement vector
$D_z^n(i,j)$ z-component of electric displacement field at the position i,j for the time step n
$\mathbf{E}$ Electric field vector
$E_{||i}$ Incident electric field component that is parallel to the scattering plane
$E_{||s}$ Scattered electric field component that is parallel to the scattering plane
E_c Coherent electric field magnitude
E_{f1} 1st Floquet mode electric field magnitude
E_{fm} mth Floquet mode electric field magnitude
$\mathbf{E}_i$ Incident electric field vector
E_i^t Transverse incident electric field magnitude
$\mathbf{E}_{i0}$ Incident electric field magnitude vector
E_{i0} Total magnitude of incident electric field
E_{ix} x-component magnitude of incident electric field
E_{iy} y-component magnitude of incident electric field
E_{iz} z-component magnitude of incident electric field
E_{lx} x-component magnitude of the electric field in the l layer
E_{ly} y-component magnitude of the electric field in the l layer
E_{lz} z-component magnitude of the electric field in the l layer
$\mathbf{E}_r$ Reflected electric field vector
E_r Reflected electric field
E_r^t Transverse reflected electric field magnitude
$\mathbf{E}_{r0}$ Reflected electric field magnitude vector
$\mathbf{E}_t$ Transmitted electric field vector
E_t^t Transverse transmitted electric field magnitude
$\mathbf{E}_{t0}$ Transmitted electric field magnitude vector
E_{tx} x-component magnitude of transmitted electric field
E_{ty} y-component magnitude of transmitted electric field
E_{tz} z-component magnitude of transmitted electric field
E_y y-component magnitude of total electric field above boundary
$E_z^n(i,j)$ z-component of electric field at the position i,j for the time step n
$\mathbf{H}$ Magnetic field strength vector
H_{ix} x-component magnitude of incident magnetic field
H_{iy} y-component magnitude of incident magnetic field
H_{iz} z-component magnitude of incident magnetic field
H_{lx} x-component magnitude of the magnetic field in the l layer
H_{ly} y-component magnitude of the magnetic field in the l layer

H_{lz} z-component magnitude of the magnetic field in the l layer
H_x x-component magnitude of total magnetic field above boundary
$H_x^n(i,j)$ x-component of magnetic field at the position i,j for the time step n
$H_y^n(i,j)$ y-component of magnetic field at the position i,j for the time step n
H_z z-component magnitude of total magnetic field above boundary
I_{fs} Forward-scattered intensity
$\mathbf{J}$ Electric current density
L Length along boundary
P_{fs} Forward-scattered power from a volume of scatterers
R Fresnel reflection coefficient for a boundary
$R_{(l+1)l}$ Fresnel reflection coefficient between the l layer and the $l+1$ layer (see Eq. 2.82)
R_{RMS} RMS roughness
$\mathbf{S}$ Poynting power vector
$S_{1,2,3,4}$ Amplitude scattering matrix components
T Transmission coefficient for a boundary
T_0 Time at which the time-average is begun
T_a Time over which the time-average is taken
$\mathbf{V}_{(l+1)l}$ Transfer matrix between the l layer and the $l+1$ layer
W_{RMS} RMS roughness wavelength

a Bilayer thickness in 1D photonic crystals, Pore center-to-center distance in 2D photonic crystals
a_n Scattering coefficient involving Riccati-Bessel function
b_n Scattering coefficient involving Riccati-Bessel function
c Speed of light ($= 3 \times 10^8$ meters/second in vacuum)
d_l Position of the l interface
$i_{||}$ Scattered intensity per unit incident intensity for light polarized parallel to the scattering plane
$\mathbf{k}$ Wave vector
k Wave vector magnitude
$\mathbf{k}_i$ Incident field wave vector
k_i Total magnitude of incident field wave vector
k_{ix} x-component magnitude of incident field wave vector
k_{iy} y-component magnitude of incident field wave vector
k_{iz} z-component magnitude of incident field wave vector
k_{lz} z-component magnitude of the field in the l layer
$\mathbf{k}_r$ Reflected field wave vector
k_r Total magnitude of reflected field wave vector
k_{rx} x-component magnitude of reflected field wave vector
k_{ry} y-component magnitude of reflected field wave vector
$\mathbf{k}_t$ Transmitted field wave vector
k_t Total magnitude of transmitted field wave vector
k_{tx} x-component magnitude of transmitted field wave vector
k_{ty} y-component magnitude of transmitted field wave vector
k_{tz} z-component magnitude of transmitted field wave vector
k_{xf1} x-component magnitude of 1st Floquet mode wave vector

k_{xfm} x-component magnitude of mth Floquet mode wave vector
k_{yc} y-component magnitude of coherent electric field wave vector
k_{yf1} y-component magnitude of 1st Floquet mode wave vector
k_{yfm} y-component magnitude of mth Floquet mode wave vector
n Integer
n_1 High refractive index in 1D photonic crystals
n_2 Low refractive index in 1D photonic crystals
n_c Refractive index of protective coating
n_{circ} Number of nodes along the circumference of the pores
n_i Refractive index of incident medium (above boundary)
n_{nodes} Number of nodes on rough interface
n_{pv} Number of peak or valley pairs on rough interface
n_s Time step number
n_T Number of time steps over which time-averaging is done
n_t Refractive index of transmitting medium (below boundary)
num_bilayers Number of bilayers in 1D photonic crystals
num_columns Number of columns of pores in 2D photonic crystals
num_rows Number of rows of pores in 2D photonic crystals
n_x Number of nodes perpendicular to layers in 1D photonic crystals or parallel to columns in 2D photonic crystals
n_y Number of nodes parallel to layers in 1D photonic crystals or parallel to rows in 2D photonic crystals
p_{it} Ratio of incident to transmitted wave vector magnitudes (see Eqs. 2.51 and 2.61)
$p_{(l+1)l}$ Ratio of the wave vectors in the $l+1$ layer and the l layer (see Eqs. 2.78 and 2.79)
$\mathbf{r}$ Radial spatial distance coordinate vector
r Reflectivity
r_0 Mean pore radius of curvature of 2D photonic crystal
r_i Radius of curvature of acircular pore
r_{rough} Reflectivity of 1D photonic crystal with rough interfaces
r_{smooth} Reflectivity of 1D photonic crystal with smooth interfaces (perfect structure)
t Transmissivity
t_1 Thickness of high refractive index layer in quarter-wave tuned 1D photonic crystal
t_2 Thickness of low refractive index layer in quarter-wave tuned 1D photonic crystal
$t_{rt,\lambda}$ Resonant transmission thickness for a wavelength of λ
x x spatial distance coordinate
$x_{pv}^{(1)}$ x-coordinate of the first peak or valley in the pair
$x_{pv}^{(2)}$ x-coordinate of the second peak or valley in the pair
y y spatial distance coordinate
y_0 y-coordinate of the mean interface position
y_i y-coordinate of the actual (rough) interface position
z z spatial distance coordinate

Δr Percent change in reflectivity of imperfect structure from perfect structure
Δt Time step magnitude
Δx Grid cell width in x direction

Δy	Grid cell width in y direction
ε	Dielectric constant
ε_0	Permittivity of free space (= 8.85 × 10^{-12} farad/meter)
ε_i	Dielectric constant of incident medium (above boundary)
ε_l	Dielectric constant of the l layer
ε_t	Dielectric constant of transmitting medium (below boundary)
θ_i	Angle between the incident wave vector and the normal of the boundary
θ_r	Angle between the reflected wave vector and the normal of the boundary
θ_t	Angle between the transmitted wave vector and the normal of the boundary
λ	Wavelength
λ_0	Nodal wavelength corresponding to the quarter-wave tuned wavelength
λ_c	Spatial wavelength corresponding to the quarter-wave tuned wavelength
λ_l	Spatial wavelength of the blue end of the bandgap
λ_{l0}	Nodal wavelength of the blue end of the bandgap
λ_h	Spatial wavelength of the red end of the bandgap
λ_{h0}	Nodal wavelength of the red end of the bandgap
μ	Permeability
μ_0	Permeability of free space (= 4π × 10^{-7} henry/meter)
μ_i	Permeability of incident medium (above boundary)
μ_l	Permeability of the l layer
μ_t	Permeability of transmitting medium (below boundary)
ν	Frequency
ξ	Incoherent field
π_n	Angle-dependent associated Legendre function
ρ	Electric charge density
τ_n	Angle-dependent associated Legendre function
ϕ_c	Phase of coherent field
ϕ_{f1a}	Positive x-direction phase of 1st Floquet mode
ϕ_{f1b}	Negative x-direction phase of 1st Floquet mode
ϕ_{fma}	Positive x-direction phase of mth Floquet mode
ϕ_{fmb}	Negative x-direction phase of mth Floquet mode
ω	Radial frequency

Chapter 1: Introduction

Throughout the field of materials science, there are numerous examples of composite structures that have properties far superior to those of the individual component materials from which they are made. This phenomenon has enabled countless technological advances: from more efficient fuel consumption to better, more effective medical treatments [Watts (1980)]. Indeed, the benefit of composite structures is not limited to mechanical improvements. In fact, research in the area of electromagnetism has led to the production of "optical composites" as well. One example of an optical composite is a photonic crystal. This is a structure consisting of a periodic arrangement of dielectric materials. Alone, these materials would have average optical properties: a typical reflectivity and transmissivity. However, when they are arranged together in a certain way, they can produce a structure that has remarkable properties: a reflectivity that is nearly perfect. This reflectivity can even surpass that of the best natural materials. Furthermore, this behavior can be tuned to occur at any wavelength simply through controlling the dielectric architecture of the structure.

For this reason, photonic crystals have been widely studied for a variety of applications, including low-loss waveguides, omnidirectional (highly reflective at all incident angles) mirrors, and optical band pass filters. Since photonic crystals can have nearly 100% reflectivity at even very large incident angles, they can be used to eliminate losses due to bends in waveguides as well as allow signals to travel very long distances with little attenuation [Grillet (2003), Miura (2003), Temelkuran (2002)]. This property also allows photonic crystals to function as highly reflective mirrors to light at all angles of incidence, which has been utilized in devices such as high-Q laser cavities [Happ (2001), Painter (1999)]. Furthermore, if a defect cavity (a dielectric section that is a different size than the other dielectric units in the crystal) is inserted into a photonic crystal, the resulting device will be a narrow optical filter, allowing only a small range of wavelengths to be transmitted [Costa (2003), Usievich (2002)].

However, the desirable optical properties of photonic crystals are based on theoretical calculations done on perfect structures. In reality, fabricated structures will deviate from these ideal analogues to some extent. In a controlled laboratory setting, where device prototypes such as the ones presented in the above references are fabricated, the amount of structural deviation from perfection will most likely be small. However, on a large-scale manufacturing setting, the same level of control would lead to a significant increase in manufacturing costs. Thus, cost minimization in this setting would correspondingly increase device imperfection, which would decrease the device performance. Thus, some balance between device cost and device performance is needed for the realization of photonic crystal device mass production.

Unfortunately, the quantitative effect of potentially large-scale imperfections on the optical response of photonic crystals is currently unknown. Therefore, it is difficult to determine how much deviation is tolerable for a given photonic crystal device. Furthermore, the effect of design parameters (i.e. the materials and architecture of the structures) on the photonic crystal's tolerance to imperfections is also unknown. Finally, there are many types of imperfections that can occur in photonic crystals. These range from deviations in the periodicity of the crystal (e.g. chirped gratings in 1D photonic crystals [Gerken (2003), Russell (1999)] or deviations in rod/pore center positions in 2D photonic crystals) to changes in the shape/topology of the individual elements in the

structure. Each of these imperfections could have very *different* optical effects, which in turn may be minimized through *different* parameter changes.

Thus, this thesis sets out to address these issues in a systematic manner for three specific types of imperfections in 1D and 2D photonic crystals that conform to the latter type of imperfection mentioned above: interfacial roughness (1D), surface scratches (1D), and acircular pores (2D). Specifically, the questions that will be addressed are:

1. How large of a decrease in a photonic crystal's reflectivity is expected for a given amount of structural deviation?
2. What materials/design parameters optimize a photonic crystal's tolerance to these structural deviations?
3. What is the physical mechanism that leads to the decreased performance in these imperfect photonic crystals?
4. Is there a way to easily predict how much the reflectivity will decrease for a specific imperfect structure?

These questions were investigated computationally, by directly simulating the optical response of imperfect photonic crystal structures. Chapters 2 and 3 provide a brief background of electromagnetism, photonic crystal theory, scattering theory, and specific simulation techniques that are typically used to solve electromagnetic problems. Chapter 4 introduces the problem of interfacial roughness in 1D photonic crystal structures, which is investigated with the Finite Difference Time Domain (FDTD) simulation method. This study finds that the reflectivity decrease in roughened 1D photonic crystals can be as large as 50% at the normal incidence quarter-wave tuned wavelength. However, the results also reveal that this decrease can be mitigated by increasing the index contrast and/or the number of bilayers in the structure. Thus, this chapter answers questions 1 and 2 above for the specific defect of interfacial roughness.

Because the results of chapter 4 oppose the trends that would be predicted from a preliminary scattering theory analysis, chapter 5 introduces a more rigorous scattering model that is applied to the simulated structures from chapter 4. The results of this model reverse the previous scattering theory predictions, producing trends that are consistent with the trends seen in chapter 4. However, the model also suggests that another

mechanism is responsible for the marked decrease in reflectivity that is seen with the roughened structures.

Therefore, chapter 6 approaches the problem of interfacial roughness by applying two approximations to the roughened structures. These approximations (the homogenization and Kirchhoff approximations) are commonly used to infer the amount of coherent scattering from single rough interfaces. Thus, they cannot be used to determine the total amount of scattering from a rough interface because they do not account for the amount of incoherent scattering. Despite this, one of the approximations (the homogenization approximation) accurately reproduces the FDTD results from chapter 4 for most of the roughened structures. This is significant because the homogenization approximation can be much more easily applied to specific experimental structures than the FDTD method, which answers question 3 above. It also provides insight into the physical mechanism leading to the reflectivity decrease (question 4). However, the success of the homogenization approximation implies that the amount of incoherent scattering from these structures is extremely small.

Thus, chapter 7 seeks to verify this surprising result by directly extracting the amount of incoherent power from the FDTD data. Indeed, the results of this analysis reveal that the amount of incoherent power is extremely small for all the structures tested ($< 5\%$ of the total reflected power). Hence, it appears that the homogenization approximation is valid for the roughness scales tested in this study (up to 20% of the photonic crystal periodicity).

Chapter 8 investigates the effect of interfacial roughness on the entire normal incidence bandgap for 1D structures. The FDTD results reveal that there is a narrowing and red-shifting of the bandgap with increasing roughness scales. Furthermore, application of the homogenization approximation again gives reflectivities that agree well with the FDTD simulations, correctly reproducing the red-shifting phenomenon. Thus, the homogenization approximation is determined to be valid over the entire normal incidence bandgap for the roughness scales tested in this thesis (question 4).

Chapter 9 explores the problem of surface scratches, and the utility of protective coatings to reduce their effect, on 1D photonic crystals. Again, the FDTD method is used, and the simulations reveal that a coating with a refractive index less than the top

layer index of the photonic crystal will increase the structure's tolerance to scratches for the entire normal incidence bandgap (questions 1 and 2). As expected, these results are again confirmed with the homogenization approximation (questions 3 and 4).

Chapter 10 branches out to 2D photonic crystals, attacking the problem of acircular pores. The FDTD results again show there can be a large change in the reflectivity (approximately 50%) for certain structures (questions 1 and 2). Although there is no equivalent approximation that can be applied to these 2D structures, the results are consistent with the general trend implied by all the other simulations in this thesis: any design parameter change that will increase the absolute reflectivity of the perfect structure will also increase its tolerance to structural imperfections (question 4).

Finally, chapter 11 compares the results found in this study to actual experimental data from imperfect structures. Specifically, the experimental reflectance spectra from two 1D photonic crystals with very large interfacial roughnesses are compared with homogenization calculations done on the actual micrographs of the structures. In both cases, the reflectance peak shapes, positions, and relative heights correlate favorably, verifying the results found in this thesis. Additionally, more experiments are proposed to further verify these findings.

Although this study has been limited to certain imperfections and certain incidence conditions, the results provide valuable quantitative information on the effect of these imperfections. They also provide a guide for design optimization, as well as a method to easily predict the exact amount of reflectivity decrease from specific structures. Future studies will focus on mapping out the conditions where the homogenization approximation becomes invalid, investigating other incidence conditions and imperfections, and further validating these results through experimental corroboration.

Chapter 2: An Introduction to Electromagnetism and Photonic Crystals

The discovery of electromagnetic waves in the late 19th century opened an entirely new branch of physics. Indeed, this achievement has been judged by many world renowned physicists as one of the greatest accomplishments of mankind. In the words of Richard P. Feynman [Feynman (1965)]:

> *From a long view of the history of mankind - seen from, say, ten thousand years from now - there can be little doubt that the most significant event of the 19th century will be judged as Maxwell's discovery of the laws of electrodynamics.*

Since this discovery, the electromagnetic theory has enabled numerous technologies, such as photonic crystals. The function of these structures is dependent on the behavior of

electromagnetic waves in complex architectures. Thus, an understanding of electromagnetic wave theory is necessary to gain insight into the utility of these devices. There are many references that can be used to obtain an understanding of electromagnetic wave theory and photonic crystals. Most of the derivations presented here have been taken from Kong (2000). However, alternative derivations can be found in other well-established references on electromagnetism, including Bekefi (1990), Bohren (1983), Hecht (1987), Jackson (1999), and Purcell (1985).

2.1 The Maxwell Equations and the Helmholtz Wave Equation

The behavior of light, or electromagnetic waves, in all space and time is governed by a set of equations known as the Maxwell Equations. They were established by James Clerk Maxwell in 1873 as a compilation of empirically observed laws previously shown to describe the behavior of electric and magnetic fields [Maxwell (1954)]. They consist of Ampere's law [Ampere (1820)], Faraday's law [Faraday (1834)], Coulomb's law [Coulomb (1785)], and Gauss' law [Gauss (1839)]:

$$\nabla \times \mathbf{H}(\mathbf{r},t) = \frac{\partial}{\partial t}\mathbf{D}(\mathbf{r},t) + \mathbf{J}(\mathbf{r},t), \tag{2.1a}$$

$$\nabla \times \mathbf{E}(\mathbf{r},t) = -\frac{\partial}{\partial t}\mathbf{B}(\mathbf{r},t), \tag{2.2a}$$

$$\nabla \cdot \mathbf{D}(\mathbf{r},t) = \rho(\mathbf{r},t), \tag{2.3a}$$

$$\nabla \cdot \mathbf{B}(\mathbf{r},t) = 0. \tag{2.4a}$$

Maxwell's contribution to these laws is the addition of the displacement current term (the term involving the time derivative) in Ampere's law.

These equations can be greatly simplified if a few reasonable assumptions are made. **E** and **D**, and **H** and **B** are related by the constitutive relations, which can be quite complicated in general. However, for isotropic materials and low field strengths, these relations simplify to

$$\mathbf{D}(\mathbf{r},t) = \varepsilon(\mathbf{r},\omega)\mathbf{E}(\mathbf{r},t), \tag{2.5}$$

$$\mathbf{B}(\mathbf{r},t) = \mu(\mathbf{r},\omega)\mathbf{H}(\mathbf{r},t). \tag{2.6}$$

Although ε and μ do vary with $\mathbf{r}$ in photonic crystals, the structures are often made of discrete sections of homogeneous materials. Because of this, the $\mathbf{r}$ dependence

of ε and μ can be removed in the equations above and the Maxwell equations can be solved in each section of the photonic crystal in a piece-wise manner with the appropriate ε and μ for that section. This will yield a correct solution for the field in the entire structure provided that the appropriate boundary conditions are enforced at the interfaces between the different dielectric segments. These boundary conditions will be discussed in the next section.

Furthermore, in general, ε and μ are also functions of frequency [Ashcroft (1976), Hunter (2001), Omar (1993)]. The specific dependence is determined by the material that the electric and magnetic fields are permeating. However, practically, only one or a small range of frequencies are important for a given problem. Therefore, assuming there is not a large variation in the values of ε and μ over the relevant frequency range, a single value can be chosen that is appropriate for those frequencies, allowing this dependence to be dropped from the equations above as well. Additionally, in source-free media, meaning there are no free charges or currents, the current and charge density terms are both zero.

Thus, under the assumptions outlined above, the Maxwell equations condense to:

$$\nabla \times \mathbf{H}(\mathbf{r},t) = \varepsilon \frac{\partial}{\partial t}\mathbf{E}(\mathbf{r},t)\,, \tag{2.1b}$$

$$\nabla \times \mathbf{E}(\mathbf{r},t) = -\mu \frac{\partial}{\partial t}\mathbf{H}(\mathbf{r},t)\,, \tag{2.2b}$$

$$\nabla \cdot \mathbf{E}(\mathbf{r},t) = 0\,, \tag{2.3b}$$

$$\nabla \cdot \mathbf{H}(\mathbf{r},t) = 0\,. \tag{2.4b}$$

Although the conditions for these equations may seem extremely restrictive, most materials under most conditions can be described to a first-order using these assumptions.

These equations can now be combined to produce a single equation in terms of only **E** or **H**. This can be done by taking the curl of Eq. 2.2*b* and using the vector identity

$$\mathbf{C} \times (\mathbf{A} \times \mathbf{B}) = \mathbf{A}(\mathbf{C} \cdot \mathbf{B}) - (\mathbf{C} \cdot \mathbf{A})\mathbf{B}\,. \tag{2.7}$$

The resulting equation,

$$\nabla(\nabla \cdot \mathbf{E}(\mathbf{r},t)) - (\nabla \cdot \nabla)\mathbf{E}(\mathbf{r},t) = \nabla \times \left(-\mu \frac{\partial}{\partial t}\mathbf{H}(\mathbf{r},t) \right), \tag{2.8}$$

can be simplified by using Eq. 2.3*b* to eliminate the first term on the left-hand side:

$$\nabla^2 \mathbf{E}(\mathbf{r},t) = \nabla \times \left(\mu \frac{\partial}{\partial t} \mathbf{H}(\mathbf{r},t) \right). \tag{2.9}$$

Furthermore, due to the symmetry of mixed partial derivatives, the spatial derivative on the right-hand side of the equation commutes with the time derivative:

$$\nabla^2 \mathbf{E}(\mathbf{r},t) = \mu \frac{\partial}{\partial t} (\nabla \times \mathbf{H}(\mathbf{r},t)). \tag{2.10}$$

Eq. 2.1*b* can now be substituted into Eq. 2.10, eliminating the magnetic field component of the equation:

$$\nabla^2 \mathbf{E}(\mathbf{r},t) = \mu\varepsilon \frac{\partial^2}{\partial t^2} \mathbf{E}(\mathbf{r},t). \tag{2.11}$$

This equation is known as the homogeneous Helmholtz wave equation. An equivalent equation in terms of **H** can be obtained in a similar manner.

The solutions to Eq. 2.11 take the form

$$\mathbf{E}(\mathbf{r},t) = \mathbf{E}_0 e^{i\mathbf{k}\cdot\mathbf{r}} e^{-i\omega t}, \tag{2.12}$$

where

$$\mathbf{k}^2 = \omega^2 \mu\varepsilon \tag{2.13}$$

through substitution of Eq. 2.12 back into Eq. 2.11. Since the imaginary part of Eq. 2.12 is unphysical, it is understood that the real part is taken to obtain the actual value of the field in space and time.

Close inspection of Eq. 2.12 reveals that this solution gives an electric field which is oscillating in time with a frequency of $\omega/2\pi$ at every point in space. Furthermore, for real values of k (magnitude of **k**), the electric field also oscillates in space with a frequency of $k/2\pi$. Thus, this solution describes an electric field wave that is oscillating in both space and time. At a set point in time, the plane determined by $\mathbf{k}\cdot\mathbf{r}$ = constant describes a constant phase front. The magnitude and direction of the electric field is the same everywhere in this plane, which is perpendicular to the vector **k** for all time. Because of this property, the solution given by Eq. 2.12 is called the uniform plane wave solution for real values of k.

As time increases, this constant phase plane moves in space (i.e. **r** changes to compensate for the increase in t in Eq. 2.12). Because the plane must stay perpendicular to **k** at all times, it must move in the direction of **k**. A little math and geometry reveals

that after a time t_0 has passed, the phase front has moved by an amount equal to $\omega t_0/k$ in the direction of $\mathbf{k}$. Thus, the speed with which the phase front moves is equal to ω/k. From Eq. 2.13, this is equivalently

$$c = \frac{\omega}{k} = \frac{1}{\sqrt{\mu\varepsilon}}. \qquad (2.14)$$

Because $\omega/2\pi$ is the temporal frequency ν, and $2\pi/k$ is the inverse of the spatial frequency (or the wavelength λ), Eq. 2.14 also means

$$c = \nu\lambda . \qquad (2.15)$$

In general, it is possible for both ε and μ to be complex, causing k to have both a real and imaginary component. Such a situation would occur in materials that are lossy, such as conductors. In this case, Eq. 2.12 would have both an oscillatory part and an exponentially decaying part. Thus, in lossy media, the electric field would continue to oscillate, but the magnitude of the field would exponentially decay. The characteristic length of this decay is called the penetration depth of the material. Additionally, it is possible for k to be entirely complex, as in a plasma medium. In this case, the electric field will not oscillate at all but instead will just exponentially decay into the medium. This type of wave is called an evanescent wave. In the case of photonic crystal structures, evanescent waves are mainly important for localized modes, which are not studied in this thesis.

A similar line of reasoning will result in a magnetic field solution equivalent to the electric field solution in Eq. 2.12 from the homogeneous Helmholtz wave equation for the magnetic field. Using these solutions, Eqs. 2.1*b* - 2.4*b* become

$$\mathbf{k} \times \mathbf{H}(\mathbf{r},t) = -\omega\varepsilon\mathbf{E}(\mathbf{r},t), \qquad (2.16)$$

$$\mathbf{k} \times \mathbf{E}(\mathbf{r},t) = \omega\mu\mathbf{H}(\mathbf{r},t), \qquad (2.17)$$

$$\mathbf{k} \cdot \mathbf{E}(\mathbf{r},t) = 0, \qquad (2.18)$$

$$\mathbf{k} \cdot \mathbf{H}(\mathbf{r},t) = 0. \qquad (2.19)$$

Written in this form, it is apparent that the vectors **H**, **E**, and **k** are all perpendicular to one another. Note that this would not necessarily be the case if the constitutive relations (Eqs. 2.5 – 2.6) were not so simple for the particular medium through which the wave is traveling. However, for isotropic, homogeneous media with no free currents or charges,

electromagnetic waves take the form of electric and magnetic field plane waves perpendicular to each other and both moving in the direction of **k**.

One other important quantity to consider in the analysis of electromagnetic waves is the Poynting vector **S**, which indicates the magnitude and direction of the power density being carried by the wave. The complex Poynting vector is defined as

$$\mathbf{S}(\mathbf{r}) = \mathbf{E}(\mathbf{r},t) \times \mathbf{H}(\mathbf{r},t)^{*}. \tag{2.20}$$

For the plane wave solution above, this quantity is independent of time and, as the name implies, is a complex quantity. However, a more physically relevant quantity is the instantaneous Poynting vector, which is real and time-dependent:

$$\mathbf{S}(\mathbf{r},t) = \mathrm{Re}\{\mathbf{E}(\mathbf{r},t)\} \times \mathrm{Re}\{\mathbf{H}(\mathbf{r},t)\}. \tag{2.21}$$

The instantaneous Poynting power can be related to the complex Poynting power by taking a time average to eliminate the time-dependence in Eq. 2.21. The result is that

$$\langle \mathbf{S}(\mathbf{r},t) \rangle = \frac{1}{2}\mathrm{Re}\{\mathbf{S}(\mathbf{r})\}. \tag{2.22}$$

Eqs. 2.20 and 2.21 reveal that the Poynting vector is perpendicular to both **E** and **H**. For the case of the plane wave solution presented above, this means that the electromagnetic power density is carried in the same direction as the propagation (i.e. aligned with **k**). Again, this would not be the case for anisotropic media.

Although Eq. 2.12 is not the only solution to the Maxwell equations, it reasonably describes many naturally encountered conditions, and thus it is widely used in describing the propagation of light in materials. Additionally, this solution can and has been used to accurately predict the optical behavior of actual devices. Because of this and its mathematical simplicity, Eq. 2.12 and the proceeding equations are appropriate for first-order analysis of the optical behavior of photonic structures.

2.2 The Behavior of Light at Boundaries

When an electromagnetic wave hits a plane boundary separating two optically different media, a reflected and transmitted wave will be generated at the boundary, as illustrated in Fig. 2.1. For an incident wave in the form of a plane wave, both the reflected and transmitted waves will also take on the form of plane waves (Eq. 2.12).

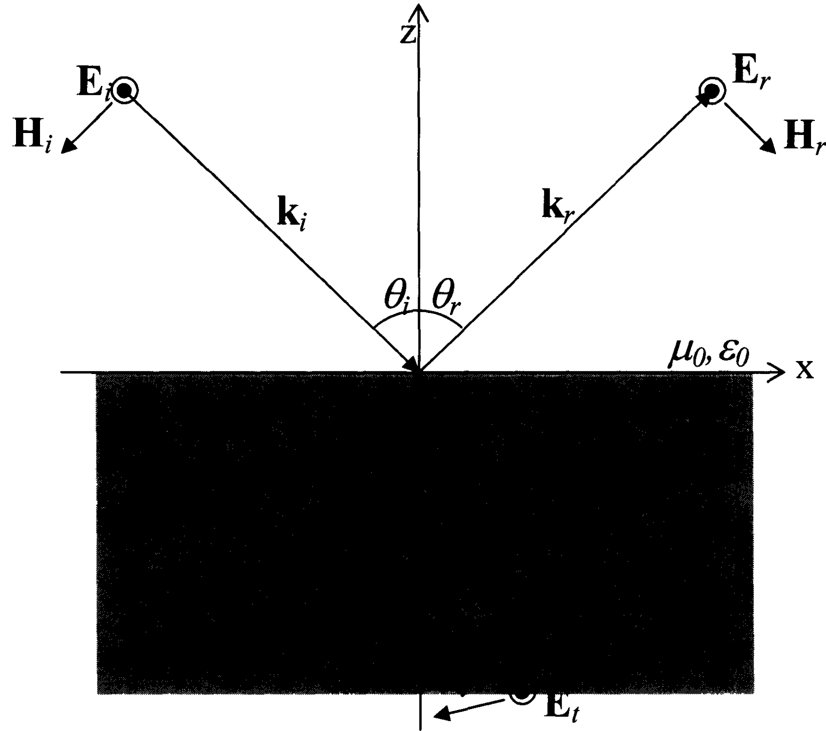

Figure 2.1 Reflection and transmission at a plane boundary from a TE polarized incident plane wave.

Although the **k** vector associated with each wave will be different, there are some general rules that relate the **k** vector components of each wave. Imagine a boundary surface separating two optically different media at the position $z = 0$. The incident, reflected, and transmitted electric field waves can be written

$$\mathbf{E}_i(\mathbf{r},t) = \mathbf{E}_{i0} \exp(i\mathbf{k}_i \cdot \mathbf{r}) e^{-i\omega t}, \tag{2.23}$$

$$\mathbf{E}_r(\mathbf{r},t) = \mathbf{E}_{r0} \exp(i\mathbf{k}_r \cdot \mathbf{r}) e^{-i\omega t}, \tag{2.24}$$

$$\mathbf{E}_t(\mathbf{r},t) = \mathbf{E}_{t0} \exp(i\mathbf{k}_t \cdot \mathbf{r}) e^{-i\omega t}. \tag{2.25}$$

Because the Maxwell equations are true for all space, it can be shown that Eqs. 2.1*b* and 2.2*b* require the tangential components of the electric and magnetic fields to be continuous at the boundary surface for all x and y in the absence of free currents [Kong (2000)]. If E_i^t, E_r^t, and E_t^t denote the magnitude of the tangential components of the electric field vectors, then this means that

$$E_i^t \exp(ik_{ix}x + ik_{iy}y) + E_r^t \exp(ik_{rx}x + ik_{ry}y) = E_t^t \exp(ik_{tx}x + ik_{ty}y). \tag{2.26}$$

In order for this equation to be true for all values of x and y, the following conditions must be met:

$$E_i^t + E_r^t = E_t^t, \tag{2.27}$$

$$k_{ix} = k_{rx} = k_{tx} = k_x, \tag{2.28}$$

$$k_{iy} = k_{ry} = k_{ty} = k_y. \tag{2.29}$$

The requirement that the tangential components of the wave vectors are conserved across a boundary (Eqs. 2.28 and 2.29) are known as the phase-matching conditions.

Because of the phase-matching conditions, k_i, k_r, and k_t must all lie in a common plane. This is called the plane of incidence, and also includes the normal to the boundary surface. Applying Eq. 2.13 to these wave vectors yields

$$k_i^2 = k_r^2 = \omega^2 \mu_i \varepsilon_i, \tag{2.30}$$

$$k_t^2 = \omega^2 \mu_t \varepsilon_t. \tag{2.31}$$

If θ_i, θ_r, and θ_t denote the angle of incidence, reflection, and transmission with respect to the surface normal, then Eq. 2.28 and 2.29 can be rewritten as

$$k_i \sin\theta_i = k_r \sin\theta_r, \tag{2.32}$$

$$k_i \sin\theta_i = k_t \sin\theta_t. \tag{2.33}$$

In light of Eq. 2.30, Eq. 2.32 means that $\theta_i = \theta_r$. Applying Eq. 2.31 to Eq. 2.33 reveals Snell's Law:

$$n_i \sin\theta_i = n_t \sin\theta_t, \tag{2.34}$$

where the definition of the index of refraction (n) was utilized:

$$n = \sqrt{\frac{\mu\varepsilon}{\mu_0\varepsilon_0}}. \tag{2.35}$$

When analyzing a reflection and transmission problem, the orientation of the coordinate system can be chosen arbitrarily in order to simplify the problem. For example, consider a boundary again parallel to the xy plane with the plane of incidence parallel to the xz plane, as shown in Fig. 2.1. For a plane wave incident on this boundary, the Maxwell Equations (Eqs. 2.16 – 2.19) corresponding to this incident wave can be written

$$E_{ix} = \frac{k_{iz}}{\omega\varepsilon_i} H_{iy}, \tag{2.36}$$

$$E_{iz} = -\frac{k_x}{\omega\varepsilon_i} H_{iy}, \tag{2.37}$$

$$E_{iy} = \frac{1}{\omega\varepsilon_i}\left(k_x H_{iz} - k_{iz} H_{ix}\right), \tag{2.38a}$$

$$H_{ix} = -\frac{k_{iz}}{\omega\mu_i} E_{iy}, \tag{2.39}$$

$$H_{iz} = \frac{k_x}{\omega\mu_i} E_{iy}, \tag{2.40}$$

$$H_{iy} = -\frac{1}{\omega\mu_i}\left(k_x E_{iz} - k_{iz} E_{ix}\right), \tag{2.41a}$$

since the y component of the wave vector is zero due to the orientation of the plane of incidence. Eq. 2.38*a* can be rewritten through substitution of the magnetic field components defined in Eqs. 2.39 and 2.40:

$$\left(k_x^2 + k_{iz}^2 - \omega^2 \mu_i \varepsilon_i\right) E_{iy} = 0. \tag{2.38b}$$

Similarly, Eq. 2.41*a* can also be rewritten through the use of Eqs. 2.36 and 2.37:

$$\left(k_x^2 + k_{iz}^2 - \omega^2 \mu_i \varepsilon_i\right) H_{iy} = 0. \tag{2.41b}$$

A similar set of equations can be derived for both the reflected wave in the region above the boundary surface and the transmitted wave in the region below the surface boundary. The above equations are general for any incident plane wave reflection and transmission problem since the orientation of the boundary and incidence planes can be chosen arbitrarily to correspond with the above orientations.

Close inspection of the above equations reveals that Eqs. 2.38*b* – 2.40 govern the behavior of a plane wave with the electric field oriented perpendicular to the plane of incidence, like the one shown in Fig. 2.1. Likewise, Eqs. 2.36 – 2.37 and 2.41*b*, which are completely decoupled from the other equations, govern a wave with the magnetic field oriented perpendicular to the plane of incidence. This allows the reflection and transmission problem at a plane boundary to be analyzed separately for each of these incident wave orientations. Because a wave with any polarization can be constructed

from the superposition of two linearly polarized waves, the solutions for each of these waves can be used to analyze the reflection and transmission of a wave with any polarization at a plane boundary. A wave with an electric field oriented perpendicular to the plane of incidence is called a TE wave, while a wave with a magnetic field perpendicular to the plane of incidence is called a TM wave. Further review of the above equations reveals that Eqs. 2.38 – 2.40*b* can be obtained from Eqs. 2.36 – 2.37 and 2.41*b* by simply replacing E with H, H with $-E$, and exchanging μ and ε. This is known as the principle of duality.

The TE wave solution can be obtained from Eqs. 2.38*b* – 2.40 for the incident, reflected, and transmitted field with the appropriate boundary conditions. In the region above the boundary, the magnitude of the total field is a superposition of the incident and reflected fields:

$$E_y = E_{i0} \exp\left(-ik_{iz}z + ik_x x\right) + R E_{i0} \exp\left(ik_{iz}z + ik_x x\right). \tag{2.42}$$

Eqs. 2.39 and 2.40 can be used to derive the magnitude of the magnetic field in this region:

$$H_x = -\frac{k_{iz}}{\omega\mu_i}\left(-E_{i0}\exp\left(-ik_{iz}z + ik_x x\right) + RE_{i0}\exp\left(ik_{iz}z + ik_x x\right)\right), \tag{2.43}$$

$$H_z = \frac{k_x}{\omega\mu_i}\left(E_{i0}\exp\left(-ik_{iz}z + ik_x x\right) + RE_{i0}\exp\left(ik_{iz}z + ik_x x\right)\right). \tag{2.44}$$

In the region below the boundary, the magnitude of the total field is simply the magnitude of the transmitted wave:

$$E_{ty} = T E_{i0} \exp\left(-ik_{tz}z + ik_x x\right). \tag{2.45}$$

Again, the magnetic field is obtained from Eqs. 2.39 and 2.40:

$$H_{tx} = \frac{k_{tz}}{\omega\mu_t}\left(T E_{i0}\exp\left(-ik_{tz}z + ik_x x\right)\right), \tag{2.46}$$

$$H_{tz} = \frac{k_x}{\omega\mu_t}\left(T E_{i0}\exp\left(-ik_{tz}z + ik_x x\right)\right). \tag{2.47}$$

With the position of the boundary at $z = 0$, the condition that the tangential field components must be continuous across the boundary requires

$$1 + R = T, \tag{2.48}$$

$$\frac{k_{iz}}{\mu_i}(1-R)=\frac{k_{tz}}{\mu_t}T. \tag{2.49}$$

These equations can be solved to find the reflection and transmission coefficients for TE waves:

$$R=\frac{1-p_{it}}{1+p_{it}}, \tag{2.50}$$

$$T=\frac{2}{1+p_{it}}, \tag{2.51}$$

where

$$p_{it}=\frac{k_{tz}\mu_i}{k_{iz}\mu_t}. \tag{2.51}$$

Eq. 2.38*b* requires

$$k_x^2+k_{iz}^2=\omega^2\mu_i\varepsilon_i, \tag{2.52}$$

which is equivalent to Eq. 2.13 since $k_y = 0$. Thus, this restates the magnitude of **k** and can be used to find k_{iz} when the angle of incidence is known. Snell's Law can be used to find the angle of transmission, allowing the equivalent of Eq. 2.52 for the transmitted wave to be used to obtain k_{tz}. When this is done, p_{it} becomes

$$p_{it}=\sqrt{\frac{\mu_i\varepsilon_t}{\mu_t\varepsilon_i}}\left(\frac{\sqrt{n_t^2-n_i^2\sin^2\theta_i}}{n_t\cos\theta_i}\right). \tag{2.53}$$

The time averaged Poynting vector for the incident, reflected, and transmitted waves can be obtained from the field expressions in Eqs. 2.42 – 2.47. As with the **k** vector, the Poynting vector is confined to the *xz* plane. From Eq. 2.20,

$$\mathbf{S}(\mathbf{r})=\mathbf{E}(\mathbf{r},t)\times\mathbf{H}(\mathbf{r},t)^*=E_yH_z^*\hat{\mathbf{x}}-E_yH_x^*\hat{\mathbf{z}}. \tag{2.54}$$

Applying Eq. 2.22 and assuming that all **k** vectors are real, the time averaged Poynting vector can be calculated for each field, resulting in

$$\left\langle\mathbf{S}(\mathbf{r},t)\right\rangle_i=\frac{|E_{i0}|^2}{2\omega\mu_i}\left(k_x\hat{\mathbf{x}}-k_{iz}\hat{\mathbf{z}}\right), \tag{2.55}$$

$$\left\langle\mathbf{S}(\mathbf{r},t)\right\rangle_r=\frac{|R|^2|E_{i0}|^2}{2\omega\mu_i}\left(k_x\hat{\mathbf{x}}+k_{iz}\hat{\mathbf{z}}\right), \tag{2.56}$$

$$\langle \mathbf{S}(\mathbf{r},t)\rangle_t = \frac{|T|^2 |E_{i0}|^2}{2\omega\mu_t}(k_x\hat{\mathbf{x}} - k_{tz}\hat{\mathbf{z}}). \tag{2.57}$$

The reflectivity of the boundary can now be calculated. This is simply the ratio of the normal components of the incident and reflected power:

$$r = \frac{\hat{\mathbf{z}}\cdot\langle \mathbf{S}(\mathbf{r},t)\rangle_r}{-\hat{\mathbf{z}}\cdot\langle \mathbf{S}(\mathbf{r},t)\rangle_i} = R^2. \tag{2.58}$$

Similarly, the transmissivity of the boundary can be found:

$$t = \frac{-\hat{\mathbf{z}}\cdot\langle \mathbf{S}(\mathbf{r},t)\rangle_t}{-\hat{\mathbf{z}}\cdot\langle \mathbf{S}(\mathbf{r},t)\rangle_i} = \frac{k_{tz}\mu_i}{k_{iz}\mu_t}T^2 = p_{it}T^2. \tag{2.59}$$

In light of Eqs. 2.50 and 2.51, it can be seen that

$$r + t = 1, \tag{2.60}$$

which is simply a statement of power conservation (i.e. the sum of the reflected and transmitted power must equal the incident power). The tangential components of the power do not factor into the derivation of Eq. 2.60 because they are conserved across the boundary by virtue of the phase matching conditions.

The TM wave solutions can be obtained in a similar manner. However, a much easier method of deriving the solutions is found by invoking the principle of duality on the TE expressions that have already been calculated above. Thus, the reflection and transmission coefficients for TM waves are equal to those for TE waves with the exception that

$$p_{it} = \frac{k_{tz}\varepsilon_i}{k_{iz}\varepsilon_t}. \tag{2.61}$$

The expressions for the reflectivity and the transmissivity remain the same as Eqs. 2.58 – 2.59.

When r is plotted versus the angle of incidence for TE and TM waves, as in Fig. 2.2, it is interesting to note that there is an incident angle where r goes to zero for TM waves. This is known as the Brewster angle. At this angle, there is no reflected wave and all the incident power is transmitted through the boundary. It is also interesting to note that the opposite (total reflection) is not possible if the index of refraction of the

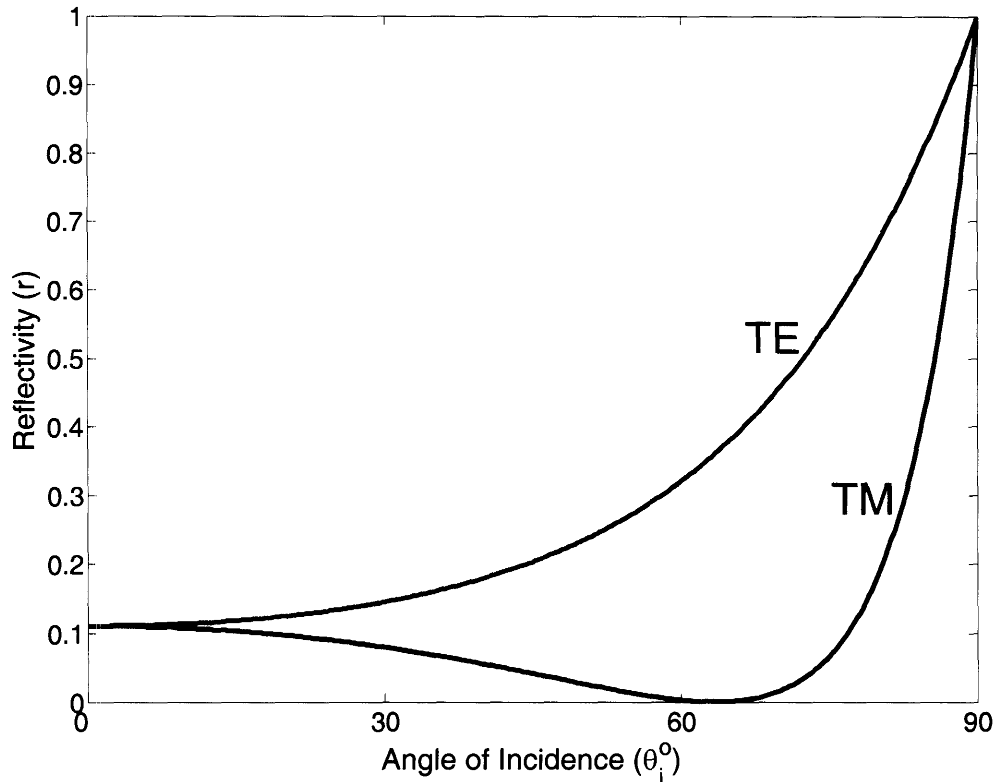

Figure 2.2 TE and TM reflection off a plane boundary with μ_i=μ_t=1.0, ε_i=1.0, and ε_t=4.0. The Brewster angle, where the TM reflectivity goes to zero, is clear.

transmission material is greater than that of the incident material (i.e. a wave hitting a material from air or vacuum). From Eq. 2.50, this would require p_{it} to be equal to zero, which can only occur if the transmission material refractive index is infinite. Although good conductors approach this limit, only perfect conductors, such as superconductors, can have a refractive index equal to infinity. Certain materials can have reflectivities that approach unity, such as gold. However, this is due to the fact that the index of refraction of gold is largely imaginary and therefore, the magnitude of R is close to one. Thus, materials do exist that have almost perfect reflectivity. However, this behavior is only valid over a fixed wavelength range, which is determined by the frequency behavior of the material's refractive index.

Nevertheless, it is theoretically possible to build a composite structure that will have nearly perfect reflectivity over any frequency range. Moreover, this composite can be built from materials that do not have very high reflectivities on their own. However, this structure, known as a photonic crystal, has a very specific architecture, which will be

addressed in section 2.4. First, an understanding of the behavior of light in a system with multiple interfaces must be addressed.

2.3 Systems with Multiple Interfaces

The reflectivity from a system with many plane boundaries can also be calculated by building on the concepts presented in Section 2.2. Consider the structure with n interfaces shown in Fig. 2.3, where the position of each interface is given by $z = -d_l$. In general, each layer in the system will have different optical properties, given by μ_l and ε_l. The region above the first interface, as well as the region below the last interface, are semi-infinite and have optical constants of μ_0 and ε_0, and μ_t and ε_t, respectively. As for a single plane boundary, the equations that govern the behavior of the electric and magnetic field in this system can be separated into TE and TM components. Thus, in analogy to Eqs. 2.36 through 2.41, the electric and magnetic fields in each layer will conform to the equations:

$$E_{lx} = \frac{k_{lz}}{\omega\varepsilon_l} H_{ly}, \tag{2.62}$$

$$E_{lz} = -\frac{k_x}{\omega\varepsilon_l} H_{ly}, \tag{2.63}$$

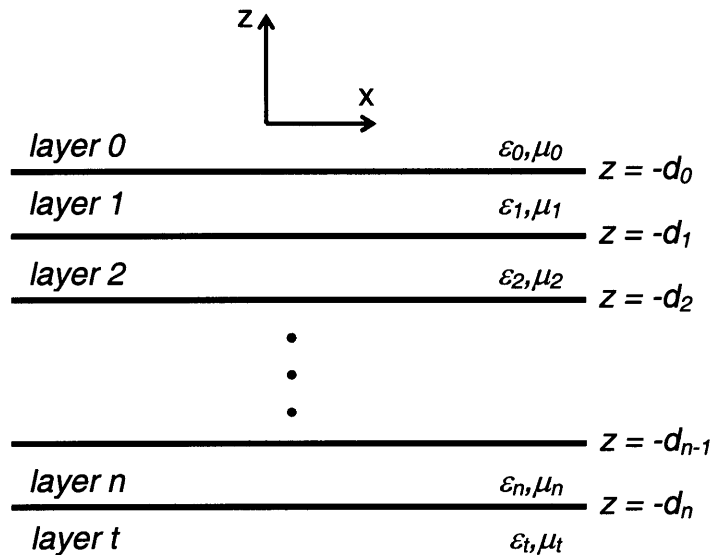

Figure 2.3 A structure consisting of n interfaces, with the position of each interface given by $z = -d_l$.

$$E_{ly} = \frac{1}{\omega \varepsilon_l}\left(k_x H_{lz} - k_{lz} H_{lx}\right), \qquad (2.64a)$$

$$H_{lx} = -\frac{k_{lz}}{\omega \mu_l} E_{ly}, \qquad (2.65)$$

$$H_{lz} = \frac{k_x}{\omega \mu_l} E_{ly}, \qquad (2.66)$$

$$H_{ly} = -\frac{1}{\omega \mu_l}\left(k_x E_{lz} - k_{lz} E_{lx}\right). \qquad (2.67a)$$

As before, Eqs. 2.64*a* and 2.67*a* can be written using Eqs. 2.62 – 2.63, and 2.65 – 2.66:

$$\left(k_x^2 + k_{lz}^2 - \omega^2 \mu_l \varepsilon_l\right) E_{ly} = 0, \qquad (2.64b)$$

$$\left(k_x^2 + k_{lz}^2 - \omega^2 \mu_l \varepsilon_l\right) H_{ly} = 0. \qquad (2.67b)$$

The TE polarized wave is governed by Eqs. 2.64*b* through 2.66, while the TM polarized wave is governed by Eqs. 2.62, 2.63, and 2.67*b*.

The field within each layer of the structure will be a combination of many transmitted and reflected fields at the multiple interfaces. However, in general, this total field can be broken up into reflected/transmitted plane waves traveling in the positive z direction and reflected/transmitted plane waves traveling in the negative z direction. Furthermore, all the plane waves traveling in the positive z direction can be combined mathematically into one wave with an amplitude A_l. Similarly, all the plane waves traveling in the negative z direction can be combined into one wave with amplitude B_l. Thus, the magnitude of the total field in each layer is a superposition of these two combined waves. For a TE wave, the electric and magnetic fields in each layer can be written as

$$E_{ly} = B_l \exp\left(-ik_{lz}z + ik_x x\right) + A_l \exp\left(ik_{lz}z + ik_x x\right), \qquad (2.68)$$

$$H_{lx} = -\frac{k_{lz}}{\omega \mu_l}\left(-B_l \exp\left(-ik_{lz}z + ik_x x\right) + A_l \exp\left(ik_{lz}z + ik_x x\right)\right), \qquad (2.69)$$

$$H_{lz} = \frac{k_x}{\omega \mu_l}\left(B_l \exp\left(-ik_{lz}z + ik_x x\right) + A_l \exp\left(ik_{lz}z + ik_x x\right)\right). \qquad (2.70)$$

The x component of the wave vector is the same in all layers due to the phase-matching conditions (Eq. 2.28). Thus, it does not need to be designated with a layer subscript.

For an incident plane wave of the form

$$E_{iy} = E_{i0} \exp(-ik_{iz}z + ik_x x), \tag{2.71}$$

the overall reflection and transmission coefficient of the multilayer structure can be related to the A and B coefficients in the surrounding semi-infinite regions. In the semi-infinite region above the top interface,

$$A_0 = RE_{i0}, \tag{2.72}$$

$$B_0 = E_{i0}. \tag{2.73}$$

Likewise, for the semi-infinite region below the bottom interface, designated as the t ($=n+1$) layer,

$$A_t = 0, \tag{2.74}$$

$$B_t = TE_{i0}. \tag{2.75}$$

The amplitude A_t is zero because there is no way for a positive z direction wave to be traveling in this medium without some boundary below it that could reflect the negative z direction light back up through it.

The coefficients A_l and B_l for each layer are related to the coefficients A_{l+1} and B_{l+1} in the next layer through the boundary conditions at the interface located between them (at $z = -d_l$). These boundary conditions require the tangential components of the field to be continuous across the interface. For TE polarized waves, this means that the E_y and H_x fields in neighboring layers must be equal at the boundaries. Thus, for the l and $l+1$ layers,

$$B_l \exp(ik_{lz}d_l) + A_l \exp(-ik_{lz}d_l) = B_{l+1} \exp(ik_{(l+1)z}d_l) + A_{l+1} \exp(-ik_{(l+1)z}d_l), \tag{2.76}$$

$$\begin{aligned} &\frac{k_{lz}}{\omega\mu_l}\left(-B_l \exp(ik_{lz}d_l) + A_l \exp(-ik_{lz}d_l)\right) \\ &\qquad = \frac{k_{(l+1)z}}{\omega\mu_{l+1}}\left(-B_{l+1} \exp(ik_{(l+1)z}d_l) + A_{l+1} \exp(-ik_{(l+1)z}d_l)\right) \end{aligned}. \tag{2.77a}$$

The latter equation can be rewritten using the change of variables introduced in Eq. 2.51:

$$\begin{aligned} &p_{(l+1)l}\left(-B_l \exp(ik_{lz}d_l) + A_l \exp(-ik_{lz}d_l)\right) \\ &\qquad = -B_{l+1} \exp(ik_{(l+1)z}d_l) + A_{l+1} \exp(-ik_{(l+1)z}d_l) \end{aligned}, \tag{2.77b}$$

where

$$p_{(l+1)l} = \frac{k_{lz}\mu_{l+1}}{k_{(l+1)z}\mu_l}. \tag{2.78}$$

An equivalent derivation can be done for TM waves, which leads to the same expressions relating A_l and B_l to A_{l+1} and B_{l+1}. The only difference is that $p_{(l+1)l}$ has a modified definition:

$$p_{(l+1)l} = \frac{k_{lz}\varepsilon_{l+1}}{k_{(l+1)z}\varepsilon_l}. \tag{2.79}$$

If the amplitudes A_l and B_l in the l layer are known, Eqs. 2.76 and 2.77 only have two unknowns: A_{l+1} and B_{l+1}. Thus, in this case, these amplitudes can be directly calculated by solving Eqs. 2.76 and 2.77:

$$A_{l+1}\exp\left(-ik_{(l+1)z}d_l\right) = \frac{1}{2}\left(1 + p_{(l+1)l}\right)\left(A_l\exp\left(-ik_{lz}d_l\right) + R_{(l+1)l}B_l\exp\left(ik_{lz}d_l\right)\right), \tag{2.80}$$

$$B_{l+1}\exp\left(ik_{(l+1)z}d_l\right) = \frac{1}{2}\left(1 + p_{(l+1)l}\right)\left(R_{(l+1)l}A_l\exp\left(-ik_{lz}d_l\right) + B_l\exp\left(ik_{lz}d_l\right)\right), \tag{2.81}$$

where

$$R_{(l+1)l} = \frac{1 - p_{(l+1)l}}{1 + p_{(l+1)l}}. \tag{2.82}$$

Eqs. 2.80 and 2.81 can be combined into a single matrix equation:

$$\begin{bmatrix} A_{l+1}\exp\left(-ik_{(l+1)z}d_{l+1}\right) \\ B_{l+1}\exp\left(ik_{(l+1)z}d_{l+1}\right) \end{bmatrix} = \mathbf{V}_{(l+1)l}\cdot\begin{bmatrix} A_l\exp\left(-ik_{lz}d_l\right) \\ B_l\exp\left(ik_{lz}d_l\right) \end{bmatrix}, \tag{2.83}$$

where

$$\mathbf{V}_{(l+1)l} = \frac{1}{2}\left(1 + p_{(l+1)l}\right)\begin{bmatrix} \exp\left(-ik_{(l+1)z}\left(d_{l+1} - d_l\right)\right) & R_{(l+1)l}\exp\left(-ik_{(l+1)z}\left(d_{l+1} - d_l\right)\right) \\ R_{(l+1)l}\exp\left(ik_{(l+1)z}\left(d_{l+1} - d_l\right)\right) & \exp\left(ik_{(l+1)z}\left(d_{l+1} - d_l\right)\right) \end{bmatrix}. \tag{2.84}$$

The matrix $\mathbf{V}_{(l+1)l}$ is called the transfer matrix or forward-propagating matrix for layer l in the multilayer structure. If the geometry of the structure is known, it can be used to find the wave amplitudes in any layer. Most often, however, the reflection and transmission coefficients (Eqs. 2.72 – 2.75) of the entire structure are desired. The transfer matrix can be used to find these parameters in the following way. The wave amplitude in the m layer is related to the wave amplitude in the l ($<< m$) layer by multiplying the transfer matrices of all the intervening layers:

$$\begin{bmatrix} A_m \exp(-ik_{mz}d_m) \\ B_m \exp(ik_{mz}d_m) \end{bmatrix} = \mathbf{V}_{m(m-1)} \cdot \mathbf{V}_{(m-1)(m-2)} \cdots \mathbf{V}_{(l+2)(l+1)} \cdot \mathbf{V}_{(l+1)l} \cdot \begin{bmatrix} A_l \exp(-ik_{lz}d_l) \\ B_l \exp(ik_{lz}d_l) \end{bmatrix}. \quad (2.85)$$

Thus, combining Eqs. 2.72 through 2.75 with Eq. 2.85, the amplitudes in the t layer can be related to the amplitudes in the 0 layer by:

$$\begin{bmatrix} 0 \\ T \end{bmatrix} = \mathbf{V}_{t0} \begin{bmatrix} R\exp(-ik_{iz}d_0) \\ \exp(ik_{iz}d_0) \end{bmatrix}, \quad (2.86)$$

where

$$\mathbf{V}_{t0} = \mathbf{V}_{tn} \cdot \mathbf{V}_{n(n-1)} \cdots \mathbf{V}_{21} \cdot \mathbf{V}_{10}. \quad (2.87)$$

The matrix $\mathbf{V}_{t0}$ is fully determined by the optical parameters and thicknesses of the layers in the structure. Thus, if the geometry of the structure is known, Eq. 2.86 can be used to calculate R and T. The reflectivity of the structure can then be calculated using Eq. 2.58. Since power conservation still must hold for this structure, once the reflectivity is known, the transmissivity can be found by utilizing Eq. 2.60. Therefore, this method can be used to determine the reflectivity and transmissivity of a 1D multilayer structure with an arbitrary geometry.

2.4 Photonic Crystals

As mentioned at the end of Section 2.2, photonic crystals are dielectric composite structures that have architectural arrangements resulting in nearly perfect reflectivity. This specific arrangement requires the constituent dielectric sections to be arranged periodically. Photonic crystals are therefore simply periodic arrangements of dielectric materials [Ho (1990), John (1991), Joannopoulos (1995), Joannopoulos (1997), Noda (2002), Yablonovitch (1993)]. They can be one-dimensional (1D), two-dimensional (2D), or three-dimensional (3D) (see Figure 2.4). Incident light with a wavelength λ and at an angle θ will scatter off the various interfaces in the crystal. For a given photonic crystal geometry, light with certain wavelengths and incident angles scatters off the interfaces in such a way that very little light is transmitted and nearly total reflection occurs. This range of wavelengths and incident angles is called the photonic bandgap.

For 1D photonic crystals, this phenomenon can be explored through the transfer matrix technique discussed in Section 2.3 [Hecht (1987), Kong (2000), Yeh (1988)].

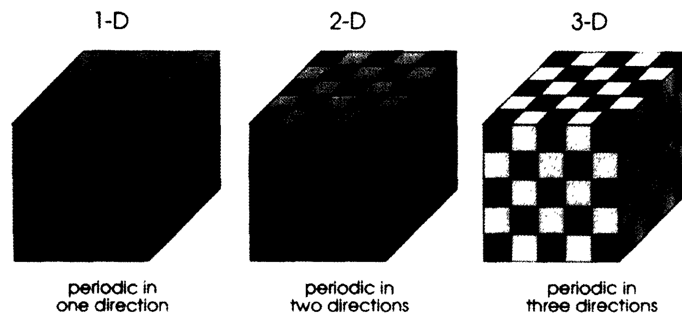

Figure 2.4 Possible photonic crystal architectures. The dielectric periodicity can occur in one dimension, two dimensions, or three dimensions [Joannopoulos (1995), reprinted with permission from Princeton University Press].

This is because 1D photonic crystals are simply multilayer stacks that are made up of a series of periodic bilayers. Each bilayer consists of a layer with a high refractive index and a layer with a low refractive index. Thus, using Eqs. 2.78 through 2.87, it is fairly straight-forward to write a simple code that will calculate the reflectivity and transmissivity for a given 1D photonic crystal geometry [Maskaly (2001)]. Figs. 2.5 through 2.8 show the results of these calculations for several 1D photonic crystal configurations. These are plots of the reflectivity of the photonic crystal versus incident angle and wavelength. Note that the results of both the TE and TM polarizations are shown. These polarizations are equivalent at an incidence angle of 0°.

In all plots, there is a range of wavelengths and incident angles where the reflectivity approaches one. This region corresponds to the photonic bandgap of the crystal. In general, there will be other photonic bandgaps which are located at harmonic wavelengths of this primary bandgap. Most often, however, the primary bandgap is the one that is utilized in photonic crystal devices. An alternative plot to the ones shown in the figures can be obtained by converting the incident wavelength to a frequency and the incident angle to the x-component of the wave vector (k_x), which is conserved across the multilayer structure due to the phase-matching conditions. This alternative plot is preferred for depicting the bandgap in infinite structures. It will be addressed again when 2D photonic crystals are discussed later in this chapter.

The variations shown in Figs. 2.5 through 2.8 reveal that there are several key parameters that can be controlled to optimize the primary bandgap of a photonic crystal [Winn (1998)]. Fig. 2.5 shows that changing the volume fraction of the constituent materials shifts the primary bandgap and also changes its width. The width will be maximized when the volume fractions correspond to the quarter-wave tuned condition. This is where the thicknesses of each layer are given by

$$t_1 = \frac{\lambda_c}{4n_1}, \tag{2.88}$$

$$t_2 = \frac{\lambda_c}{4n_2}. \tag{2.89}$$

A photonic crystal with layer thicknesses that conform to Eqs. 2.88 and 2.89 is called a quarter-wave stack. The wavelength, λ_c, to which the photonic crystal is tuned is called the quarter-wave tuned wavelength. This wavelength will lie roughly at the center of the primary bandgap. Because the Maxwell Equations are valid at any length scale, the position of the primary bandgap can be controlled by simply manipulating the thicknesses of the layers in the quarter-wave stack. This allows photonic crystals to be extremely useful reflectors at any desired wavelength.

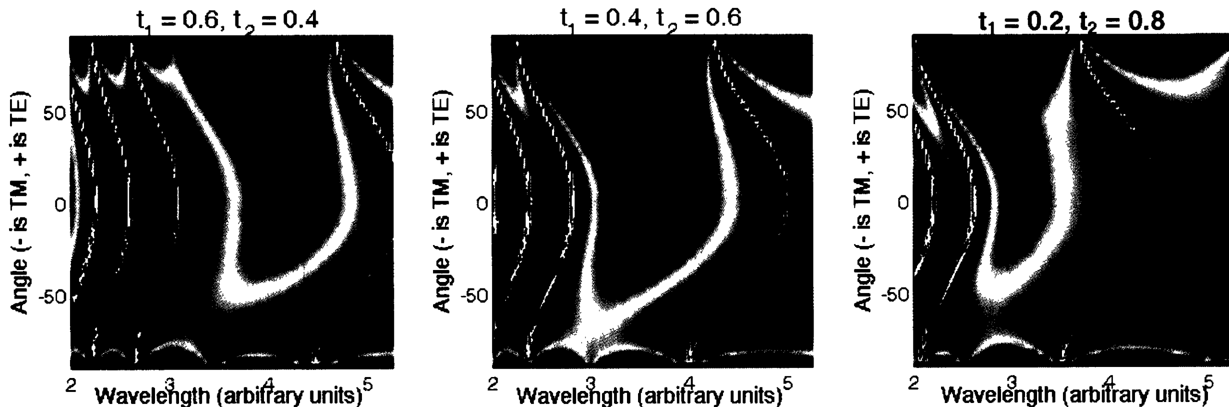

Figure 2.5 Plot of the reflectivity versus wavelength and incident angle for three different photonic crystal structures. The red region in each plot indicates a high reflectivity, while the blue region corresponds to a low reflectivity. All three systems have 4 bilayers with n_1=2.25 and n_2=1.5. However, the volume fraction of the constituent materials changes, as indicated by the t_1 and t_2 values. The center plot corresponds to a quarter-wave stack configuration.

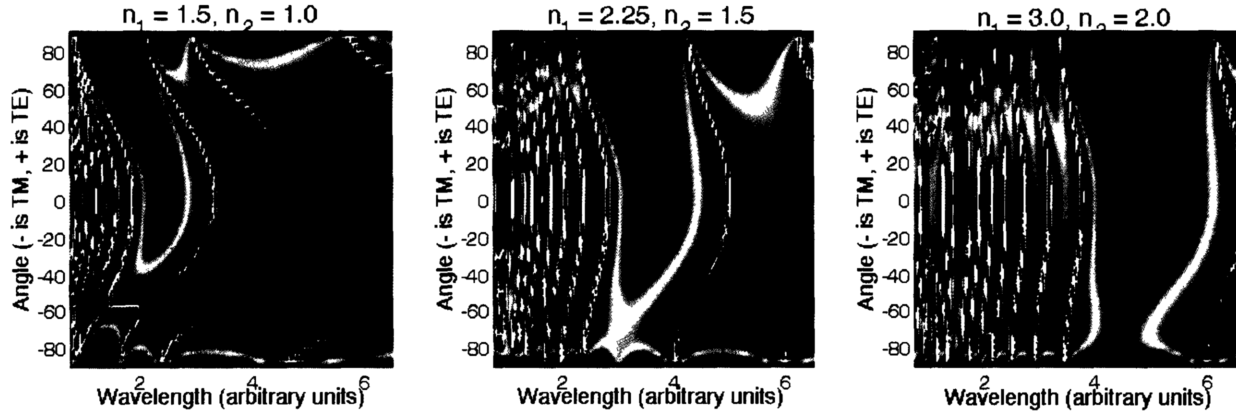

Figure 2.6 Plot of the reflectivity versus wavelength and incident angle for three quarter-wave stack structures that all have 4 bilayers and $n_1/n_2 = 1.5$. As the average refractive index of the structure increases, the width of the bandgap also increases.

Fig. 2.6 reveals that increasing the average index of the materials in a photonic crystal will also increase the width of the primary bandgap. In fact, the bandgap can become so large, that an external omnidirectional reflectance window will open [Winn (1998)]. This corresponds to a range of wavelengths that has nearly perfect reflectivity at all incident angles. Figs. 2.7 and 2.8 show that increasing both the refractive index contrast (n_1/n_2) and the number of bilayers in the photonic crystal structure will increase the absolute reflectivity in the bandgap. Thus, in general, a photonic crystal device's performance will be optimized at a given wavelength if the average index, the index contrast, and the number of bilayers are all made as large as possible.

For 2D and 3D photonic crystals, the above analysis using the transfer matrix is no longer valid because the structure is not one-dimensional. Instead, the bandgap must be determined by solving the Maxwell Equations for an infinite structure using an eigenvalue approach. This technique will not be addressed in detail in this thesis, but more information on it can be found in Joannopoulos, et al. (1995). This approach is very similar to the traditional analysis done for semiconductor electronic bandgaps [Ashcroft (1976), Kittel (1996), Omar (1993)].

Briefly, the Helmholtz wave equation can be seen as an eigenvalue equation for time harmonic fields [Joannopoulos (1995), Johnson (2001), Zhang (1990)]:

$$\nabla \times \left(\frac{1}{\varepsilon} \nabla \times \mathbf{H}(\mathbf{r}) \right) = \left(\frac{\omega}{c} \right)^2 \mathbf{H}(\mathbf{r}) . \tag{2.90}$$

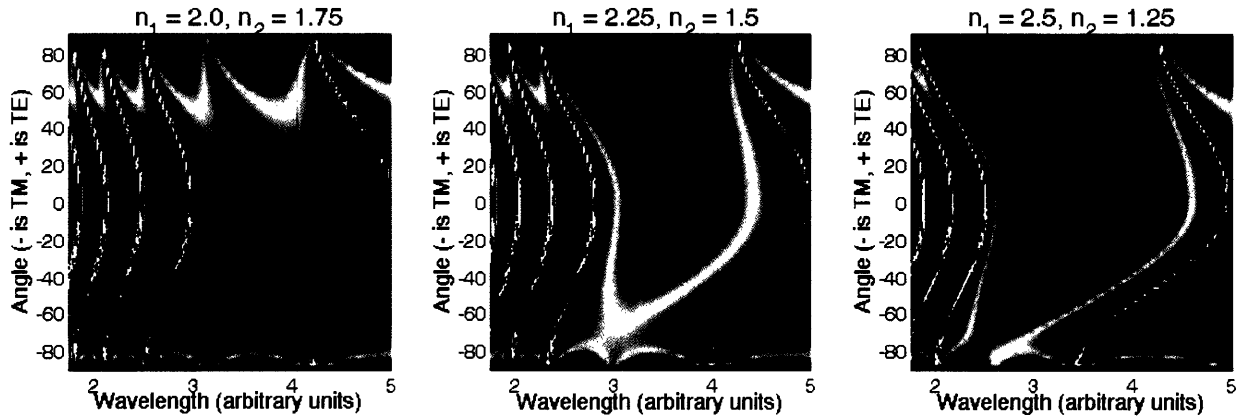

Figure 2.7 Plot of the reflectivity versus wavelength and incident angle for three quarter-wave stacks that all have 4 bilayers and average refractive indices of 1.875. As the index contrast of the photonic crystal increases, the absolute reflectivity in the bandgap also increases.

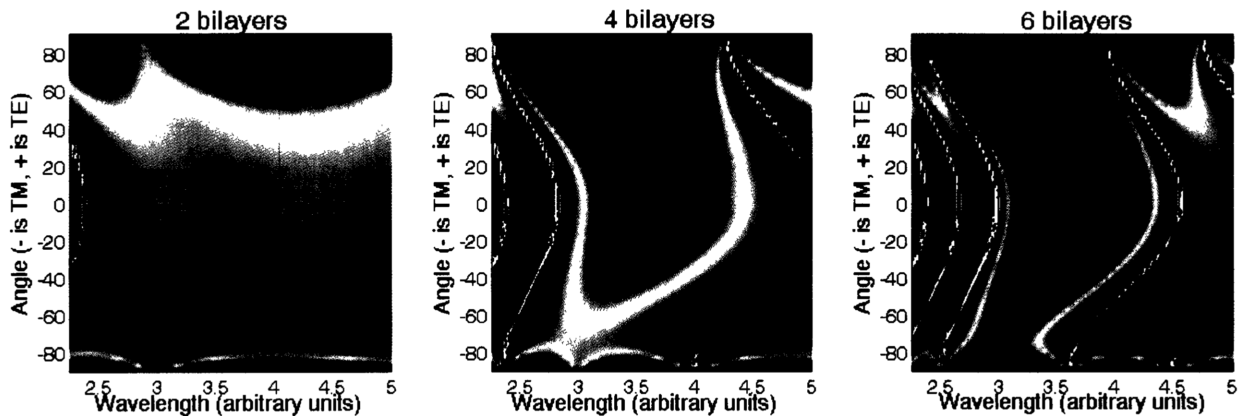

Figure 2.8 Plot of the reflectivity versus wavelength and incident angle for three quarter-wave stacks with various bilayers. All structures have n_1=2.25 and n_2=1.5. As the number of bilayers increases, the absolute reflectivity in the bandgap also increases.

Here, the eigenfunction is $\mathbf{H}(\mathbf{r})$ with a corresponding eigenvalue of $(\omega/c)^2$. The solution of the eigenfunction is simply given by Eq. 2.12, where the wave vector $\mathbf{k}$ can now be used to characterize the different electromagnetic eigenmodes of the structure. The wave vector directions are given by the irreducible Brillouin zone of the photonic crystal lattice. This is shown schematically in Fig. 2.9 for a 2D photonic crystal system with a hexagonal lattice, along with its band structure. The lines on the diagram represent the eigenmodes of the structure. The frequency range where no modes occur for any wave vector corresponds to the photonic bandgap. Because no electromagnetic modes can

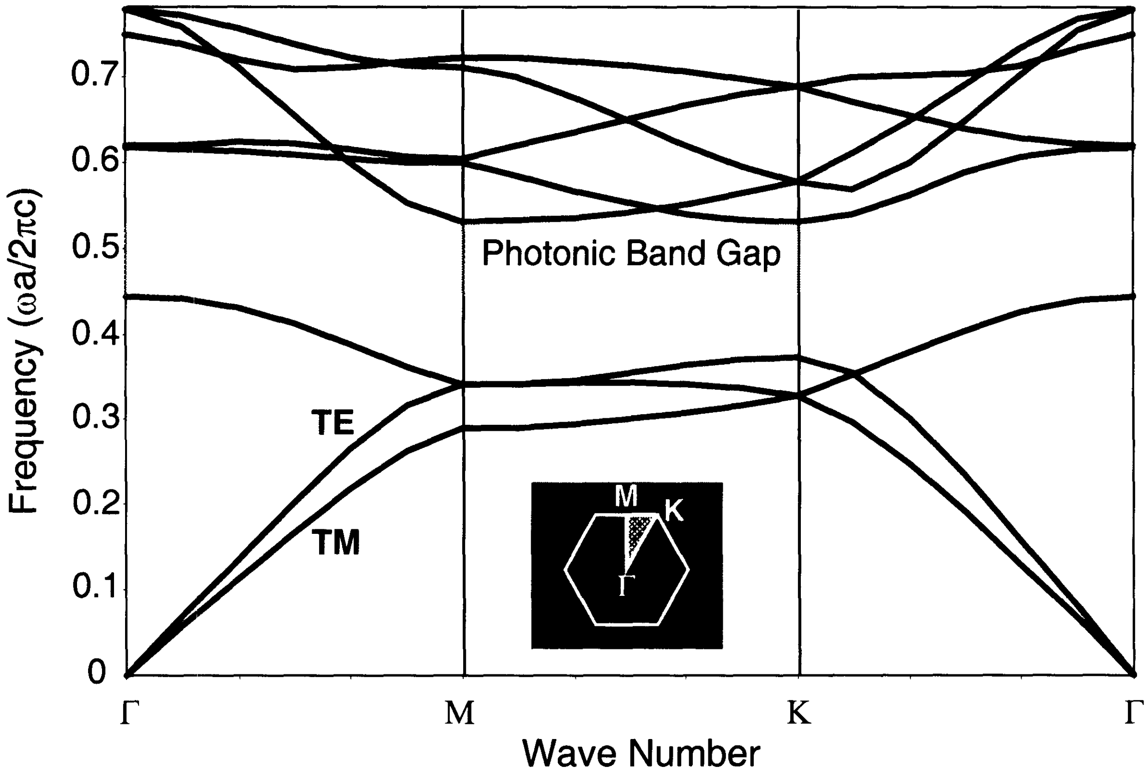

Figure 2.9 Band diagram for a 2D hexagonal lattice (shown in the inset) where the pores/rods have a refractive index of 1.0 and the matrix has a refractive index of 3.5. Also shown is the Brillouin zone with the irreducible section shaded in yellow. The photonic bandgap, where no eigenmodes exist for any wave vector, is shown in yellow.

exist in the structure at those frequencies, incident light within that frequency range will be completely reflected by the crystal.

In general, as in the 1D structures, the existence and positioning of the bandgap will depend on the geometry of the crystal. However, unlike the 1D structures, there is no rule-of-thumb for the conditions that will optimize the width of the primary bandgap for a given set of materials. Thus, modeling is required to determine these optimal conditions in 2D photonic crystals. Such modeling will be addressed in chapter 3.

2.5 Mie Scattering Theory

Some of the imperfections investigated in this thesis scatter light in a similar way to small spherical particles. Because of this, a brief introduction to scattering theory is in order. Again, only the relevant equations will be presented here, but more information can be found in Bohren and Huffman, (1983).

When light is incident on a small spherical particle, it will be scattered [Bohren (1983), Kerker (1969), Kong, (2000), Mie (1908), Shifrin (1951), van de Hulst (1957)]. Consider a spherical particle illuminated by a plane wave propagating in the positive z direction ($\hat{z}$). The incident light will be scattered by the particle outward in all directions ($\hat{r}$). The plane defined by the scattering direction and the incident direction is called the scattering plane, which is analogous to the plane of incident in the boundary reflection problem discussed in Section 2.2. Similar to the TE and TM polarizations of plane boundaries, it is common to separate the scattered electric field into components that are parallel and perpendicular to the scattering plane. The magnitude of these scattered field components is related to the incident field by the amplitude scattering matrix:

$$\begin{bmatrix} E_{\parallel s} \\ E_{\perp s} \end{bmatrix} = \frac{\exp\left(ik(r-z)\right)}{-ikr} \begin{bmatrix} S_2 & S_3 \\ S_4 & S_1 \end{bmatrix} \begin{bmatrix} E_{\parallel i} \\ E_{\perp i} \end{bmatrix}. \tag{2.91}$$

In general, the components of the scattering matrix will be a function of the angle between the incident direction and scattering direction in the scattering plane. For spherical particles, there is no way to couple parallel polarized incident light into perpendicularly polarized scattered light, and vice versa. Thus, S_3 and S_4 are both zero. Furthermore, the functional form for S_1 and S_2 has been worked out explicity for spherical particles:

$$S_1 = \sum_n \frac{2n+1}{n(n+1)} \left(a_n \pi_n + b_n \tau_n\right), \tag{2.92}$$

$$S_2 = \sum_n \frac{2n+1}{n(n+1)} \left(a_n \tau_n + b_n \pi_n\right). \tag{2.93}$$

Unfortunately, both S_1 and S_2 involve infinite sums of the angle-dependent associated Legendre functions (π_n and τ_n) and the scattering coefficients (a_n and b_n), which involve Riccati-Bessel functions. However, a sufficient number of terms in the sums will produce an approximate answer that is very close to the infinite value. Furthermore, the Ricatti-Bessel functions only depend on the size of the scatterer relative to the incident wavelength, and the refractive index contrast between the scatterer and the ambient medium. Thus, the intensity of the scattered field only depends on these parameters.

If the incident field magnitude is known, Eqs. 2.92 and 2.93 can be combined with Eq. 2.91 to solve for the scattered field magnitude as a function of angle. If the incident field is polarized perpendicular to the scattering plane (similar to the TE polarization), then the scattered intensity per unit incident intensity is given by

$$i_{\perp} = |S_1|^2 . \tag{2.94}$$

Similarly, if the incident field is polarized parallel to the scattering plane (resembling the TM polarization), then the normalized scattered intensity is

$$i_{\parallel} = |S_2|^2 . \tag{2.95}$$

As mentioned above, these intensities are also both functions of angle. In order to get the total amount of forward-scattered intensity, Eqs. 2.94 and 2.95 need to be integrated between the angles of -90° and 90°:

$$I_{fs} = \int_{-90^o}^{90^o} i_{\perp/\parallel}(\theta)\, d\theta . \tag{2.96}$$

A similar expression would be obtained for the total amount of back-scattered intensity.

When the above expressions are evaluated for various values of the index contrast and scatterer size, the dependence of the scattered intensity on these parameters can be determined. The angle dependent intensity for perpendicularly polarized light is shown

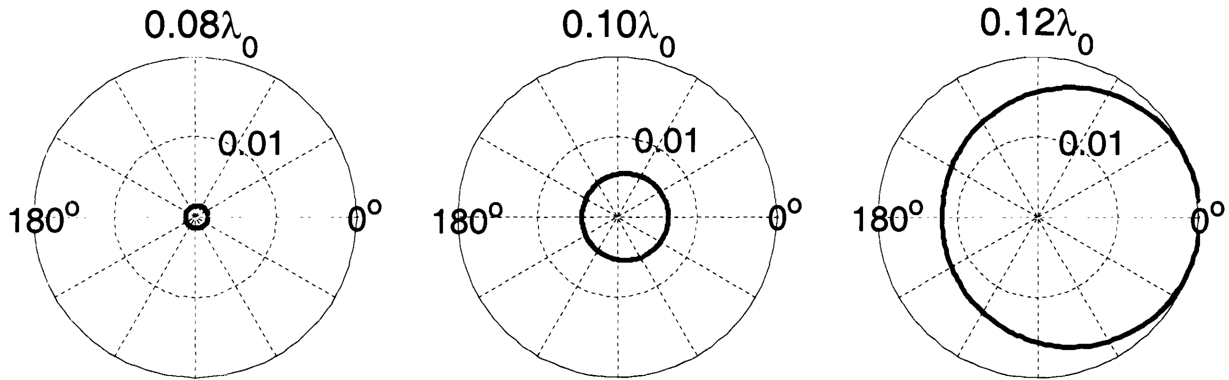

Figure 2.10 Angle-dependent scattering intensity as a function of scatterer radius from perpendicularly polarized incident light at wavelength λ_0. As the radius (indicated on top of each plot) increases, the magnitude of the scattered intensity also increases. The index contrast between the scatterer and the ambient was 1.5 in all cases.

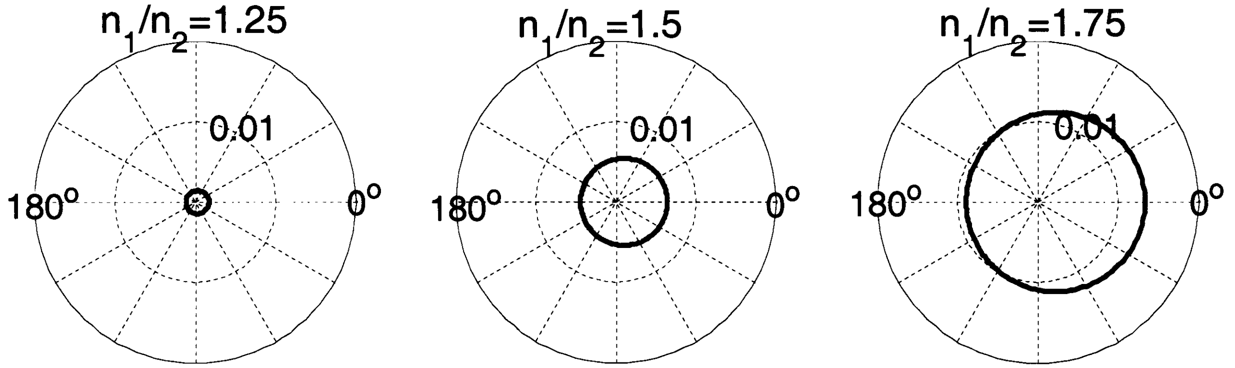

Figure 2.11 Angle-dependent scattering intensity as a function of index contrast from perpendicularly polarized incident light at wavelength λ_0. As the index contrast increases, the amount of scattered intensity also increases at every angle. The radius of the scatterer here is $0.10\lambda_0$.

for various values of these parameters in Figs. 2.10 and 2.11. The forward-scattering direction is at 0° on each plot. These calculations reveal that the intensity of scattering increases at all angles as both the scatterer size and the index contrast increase. This results is a general finding of Mie theory.

The above equations can be used to find the total amount of scattered power from a volume containing many scatterers [Jonasz (2005)]. The amount of scattered power per angle is given by the angular cross section of each particle times the magnitude of the incident intensity. For perpendicularly polarized light, the angular cross section is related to the amplitude scattering matrix components by

$$C_{ang,\perp}(\theta) = \frac{|S_1|^2}{k^2}, \tag{2.97}$$

$$C_{ang,\parallel}(\theta) = \frac{|S_2|^2}{k^2}. \tag{2.98}$$

The amount of scattered power per unit incident power from a volume of scatterers can be found by multiplying the appropriate angular cross section by the number of scatterers per unit irradiated area (projection of the volume onto the plane normal to the incident direction). Again, because this quantity is a function of angle, the total amount of forward-scattered power must be obtained through integration:

$$P_{fs} = \int_{-90^o}^{90^o} C_{ang,\perp/\parallel}(\theta)\,\delta\,d\theta = \int_{-90^o}^{90^o} \frac{|S_{1/2}|^2}{k^2}\,\delta\,d\theta\,. \tag{2.99}$$

The above analysis assumes that the scatterers in the volume are independent of one another (i.e. there is no coupling or shadowing between scatterers). If the density of scatterers becomes large enough that the particles are effecting each other, then the above values will deviate from the actual results. However, the order of magnitude of the forward and back scattered power will most likely still be correct. Thus, the above equations can still be used to estimate the amount of scattered power even in correlated systems.

Chapter 3: Methods for Simulating Electromagnetic Responses

The concepts presented in the previous chapter can be used to simulate the behavior of electromagnetic waves in complex media. There are several methods that can be used to do this. All of these methods start with the Maxwell Equations (Eqs. 2.1 through 2.4) and numerically solve them in a variety of ways. However, each technique has inherent assumptions and constraints associated with it. Thus, certain problems may be more appropriately solved with one technique over another. The following chapter will present three techniques that are commonly used to simulate electromagnetic waves. The merits and drawbacks of each method will also be presented.

3.1 1D Transfer Matrix Method

The 1D transfer matrix method can be used to quickly calculate the reflectivity and transmissivity from a multilayer structure with an arbitrary geometery [Hecht (1987), Kong (2000), Yeh (1988)]. It can also be used to calculate the field amplitude anywhere within the stack. The thicknesses and optical properties of each layer can have any value. The only constraints on the structure are that it must have a finite number of layers and it can not have any architectural variation along the layers. Thus, the layer materials must be homogeneous, but they do not need to be isotropic.

The 1D transfer matrix technique is simply a numerical solution of the equations presented in Section 2.2. It is straight-forward to apply this technique to any multilayer structure if the refractive indices and thicknesses of each layer are known. These are the only parameters that are needed to calculate the transfer matrix for each layer in the stack (Eq. 2.84) as a function of the incident wavelength and the incident angle:

$$\mathbf{V}_{(l+1)l} = \frac{1}{2}\left(1 + p_{(l+1)l}\right)\begin{bmatrix} \exp\left(-ik_{(l+1)z}\left(d_{l+1} - d_l\right)\right) & R_{(l+1)l}\exp\left(-ik_{(l+1)z}\left(d_{l+1} - d_l\right)\right) \\ R_{(l+1)l}\exp\left(ik_{(l+1)z}\left(d_{l+1} - d_l\right)\right) & \exp\left(ik_{(l+1)z}\left(d_{l+1} - d_l\right)\right) \end{bmatrix}. \quad (3.1)$$

The value of $d_{l+1} - d_l$ corresponds to the thickness of layer l. The k_z values in each layer can be related to the refractive index of the layer using the dispersion relation (Eq. 2.52):

$$k_x^2 + k_{lz}^2 = \omega^2 \mu_l \varepsilon_l = k_l^2. \quad (3.2)$$

Because of the phase-matching conditions (Eq. 2.28), the x component of the wave vector is conserved across all the interfaces in the multilayer structure. Thus, the x component of the incident wave vector can be used for the value of k_x in Eq. 3.2:

$$k_i^2 \sin^2\theta_i + k_{lz}^2 = k_l^2. \quad (3.3)$$

Utilizing the fact that k is inversely proportional to the wavelength, Eq. 3.3 can be rewritten in terms of the incident wavelength and the wavelength in the layer:

$$\frac{4\pi^2}{\lambda_i^2}\sin^2\theta_i + k_{lz}^2 = \frac{4\pi^2}{\lambda_l^2}. \quad (3.4)$$

The wavelength in the layer will be equal to the wavelength in vacuum divided by the index of refraction of the layer. Thus, for a wave incident from vacuum, Eq. 3.4 becomes

$$\frac{4\pi^2}{\lambda_i^2}\sin^2\theta_i + k_{lz}^2 = \frac{4\pi^2 n_l^2}{\lambda_i^2}. \quad (3.5)$$

This expression can then be used to solve for k_{lz} in terms of the incident wavelength, incident angle, and refractive index of the layer:

$$k_{lz} = \frac{2\pi}{\lambda_i}\sqrt{n_l^2 - \sin^2\theta_i}\ . \tag{3.6}$$

If the incident medium has a refractive index other than 1.0, then Eq. 3.6 simply becomes:

$$k_{lz} = \frac{2\pi}{\lambda_i}\sqrt{n_l^2 - n_i^2\sin^2\theta_i}\ , \tag{3.7}$$

where λ_i is the incident wavelength in vacuum.

Both $p_{(l+1)l}$ and $R_{(l+1)l}$ are only dependent on k_{lz}, $k_{(l+1)z}$, and the optical properties of the layers through Eqs. 2.78, 2.79, and 2.82. Combining Eqs. 2.78 and 2.79 with Eq. 3.7,

$$p_{(l+1)l} = \frac{\mu_{l+1}\sqrt{n_l^2 - n_i^2\sin^2\theta_i}}{\mu_l\sqrt{n_{l+1}^2 - n_i^2\sin^2\theta_i}}\ , \tag{3.8}$$

$$p_{(l+1)l} = \frac{\varepsilon_{l+1}\sqrt{n_l^2 - n_i^2\sin^2\theta_i}}{\varepsilon_l\sqrt{n_{l+1}^2 - n_i^2\sin^2\theta_i}}\ , \tag{3.9}$$

where Eq. 3.8 applies to TE polarized waves and Eq. 3.9 applies to TM polarized waves. These equations can be applied to Eq. 2.82 to get an expression for $R_{(l+1)l}$. Thus, the optical constants and layer thicknesses are all that is needed to calculate the transfer matrix for each layer. Once this is done, the wave amplitudes in any layer, as well as the reflectivity and transmissivity of the entire structure, can be calculated using Eqs. 2.85 and 2.86.

Because the above equations are rigorous analytical solutions to the Maxwell Equations, this technique can be used to determine the exact result for structures that satisfy the constraints outlined at the beginning of this section. The disadvantages of this technique are that it is limited to finite structures that are only one-dimensional. Thus, the optical properties of 2D and 3D photonic crystal geometries cannot be determined with this method. Another technique is needed that can calculate the band diagram for these structures.

3.2 Frequency Domain Method

As discussed briefly in chapter 2, the Helmholtz wave equation can be seen as an eigenvalue equation for time harmonic fields [Joannopoulos (1995), Johnson (2001), Zhang (1990)]:

$$\nabla \times \left(\frac{1}{\varepsilon} \nabla \times \mathbf{H}(\mathbf{r}) \right) = \left(\frac{\omega}{c} \right)^2 \mathbf{H}(\mathbf{r}). \tag{3.10}$$

Here, the eigenfunction is $\mathbf{H}(\mathbf{r})$ with a corresponding eigenvalue of $(\omega/c)^2$. The solution of the eigenfunction is simply given by Eq. 2.12, where the wave vector **k** can now be used to characterize the different electromagnetic eigenmodes of the structure. The frequency domain method employs a numerical eigensolver to obtain the eigenmodes and corresponding eigenvalues for specific wave vectors.

In essence, these are the natural modes for a given structure geometry. Like any periodic system, the natural modes of a photonic crystal will have specific frequencies that correspond to its structural periodicity. For most architectures, this structural periodicity varies with direction. For example, consider a 2D square lattice of rods with the unit cell edges parallel to the x and y axes. The distance between rods in the x or y direction is a, the length of the unit cell edge. However, in the $x+y$ direction (i.e. the diagonal of the unit cell), the distance between rods is $\sqrt{2}a$. Thus, wave vectors at different directions will have different frequencies corresponding to their eigenmodes.

The calculations of the eigenfrequencies for different wave vector gives rise to a band diagram for a given structure. This is a plot of the frequency values associated with the eigenmodes for each wave vector in the structure (see Fig. 2.9). Because photonic crystals are periodic, each structure only has a limited range of unique wave vector directions. Again, consider the 2D square lattice of rods described above. The periodicity in the x and y direction is the same. So calculating the eigenmodes associated with wave vectors in each of these directions would be redundant. The construct that outlines the unique directions of a periodic lattice is the irreducible Brillouin zone. Thus, only wave vectors in the irreducible Brillouin zone of the structure need to be considered. All other wave vectors in the crystal will be repeats of those in the irreducible Brillouin zone.

Because of the inherent periodic nature that is required for the eigenmode calculations, the frequency domain method is only applicable to structures that can be represented through infinite periodic repetitions of a unit cell. Thus, calculations of finite structures are not possible. Because of this, experimentally measurable quantities from finite structures, such as reflectivity or transmissivity cannot be extracted from these calculations. However, this method can be used to quickly compute the eigenmodes of any infinitely periodic geometry in one, two, or three dimensions. Thus, it is very useful in determining the expected frequency range of the bandgap for a given photonic crystal geometry. This is especially beneficial for 2D and 3D architectures, where the bandgap frequency cannot be easily predicted simply from the geometry and constituent refractive indices.

3.3 Finite Difference Time Domain (FDTD) Method

The finite difference time domain method is a numerical solution of the Maxwell Equations on a discretized grid [Kunz (1993), Sullivan (2000), Taflove (2000)]. This requires rewriting Eqs. 2.1 and 2.2 in terms of discrete derivatives. First, a change of variables is made to make the finite difference formulation simpler:

$$\widetilde{\mathbf{E}}(\mathbf{r},t) = \sqrt{\frac{\varepsilon_0}{\mu_0}}\mathbf{E}(\mathbf{r},t), \tag{3.11}$$

$$\widetilde{\mathbf{D}}(\mathbf{r},t) = \sqrt{\frac{1}{\mu_0\varepsilon_0}}\mathbf{D}(\mathbf{r},t). \tag{3.12}$$

Then, Eqs. 2.1 and 2.2 are rewritten in terms of these new variables:

$$\frac{1}{\sqrt{\mu_0\varepsilon_0}}\nabla\times\mathbf{H}(\mathbf{r},t) = \frac{\partial}{\partial t}\widetilde{\mathbf{D}}(\mathbf{r},t), \tag{3.13}$$

$$-\frac{1}{\sqrt{\mu_0\varepsilon_0}}\nabla\times\widetilde{\mathbf{E}}(\mathbf{r},t) = \frac{\partial}{\partial t}\mathbf{H}(\mathbf{r},t). \tag{3.14}$$

In two dimensions, these equations can be broken up into TE and TM modes (see chapter 2). If the simulation plane is parallel to the *xy* plane, then the field equations governing the TE mode can be written as

$$\frac{\partial D_z}{\partial t}=\frac{1}{\sqrt{\varepsilon_0\mu_0}}\left(\frac{\partial H_y}{\partial x}-\frac{\partial H_x}{\partial y}\right), \tag{3.15}$$

$$\frac{\partial H_x}{\partial t}=-\frac{1}{\sqrt{\varepsilon_0\mu_0}}\frac{\partial E_z}{\partial y}, \tag{3.16}$$

$$\frac{\partial H_y}{\partial t}=\frac{1}{\sqrt{\varepsilon_0\mu_0}}\frac{\partial E_z}{\partial x}. \tag{3.17}$$

In the above equations, the ~ notation was dropped with the understanding that both the electric and displacement field are in their normalized forms (Eqs. 3.11 and 3.12). Rewriting Eqs. 3.15 through 3.17 with discrete derivatives,

$$\begin{aligned}\frac{D_z^{n+1/2}(i,j)-D_z^{n-1/2}(i,j)}{\Delta t}&=\frac{1}{\sqrt{\varepsilon_0\mu_0}}\left(\frac{H_y^n(i+1/2,j)-H_y^n(i-1/2,j)}{\Delta x}\right)\\&-\frac{1}{\sqrt{\varepsilon_0\mu_0}}\left(\frac{H_x^n(i,j+1/2)-H_x^n(i,j-1/2)}{\Delta y}\right),\end{aligned} \tag{3.18}$$

$$\frac{H_x^{n+1}(i,j+1/2)-H_x^n(i,j+1/2)}{\Delta t}=-\frac{1}{\sqrt{\varepsilon_0\mu_0}}\frac{E_z^{n+1/2}(i,j+1)-E_z^{n+1/2}(i,j)}{\Delta y}, \tag{3.19}$$

$$\frac{H_y^{n+1}(i+1/2,j)-H_y^n(i+1/2,j)}{\Delta t}=\frac{1}{\sqrt{\varepsilon_0\mu_0}}\frac{E_z^{n+1/2}(i+1,j)-E_z^{n+1/2}(i,j)}{\Delta x}. \tag{3.20}$$

In the above equations, the time step is denoted by the superscript, and the spatial grid position of the field is denoted by the i and j arguments in parentheses. Note that the above algorithm uses a staggered grid: the magnetic field is calculated at half intervals from the electric field in both space and time. This formulation was first proposed by Yee in 1966 and it has since been adopted as a common practice in FDTD simulations due to the increased stability of the calculation [Yee (1966)].

The grid used in most simulations takes $\Delta x=\Delta y$ for simplicity. Indeed, all the FDTD simulations in this thesis also conformed to this standard. Furthermore, the time step Δt in the simulation is related to the spatial step Δx by the speed of light. In one dimension, in order to properly reproduce physical behavior, the simulated time step cannot exceed the value of $\Delta x/c$ because the wave can only travel one grid point per simulation step. In two dimensions, the wave can also travel along the diagonal of a grid interval. This, therefore, further restricts the time step to be less than $\Delta x/\sqrt{2}c$ [Press

(2002), Schneider (1999)]. In order to simplify the finite differenced equations, a time step of $\Delta x/2c$ was used in the simulations presented in this thesis.

Applying this value of the time step to Eqs. 3.18 through 3.20,

$$\begin{aligned} D_z^{n+1/2}(i,j) - D_z^{n-1/2}(i,j) = &\frac{1}{2}\left(H_y^n(i+1/2,j) - H_y^n(i-1/2,j)\right) \\ &-\frac{1}{2}\left(H_x^n(i,j+1/2) - H_x^n(i,j-1/2)\right) \end{aligned}, \tag{3.21}$$

$$H_x^{n+1}(i,j+1/2) - H_x^n(i,j+1/2) = -\frac{1}{2}E_z^{n+1/2}(i,j+1) + E_z^{n+1/2}(i,j), \tag{3.22}$$

$$H_y^{n+1}(i+1/2,j) - H_y^n(i+1/2,j) = \frac{1}{2}E_z^{n+1/2}(i+1,j) - E_z^{n+1/2}(i,j). \tag{3.23}$$

The value of the fields at the next time step can now be solved in terms of the field values at the previous time step:

$$\begin{aligned} D_z^{n+1/2}(i,j) = D_z^{n-1/2}(i,j) + &\frac{1}{2}\left(H_y^n(i+1/2,j) - H_y^n(i-1/2,j)\right) \\ &-\frac{1}{2}\left(H_x^n(i,j+1/2) - H_x^n(i,j-1/2)\right) \end{aligned}, \tag{3.24}$$

$$H_x^{n+1}(i,j+1/2) = H_x^n(i,j+1/2) - \frac{1}{2}E_z^{n+1/2}(i,j+1) + E_z^{n+1/2}(i,j), \tag{3.25}$$

$$H_y^{n+1}(i+1/2,j) = H_y^n(i+1/2,j) + \frac{1}{2}E_z^{n+1/2}(i+1,j) - E_z^{n+1/2}(i,j). \tag{3.26}$$

These equations, in the order presented here, are used in the FDTD code to propagate the electromagnetic field through the simulation domain. They are evaluated at every point on the spatial grid for each time step. A loop is used to increment the time step up to the maximum number of steps, which is usually input by the user.

A source of the electromagnetic radiation must also be added to the FDTD formulation. This can be done by adding a source term on top of the calculated field at a set of grid points in the simulation domain. For a plane wave source, a sine wave with amplitude E_0 and frequency c/λ_i can be added to each grid point in one row of the domain. If the propagation direction of the plane wave is perpendicular to this row in the domain, then the amplitude of the sine wave will be the same for every grid point in the row at a given time step (i.e. no phase needs to be added to the source based on the location of the grid point in the row). This allows the incident wave information to be

contained in a separate one-dimensional array. This source term added to each grid point in the row would therefore be

$$source = E_0 \sin(\omega t) = E_0 \sin\left(\frac{2\pi c}{\lambda_i} \Delta t \, n_s\right). \tag{3.27}$$

In addition to a computational time benefit, this way of handling the source can also be used to constrain the source emission to one direction into the simulation space [Mur (1981), Umashankar (1982)]. This is shown schematically in Fig. 3.1. This creates two regions in the simulation domain: one that contains the total field (incident and reflected), and one that only contains the reflected wave. The total wave domain is truncated by modifying the values of the total field at the edges of this domain for each time step. If a grid point is located at a position near the edge of the total wave domain, then the neighboring field values, which are just on the other side of the domain edge, will be used when its value is updated at the next time step. Thus, in order to prevent the incident field from "leaking" out of the domain, it needs to be subtracted out of the total field calculation for these grid points. The incident field value at each time step is held in the one-dimensional array. Thus, the appropriate value of the incident field for each affected grid point will be given by the corresponding value in the incident wave array.

As a consequence of this formulation, it is very easy to separate the reflected field in the simulation from the incident field. This is because the only field in the region outside of the total wave domain will be the reflected field. Thus, the magnitude of the reflected wave can be extracted from the simulation by only analyzing the field in the region outside of the total wave domain.

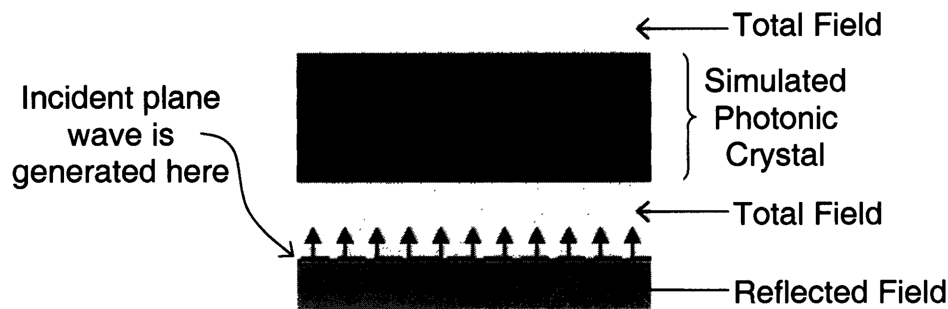

Figure 3.1 Schematic of the simulation domain illustrating the unidirectional source that allows separation of the total field and the reflected field.

Unfortunately, the above formulation only works if the incident field direction is perpendicular to the rows in the simulation grid. If the incident field propagates in a different direction, then the source term (Eq. 3.27) would include a phase shift that depends on the position of the grid points in the simulation domain. Thus, the incident field information could no longer be stored in a one-dimensional array. However, in theory, it would still be possible to implement the above unidirectional source algorithm with a two-dimensional incident array. But the code used in this thesis was a modification of the code presented in Sullivan (2000), which uses a one-dimensional incident array. Therefore, a substantial reformulation of the code would be needed in order to implement a two-dimensional incident array algorithm. Since a considerable amount of insight could be gained by using the code in its current state, this reformulation was considered unnecessary for the studies presented in this thesis. However, future studies could be done using a two-dimensional incident array to simulate other incidence conditions.

In general, there are two types of boundary conditions that are used in FDTD simulations: periodic and absorbing boundary conditions. Periodic boundary conditions can be used to simulate structures that have infinite lengths or widths [Alexanian (1996), Cangellaris (1993), Celuch-Marcysiak (1995), Chan (1991), Kelly (1994), Kesler (1996), Navarro (1993), Okoniewski (1993), Tsay (1993)]. When the value of the field just outside of the simulation domain is required, the value of the field at the opposite boundary is used. Mathematically, for incident waves traveling perpendicular to the rows in the domain, this appears as

$$E_z^n(n_x+1, j) = E_z^n(1, j), \tag{3.28}$$

$$E_z^n(i, n_y+1) = E_z^n(i, 1), \tag{3.29}$$

for periodic boundaries in the x and y directions, respectively. Thus, it is fairly easy to add periodic boundary conditions to an FDTD code by simply appending a conditional statement to the field calculations that includes Eqs. 3.28 and/or 3.29.

Absorbing boundary conditions are used to prevent reflections off of the domain walls in the simulation. When a field reaches a domain wall that does not have an absorbing (or periodic) boundary condition, it will reflect off of the wall due to the nature of the field calculations. However, most often it is desirable to create a simulation

domain that appears to continue to infinity outside of the domain walls. Many methods have been proposed to achieve absorbing boundaries. [Bayliss (1980), Bayliss (1982), Berenger (1994), Engquist (1977), Givoli (1991), Halpern (1986), Higdon (1986), Higdon (1987), Liao (1984), Moore (1988), Mur (1981), Ramahi (1997), Ramahi (1998), Trefethen (1986)]. However, the most widely used absorbing boundary condition algorithm in FDTD simulations is known as the perfectly matched layer (PML) algorithm, which was developed by Berenger in 1994 [Berenger (1994)]. As in electronic circuits, it achieves absorbing boundary conditions through impedance matching at the domain walls. It creates several layers in the simulation domain near the boundary. Each layer has some amount of absorbance, which is controlled by the value of ε and μ in the layer. For each subsequent layer, the absorbance gradually increases, damping out any impinging wave. Thus, this algorithm can be used to prevent any unpredictable reflections off of the boundaries. In general, the specific parameters for each PML layer, as well as the total number of PML layers, should be tuned to minimized the amount of reflection.

The FDTD method is extremely flexible. It can be used to calculate the electromagnetic response of any arbitrary dielectric geometry. The results of the simulations can be easily related back to measurable quantities, such as reflectivity or transmissivity. Moreover, because this method directly solves the Maxwell Equations, it can produce results that are very nearly exact if the discrete grid is fine enough. As a general rule of thumb, a cell width (Δx) smaller than $1/30^{th}$ of a wavelength is sufficiently fine to produce accurate results in the Yee algorithm [Liu (1996)]. The grids used in the FDTD simulations presented in this thesis had cell widths between $1/330^{th}$ and $1/480^{th}$ of a wavelength.

Although there are many advantages to the FDTD method, it does have one major draw back. The larger the structure, the longer the FDTD simulation will take to run. 3D structures can take an extremely long amount of time due to the numerous field calculations and time steps required to reach steady state. However, even 2D structure simulations, such as the ones studied in this thesis, can be very computationally expensive when the appropriate grid resolution is used. Thus, the FDTD method should only be used when all other faster simulation methods have been exhausted.

This is the case for the studies done in this thesis. Because imperfect photonic crystals are being investigated, the structures have dielectric variations in two dimensions. This prevents the 1D transfer matrix technique from being used to solve the problems addressed here. Furthermore, these imperfections also destroy the intrinsic periodicity of the photonic crystal. Therefore, the frequency domain method cannot be used either. Thus, the FDTD method is the best technique to obtain the optical responses from these structures.

Chapter 4: Interfacial Roughness in 1D Photonic Crystals: An FDTD Study

The well-known and technologically useful properties of one-dimensional photonic crystals (1DPCs), in particular the presence of a bandgap for certain wavelength ranges and polarizations, are based on the theoretical crystal models presented in chapter 2. These models assume structures with perfectly flat interfaces between the constituent layers [Joannopoulos (1995), Yeh (1988), Winn (1998)]. Despite this, the existence of photonic bandgaps in 1DPCs has been demonstrated experimentally through laboratory fabrication of various 1DPC configurations [Temelkuran (2001), Deopura (2001), Fink (1998), Chigrin (1999)]. These and other experiments demonstrate that predicted photonic bandgaps in idealized structures are somewhat robust because laboratory

processing inevitably introduces interfacial roughness and other defects that were not treated in the models. However, for the economic design of large-scale manufacturing processes, where the control of interfacial roughness and defects may be costly, the question arises: how tolerant are the optical properties of 1DPCs to manufacturing defects such as interfacial roughness?

There are several "real world" examples of structures that exhibit significant amounts of interfacial roughness. One such structure is shown in Fig. 4.1. This is a structure that is currently being researched at the University of Buffalo by K. Hsiao, et al. as a tunable 1D photonic crystal [Hsiao (2004)]. It was produced by incorporating a liquid crystal material into a multilayer stack. The refractive index of the liquid crystal layers can be changed by placing the structure in an electric field. This allows the optical response of the structure to be adjusted based on its electrical environment. Its perfect analogue, on which the theoretical optical response of the device is based, is shown schematically next to it. It is clear that the actual structure deviates significantly from the ideal one. In fact, the roughness associated with the interfaces in this structure is so severe that some of the layers themselves are discontinuous (i.e. the roughness scale is comparable to the thickness of the layers).

Another example of a currently researched structure with rough interfaces is porous silicon multilayers. When silicon is anodized in a hydrofluoric acid solution,

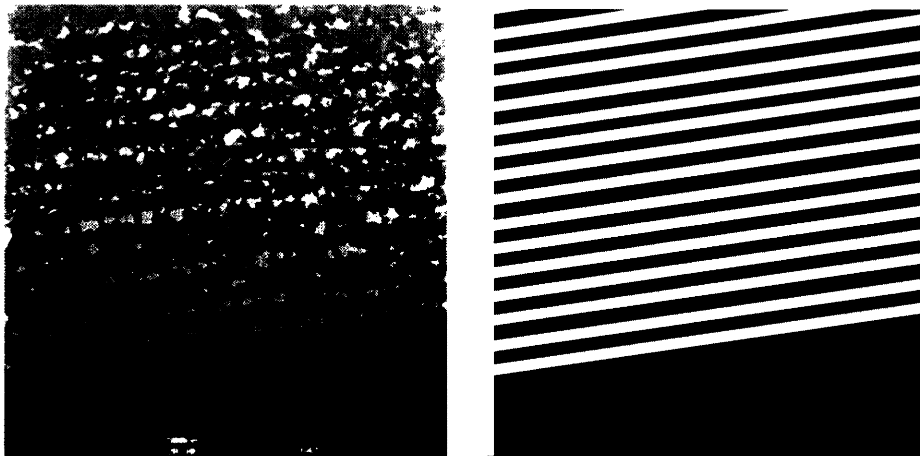

Figure 4.1 One example of a "real world" structure with a large amount of interfacial roughness. This particular structure is a liquid crystal multilayer fabricated by K. Hsiao, et al. [Hsiao (2004), reprinted with permission]. The micrograph on the left is the actual structure, while the schematic on the right is the idealized structure on which the theoretical optical response of the device is based.

pores are etched into the surface of the silicon. The size of these pores can be directly controlled by the amount of current that is passed during the anodization process. Thus, a modulation of the current during the anodization will result in a modulation of the pore size into the surface of the silicon. This consequentially also results in a modulation of the index of refraction, creating a multilayer structure where the low index layer has large pores and the high index layer has smaller ones. The advantage of creating multilayer structures with this method is that the electrochemical anodization technique is cheap, fast, and can be used to create these structures on a large scale. An example of this porous silicon multilayer structure is shown in Fig. 4.2 [Agarwal (2003)]. Again, although this structure does not deviate from its ideal as much as the liquid crystal multilayer in Fig. 4.1, some interfacial roughness is still evident in the structure.

Other studies have looked at interfacial roughness in multilayers using perturbation analyses [Amra (1994), Elson (1995)]. However, these studies are limited to roughness scales much less than the wavelength of light and cannot be simply modified for specific 1DPC configurations. Furthermore, practical implications, such as reflectivity dependence on index contrast and interfacial roughness measures are not readily derivable from these results. In this chapter, the results of a two-dimensional Finite Difference Time Domain (FDTD) simulation of 1DPCs with interfacial roughness are presented [Maskaly (2004)]. As described below, the roughness is simulated by

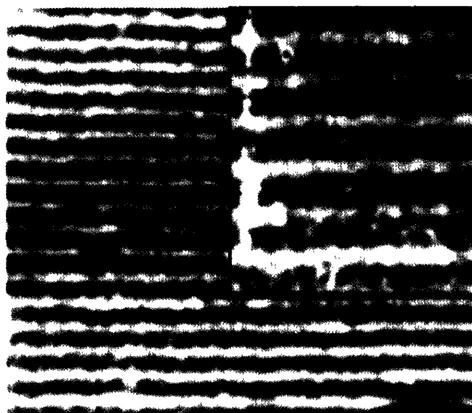

Figure 4.2 A micrograph of a porous silicon multilayer structure fabricated by Agarwal, et al. (reprinted with permission from V. Agarwal and J. A. del Río, *Applied Physics Letters*, 82, 1512 (2003), copyright 2003, American Institute of Physics). Although this structure does not deviate from its ideal as much as the structure in Fig. 4.1, some amount of interfacial roughness is still evident.

direct specification of a random amplitude and subsequently characterized with an average wavelength. Therefore, this method is not limited to small roughness amplitudes and can be extended to general 1DPC configurations.

Because of the particular relevance and wide-spread use of quarter-wave stacks in 1DPC devices, this study focused on quarter-wave tuned 1DPCs at normal incidence. The incident wavelength used in the simulations is that to which the quarter-wave stack is tuned. Additionally, each stack is arranged so that the top layer is the higher index material. This was done in order to simulate the architecture typically used in 1D photonic crystal devices. The simulations were done on free-standing crystals – the surrounding medium on both sides of the crystals is vacuum (dielectric constant 1.0).

4.1 Interfacial Roughness Parameters

The simulated 1DPCs were analyzed in terms of two roughness parameters, illustrated in Fig. 4.3. The first parameter, the RMS interface roughness, is:

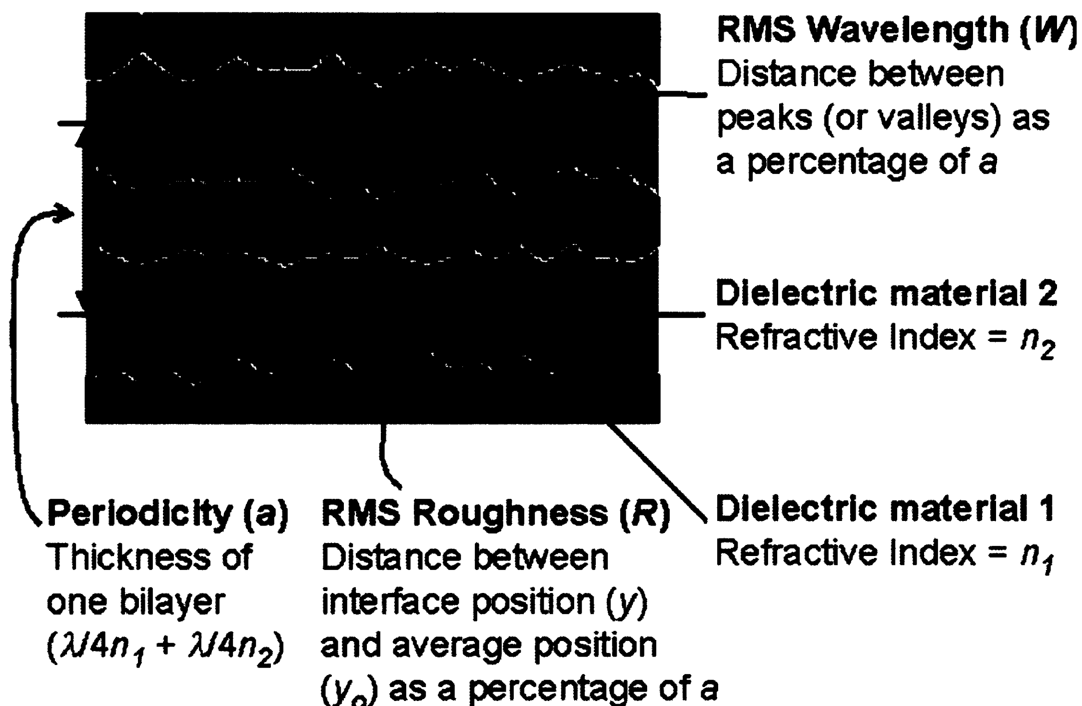

Figure 4.3 Schematic of the rough interfaces in the simulated structures illustrating the two parameters that were used to characterize each roughened structure: RMS roughness and RMS wavelength. Also shown is the characteristic periodicity (a) of the photonic crystal.

$$R_{RMS} \equiv \left(\frac{1}{L} \int_0^L (y_i - y_0)^2 \, dx \right)^{1/2} \cong \left(\frac{1}{n_{nodes}} \sum_1^{n_{nodes}} (y_i - y_0)^2 \right)^{1/2}. \quad (4.1)$$

Because the nodes in the FDTD simulation are equally spaced, R_{RMS} is independent of L, the size of the simulation domain parallel to the layer interfaces. As defined, R_{RMS} is comparable to the roughness parameter obtained by profilometry [Tencor (1996)].

The second parameter, the RMS interface roughness wavelength, is a measure of the RMS peak-to-peak or valley-to-valley distance of the roughness features, defined as:

$$W_{RMS} = \left(\frac{1}{n_{pv}} \sum_1^{n_{pv}} \left(x_{pv}^{(2)} - x_{pv}^{(1)} \right)^2 \right)^{1/2}, \quad (4.2)$$

Both the x and y interface positions are specified as a fraction of a, the characteristic photonic crystal periodicity. Because all the photonic crystals simulated were quarter-wave stacks, this periodicity corresponded to

$$a = t_1 + t_2 = \frac{\lambda_0}{4n_1} + \frac{\lambda_0}{4n_2}. \quad (4.3)$$

All of the results are therefore independent of absolute length scale.

4.2 Generation of the Roughened Structures

The simulated 1DPC structures were generated with a C++ code, which created a zero roughness 1DPC structure and then randomly displaced the interface nodes based on a specified amplitude. The RMS interface roughness wavelength was controlled by skipping over a certain number of specified nodes between each displacement. The indices of refraction of the constituent layers, the number of bilayers in the structure, and the total number of nodes in the simulation domain parallel and perpendicular to the interfaces were input. The corresponding nodal thicknesses of the quarter-wave stack layers were then calculated. This was done by first calculating the photonic crystal periodicity (i.e. the thickness of a single bilayer) from the total number of nodes perpendicular to the interfaces and the number of bilayers. Specifically,

$$a = \frac{n_y}{num_bilayers}. \quad (4.4)$$

The nodal thickness of each layer was then calculated based on the refractive indices of the layers:

$$t_1 = \frac{an_2}{(n_1 + n_2)}, \tag{4.5}$$

$$t_2 = \frac{an_1}{(n_1 + n_2)}. \tag{4.6}$$

Values for the indices of refraction, the number of bilayers, and the total number of perpendicular nodes were selected such that a, t_1, and t_2 were all integer values. A two-dimensional array with a size equal to the total number of nodes in the simulation domain was then generated for a spatial representation of the structure. Refractive index values were written into the array corresponding to a 1DPC structure with flat interfaces. Buffer layers with refractive index values of 1.0 (corresponding to air or vacuum) were written above and below the structure as well in order to allow both positive and negative displacements for the first and last interfaces in the structure (the interfaces adjacent to the ambient).

Values for the maximum displacement for an interface node and the number of interface nodes between displaced nodes (for control over the RMS wavelength) were also given as inputs. These values were used to generate a list of numbers, with each member of the list corresponding to an interface node in the structure. The input values were converted from percentages of a to number of nodes. A random number was chosen between 0 and the value corresponding to the maximum displacement. Additionally, a random angle was chosen between 0 and 2π. If the random angle was greater than π, the random number was made negative, allowing for negative displacements of the interface. This random number was then entered into the list, and the proceeding and preceding members of the list, up to the number of nodes to skip, were given values equal to the random number multiplied by a Gaussian with a standard deviation equal to half the number of skipped interface nodes. This was done in order to smooth the roughness displacements and avoid sharp discontinuities along the interface.

The numbers in the list for each interface were then summed. A sum greater than zero meant that the interface had a net positive displacement. This would shift the mean thickness of the layer to be greater than a quarter-wave thickness. In order to remedy

this, the roughness feature on that interface with the maximum displacement was located. The displacement amount for each node corresponding to that Gaussian roughness feature was then decreased by one (starting with the node at the center of the Gaussian and then moving outward in each direction) until the total sum for the interface became zero. If all the nodes of the roughness feature were decreased and the sum was still greater than zero, then the process was repeated until a zero net displacement for that interface was achieved. Alternatively, if the displacement sum for an interface was negative, then the above process was performed but the node displacements were increased instead of decreased until a zero net displacement was achieved.

The array positions of the interface nodes were then determined. The nodes on each interface were displaced according to the displacement list. This was achieved by writing the appropriate refractive index value into each member of the array above (or below) the interface node up to the value in the displacement list for that node. For example, if the interface was a high-to-low index interface and the displacement for one particular node on that interface was positive 10, then the members of the array up to 10 above the interface node were written with the refractive index value of the high index

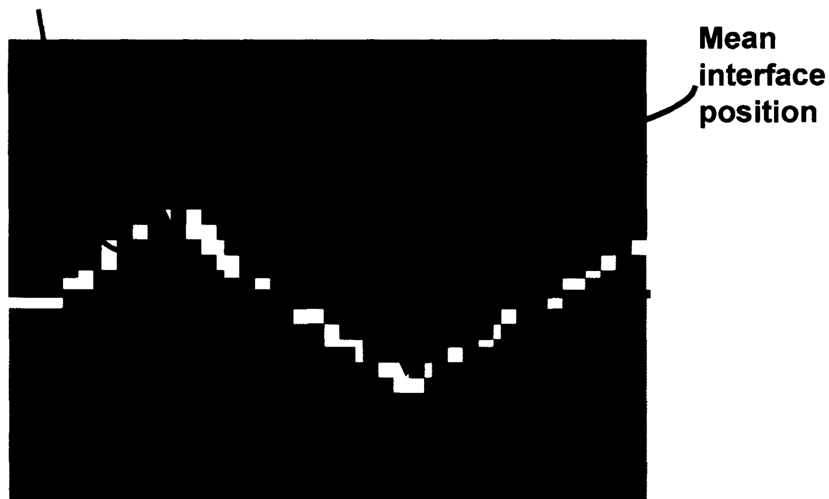

Figure 4.4 Close up of a roughened interface illustrating the process used to create the roughness features.

material. Alternatively, if the displacement for that node was negative 10, then the members of the array up to 10 below that interface node were written with the refractive index value of the low index material. This process is illustrated in Fig. 4.4.

The RMS roughness and RMS wavelength for the roughened structure was then calculated from the displacement list using Eqs. 4.1 and 4.2. The refractive index array was written to an output file, which was then used as an input into the FDTD code. The nodal magnitude of the incident wave was also input into the FDTD simulation. For all the following simulations, the quarter-wave-tuned wavelength was used as the incident wave. The nodal magnitude corresponding to this wavelength can be calculated from the structure parameters in the following way. Combining Eqs. 4.3 and 4.4,

$$a = \frac{\lambda_0}{4n_1} + \frac{\lambda_0}{4n_2} = \frac{n_y}{num_bilayers}. \tag{4.7}$$

Solving Eq. 4.7 for λ_0 gives the nodal magnitude of the wavelength:

$$\lambda_0 = \frac{4n_y}{num_bilayers}\left(\frac{n_1 n_2}{n_1 + n_2}\right). \tag{4.8}$$

Because the Maxwell Equations are valid and take the same form for any length scale, once this is calculated, all other wavelengths can be scaled to nodal magnitudes using Eq. 4.8 to obtain a scaling factor. This was not necessary for the simulations presented in this chapter, but it was used for the simulations that studied wavelengths spanning the full bandgap at normal incidence. These simulations will be presented in chapter 8.

4.3 Simulation and Analysis Method

Each structure was modeled using a 2D FDTD code utilizing the Yee algorithm, as described in chapter 3, for calculation of both the electric and magnetic fields [Yee (1966), Sullivan (2000), Taflove (2000)]. Two types of boundary conditions were used in the simulation. Periodic boundary conditions were specified on the domain walls perpendicular to the 1DPC layers. The boundaries parallel to the layers were simulated as PML absorbing boundaries [Berenger (1994)]. These conditions produced a 1DPC that is infinite in length with a finite number of bilayers. Independence of the simulation with respect to distance between periodic boundaries was checked by calculating results

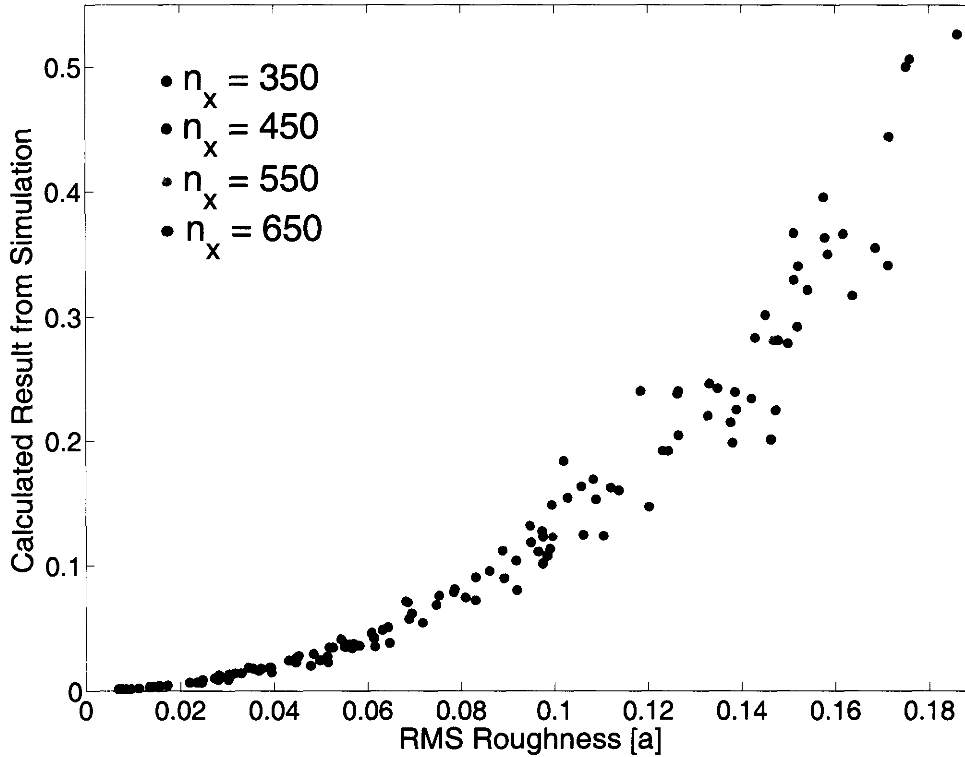

Figure 4.5 Simulation results showing that the size of the domain between periodic walls was sufficiently large. The distance between periodic walls is given by the parameter n_x. An n_x value of 450 was used for all the FDTD simulations presented in this thesis.

for both longer and shorter periodic cells and verifying that the results are statistically equivalent. The results of these calculations are shown in Fig. 4.5.

The exact FDTD code used was a modification of the code provided in Sullivan (2000), which does not use any periodic boundaries but instead uses PML absorbing boundaries on all the simulation domain walls. One advantage of this code, however, is that it provides a method for simulating a unidirectional plane wave source. This allows the reflected wave to be easily separated from the incident field, as was described in chapter 3. The code also provides a straightforward means of implementing the Yee algorithm and the PML boundary conditions.

Normalized reflectivities, r, were obtained from the time-averaged squared electric or magnetic field of only the reflected wave over several periods after initial transient behavior had disappeared. For TE polarized light, this takes the form:

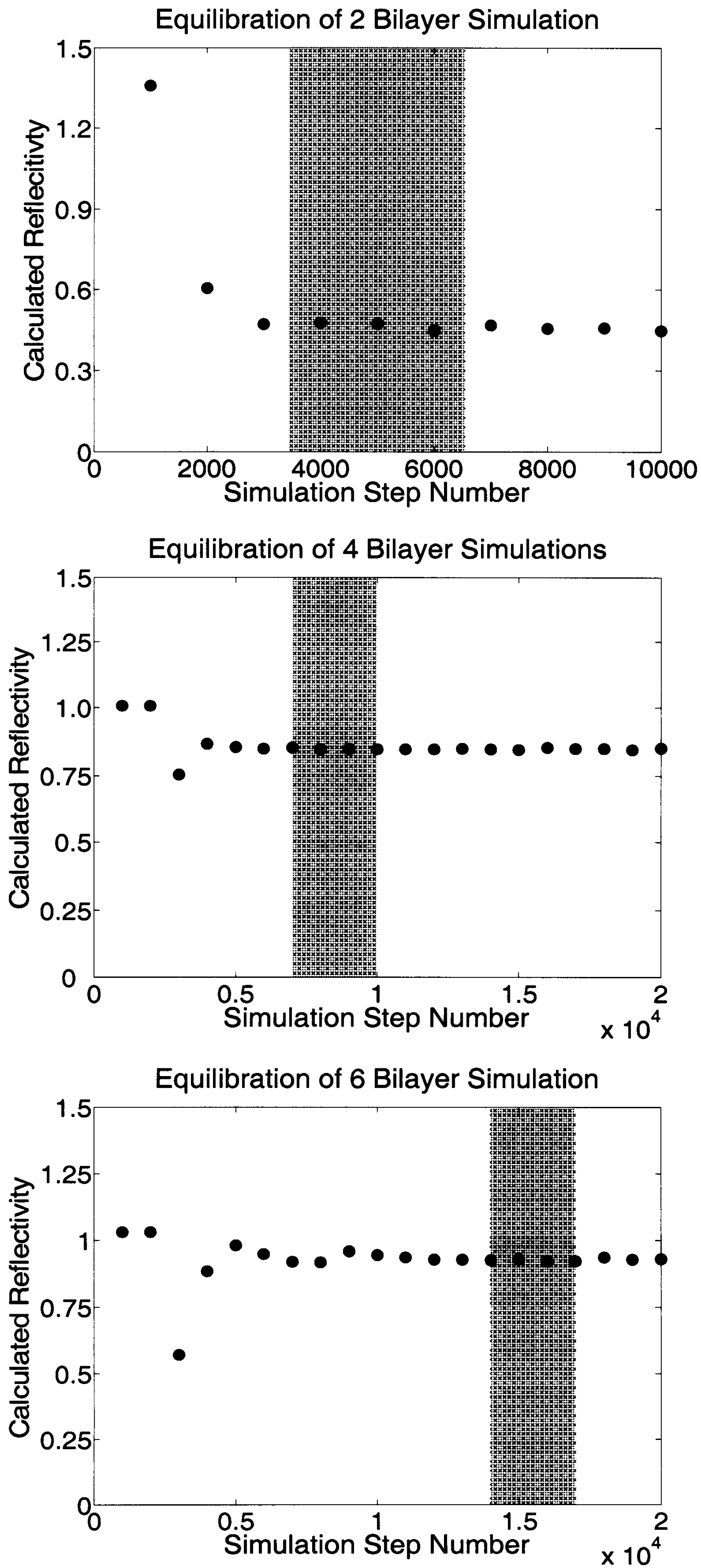

Figure 4.6 The equilibration of three simulated bilayer systems. The pink region corresponds to the time steps over which the time average was taken in Eq. 4.9.

$$r = \frac{\left\langle \frac{1}{T_a} \int_{T_0}^{T_0+T_a} E_r^2 dt \right\rangle}{\left\langle \frac{1}{T_a} \int_{T_0}^{T_0+T_a} E_r^2 dt \right\rangle + \left\langle \frac{1}{T_a} \int_{T_0}^{T_0+T_a} E_t^2 dt \right\rangle} = \frac{\left\langle \frac{1}{n_T} \sum_1^{n_T} E_r^2 \right\rangle}{\left\langle \frac{1}{n_T} \sum_1^{n_T} E_r^2 \right\rangle + \left\langle \frac{1}{n_T} \sum_1^{n_T} E_t^2 \right\rangle} . \quad (4.9)$$

The same formulation can be applied to simulations using TM polarized light except that the magnitude of the magnetic field is used instead of the electric field. Fig. 4.6 shows the instantaneous amplitude of the reflected electric field versus the time step in the simulation for three different simulated systems. This figure illustrates that the reflected electric field reaches a stead-state value after a certain number of simulation steps. The pink area in the figure indicates the region over which the above time average was taken for each structure. This corresponds to an averaging over 8 full cycles of the reflected wave. Because absorption (i.e. imaginary values for the indices of refraction) was not simulated in this study, the denominator in Eq. 4.9 is equivalent to the time-averaged squared incident field. Therefore, this method is equivalent to taking the ratio of the time-averaged Poynting vectors for the reflected and incident fields [Kong (2000)]. Again, the time scale disappears from Eq. 4.9 because the time step remains constant throughout the simulation. The angled brackets indicate that a spatial average is taken after the time average to obtain one number for the reflectivity.

The results of the code were verified by comparing the reflectivity from a perfect (smooth) crystal obtained by the FDTD method to a 1D transfer matrix calculation. This also allowed tuning of the parameters that determine the absorbing capabilities of the PML layers. After the PML boundaries were optimized, the results of the two calculations were identical to within 0.005%. This also provided verification that the grid used in the FDTD simulation was fine enough to produce accurate results. The width of each grid point was between $1/330^{th}$ and $1/480^{th}$ of a wavelength for all simulations.

The metric used to evaluate the optical response of the roughened structures was the percent change in the reflectivity of the roughened structure from the perfect structure. The reflectivity from each simulation, r_{rough}, was normalized by the reflectivity of an equivalent structure with zero roughness, r_{smooth}. The percent change in reflectivity Δr is reported as a measure of the "optical leakiness" of the simulated structure:

$$\Delta r = 1 - \frac{r_{rough}}{r_{smooth}}. \tag{4.10}$$

4.4 TE Polarization Reflectivity Results

Over 700 simulations at varying conditions were done in order to systematically study the effects of refractive index contrast, average refractive index, and number of bilayers on the change in the normal reflectivity from roughened 1D photonic crystals. This study was done to determine design conditions that would aid in minimizing the effects of the roughened interfaces. Reflectivities for a TE-polarized normal incidence plane wave impinging on several different simulated quarter-wave stacks were obtained.

The Δr for a 4-bilayer quarter-wave stack with $n_1 = 2.25$ and $n_2 = 1.5$ is plotted in Fig. 4.7 as a function of R_{RMS} and W_{RMS}. Each of the 120 simulations done for this study is represented by a dot in the figure. These simulations corresponded to structures with W_{RMS} values ranging from about $0.1a$ to $1.0a$ and R_{RMS} values ranging from about $0.005a$ to $0.175a$. Above this upper limit on the roughness value, several roughness features had heights greater than the thickness of the neighboring layer, causing the measure of roughness as defined in Eq. 4.1 to no longer accurately represent the specific morphology of the structure. A surface was fit to the reflectivity results from each of these simulations using a triangle-based cubic interpolation scheme. In this way, the dependence of Δr on both parameters can be easily seen with a 3D surface plot. In addition to the Δr results, Fig. 4.7 also shows four example structures for four particular simulations in order to provide a better understanding of what structures with those values of R_{RMS} and W_{RMS} would look like. Notice that the structures with the largest roughness values still produce multilayer stacks that have discontinuous layers even though most of the roughness features have heights below the thickness of the neighboring layer. This is because the layers can become discontinuous if two roughness features on either interface of a layer grow towards each other and combine to cut off the intervening layer.

There are two primary conclusions that can be drawn from the results presented in Fig. 4.7. First, not surprisingly, there is a strong dependence of the change in reflectivity from roughened structures on the RMS roughness of the structures. Fig. 4.7 is plotted on

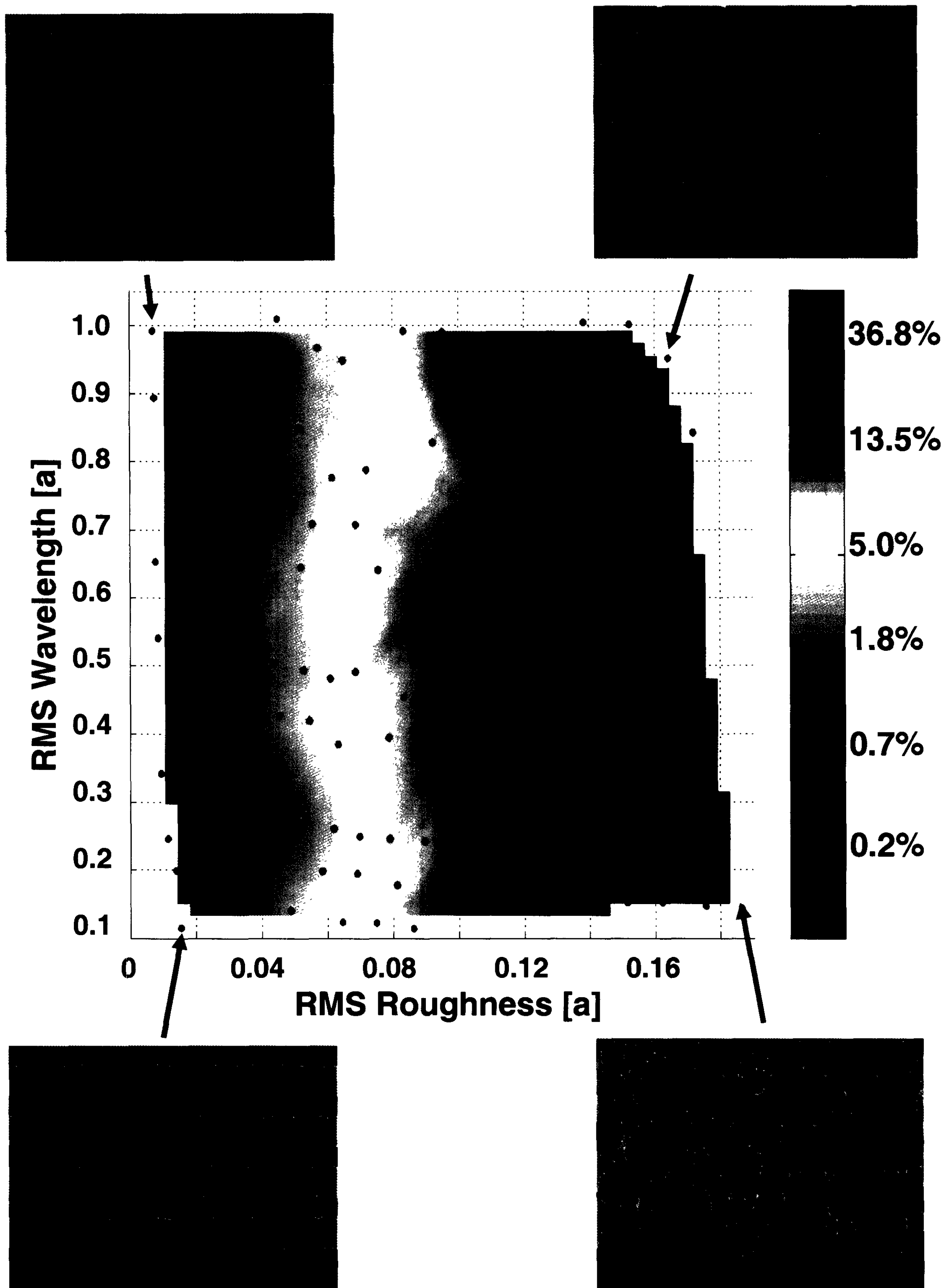

Figure 4.7 The calculated percent change in the TE-polarized normal incidence reflectivity for roughened 4-bilayer quarter-wave stacks with n_1=2.25 and n_2=1.5. Also shown are four example structures for four particular simulations.

a log-scale in order to show the features of the plot more clearly. At the most extreme values of RMS roughness tested (~19% of *a*), the change in reflectivity from a perfect structure reaches more than 50%. The second conclusion that can be drawn from these results is that there is no detectable dependence of the RMS wavelength on the percent change in reflectivity. This is a more surprising result, which will be explained later when the mechanism that causes this change in reflectivity will be investigated. Nonetheless, this result allows the data to be condensed to a 2D plot with only the RMS roughness as a parameter. This plot is shown in Fig. 4.8, along with the results from several other simulations for different 4-bilayer quarter-wave stack configurations with varying values for the high and low refractive indices of the quarter-wave stacks. Because the previous study showed there was no effect of the RMS wavelength on the simulation results, a mid-range wavelength was chosen for all of these simulations.

These additional simulations were done in order to systematically study the effect

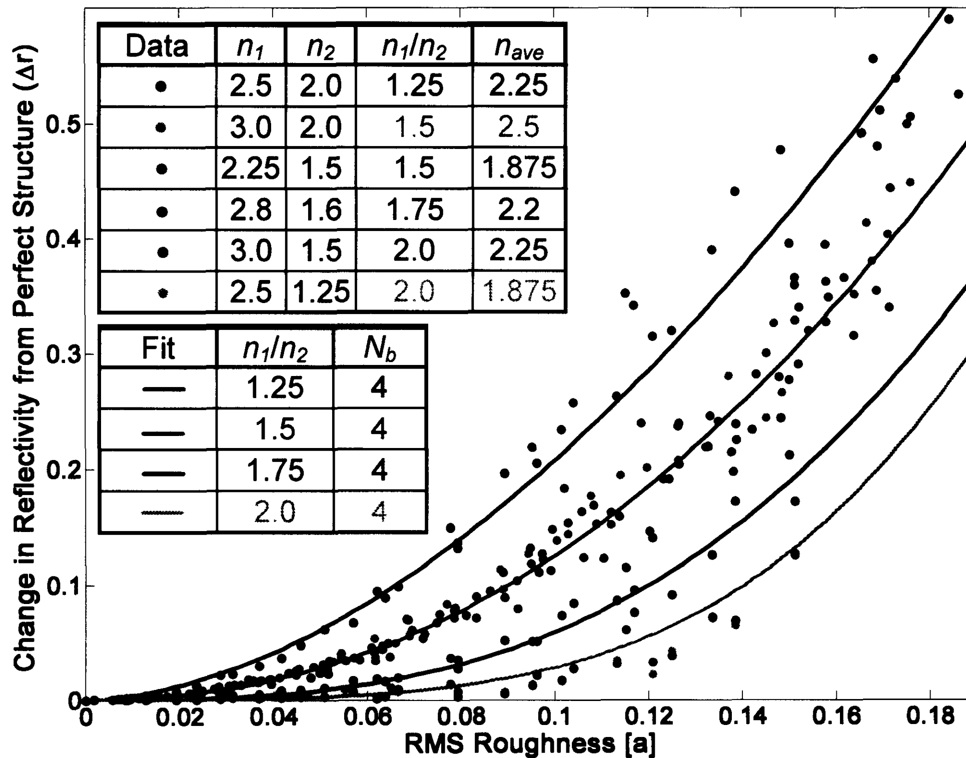

Figure 4.8 The calculated percent change in reflectivity for several 4-bilayer quarter-wave stack configurations. Empirical fits to the data, with index contrast and number of bilayers as the only parameters, are also shown.

of average refractive index and index contrast on the change in reflectivity from roughened 1D photonic crystals. These two parameters were chosen in particular because of their relevance to the optical properties of perfect 1D photonic crystals, as was discussed in chapter 2. These simulations reveal that the percent change in reflectivity is also independent of the 1DPC's average refractive index. This is illustrated by the fact that the results for the two structures that both have index contrasts of 1.5 overlap, despite the fact that they have vastly different average index values. This same behavior is seen with the two structures that both have index contrasts of 2.0. This result makes sense in light of scattering theory, which holds that the amount of scattered power from a scattering center is only proportional to the index contrast between the scattering center and the ambient medium.

Thus, the only refractive index parameter that determines how tolerant a 1DPC will be to interfacial roughness is the refractive index contrast. As revealed in Fig. 4.8, a higher index contrast crystal will be more robust, having a smaller change in reflectivity for the same RMS roughness as a lower index contrast system. In fact, the difference in the reflectivity results for different index contrast systems can be quite large. For example, at about 15% RMS roughness, the change in reflectivity for a 1.25 index contrast system reaches almost 40%, while a 2.0 index contrast system sees a change of only 15%. This conclusion starkly contrasts the prediction that would be made by scattering theory, which maintains that the amount of scattered power increases with increasing index contrast. However, a more rigorous scattering theory analysis for these structures will reveal a result that is consistent with the above conclusion. This analysis will be the subject of chapter 5.

Additional simulations were done to study the effect of the number of bilayers on the change in reflectivity due to interfacial roughness. The results of these simulations for a photonic crystal with indices n_1=2.25 and n_2=1.5 are shown in Fig. 4.9. They reveal that the number of bilayers also plays an important role in determining the change in reflectivity from roughened structures. As the number of bilayers decreases, the crystal becomes less tolerant to interfacial roughness. Again, this difference can be quite large, with a 2-bilayer system having a change of more than 40% at an RMS roughness of 15%, while a 6-bilayer system has a change of only about 15% at the same roughness value.

Again, traditional scattering theory would predict an opposite trend because the greater the number of bilayers, the more scattering centers and therefore the larger loss in reflected power due to scattering. However, again, the analysis in chapter 5 will reveal a result which is consistent with the above trend.

Ten other structures were simulated with varying values of the refractive index contrast and number of bilayers. These additional simulations were done to map out the reflectivity response to roughness over the parameter space encompassing index contrasts between 1.25 and 2.0, and bilayers between 2 and 6. A multi-parameter fit of the data from all the simulations was then done to provide an empirical estimate of reflectivity robustness to roughness. The fit was performed using OriginLab curve fitting software. A general form for the fit that represented the data was chosen:

$$\Delta r = aR^{b}. \tag{4.11}$$

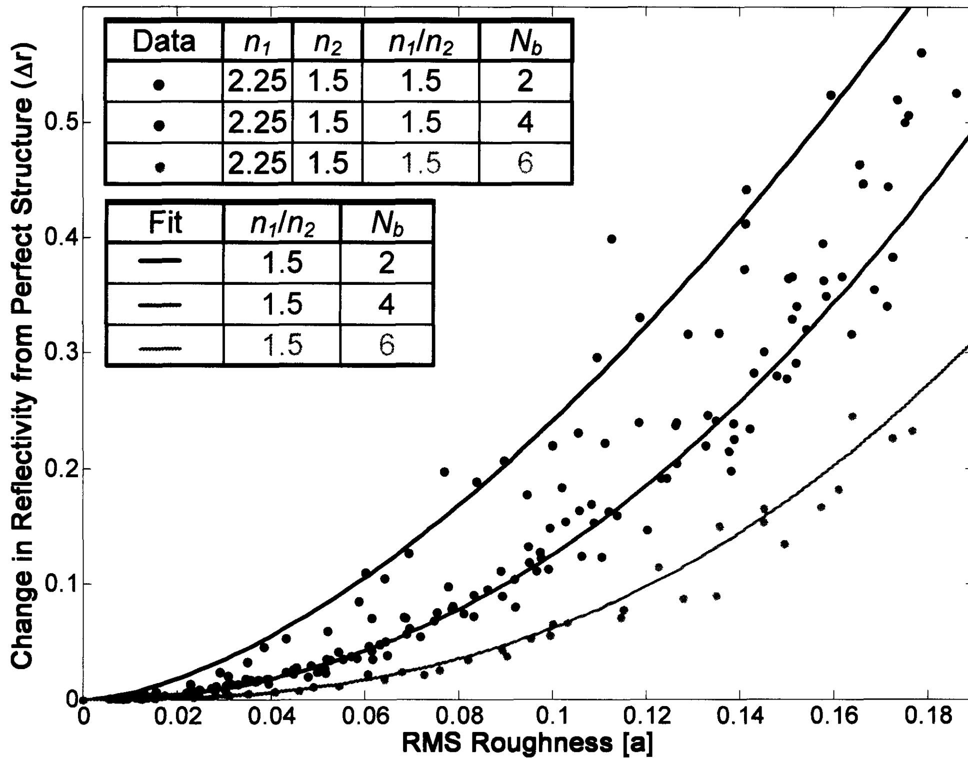

Figure 4.9 The calculated percent change in reflectivity for several n_1=2.25, n_2=1.5 quarter-wave stack configurations with varying bilayer numbers. Again, empirical fits to the data, with index contrast and number of bilayers as the only parameters, are also shown.

The variation of the parameters a and b with respect to the index contrast and the number of bilayers was then determined. First, the index contrast dependence was ascertained by identifying the functions that best fit each parameter as a function of index contrast while holding the number of bilayers constant. These functions were

$$a = A_1 - B_1 \exp\left[-\frac{C_1(n_1/n_2)}{D_1}\right], \tag{4.12a}$$

$$b = A_2 + B_2 \frac{\exp[-C_2((n_1/n_2) - D_2)]}{(1 + \exp[-C_2((n_1/n_2) - D_2)])^2}. \tag{4.13a}$$

The values of A_1, B_1, etc. varied with the value of the number of bilayers. These parameters were then also fit to an arbitrary function that only depended on the number of bilayers. This provided the form of the bilayer dependence of a and b. After this process, the final form for the parameters a and b in Eq. 4.9 were found to be

$$a = 12.15 - \frac{3.20}{(N_b - 2.46)} - \frac{13.61\exp\left[-(n_1/n_2)(16.93 - 8.05N_b)(N_b - 1.44)^{-1}\right]}{1 + 3630.98N_b - 1815.70N_b^2}, \tag{4.12b}$$

$$b = 1.44 + \frac{67.99\exp[-3.58((n_1/n_2) - 2.22) - 0.87(N_b - 5.63)]}{(1 + \exp[-3.58((n_1/n_2) - 2.22)])^2(1 + \exp[-0.87(N_b - 5.63)])^2}. \tag{4.13b}$$

This fit evaluated for the various structures tested is also shown plotted over the corresponding FDTD data in Figs. 4.8 and 4.9.

One caveat about this fit is that it is only known to be accurate for values of the index contrast between 1.25 and 2.0 and values of the number of bilayers between 2 and 6. The change in reflectivity for multilayer stacks that fall out of this parameter space cannot be predicted using the above fit. Furthermore, because these simulations are for normal incident waves, the above fits do not apply for oblique incident angles. However, light hitting the crystal at these angles will most likely be more sensitive to any interface roughness, and therefore, these estimates provide an upper limit of the robustness of a given 1DPC configuration. Unfortunately, as discussed in chapter 3, FDTD simulations of plane waves incident at angles other than normal incidence are extremely difficult. It either requires the development of new FDTD algorithms to get around the problem imposed by the periodic boundary conditions, or simulations done with absorbing boundary conditions on all domain walls with an extremely large domain in order to catch any reflections occurring at shallow angles and avoid edge effects. Both cases are

beyond the scope of this thesis. However, there are devices, such as vertical-cavity lasers and distributed bragg reflectors [Tropper (2004), Iga (2000)], that rely primarily on normal incidence reflectivity for their operation. The above analysis would be useful in evaluating or predicting the performance of these and other such devices, or setting constraints on the manufacturing process in order to achieve the desired level of device performance. For example, Eq. 4.9 could be inverted to obtain an estimate of an upper bound to roughness, given a normal incidence reflectivity tolerance:

$$R = \left(\frac{\Delta r}{a} \right)^{1/b}. \tag{4.14}$$

This in turn could be used to evaluate how precise the manufacturing process of the device needs to be in order to avoid roughness features larger than the upper bound given by this equation.

There is one other issue that needs to be addressed with the above analysis. All simulations presented above have been done with TE polarized light. However, most devices will rely on the reflectivity of both TE and TM polarizations. Therefore, the reflectivity response of roughened structures to TM polarized light also needs to be investigated. This is the topic of the next section.

4.5 TM Polarization Reflectivity Results

As with the TE polarization, a series of simulations were done with a TM polarized normal incidence plane wave to determine the dependence of the percent change in reflectivity on R_{RMS} and W_{RMS}. This required significant modification of the code in Sullivan [Sullivan (2000)] since that code was only written for TE polarized plane waves. Again, 120 simulations, corresponding to the same 120 structures of various W_{RMS} and R_{RMS} values studied in the TE polarization simulations, were done for a 4-bilayer quarter-wave stack with $n_1 = 2.25$ and $n_2 = 1.5$. The results of these simulations are shown in Fig. 4.10. As with the TE polarization results, the change in reflectivity shows a strong dependence on the RMS roughness of the structure, and correspondingly, no dependence on the RMS wavelength. Thus, the results of these simulations can also

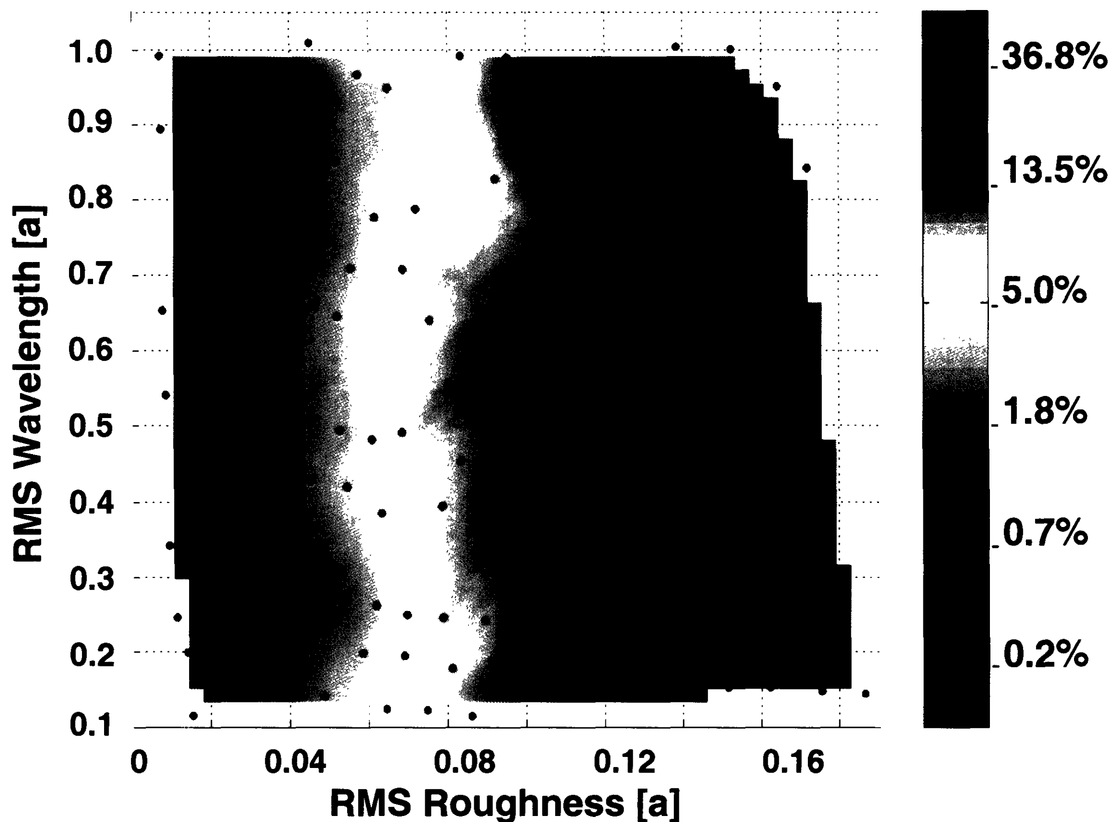

Figure 4.10 The calculated percent change in the TM-polarized normal incidence reflectivity for roughened 4-bilayer quarter-wave stacks with n_1=2.25 and n_2=1.5.

be collapsed onto a 2D plot with RMS roughness as the only parameter. This allows easy comparison of these results to the results of the corresponding TE polarization simulations. Fig. 4.11 shows this comparison, which indicates that TE and TM polarized stacks within the parameter ranges tested. This result may seem surprising, but again, it can be easily explained once the physical mechanism for the reflectivity decrease is understood.

The fact that the TE and TM response for the roughened structures is equivalent leads to another significant conclusion. Since all plane waves that are incident on a 3D roughened surface will simply be a linear combination of TE and TM polarized waves (see chapter 2), the above results for TE waves can be applied to full 3D roughened quarter-wave stacks for plane waves at normal incidence. Thus, the correct reflectivity response for a 3D roughened multilayer stack within the parameter space tested can be obtained from just a 2D FDTD simulation. This saves a significant amount of computing

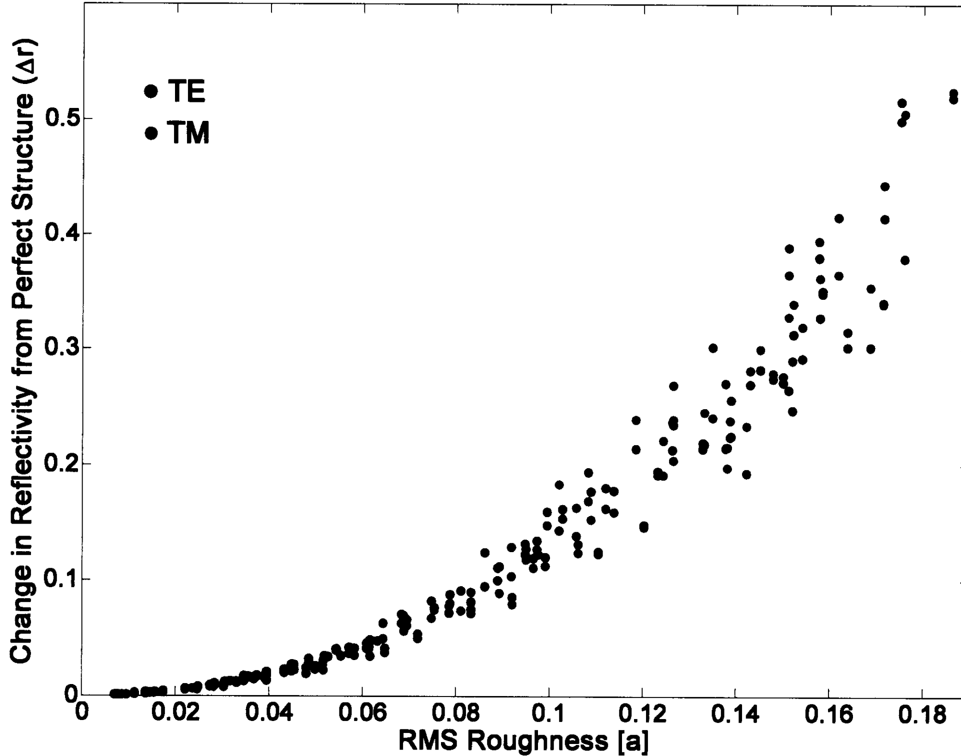

Figure 4.11 Comparison of the TE and TM polarization reflectivity results.

time. Once a model to physically explain the above results is identified, this conclusion will be even more significant because it will mean that simple application of the model can lead to accurate results for 3D structures.

4.6 Conclusions

In order to determine the optical effect of rough interfaces, 2D FDTD simulations have been done on several 1DPC quarter-wave stacks at normal incidence with the quarter-wave-tuned wavelength. Several conclusions can be made from the results of these calculations.

1. The percent change in the reflectivity of the rough structures from the ideal structure strongly depends on the RMS roughness of the interfaces in the structure. For example, an RMS roughness of 0.05*a* can lead to a change in reflectivity of almost 10% in some structures.

2. The percent change in the reflectivity of the rough structures is independent of RMS distance between rough peaks or valleys (W_{RMS}) when this parameter is within the range of $0.1a$ to $1.0a$.
3. The percent change in the reflectivity of rough structures is independent of the average refractive index of the photonic crystal.
4. The percent change in the reflectivity of rough structures strongly depends on the 1DPC's refractive index contrast. Systems with higher index contrast are more robust, having a smaller percentage change in the reflectivity than a smaller index contrast system with the same interfacial roughness. This result is counter-intuitive to simplified scattering theory predictions.
5. The percent change in the reflectivity of rough structures strongly depends on the number of bilayers in the 1DPC. An increase in the number of bilayers results in a more robust structure. This is also counter-intuitive to simplified predictions made from scattering theory.
6. TE and TM polarized light produce equivalent optical responses from roughened structures within the parameter ranged tested ($R_{RMS} = 0.005a$ to $0.175a$, $W_{RMS} = 0.1a$ to $1.0a$). This allows the above results for TE polarized light to be applied to full 3D roughened structures.

Furthermore, an empirical fit based on the results of the simulations was reported to provide estimates of interfacial roughness tolerances for devices.

Light that is incident on a rough surface will be scattered by that surface because the roughness features act as scattering centers. Because several of the conclusions reported above contradict predictions that would be made by scattering theory, a more rigorous scattering theory analysis for these specific structures is in order. This analysis will be the topic of the next chapter.

Chapter 5: A Scattering Model of Interfacial Roughness

The previous chapter presented the results of several FDTD simulations that were done to systematically study the effect of interfacial roughness on the optical properties of 1D photonic crystals. Several conclusions that were drawn from these results contradict the predictions made from a preliminary analysis using classical scattering theory (known as Mie theory) [Bohren (1983)]. The relevant conclusions of the preceding chapter and the corresponding Mie theory predictions are presented below.

The reflectivity of a roughened 1DPC does not depend on its average refractive index. This conclusion is actually intuitive when seen through the eyes of Mie theory. As explained in chapter 2, the intensity of the scattered field only depends on the index contrast between the scatterer and the surrounding medium. Thus, the absolute sizes of the refractive indices never comes into play except when considering the incident

wavelength, which will be equal to the wavelength of the light in vacuum divided by the index of refraction of the surrounding medium. This fact will be utilized later when analyzing the scattering from each interface in the photonic crystal because it means that certain interfaces within the crystal will produce more scattering then others. But each photonic crystal will have the same amount of internal scattering if it has the same index contrast, independent of the average index.

A high index contrast roughened photonic crystal will have a smaller change in the reflectivity than a low index contrast crystal with the same roughness. This result is counter-intuitive to the predictions of Mie theory. As stated above, the intensity of the scattered field does depend on the magnitude of the refractive index contrast between the scatterer and the surrounding medium. So the fact that a dependence on this parameter is seen with the FDTD simulations does not contradict Mie theory. However, scattering theory would predict the opposite dependence: that the higher index contrast structures would be less tolerant to interfacial roughness than the low index contrast structures. This is because the intensity of the scattered field increases with increasing index contrast. So the interfaces in the higher index contrast structures will scatter a higher percentage of the incident light than the lower index contrast structures. Thus, the lower index contrast structures would experience less loss of the reflectivity due to scattering than the higher index contrast structures. A more rigorous application of Mie theory to these specific structures will be needed in order to remedy this apparent contradiction.

A roughened photonic crystal that has a large number of bilayers will have a smaller change in the reflectivity than a photonic crystal with a small number of bilayers at the same roughness. Again, this is an apparent contradiction of classical scattering theory. A larger number of bilayers in a structure means that it has more interfaces, and therefore more roughness features to act as scatterers, than a structure with a smaller number of bilayers. Thus, classical scattering theory would predict that more light would be lost due to scattering in a structure with a larger number of bilayers. Again, a more rigorous application of Mie theory to these structures will be needed to correct this discrepancy.

These apparent contradictions prompted a more methodical approach of applying Mie theory to these structures. A model was used to imitate the role of the roughness

features as scatterers on each interface in the crystal. This model and the results of its implementation are described in the remainder of this chapter.

5.1 Scattering Model

The scattering model presented here is based on the following hypothesis: the forward scattering from the roughness features on each interface is pushing field intensity through the subsequent layer that would otherwise have been reflected if the interface were smooth. This is what is causing the decrease in reflected power and increase in transmitted power. In essence, the roughness features are therefore changing the reflection and transmission coefficients of each layer in the photonic crystal. This effect can be imitated by removing the roughness features and changing the refractive index of each layer to account for the change in reflection and transmission, as illustrated in Fig. 5.1.

The following algorithm was developed in order to calculate the modified refractive index for each layer based on the forward scattered intensity at each interface. The problem will first be solved for a single interface separating two semi-infinite spaces. It will then be applied to the simulated systems, which have multiple interfaces. For a single smooth interface between two semi-infinite spaces, an expression can be obtain for the transmissivity (or transmitted intensity) of the interface using Eqs. 2.51 and 2.59:

$$t = \frac{4p_{it}}{(1+p_{it})^2}. \tag{5.1}$$

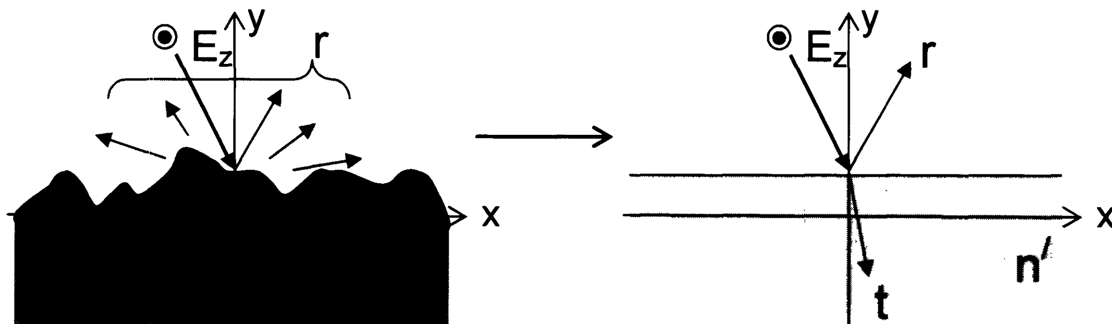

Figure 5.1 Schematic illustrating the idea of mimicking the change in reflection and transmission due to the roughness features by replacing the rough surface with a smooth surface and correspondingly modifying its refractive index.

The parameter p_{it} is related to the index of refraction of the spaces above and below the interface by Eq. 2.53. At normal incidence, utilizing Eq. 2.35, this expression becomes

$$p_{it} = \sqrt{\frac{\varepsilon_t}{\varepsilon_i}} = \frac{n_t}{n_i}, \tag{5.2}$$

since $\mu_t = \mu_i$ for the structures tested here. Although the TE polarization expressions from chapter 2 were used to derive Eq. 5.2, the relationship between p_{it} and the refractive indices is the same if the TM polarization expressions are used instead. This is because the TE and TM polarizations are equivalent (i.e. they results in the same orientation of the fields) at normal incidence.

If the interface has roughness features, the hypothesis stated above postulates that the forward scattered intensity from the roughness features adds to the transmissivity that would result if the interface were smooth. Therefore, the modified transmissivity for the rough interface is

$$t' = t + I_{fs}. \tag{5.3}$$

This new transmissivity can then be related back to a modified p_{it} by

$$t' = \frac{4p'_{it}}{(1 + p'_{it})^2}. \tag{5.4}$$

Combining Eqs. 5.3 and 5.4, an expression for the new p_{it} can be found in terms of the transmissivity of the smooth interface and the forward scattered intensity:

$$p'_{it} = \frac{2 - t' \pm 2\sqrt{1 - t'}}{t'} = \frac{2 - t - I_{fs} \pm 2\sqrt{1 - t - I_{fs}}}{t + I_{fs}}. \tag{5.5}$$

This in turn can be related back to a modified value for the refractive index of the half space below the interface:

$$n'_t = p'_{it} n_i. \tag{5.6}$$

So the increased transmissivity of the rough interface can be imitated by replacing it with a smooth interface and modifying the refractive index of the region below the interface in the manner described above.

The plus/minus sign in Eq. 5.5 indicates that there are two solutions for the modified refractive index. This is because the value of the refractive index can either be greater than or less than the refractive index of the medium above the interface. The plot

of refractive index vs. transmissivity in Fig. 5.2 illustrates this. For a given transmissivity, there are two possibilities for the refractive index of the transmitting medium: one that is greater than n_0 and one that is less. Therefore, when applying Eq. 5.5 to a multilayer stack, the appropriate index value for each layer must be carefully considered.

The amount of forward scattering can be calculated using the Mie theory equations presented in chapter 2. The roughness features that are first encountered by the incident light are those that protrude into the incident medium from the transmitting medium. These roughness features can be approximated as circular scatterers, with radii equal to the RMS roughness of the interface and refractive indices equal to the refractive index of the transmitting medium. Although the appropriate three-dimensional analogues of these circular scatterers are cylinders, the amount of scattering was approximated

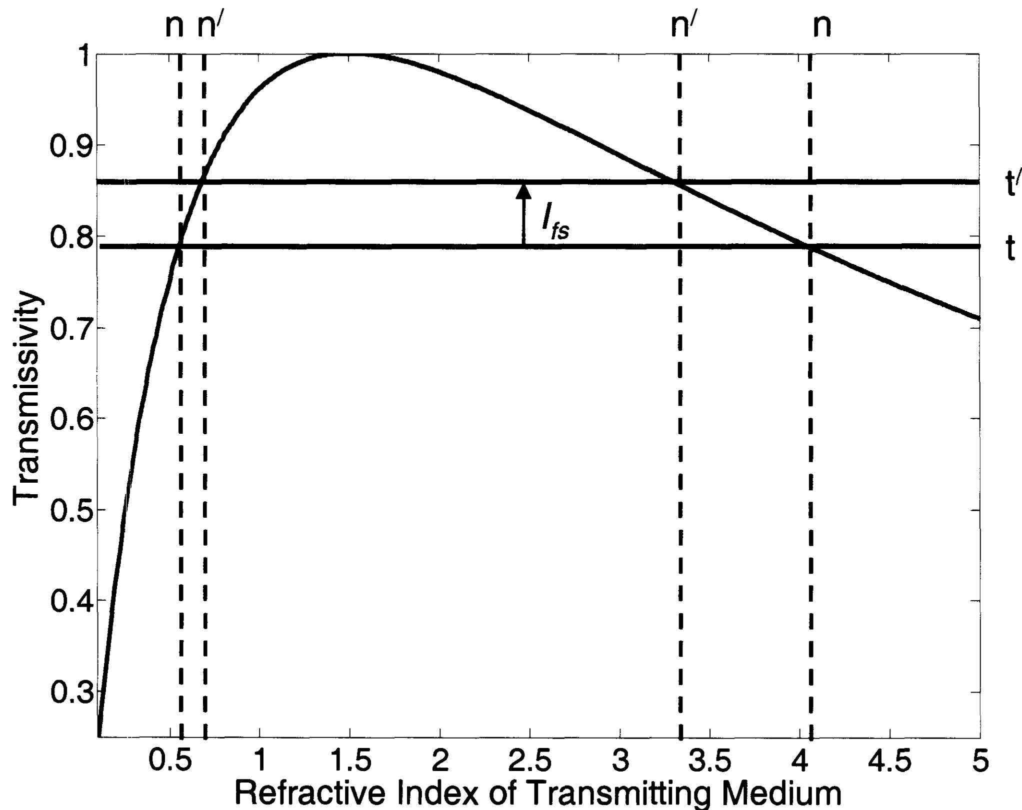

Figure 5.2 Transmissivity vs. the transmitting medium's refractive index (n_t) for an incident medium with refractive index n_i=1.5. Notice that for a given transmissivity (t) there are two possibilities for n_t, one larger than n_i and one smaller.

using spheres instead. This is because many freeware codes exists that calculate the amount of scattering from spherical scatterers, and the calculations themselves are straightforward. On the other hand, no freeware codes exist that calculate scattering from cylindrical scatterers, and the calculations are much more complicated, requiring infinite sums of cylindrical Bessel functions. Furthermore, the amount of scattering from a cylinder will be close (same order of magnitude) to the amount of scattering from a sphere with the same radius. Since this model is simply being used to examine the trends seen with the FDTD results, and absolute reflectivities are not expected to match the simulation results anyway, approximating the amount of scattering using spherical scatterers was deemed acceptable.

Once the roughness features are approximated as spherical scatterers, the intensity of scattered light normalized to the intensity of incident light, which is essentially the percentage of incident intensity that is scattered, is provided by Eq. 2.94. The radius of the scatterers is equal to the RMS roughness of the interface, and the index contrast between the scatterers and the ambient is the index contrast between the medium after the interface and the medium before the interface. Note that this definition of index contrast can result in index contrasts which are less than one if the ambient medium has a higher refractive index than the scatterer. Furthermore, the wavelength of light incident on the scatterers is the wavelength of the incident light in vacuum divided by the index of refraction of the incident medium.

The scattered intensity in Eq. 2.94 is given as a function of scattering angle. In order to find the forward scattered intensity, the scattered intensity can be integrated between the scattering anlges of -90° and 90°, which corresponds to all forward-directed scattering. This integrated value was the value used for I_{fs} in calculating the modified refractive index of each layer in the simulated structures from Eqs. 5.5 and 5.6.

If there is a large index contrast between the incident and transmitting media, then the forward scattered intensity will be large, resulting in a large modification of the index. On the other hand, a smaller index contrast interface would have a smaller amount of forward scattered intensity for the same roughness size and therefore a smaller change in the refractive index of the transmitting medium. Therefore, this algorithm follows the trends predicted by Mie theory.

5.2 Implementation of the Model

Using the above algorithm, the indices of refraction of each layer in the tested structures was modified based on the index contrast at each interface in the structure and the RMS roughness of the interface. A freeware Matlab code called Matlab Mie [Barnett (1997)] was used to perform the scattering calculations using Eqs. 2.92 through 2.95. This code was verified by calculating a scattering profile under a certain set of conditions with a different software package (Scatlab [Bazhan (2005)]) and confirming that the results from the Matlab Mie codes for the same conditions were equal. Nodal magnitudes were used for the scatterer radius and the incident wavelength since only the ratio of those values matters.

The value of I_{fs} for each interface in the photonic crystal structure was calculated by integrating the forward-directed scattered intensity according to the above method. There are four distinct interfaces in the simulated quarter-wave stacks, as shown in Fig. 5.3. These are: the air-to-high index interface, the low-to-high index interface, the high-to-low index interface, and the low-to-air interface. Each of these interfaces will result in a different forward scattered intensity, which in turn will lead to a different modified

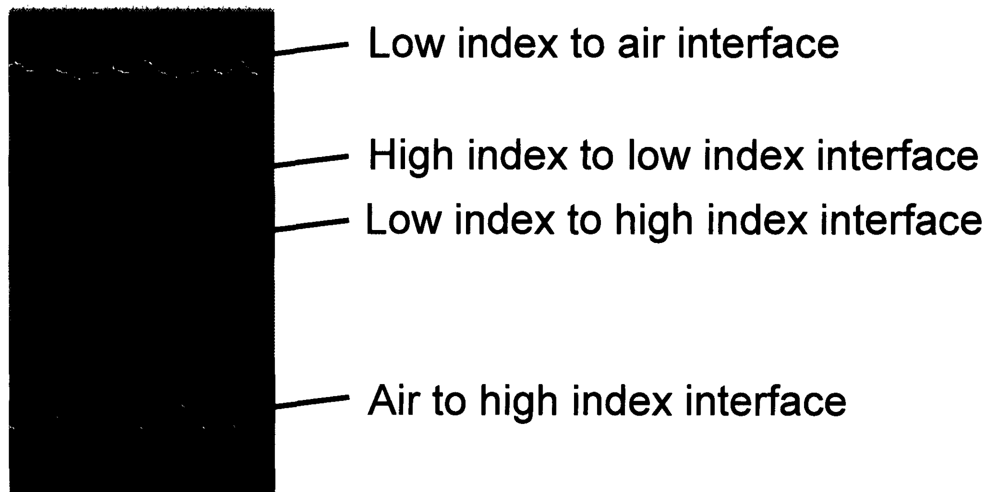

Figure 5.3 Illustration of the four distinct interfaces in the simulated quarter-wave stacks. Each interface results in a different amount of scattering.

refractive index value. Thus, the top layer in the photonic crystal structure, which is a high index layer, will have a different modified index than the other high index layers in the crystal. This is because the modified index for this top layer will be determined by the amount of forward scattered intensity from the air-to-high index interface, while the other high index layers will have modified values based on the scattering at the low-to-high index interfaces. Thus, the value of the modified index for each layer will be determined by the scattering characteristics of the preceding interface.

When calculating the amount of forward scattering at internal interfaces in the structure, the actual value, rather than the modified value, of the refractive index of the preceding layer is used to calculate the index contrast of the interface. This is done because the actual amount of forward scattering at this interface is determined by the actual index contrast of the interface, not the modified index contrast. Furthermore, in calculating the modified value of the refractive index of each layer, the actual value of the preceding layer's refractive index is used (i.e. Eq. 5.6). If the modified value was used instead, the high and low refractive indices of the layers in the modified structure would progressively approach some mean value as the layers went deeper into the structure. The resultant modified structure would no longer accurately represent what is physically happening in the system. The percentage of reflected light at each interface would gradually decreases as the interfaces become deeper in the structure. In reality, the correct implementation of the above hypothesis would create a structure where the percentage of reflected light at an equivalent interface in the structure would remain the same. The only role of the roughness features is to push more intensity to the next interface than a smooth interface would. Once this increased intensity reaches the next interface, the same percentage that was pushed through on the last equivalent interface should be pushed through again. This is achieved if the actual refractive index value of the preceding layer, rather than the modified value, is used to calculate the modified value of the refractive index of each layer in the structure.

Recalling that there are two solutions for the value of the modified index (from Eq. 5.5), the correct value for the new index in the simulated structures is determined by the appropriate value relative to the index of the preceding layer. For example, for modification of a high index layer value, the solution that gives a modified index value

above the preceding layer's index would be the appropriate choice. This retains the photonic crystal high-low index bilayer structure.

The implementation of this model to the simulated quarter-wave stacks reveals that there are certain interfaces in the stacks that cause much more scattering than others. Recall that the scattered intensity is determined by two factors: (1) the index contrast between the surrounding medium and the scatterer, and (2) the size of the scatterer relative to the incident wavelength. The highest index contrast interface in the quarter-wave stacks is the air-to-high index interface. However, the wavelength that is incident on this interface is equal to the vacuum wavelength, which will be extremely large compared to even the largest roughness features. So the roughness on this interface contributes very little to the overall scattering of the structure in most cases. The remaining interfaces in the structure have very similar index contrasts, and the interface with the higher index contrast will depend on the actual refractive index values used. However, the incident wavelength for each of the remaining interfaces varies significantly based on the refractive index of the preceding layer. This is illustrated in Fig. 5.4.

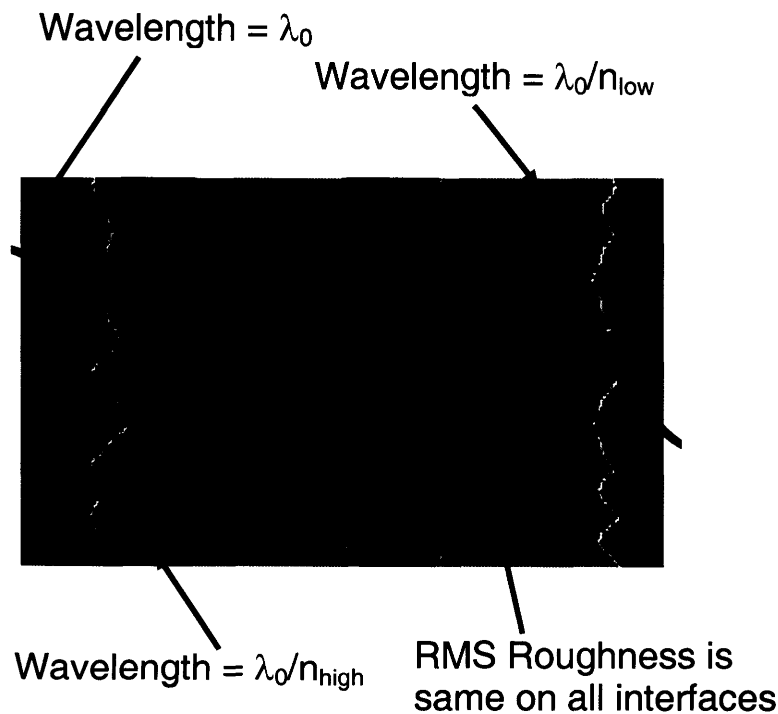

Figure 5.4 Schematic illustrating that the incident wavelength for each interface depends on the refractive index of the preceding layer, while the scatterer size remains the same.

The interface that has the shortest incident wavelength is the high-to-low index interface. Thus, the size of the roughness features relative to the wavelength is much larger at that interface than the other interfaces. This causes the high-to-low index interface to be the most critical interface in terms of scattering in most systems. The index modification model supports this by the fact that the low index layers experience a larger change in their refractive indices than any of the other layers in the structure. Furthermore, the amount of scattering from an interface will also depend on the amount of power incident on it. Therefore, since the power of the incident wave decays as it proceeds through the structure, the first high-to-low index interface will experience the highest incident power. Thus, this specific interface will be the most critical one in most devices. It is possible to imagine a case where the penetration depth in a structure is so short that only a small amount of power reaches even the first high-to-low interface. In that case, the relative amount scattering at each interface will have to be directly compared in order to determine which one is most critical.

An example of the implementation process applied to one of the simulated structures is shown in Fig. 5.5. The initial structure has 4 bilayers with n_1=2.25 and n_2=1.5, and an RMS roughness of $0.1a$. Note that the index value of the top layer is different than the values of the other high index layers in the modified structure. Also note that the high-low bilayer structure is retained, but the index contrast of the modified structure is much lower than that of the initial structure due to the high indices decreasing and the low indices increasing from the modification. This change makes sense because it allows more light to be transmitted through the modified structure, mimicking the hypothesized effect of the roughness features correctly.

5.3 Results of the Model

The above process was used to create several modified structures corresponding to the same photonic crystal systems tested with the FDTD calculations. Because the modified structures are one-dimensional (i.e. there is only structural variation in the direction into the crystal), a 1D transfer matrix code could be used to determine the reflectivity of the modified structures and the corresponding percent change in reflectivity from the perfect structure. Figs. 5.6 and 5.7 show the results of those

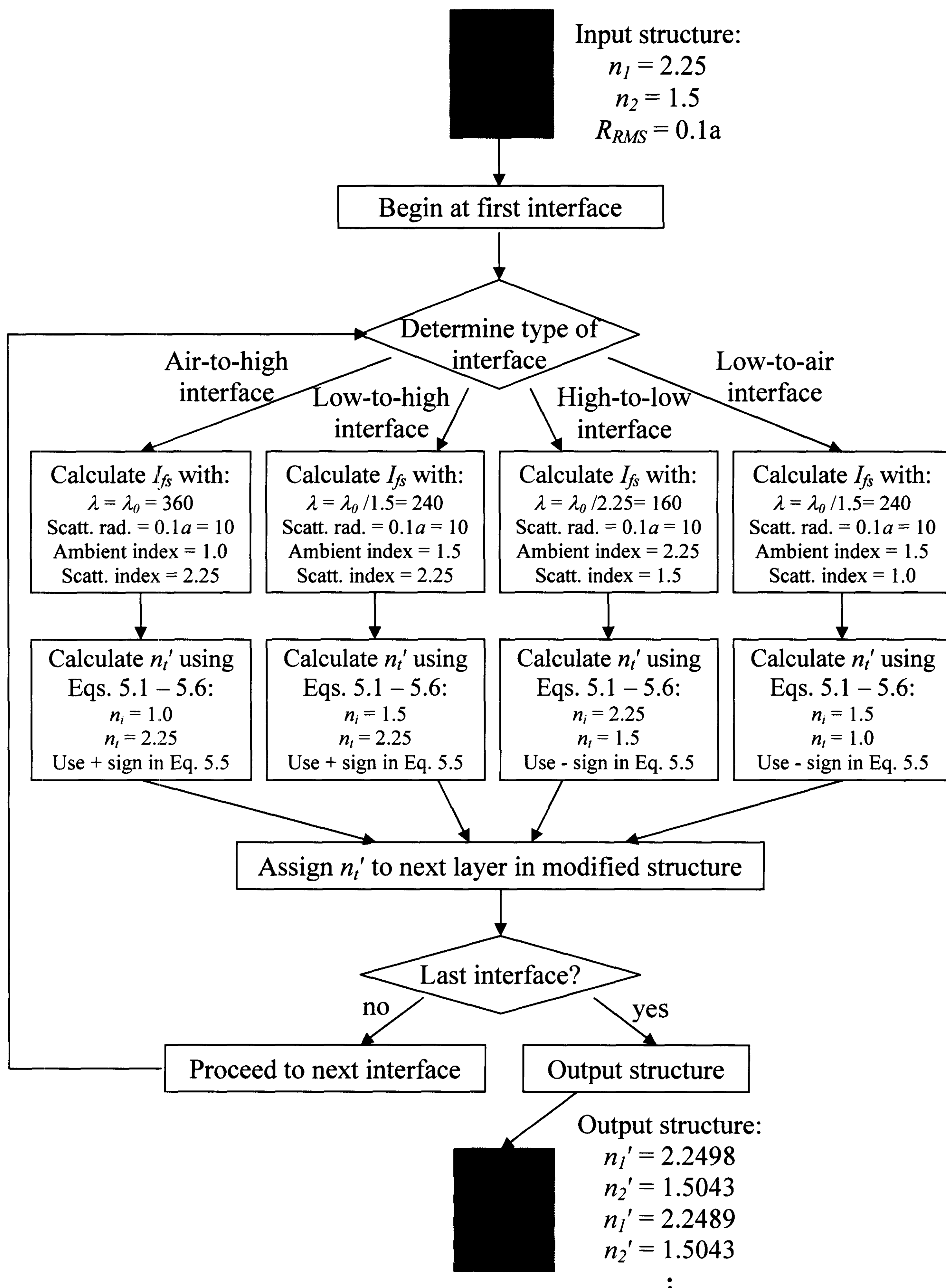

Figure 5.5 The index modification process applied to a 4-bilayer structure with n_1=2.25, n_2=1.5, and $R_{RMS} = 0.1a$.

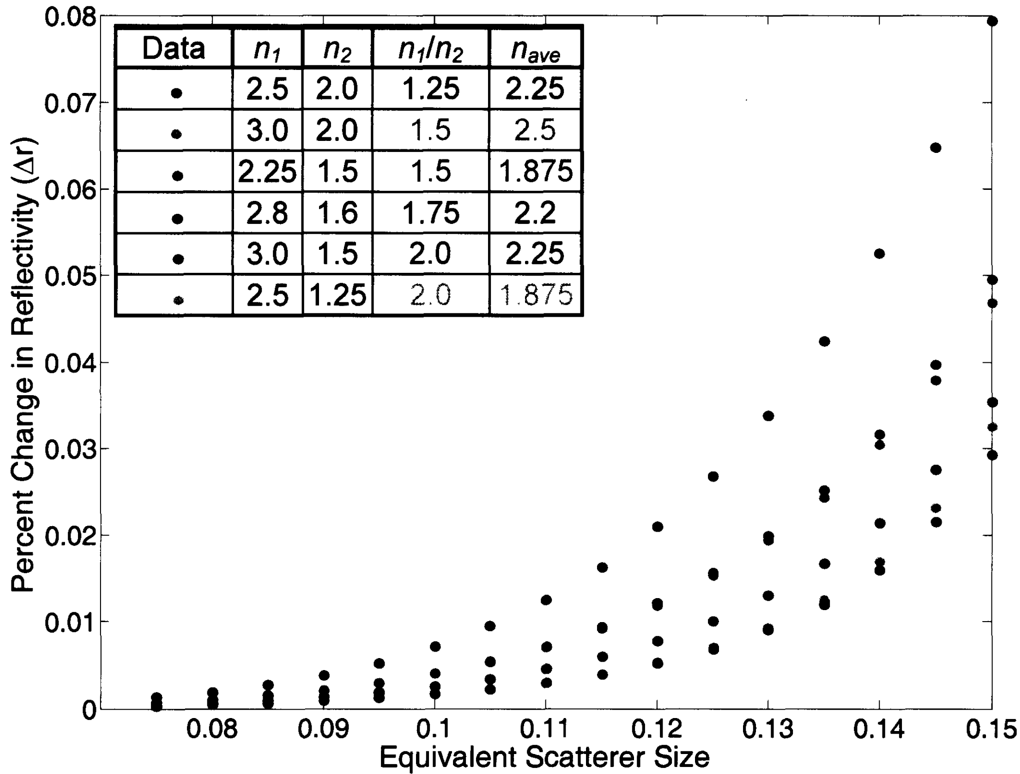

Figure 5.6 Index modification results for the same 4-bilayer systems presented in chapter 4. The scatterer sizes reported on the plot have been scaled to the equivalent RMS roughness value. The trends predicted with this model agree with the FDTD results.

calculations for the same photonic crystal systems presented in chapter 4. Surprisingly, the trends predicted with this scattering model are consistent with the results of the FDTD calculations. Thus, even though the higher index contrast structures experience larger modifications to their constituent refractive indices, they still show a smaller percent change in the reflectivity than the lower index contrast structures. This suggests that the higher index contrast structures are more tolerant to structural changes than the lower index contrast structures. Similarly, structures that have a higher number of bilayers are more tolerant to structural deviations from perfection.

These trends are consistent with the idea that the magnitude of the absolute reflectivity of a photonic crystal system will be an indication of how tolerant it is to structural changes. Either a high number of bilayers and/or a high index contrast will result in structures with a high value for the absolute reflectivity. For example, the 4-bilayer system with n_1=3.0 and n_2=1.5 (n_1/n_2=2.0) has an absolute reflectivity at the

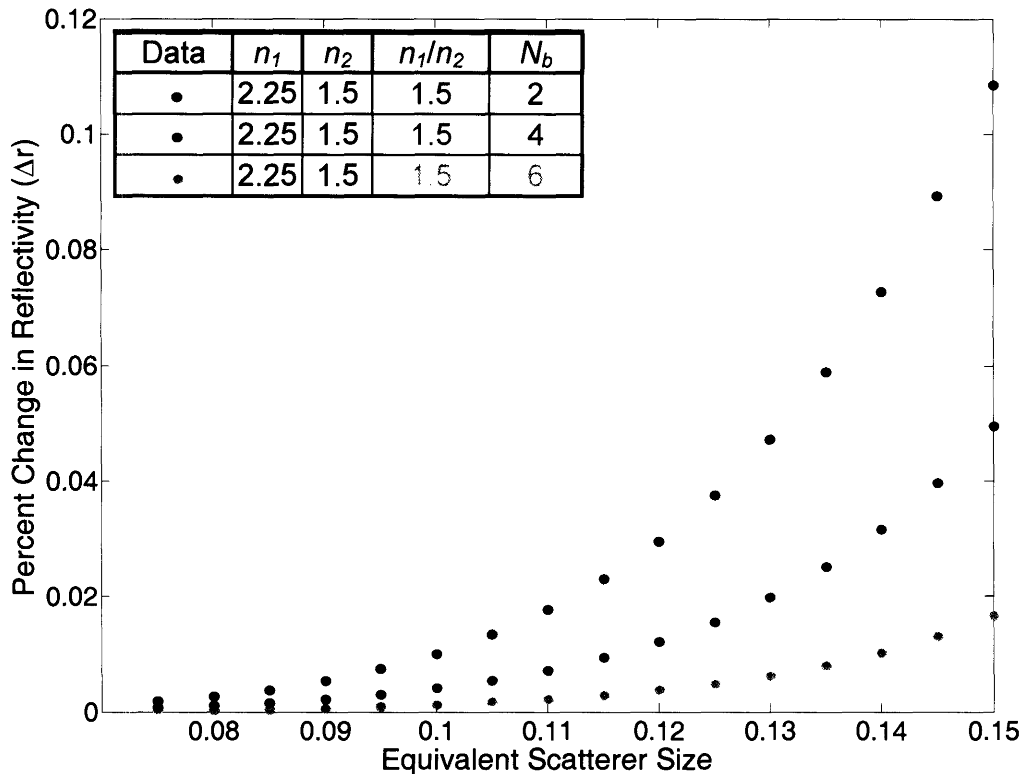

Figure 5.7 Index modification results for the same n_1=2.25, n_2=1.5 bilayer systems presented in chapter 4. The scatterer sizes above have been scaled to their equivalent R_{RMS} value. Again, the trends are consistent with those seen from the FDTD results.

center of the bandgap of 0.9845, while the 4-bilayer system with n_1=2.5 and n_2=2.0 (n_1/n_2=1.25) only has an absolute reflectivity of 0.5079 at the center of the bandgap. Likewise, the 6-bilayer system with n_1=2.25 and n_2=1.5 (n_1/n_2=1.5) has an absolute reflectivity of 0.9696, while the 2-bilayer system with the same values for the refractive indices has an absolute reflectivity of 0.449. Thus, the tolerance of a photonic crystal to structural changes mirrors the absolute reflectivity of the crystal at the center of the bandgap.

Although the index modification calculations predict trends that are consistent with the FDTD results, they do not accurately reproduce the magnitude or the curve shape of the FDTD data. The index modification curves rise too steeply and they result in reflectivity changes that are too small. This is illustrated in Fig. 5.8, which compares the results of the FDTD calculations to the index modification calculations for the same structure. Although the absolute magnitudes of the two calculations were not expected to

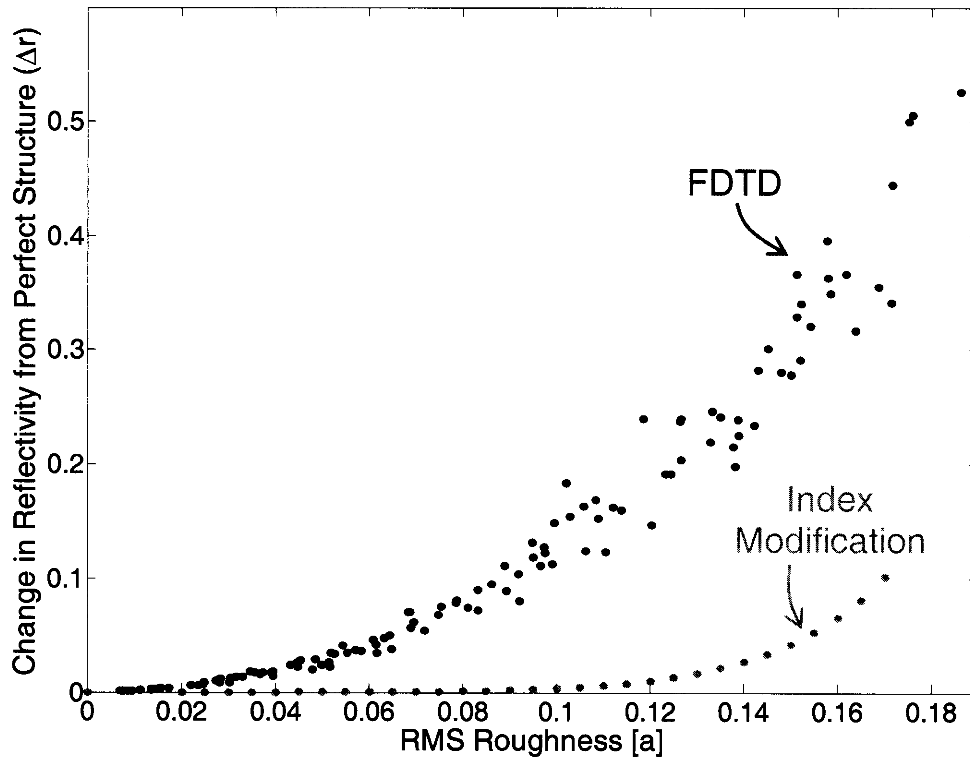

Figure 5.8 Comparison of the results from the FDTD calculations and the index modification model for the 4-bilayer n_1=2.25, n_2=1.5 system. Although the index modification model correctly predicts the trends seen with the FDTD calculations, it fails to reproduce the actual magnitude and curve shape of the FDTD data.

match, it is clear that the amount of scattering that is resulting from these structures is much too small to account for the change in the reflectivity that is being seen with the FDTD results. This is especially true in the region before the point where the index modification curve starts to rise steeply ($R_{RMS} < 0.1a$). The amount of scattering in this region is so small that the change in reflectivity is very close to zero. This points to the need for another model that will explain the FDTD results and give some insight into the physical mechanism that is causing the large change in reflectivity. This model, along with the physical insight, will be revealed in the next chapter.

5.4 Conclusions

In order to gain more insight into the counter-intuitive results of the last chapter, a model was developed to mimic the effect of scattering from the roughness features at each interface in the photonic crystal structures. This model was based on the hypothesis

that the forward scattering from the roughness features is pushing extra field through each layer in the photonic crystal. This field leakage was approximated by modifying the transmission coefficient of each layer through modification of the refractive index based on the amount of forward scattering at each interface.

When applied to the same structures tested in the FDTD calculations, the results of the model revealed trends that are consistent with the FDTD results. Namely, the higher index contrast structures and the structures with a larger number of bilayers showed a smaller change in the reflectivity than their counterparts. Thus, a more rigorous application of scattering theory to the specific structures tested here results in trends that contradict the intuitive predictions of scattering theory. Furthermore, the model's results suggest that the absolute reflectivity of a structure is an indication of how tolerant it is to structural imperfections. Specifically, structures with a higher absolute reflectivity will be more tolerant to structural imperfections than lower reflectivity structures.

However, although the trends predicted by this model agree with the FDTD results, the model does not reproduce the FDTD data accurately. The sizes of the reflectivity changes are much too small, especially at R_{RMS} values less than $0.1a$. Thus, another model is needed that will capture the magnitude of the reflectivity changes and provide insight into what is physically happening in the structures. Two approximations that are commonly used to calculate the amount of coherent scattering from single rough surfaces will be employed to provide this insight. These approximations, along with the results of their application to the simulated structures, will be presented in the next chapter.

Chapter 6: Homogenization and Kirchhoff Approximations for Interfacial Roughness

Although the results of the model developed in the previous chapter predicted the same general trends as those observed with the FDTD results, they failed to reproduce the magnitude and curve shape of the FDTD data. Therefore, another model was sought that could more accurately reproduce the data and provide physical insight into the mechanism for the decreased optical response of the structures.

In an attempt to identify this model, two approximations that are commonly used to calculate the amount of coherent scattering from single rough surfaces were applied to the simulated structures. It is important to note that these approximations only apply to coherent reflections from roughened surfaces, which only occur in the direction of

spectral reflection [Kong (2000)]. Thus, the representation of a 2D roughened surface with one or a series of several 1D surfaces, as these approximations do, remains valid despite the introduction of additional symmetries that are not present in the original structure. But because of this, these approximations provide no insight into the magnitude of the incoherent scattering from the roughened surfaces. Therefore, the magnitude of the incoherent scattering from the simulated structures will need to be explored by another method, which will be presented in chapter 7. So any comparison made between the results of these approximations and the FDTD results will only be valid for the coherent portion of the reflected wave. This chapter will present both of these approximations along with the results of their application to the simulated structures.

6.1 The Homogenization Approximation

The homogenization approximation is illustrated in Fig. 6.1. It involves averaging the dielectric constant (the square of the refractive index, Eq. 2.35) of the roughened portion of the surface in order to approximate the structure with a graded interface [Beckmann (1963), Gaylord (1986), Ogilvy (1991), Sentenac (1998), Voronovich (1994)]. Specifically, if the region containing the rough interface is discretized into several infinitely thin strips oriented parallel to the surface, then the dielectric constant would be averaged in each of these strips to produce an average dielectric constant function $<\varepsilon>(y)$ that is characteristic of the interface. Mathematically, if $f_h(x)$ describes the height of the roughness profile as a function of distance along the interface, then $<\varepsilon>(y)$ can be calculated through piece-wise integration:

$$\varepsilon(x,y) = n_i^2 \quad \text{if} \qquad y > f_h(x), \tag{6.1}$$

$$\varepsilon(x,y) = n_t^2 \quad \text{if} \qquad y \le f_h(x), \tag{6.2}$$

$$\langle \varepsilon \rangle (y) = \frac{1}{2L} \int_{-L}^{L} \varepsilon(x,y) dx. \tag{6.3}$$

This function only depends on the distance into the interface. Thus, the above process collapses a two-dimensionally structured surface to a 1D structure that has a graded refractive index profile at the interface. The length over which the profile is graded depends on the roughness of the interface. An interface with a larger RMS roughness

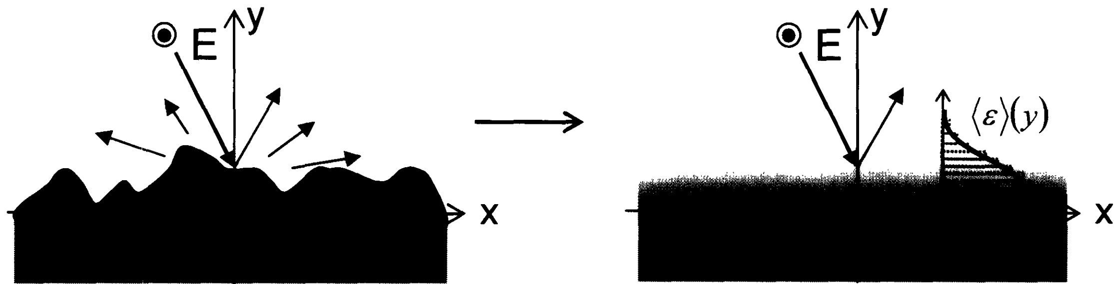

Figure 6.1 Schematic depicting the homogenization approximation for a single rough interface. The dielectric constant in the region of the rough interface is average to produce a smoothed dielectric constant function. The smooth dielectric constant is then approximated with a series of layers.

will result in a 1D structure with a more gradual interface, while a smaller RMS roughness will result in a sharper interface.

Once $<\varepsilon>(y)$ is calculated for the interface, it can be approximated by a series of layers with increasing dielectric constant values. The thickness of each layer is determined by the gradient of $<\varepsilon>(y)$ at that position – the larger the gradient, the thinner the layer. This allows the curve shape of $<\varepsilon>(y)$ to be accurately represented by the discrete layers. After the graded interface is approximated with a multilayer stack, a 1D transfer matrix calculation can be performed on the structure to find the coherent reflectivity.

The homogenization approximation is valid for rough surfaces where the roughness features are fairly small and close to one another relative to the incident wavelength. Furthermore, the rough surfaces should be truly random – there should not be a large variation in the size/shape of the roughness features from one region of the interface to another. In essence, a given region on the interface should look like any other region in terms of the RMS height and distance between the roughness features. These restrictions create a surface with optical properties that appear "smeared out" or averaged to the incoming wave. The equivalent theory for bulk media is the effective medium approximation [Bohren (1983)].

6.2 The Kirchhoff Approximation

The Kirchhoff approximation is illustrated in Fig. 6.2. It involves approximating the roughened structure with several smooth structures that have various interface

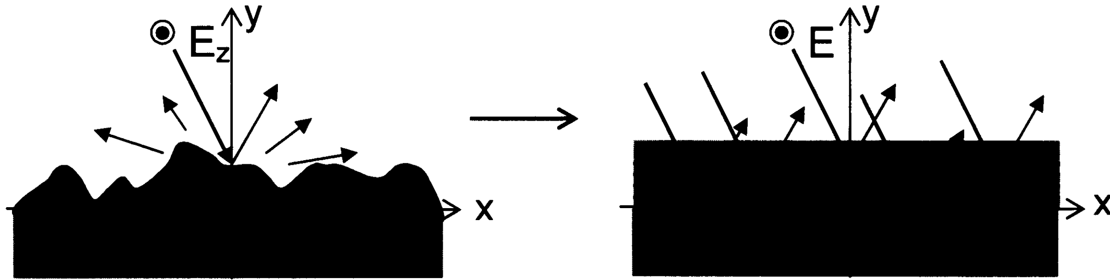

Figure 6.2 Schematic depicting the Kirchhoff approximation for a single rough interface. The reflectivity of the roughened surface is estimated by averaging the reflection coefficients from several smooth surfaces with varying heights. The height distribution of the smooth structures is equal to the height distribution of the rough interface.

positions [Baylard (1993), Beckmann(1963), Kong (2000), Ogilvy (1991), Sanchez (1995), Sentenac (1998), Thorsos (1988), Voronovich (1994)]. The height of each interface is determined by the height distribution of the rough interface $f_h(x)$. For example, the number of structures that will have interface positions between y and $y+\Delta y$ is proportional to the probability that the rough interface height is between those values. Thus, a histogram of $f_h(x)$ would be equal to a plot of the interface position of the smooth structures versus the number of structures with that interface position. If $f_h(x)$ is a continuous function, this method requires discretization of the height distribution in order to approximate the rough surface with a finite number of smooth surfaces. Thus, as with the homogenization approximation, the discretization should be fine enough that it accurately represents the function $f_h(x)$.

Once the rough surface is represented with a finite number of smooth surfaces, the reflection coefficient (Eq. 2.50) is calculated for each smooth structure. These reflection coefficients are then averaged, and the reflectivity is calculated by squaring the magnitude of this averaged value (Eq. 2.58). This is the approximated coherent reflectivity of the rough surface.

The Kirchhoff approximation is valid for rough surfaces where the roughness features are significantly separated from one another and are fairly flat (i.e. the gradient of $f_h(x)$ stays small) relative to the incident wavelength. The approximation neglects any multiple scattering or higher order effects. Thus, the distance between roughness features needs to be large enough that this assumption is valid. However, by averaging the reflection coefficients from deviate smooth structures, any phase interference induced

from reflection off roughness features of different heights is taken into account. The reflection coefficients will be imaginary numbers, having both a magnitude and a phase. The magnitude will be the same for all the smooth structures since this is essentially the reflectivity of the surface, which is just determined by the refractive index of the structure. However, the phase will be very different for each structure because it is determined by the position of the interface relative to zero (see chapter 2). This approximation of phase interference will become more valid as the roughness features themselves become flatter.

6.3 Implementation of the Homogenization Approximation

Both of the above approximations were applied to the simulated quarter-wave stacks, as outlined in Figs. 6.3 and 6.5. For the homogenization approximation, the dielectric constant was averaged across the rows of each roughened structure. This created a corresponding 1D structure that had diffuse index profiles at all the interfaces. As stated above, the length over which the interfaces were graded depended on the roughness of the structure. Structures that had a very large RMS roughness resulted in index profiles where the refractive index never reached the high/low index value corresponding to the actual structure. This is illustrated in Fig. 6.4, which plots the averaged refractive index profiles for four R_{RMS} values in the 4-bilayer, n_1=2.25, n_2=1.5 system. For the R_{RMS} values of 0.1453a and 0.1759a, the index of refraction in the

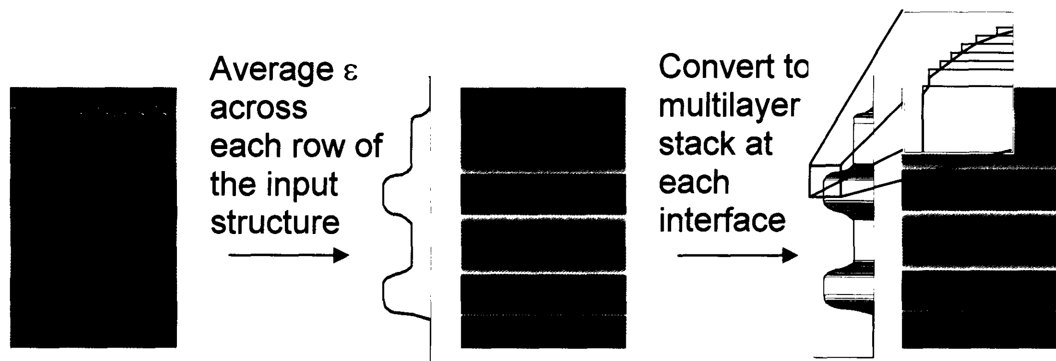

Figure 6.3 Application of the homogenization approximation to the roughened quarter-wave stacks. The dielectric constant is averaged across each row of the input structure. The smooth profile is then converted into a series of layers.

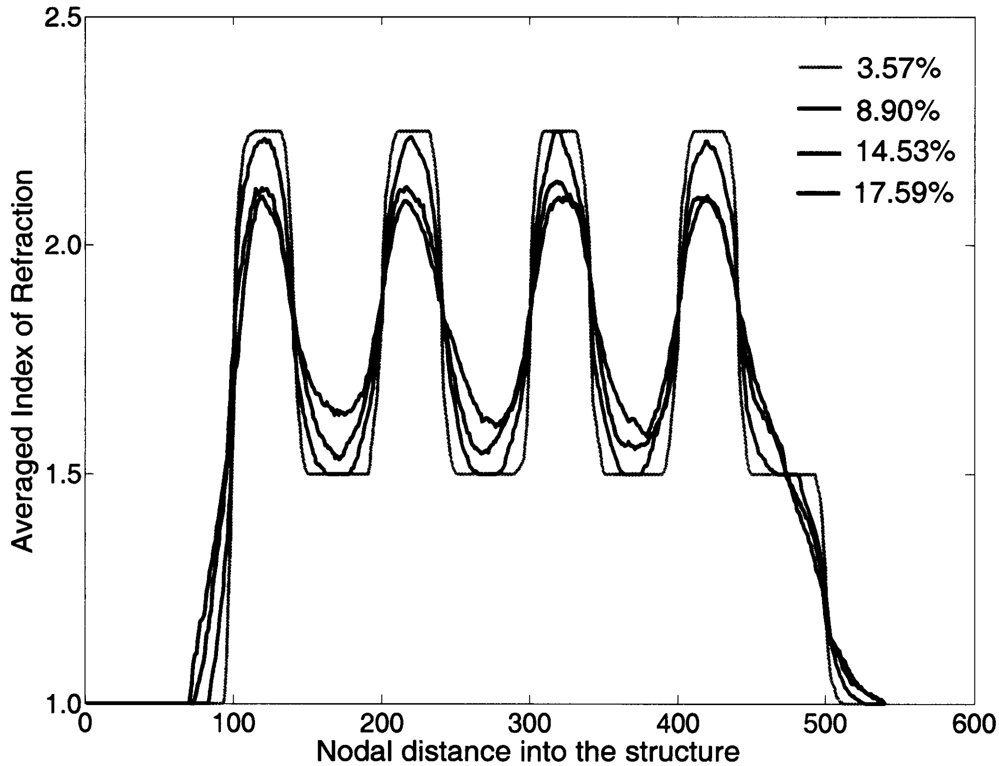

Figure 6.4 The averaged refractive index profiles for four R_{RMS} values in the 4-bilayer, n_1=2.25, n_2=1.5 system. For the R_{RMS} values of 0.1453a and 0.1759a, the index of refraction in the approximated structure never reaches the extreme values of 2.25 and 1.5.

approximated structure never reaches the extreme values of 2.25 and 1.5. Yet, even at the highest values of R_{RMS}, the index modulation characteristic of a photonic crystal is never completely lost. In this way, this approximation produced structures similar to those obtained with the index modification model presented in chapter 5. The two important differences, however, are that the index modification seen here is not based on the magnitude of the forward scattering from the roughness features, and the interfaces between layers are diffuse.

The diffuse index profile for each structure was then converted to a series of layers. As described above, the thickness of each layer was based on the gradient of the index profile. An algorithm was developed to implement this conversion. The averaged index value corresponding to the first row in the input structure was held as a reference. Each subsequent index value was then scanned until an index greater than a certain threshold value above the reference index was found. A layer was then made to approximate the averaged index curve within this range. The layer had a refractive index

equal to the average between the reference index and the above-threshold index. The thickness of the layer was given by the distance between the reference index and the above-threshold index. The above-threshold index was then taken as the next reference value and the process was repeated for the remainder of the averaged index curve. This resulted in a series of layers at each interface, shown in the inset in Fig. 6.3, that approximated the diffuse interfaces of the averaged structure. For all structures except the 4-bilayer, n_1=2.8, n_2=1.6 system, the threshold value used was 0.01. It was found that a lower threshold value of 0.002 was needed to accurately represent the diffuse interfaces in the 4-bilayer, n_1=2.8, n_2=1.6 structure.

After the averaged index profiles were converted into multilayer stacks for each structure, a 1D transfer matrix calculation was performed to obtain the reflectivity. The percent change in reflectivity could then be found by applying Eq. 4.10 to the results of the transfer matrix calculations. This allowed the results of this approximation to be directly compared to the FDTD results reported in chapter 4.

6.4 Implementation of the Kirchhoff Approximation

The process used to apply the Kirchhoff approximation to the simulated structures is shown in Fig. 6.5. Each structure was divided into several slices, with each slice having the width of one column of the structure. The slices corresponded to several 1D deviate structures, where the thicknesses and interface positions of each layer in the deviate structures was determined by the roughness profile of the original structure. A

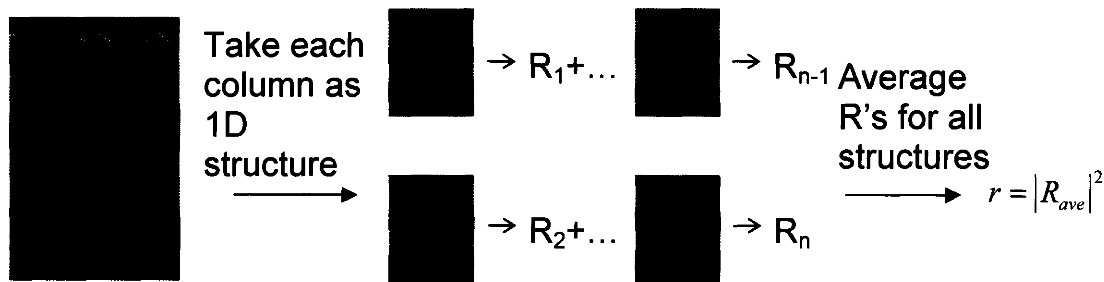

Figure 6.5 Application of the Kirchhoff approximation to the roughened quarter-wave stacks. The structure is broken up into many structures by taking each column of the rough structure as a separate 1D structure. The reflection coefficients for each structure are calculated and averaged to give the estimated reflectivity of the roughened structure.

1D transfer matrix calculation was then used to find the reflection coefficient for each of the deviate structures. The reflectivity corresponding to the simulated structure was calculated by averaging the reflection coefficients of the deviate structures and squaring the magnitude of this averaged value (Eq. 2.58). As with the homogenization approximation, the percent change in reflectivity was calculated with Eq. 4.10 to allow direct comparison of these results to the FDTD results.

Unlike the single interface case, the reflection coefficients of the deviate structures varied in both magnitude and phase because of the variation of layer architecture between the different structures. However, because the transfer matrix technique keeps track of phase, the phase interference contribution to the coherent reflection taken into account by this approximation was retained, even between the internal interfaces in the structures. In reality, the variation in the magnitude of the reflection coefficients is also a result of phase interference taking place within the structure. This is a consequence of the deviate structures drifting from the resonant quarter-wave condition of the photonic crystal. This drifting results in phase shifts at the internal interfaces, which cause the overall reflectivity of the structure to change. Thus, there was an additional contribution to the averaged reflectivity of the structures from the variation in the magnitude of the reflection coefficients.

6.5 Results of the Applied Approximations

A comparison of the FDTD results with the results of both the homogenization and Kirchhoff approximations for the same 4-bilayer systems presented in chapter 4 is shown in Fig. 6.6. In all cases, the Kirchhoff approximation does a poor job at reproducing the FDTD results. For the n_1/n_2=1.25 system, the Kirchhoff approximation under-estimates the change in reflectivity seen with the FDTD simulations. On the other hand, it over-estimates the reflectivity change for the higher index contrast systems, and the magnitude of this over-estimation gets worse as the index contrast increases. Although this approximation only predicts the coherent reflectivity of roughened surfaces, this shifting behavior between over-estimating and under-estimating the FDTD results suggests that the Kirchhoff approximation is not valid for the structures tested in this thesis. This idea is further reinforced by the fact that an under-estimation would not

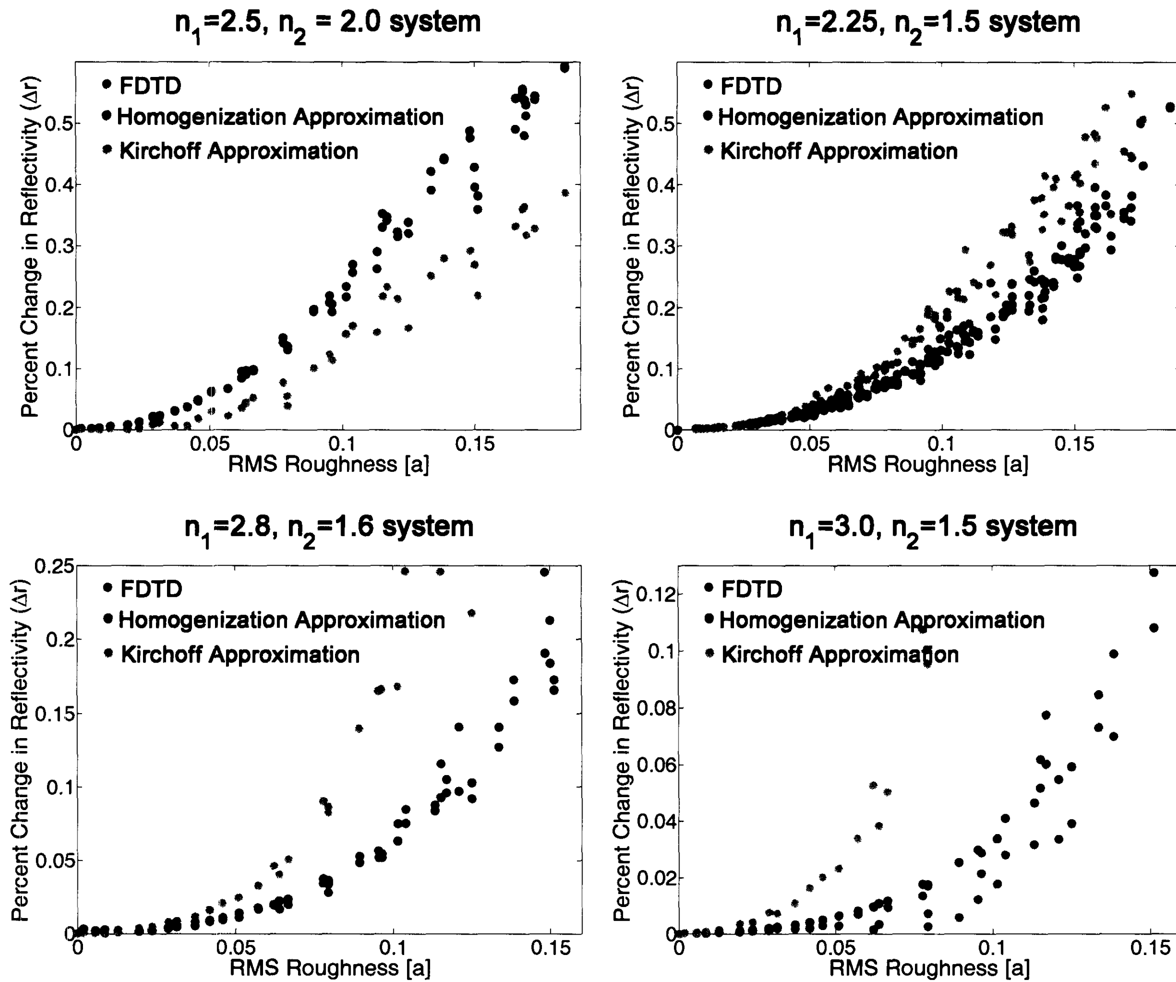

Figure 6.6 Comparison of the FDTD results with the results of both the homogenization and Kirchhoff approximations for the same 4-bilayer systems presented in chapter 4. The Kirchhoff approximation does a poor job at reproducing the data, but the homogenization approximation matches the FDTD results very well.

be observed if the coherent reflectivity was being accurately predicted but the incoherent power contribution was causing the FDTD results to differ. If the incoherent power contributes significantly to the overall reflected power, then the FDTD calculations will deviate from the approximation results because the FDTD accounts for both the incoherent and coherent reflected power. However, the situation described above would result in an over-estimation of the percent change in reflectivity because the approximation would only be accounting for part of the reflected power. Thus, the roughness regime tested in the simulated structures does not overlap with the regime where the Kirchhoff approximation is valid.

Although the Kirchhoff approximation is not valid for the structures tested, it is curious that it under-estimates the FDTD results in some cases and over-estimates it in others. This inconsistent behavior can be explained with the series of plots shown in Fig. 6.7. The Kirchhoff approximation relies on the reflection coefficient from deviate structures. As mentioned above, the reflectivity of these structures will differ due to their different layer architectures. Some deviate structures will have reflectivities lower than the ideal structure (i.e. a quarter-wave tuned structure with smooth interfaces) at the quarter-wave tuned wavelength. Others will have reflectivities higher than the ideal structure. The curves in Fig. 6.7 show the extreme cases of each of these types of deviate structures. For each of the plots, the curve with the highest reflectivity at the quarter-wave tuned wavelength corresponds to the deviate structure that had the highest reflectivity out of all the deviate structures. Similarly, the curve with the lowest reflectivity at the quarter-wave tuned wavelength corresponds to the deviate structure with the lowest reflectivity out of all the structures. The middle curve corresponds to the reflectivity from the ideal structure. Notice that the ideal curves for the higher index contrast structures have a much higher absolute reflectivity than the low index contrast structure.

The positioning of the deviate curves in the high index contrast plots suggests that there are only a small number of possibilities for deviate structures that will result in a higher reflectivity at the quarter-wave tuned wavelength than the ideal structure. On the other hand, it appears that there are many possibilities for deviate structures that will result in higher reflectivities for the low index contrast structure. This is because the low index contrast structure has a low absolute reflectivity and so there are many possible structural deviations that actually improve the reflectivity of the structure. However, the higher index contrast structures already have a very high reflectivity, so there are not a lot of structural changes than can result in an even higher reflectivity. Assuming that the reflectivities of all the deviate structures will be distributed symmetrically between the two extreme curves, the average reflectivity that would be obtained from the Kirchhoff approximation can be estimated by simply averaging the reflectivity of the extreme curves. This is shown on each plot by the dotted line. The results of the FDTD calculation for the same structure are given by the dashed lines. This reveals that the

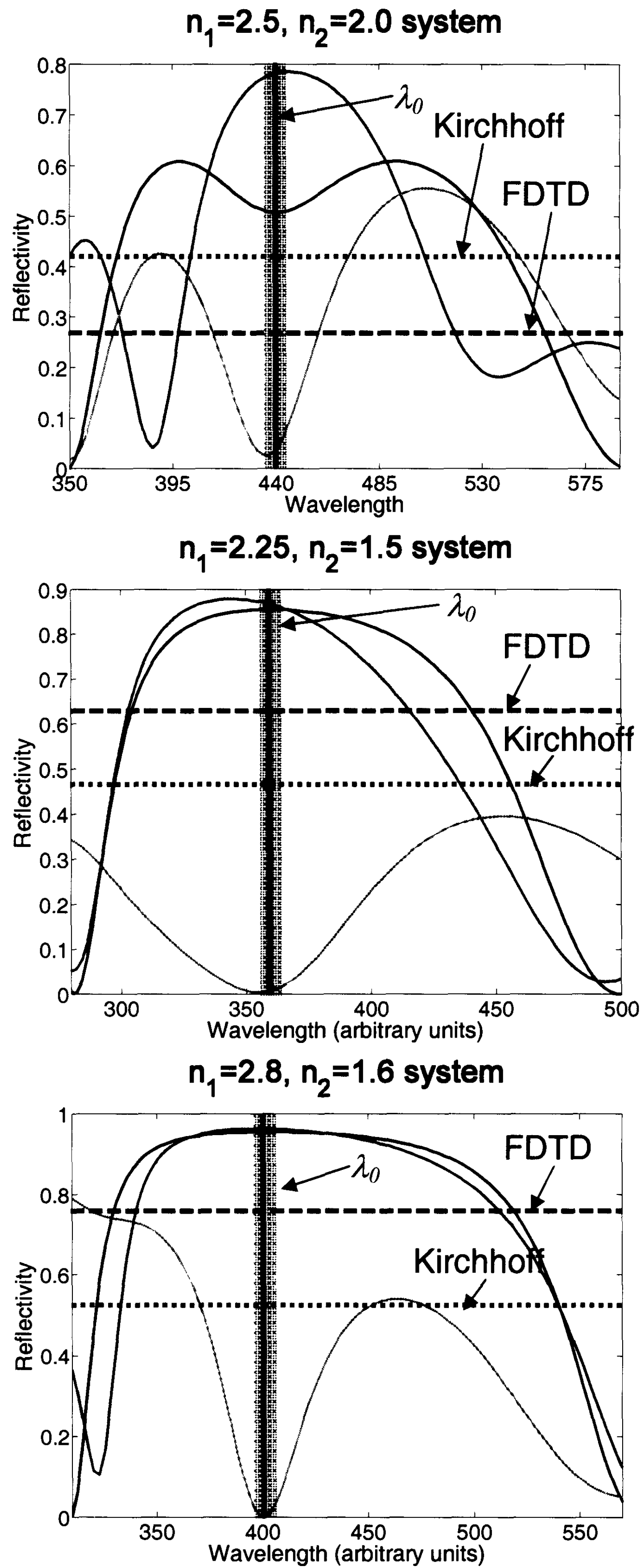

Figure 6.7 Explanation for why the Kirchhoff approximation under-estimates in some cases and over-estimates in others. The pink region is the quarter-wave tuned wavelength. The dashed line is the FDTD result and the dotted line is the Kirchhoff result.

higher reflectivity structures are biased towards lower reflectivities due to the inbalance of deviate structure reflectivities. This causes the change in the reflectivity to be over-estimated for these structures. Alternatively, the low index contrast structure is biased toward higher reflectivities, resulting in an under-estimation of the reflectivity change.

On the other hand, the homogenization approximation matches the FDTD results extremely well. For the structures with index contrasts between 1.25 and 1.75, the curves resulting from each method actually overlap. Since the homogenization approximation only predicts the coherent reflectivity, this suggests that the incoherent portion of the reflected wave is extremely small for these structures. For larger index contrast systems (i.e. the n_1/n_2=2.0 system), the approximation starts to deviate slightly from the FDTD results, over-estimating the reflectivity change for R_{RMS} values less than $0.12a$. This is most likely due to the fact that the incoherent reflected power is becoming a significant part of the overall reflectivity change. Two factors contribute to this: (1) the amount of scattering increases as the index contrast increases, and (2) the overall change in the reflectivity becomes much smaller as the index contrast increases. So the amount that the coherent reflectivity is decreasing approaches the total amount of incoherent reflected power. This will cause the incoherent part of the reflected wave to play a larger role in the overall change in reflected power. This idea will be revisited in the next chapter when the magnitude of the incoherent reflected power is extracted from the FDTD data.

The results of the homogenization and Kirchhoff approximations for the n_1=2.25, n_2=1.5 bilayer systems are shown in Fig. 6.8. The Kirchhoff approximation matches the 2-bilayer FDTD results well, but quickly deviates as more bilayers are added. Furthermore, as with the increasing index contrast systems, the over-estimation of the Kirchhoff approximation gets worse as the number of bilayers in the system increases. Thus, again, the Kirchhoff approximation results fail to reproduce the FDTD data.

However, as with the previous systems, the homogenization approximation matches the FDTD results extremely well. Thus, it appears that the roughness regime covered by the simulated structures (except the n_1/n_2=2.0 system) is within the regime where the homogenization approximation is valid. This is the parameter space containing R_{RMS} values up to about $0.2a$ and W_{RMS} values up to about $1.0a$, for systems with index contrasts up to 1.75 and number of bilayers up to 6. The fact that the homogenization

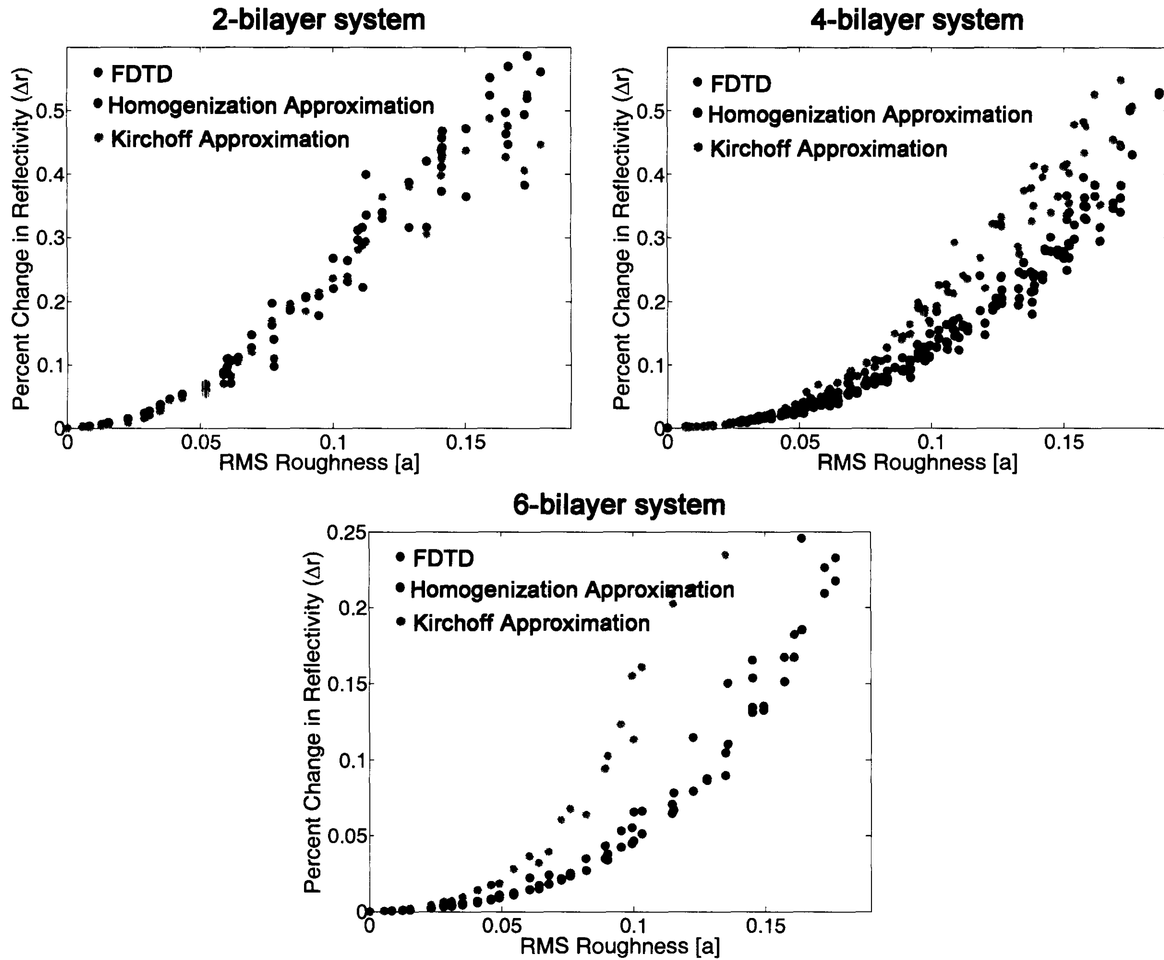

Figure 6.8 Comparison of the FDTD results with the results of both the homogenization and Kirchhoff approximations for the n_1=2.25, n_2=1.5 systems presented in chapter 4. Again, the Kirchhoff approximation does not predict the FDTD results, while the homogenization approximation matches them very well.

approximation is valid for all the RMS wavelengths tested explains why no W_{RMS} dependence was seen in the results presented in chapter 4. If the structure can be approximated as a 1D structure with diffuse interfaces, the two-dimensional configuration of the interface can not be expected to play any role in the results. All information on the RMS wavelength of the structure will be erased when the structure is converted to its 1D approximation. Additionally, the fact that this 1D approximation is valid for these structures explains why the results for the TE and TM polarizations were equivalent. For 1D structures, the TE and TM polarizations result in the same orientation of the fields at normal incidence (see chapter 2). Thus, the polarizations themselves are equivalent, so it is not surprising that they would produce equivalent results.

Beyond this, however, the homogenization approximation can actually be used to accurately predict the total change in reflectivity of the roughened structures within the above mentioned parameter space. And the fact that the TE and TM responses are equivalent means that the approximation can be used to predict the optical response of 3D roughened structures, as explained in chapter 4. This is significant because the FDTD simulations are extremely time consuming while the calculations done with the homogenization approximation on the same structures take a small fraction of that time. For example, a curve consisting of 40 data points would take a few days to calculate with the FDTD code. However, the same curve would be generated in a few minutes using the homogenization approximation.

The fact that the homogenization approximation is valid for the simulated structures also provides insight into what is physically occurring in the structures. The main role of the roughness features within the tested parameter space is not to scatter the incoming wave, but instead to simply "smear out" the refractive index in the vicinity of the interfaces. Thus, the RMS roughness and RMS wavelength scales tested here (although large compared to a, see Fig. 4.5) are small enough compared to the incident wavelength that the incident wave just "sees" an effective diffuse refractive index profile at each interface in the structure.

Considering the regime where the Kirchhoff approximation is valid, the FDTD results may begin to approach the results of this approximation for very large W_{RMS} values. However, such values were not tested with this study because they do not accurately represent the structural deviations that are actually seen in experimental systems. For example, the W_{RMS} value for the liquid crystal multilayer structure presented in chapter 4 (Fig. 4.1) is around $1.0a$. Additionally, the W_{RMS} value for the porous silicon structure (Fig. 4.2) is much less than a. Thus, both of these structures are within the tested roughness regime.

6.6 Conclusions

Two approximations, the homogenization and Kirchhoff approximations, were applied to the simulated quarter-wave stacks in an attempt to gain some physical insight into the mechanism for the decreased reflectivity of the roughened structures. These

approximations are commonly used to calculate the amount of coherent reflection from single rough interfaces. However, when they were applied to the simulated multilayer structures, it was found that the results from one of the approximations, the homogenization approximation, matched the FDTD results extremely well for all systems except the highest index contrast system (n_1/n_2=2.0). The Kirchhoff approximation, on the other hand, did not accurately predict the FDTD results, underestimating in some cases and over-estimating in others. This implies that the roughness regime covered by the simulated structures is within the regime where the homogenization approximation is valid. Furthermore, it reveals that the primary role of the roughness features is to grade the interfaces in the multilayer stack, rather than to scatter the incoming light.

The fact that the homogenization approximation results actually overlap the FDTD results means that the application of this approximation to structures within the parameters space tested can predict reflectivity changes accurately. This is significant because the homogenization approximation calculations are much faster than the FDTD calculations. Thus, it is extremely computationally beneficial to be able to use such an approximation to predict optical behavior accurately.

Because the homogenization approximation predicts only the amount of coherent reflection, the close match between it and the FDTD results implies that the amount of incoherent reflection for these systems is small compared to the amount of coherent reflection loss. This is consistent with the results of chapter 5, which found that the change in reflectivity was much too small when only the scattering loss was considered. Because the FDTD calculations include both the coherent and incoherent portions of the reflected power, the above conclusion can be independently verified by extracting the incoherent power from the FDTD results. This process will be presented in the next chapter.

Chapter 7: Calculation of the Scattered Power from Interfacial Roughness

The results of the last chapter revealed that the homogenization approximation reproduces the FDTD results when it is applied to the simulated structures. However, the FDTD results include both the coherent and incoherent reflected power, while the homogenization approximation only considers the coherent reflection. Therefore, the close match between the approximation and the FDTD results implies that the amount of incoherent power in the reflected wave is small. This implication can be directly verified by extracting the amount of incoherent power in the reflected field from the FDTD calculations. The following chapter will outline the steps involved in the above process and present the results of its application to the simulated structures.

7.1 General Form of the Reflected Wave

Extraction of the incoherent field from the total reflected field will require careful consideration of the exact form of the reflected wave. In general, the reflected wave in an FDTD simulation with periodic boundary conditions will have several parts. For a normal incident TE polarized plane wave, this general form is given by:

$$\begin{aligned} E(x,y) = {} & E_c \exp\left(-ik_{yc}y+\phi_c\right) \\ & + E_{f1}\exp\left(-ik_{yf1}y\right)\left[\exp\left(ik_{xf1}x+\phi_{f1a}\right)+\exp\left(-ik_{xf1}x+\phi_{f1b}\right)\right]+\cdots \\ & + E_{fm}\exp\left(-k_{yfm}y\right)\left[\exp\left(ik_{xfm}x+\phi_{fma}\right)+\exp\left(-ik_{xfm}x+\phi_{fmb}\right)\right]+\cdots \\ & + \xi(x,y). \end{aligned} \tag{7.1}$$

Each part of Eq. 7.1 will be explained below.

<u>The Coherent Field.</u> The first line in equation 7.1 corresponds to the coherent portion of the reflected wave. As mentioned in chapter 6, the coherent reflection from a rough surface will only occur in the direction of spectral reflection [Kong (2000)]. This means that the wave vectors corresponding to the coherent part of the reflected field will satisfy Snell's Law and the phase-matching conditions presented in chapter 2 (Eqs. 2.28 – 2.34). Thus, for a normal incident plane wave, the coherent reflection will also be normal to the reflecting surface, having only a normal component of the wave vector. For the above equation, the direction normal to the interfaces in the crystal is the y direction. Therefore, the coherent portion of the reflected field has only a y component of the wave vector. Furthermore, by virtue of Eq. 2.30, the magnitude of this wave vector will match the magnitude of the incident wave vector:

$$k_{yc} = k_i = \omega\sqrt{\mu_i \varepsilon_i} = \frac{2\pi}{\lambda_0}. \tag{7.2}$$

In general, there will also be a phase shift (ϕ_c) associated with the coherent wave that depends on the time step in which the wave is being examined. Thus, for completeness, it is also included in Eq. 7.1.

<u>The Propagating Floquet Modes.</u> The second line in Eq. 7.1 corresponds to the propagating Floquet modes present in the reflected wave. Floquet modes are modes associated with reflection off a periodic surface [Kong (2000), Taflove (2000)]. Because the FDTD simulations utilized periodic boundaries on the domain walls perpendicular to

the layers, the simulated structures were periodic in the direction parallel to the layers (the x direction in Eq. 7.1). Hence, Floquet modes were set up in the reflected wave corresponding to this periodicity.

These modes have both an x and y component of their wave vectors. The magnitude of the x component is constrained by the periodicity imposed in that direction by the periodic boundaries. Thus, the periodicity of the Floquet modes in that direction must match the periodicity of the surface. This requires the x component of the Floquet mode wave vectors to be

$$k_{xfn} = \frac{2\pi n}{n_x}, \tag{7.3}$$

if n_x is the length of the simulation domain in the x direction. The n in Eq. 7.3 corresponds to the order of the mode. The first order mode will have a wavelength in the x direction equal to n_x, the second order mode will have a wavelength in the x direction equal to $n_x/2$, and so on.

The y component of the wave vectors is constrained by the fact that the total magnitude of the wave vectors must equal the magnitude of the incident wave vector. This is because the wavelength of the Floquet modes is equal to the incident wavelength since both waves are propagating in the same medium (the ambient) and have the same frequency (due to the fact that the incident wave is the source of the Floquet modes). Thus, the y component of the Floquet mode wave vectors is given by

$$k_{yfn} = \sqrt{k_i^2 - k_{xfn}^2}\,. \tag{7.4}$$

In general, each Floquet mode has two possible wave solutions, one that is propagating toward the negative x direction and one that is propagating toward the positive x direction. Since the reflections off a random rough surface do not prefer any particular direction, the reflections from the simulated structures couple into these two waves equally. This results in a standing wave in the x direction, which is given by the portion in the square brackets on the second line in Eq. 7.1. Again, there will be a phase shift (ϕ_{fn}) associated with the Floquet modes that depends on the time step in which the wave is being examined. Each wave solution can have a different corresponding phase, and so there are two phase values included for each Floquet mode in Eq. 7.1.

The Evanescent Floquet Modes. The third line in Eq. 7.1 corresponds to the evanescent Floquet modes in the reflected wave. As the value of n in Eq. 7.3 gets larger, it will eventually cause the x component of the Floquet mode wave vector to be larger than the total wave vector magnitude. This in turn requires k_{yfn} to become imaginary according to Eq. 7.4. Thus, this part of the reflected wave looks very similar to the propagating Floquet mode. The one difference is that the leading exponential factor no longer has an imaginary argument, causing this mode to exponentially decay in the y direction rather than propagate. Note, however, that a standing wave in the x direction is still present. As with the propagating Floquet modes, this standing wave will have a wavelength that is characteristic of the mode order.

Eq. 7.1 corresponds to the situation where the mth Floquet mode is the first mode that has an imaginary y component of the wave vector. This mode will have m periods in the x direction within the periodic domain, but will decay in the y direction at a rate determined by the magnitude of k_{yfm}. All modes higher than the mth mode will also be evanescent, but they will decay faster and have more periods associated with them.

The Incoherent Field. The fourth line in Eq. 7.1 corresponds to the incoherent portion of the reflected wave. This part of the field is a noisy fluctuating offset to the other components. For the structures tested in this thesis, this field is a result of the diffuse scattering from the roughness features that does not coherently combine to produce either the coherent reflection or the Floquet modes.

7.2 Calculation of the Scattered Power

The amount of power contained in the reflected scattered field was calculated by applying the above general wave form to the reflected wave obtained with the FDTD simulations. The reflected wave was extracted from the FDTD results by taking the electric field in the region in front of the unidirectional source (see chapter 3) at the final time step of the simulation run (i.e. after steady-state was achieved, see Fig. 4.4). A three-dimensional fit based on Eq. 7.1 was then performed on the reflected wave with TableCurve3D curve fitting software. This fit included only the coherent reflection and the propagating Floquet mode portions of Eq. 7.1. Inclusion of the other parts of the

reflected wave in the fit caused the fitting algorithm to be unstable due to the large number of fit parameters.

Fig. 7.1 shows the reflected wave for one of the simulated structures. The large modulation in the y direction corresponds to both the coherent reflected wave and the y component of the propagating Floquet mode. However, the secondary modulation in the x direction corresponding to the standing wave of the first order Floquet mode is also clear. The various shading in the plot corresponds to the spatial distribution and magnitude of the residual after the wave was fit in the manner described above. This residual, with the fit subtracted out, is shown in Fig. 7.2. Plotted in this way, the second order Floquet mode, which is evanescent, is clearly seen displaying two periods in the x

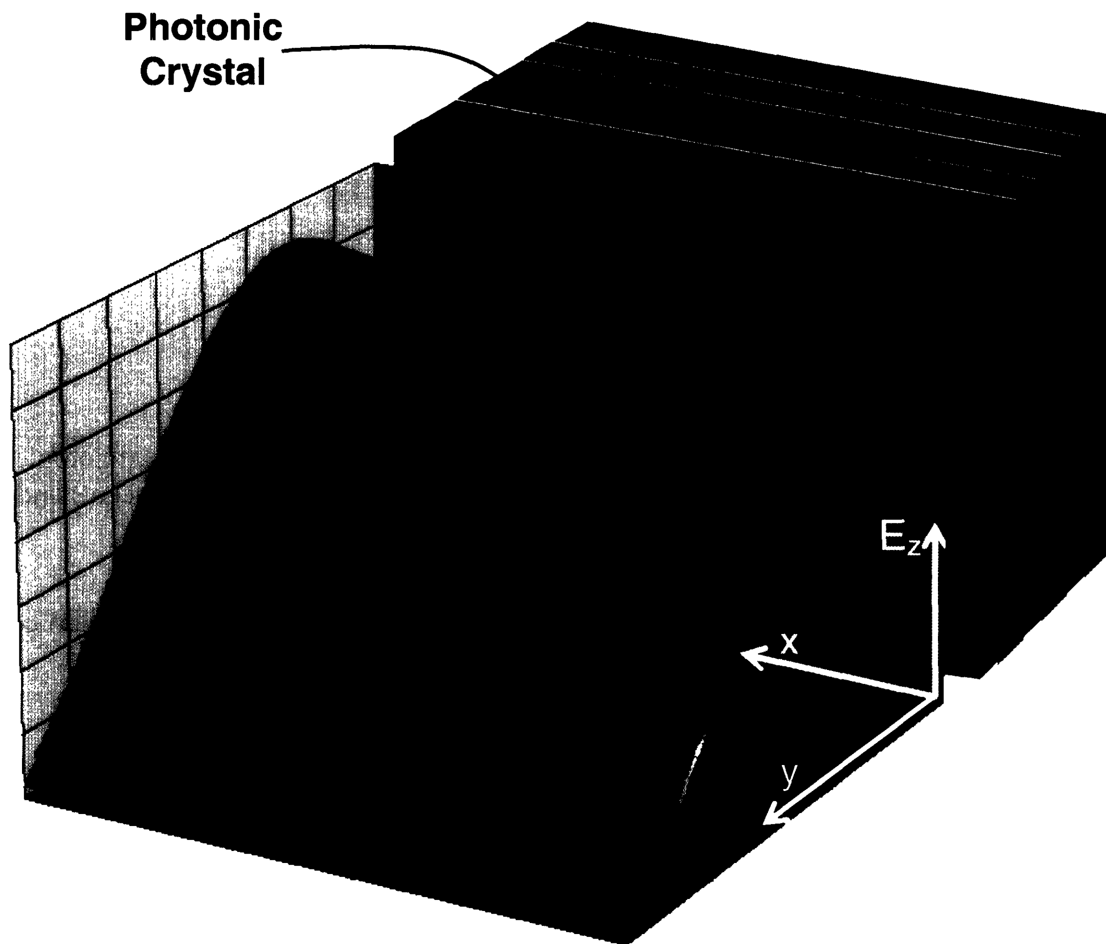

Figure 7.1 The simulated reflected wave for one of the roughened structure. As shown, the photonic crystal is positioned behind the wave. Thus, the direction of propagation is out of the page. The periodic boundaries of the domain are located along the yz planes.

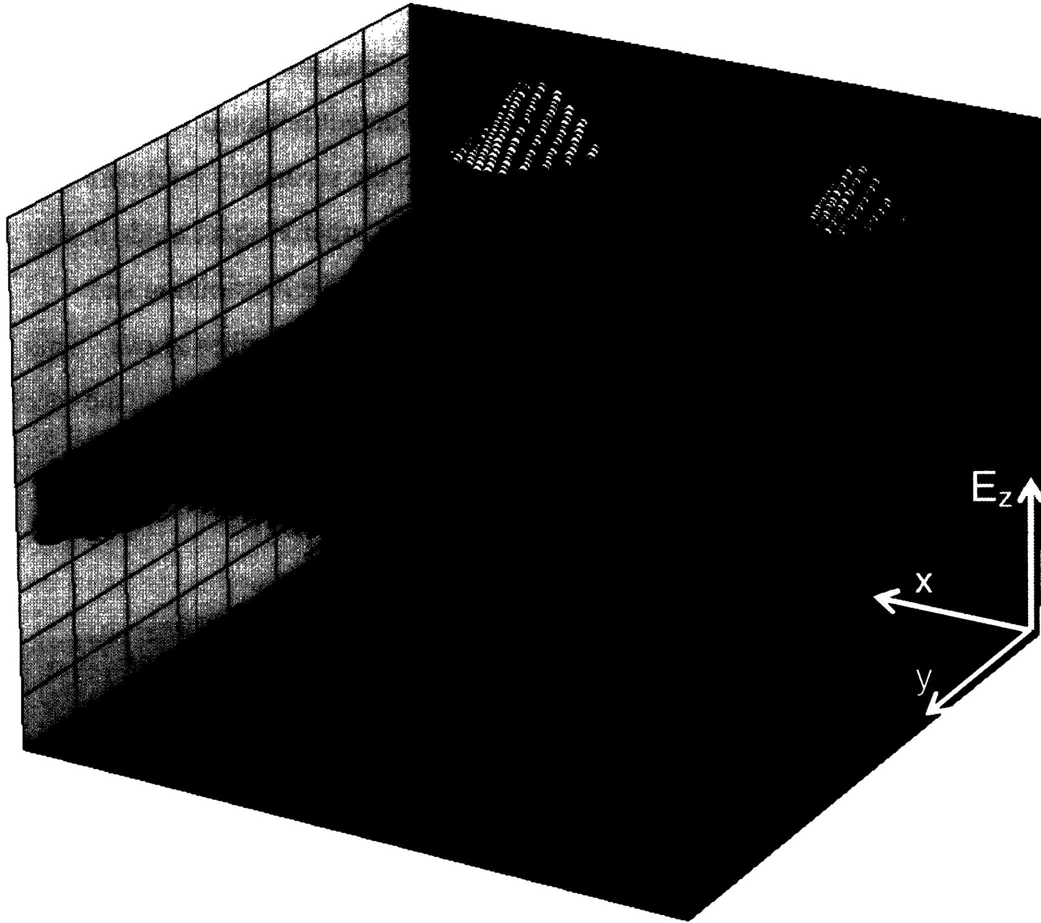

Figure 7.2 The residual of the fit to the reflected wave. The orientation of the photonic crystal is the same as that in Fig. 7.1. The second order Floquet mode (evanescent) and the incoherent field are apparent.

direction and an exponential decay in the y direction. The incoherent fluctuating part of the field is also clear. Note that the evanescent mode decays to a magnitude that is negligible compared to the incoherent field within the analysis region shown here.

The values of the wave vectors were fixed in the fit since they could be calculated using the simulation parameters and Eqs. 7.2 – 7.4. The coherent wave vector was obtained by combining Eq. 7.2 with Eq. 4.8 for the nodal magnitude of the incident wavelength. Furthermore, for all simulations, the width of the simulation domain (n_x) was small enough that the first order Floquet mode was the only one that was not evanescent. Therefore, only one Floquet mode needed to be included in the fit. The

wave vector components corresponding to this mode were calculated with Eqs. 7.3 and 7.4, with n=1 and the known values of n_x and k_{yc} from above. Therefore, the only variable parameters in the 3D fit were the amplitudes of the coherent field (E_c) and the propagating Floquet mode (E_{fl}), and the phases associated with these parts of the field ($\phi_c, \phi_{fla}, \phi_{flb}$).

In order to confirm that the fit had reached a global minimum, the fitting algorithm was run several times with different initialization values for the fit parameters. The fit that produced the highest r^2 value was taken as the best fit of the data. All of the accepted fits had r^2 values greater than 0.99, with the majority of fits having r^2 values greater than 0.999. As expected, the r^2 value of the accepted fit was lower for rougher structures. This is because the residual of the fit contained the incoherent portion of the field, which would be increasing in magnitude as the roughness size increased.

The power in the incoherent field was therefore extracted from the residual of the fit. Since the residual also contained the evanescent Floquet modes, the incoherent power had to be extracted from a region where the evanescent modes had decayed to be negligible. This region was determined by eye through plotting the square of the residual collapsed onto two dimensions (collapsing the x dimension). Fortunately, the region where the reflected wave was analyzed was far enough away from the surface of the structure that the second order Floquet mode was the only evanescent mode still apparent in the residual. All other modes had much shorter decay lengths, so they had "disappeared" by the time they reached the analysis region. After identifying the region where the remaining Floquet mode had decayed to be negligile, the incoherent power was obtained by taking the average of the square of the incoherent field in that region [Kong (2000)]:

$$Incoherent\ Power = \left\langle \left| \xi(x,y) \right|^2 \right\rangle . \tag{7.5}$$

Because the propagating Floquet mode was an artifact of the periodic boundaries, the power carried by this mode was considered to be power that would have otherwise contributed to the incoherent power. The reason for this is that any power that was coupled into the propagating Floquet mode was undoubtedly power that had been diffusely scattered. This is evidenced by the fact that the wave vector associated with this

mode had an off-normal component, which could have only originated from diffuse scattering. Therefore, this power was also extracted from the FDTD data by taking the amplitude of the mode found with the fit and squaring it:

$$\textit{Floquet Mode Power} = \left|E_{f1}\right|^2. \tag{7.6}$$

The evanescent Floquet modes carry no power so they did not need to be considered.

7.3 Results for the Simulated Structures

Both the incoherent power and the power in the propagating Floquet mode were calculated using the method described above for the 4-bilayer, n_1=2.25, n_2=1.5 system. The results of these calculations are shown in Figs. 7.3 and 7.4. Again, each of the 120 simulations done for this system is represented by a dot in the figures. The shading is a cubic interpolated fit of the results of the power calculations corresponding to each of these simulations.

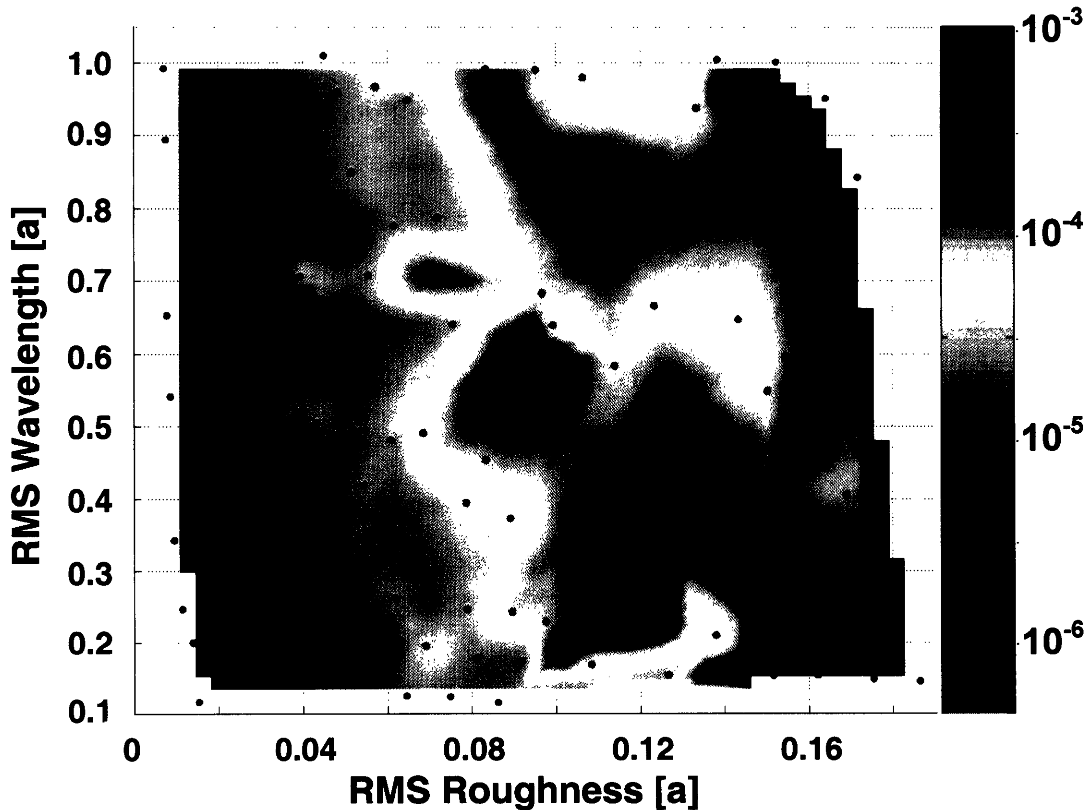

Figure 7.3 Incoherent power from the 4-bilayer n_1=2.25, n_2=1.5 system. Note that the largest amount of incoherent power is only about 10^{-3} for an incident wave power of 1.0.

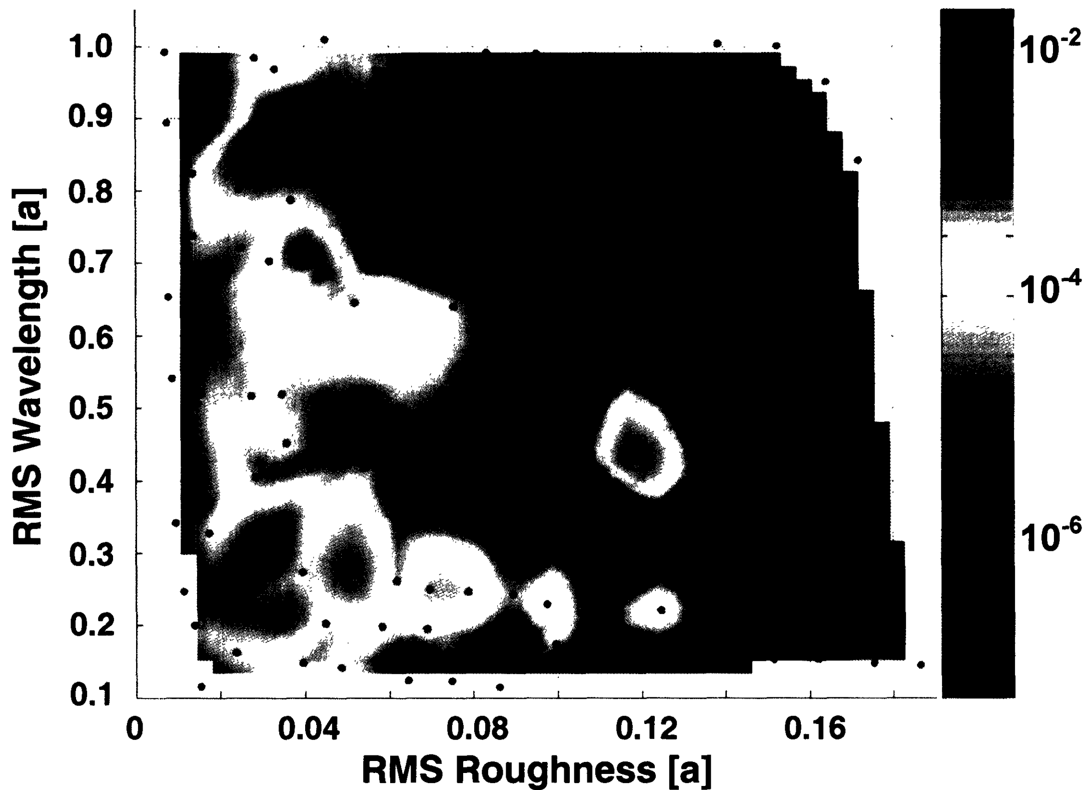

Figure 7.4 The power in the propagating Floquet mode for the 4-bilayer, n_1=2.25, n_2=1.5 system. Again, note that the maximum power is only 10^{-2} for an incident wave power of 1.0.

Both of these plots reveal that although there is some fluctuation in the calculated powers with increasing RMS wavelength, the main parameter in both plots is the RMS roughness. This is not surprising since the source of both of these field components is the diffuse scattering from the rough interfaces, and the magnitude of this scattering is expected to strongly depend on the size of the roughness features. Furthermore, these plots show that the magnitudes of both the incoherent and Floquet mode powers are extremely small. The largest incoherent power is on the order of 10^{-3}, while the Floquet mode power only reaches 10^{-2}. Recall that this is normalized to an incident wave power of 1.0. Also, note that these results both needed to be plotted on log scales in order to show the features of the plots. So there are order-of-magnitude changes taking place in the amount of power carried by these parts of the field, but they are still extremely small, even at their largest value, compared to the incident power. Although this result may seem surprising, it is consistent with the conclusions made in the preceding chapter.

There, it was postulated that the amount of incoherent power was extremely small because the homogenization approximation matched the FDTD results so well.

Because the magnitude of the diffuse scattering is expected to increase with higher index contrast systems, the incoherent and Floquet mode powers were also calculated for the 4-bilayer, n_1=3.0, n_2=1.5 system. These results, along with the previous system's results for comparison, are presented in Figs. 7.5 and 7.6. Since RMS roughness was shown to be the main parameter from the previous study, the data here has been collapsed onto 2D plots. However, these results are also plotted on a log scale in order to show the order-of-magnitude changes occurring at the small roughness scales.

Fig. 7.5 reveals that the higher index contrast system has a slightly larger amount of incoherent power, as would be expected from scattering theory. For comparison, the Mie theory calculation of the integrated backscattered power from spherical scatterers is shown in Fig. 7.7. In chapter 5, it was discovered that the roughness features on the

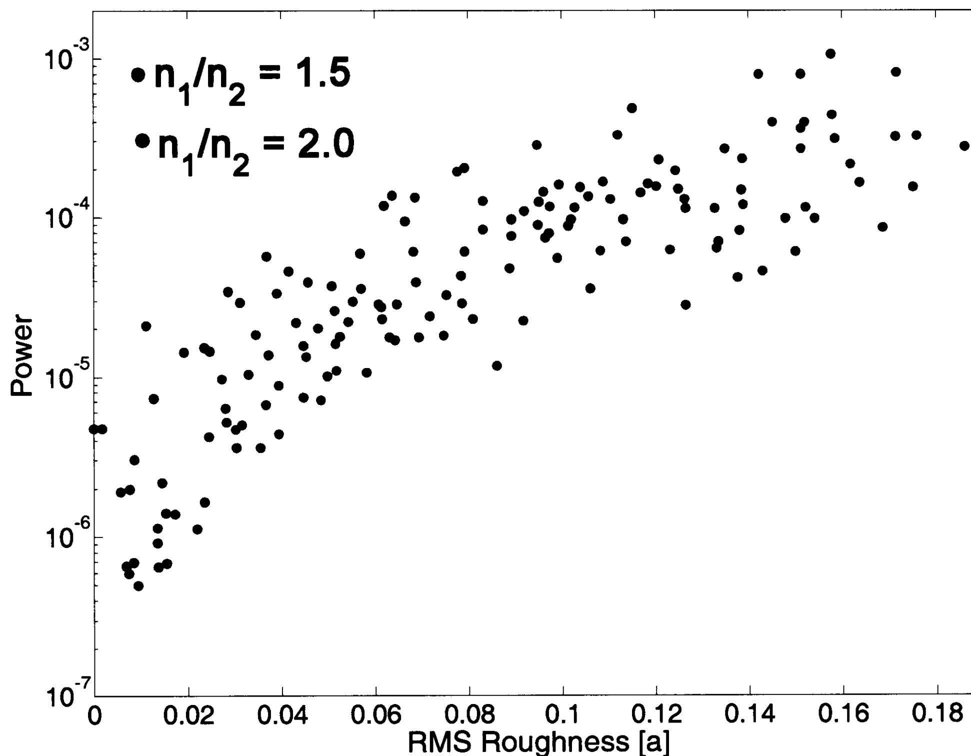

Figure 7.5 The incoherent power from two 4-bilayer systems presented in chapter 4: n_1=2.25, n_2=1.5, and n_1=3.0, n_2=1.5. The higher index contrast system shows slightly more incoherent power, but the magnitude is still extremely small (< 10^{-3}).

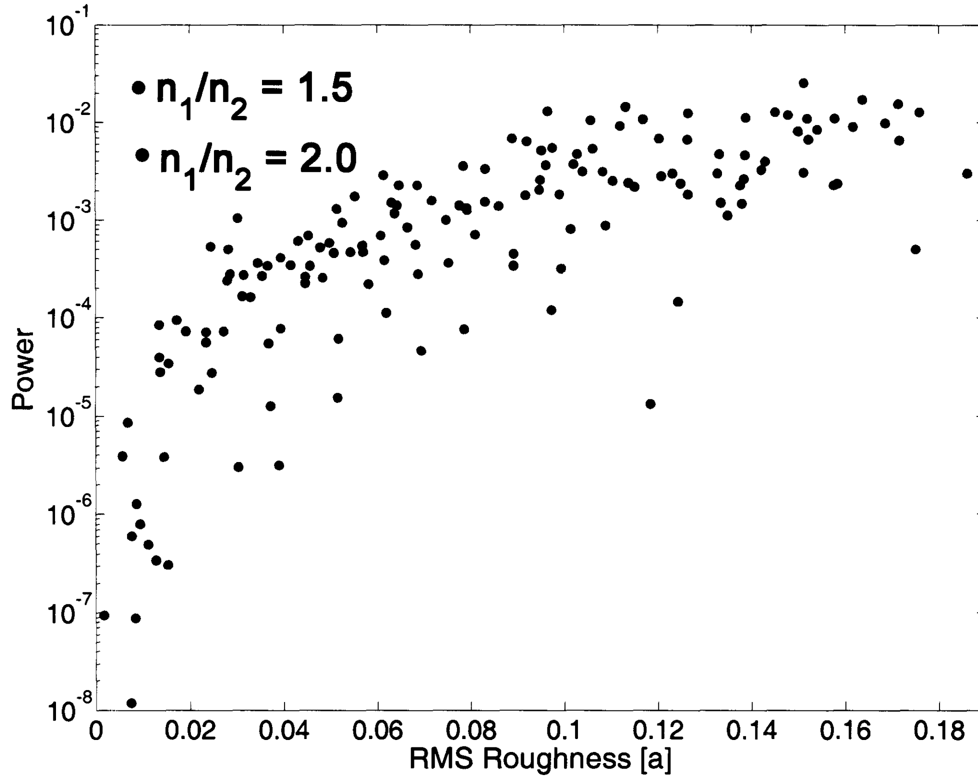

Figure 7.6 The power in the propagating Floquet mode from the same two 4-bilayer systems shown in Fig. 7.6. Again, the magnitude of the power in both systems is extremely small (< 10^{-2}).

high-to-low index interface cause the most amount of diffuse scattering in a quarter-wave stack configuration. Because of this, the conditions corresponding to scattering from that type of interface was used to generate the plot in Fig. 7.7. This means that the incident wavelength used was the vacuum wavelength divided by the high refractive index, and the index contrast between the scatterer and the ambient was actually the low refractive index divided by the high index value. Specifically, Eq. 2.92 through 2.99 were used to perform the calculations. Additionally, the RMS wavelengths of the structures were used to estimate the density of scatterers. This gives rise to the width of the curves in Fig. 7.7. Notice that both the curve shape and the trend predicted by the Mie theory calculation are consistent with the incoherent power calculation from the FDTD data.

The magnitude of the calculated power, however, is much smaller for high R_{RMS} values and much larger for low R_{RMS} values than the Mie theory prediction. On the low end, because the absolute magnitude of the power is getting so small, numerical noise is starting to play a significant role in increasing the value of the calculated power. On the

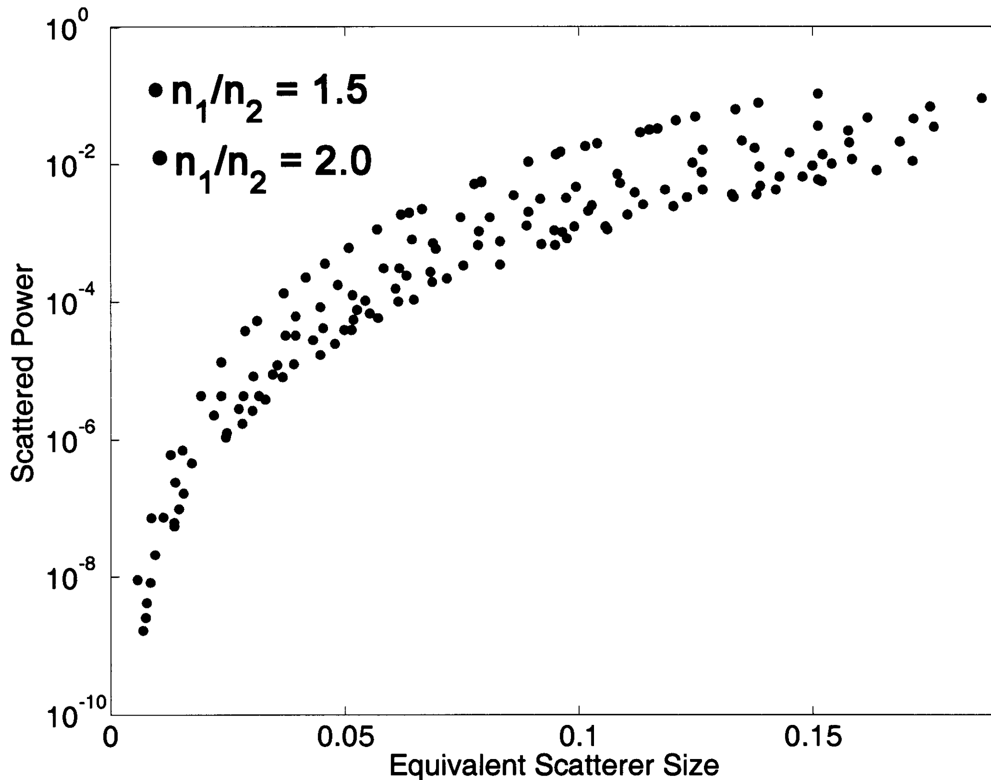

Figure 7.7 Mie theory prediction of the amount of scattered power from the high-to-low index interfaces in the n_1=2.25, n_2=1.5 and n_1=3.0, n_2=1.5 structures. Notice that both the curve shape and the trend predicted here are consistent with the incoherent power calculation from the FDTD data of the same systems.

high end, the power in the Floquet mode, shown in Fig. 7.6, must also be considered, because that power would have been scattered into the incoherent field if the periodic boundary conditions were not present. When this power is added to the incoherent power, the magnitude of the total scattered power on the high end matches the Mie theory calculations much better.

It is curious that the amount of power in the Floquet mode is actually very similar between the high and low index contrast systems. These modes are essentially diffraction modes, and correspondingly, there will be a certain efficiency associated with coupling power into them [French (1971)]. The modes in the two systems compared here are not the same due to differing simulation conditions. So it is difficult to predict what particular trend should be observed. However, since the source of the power in the mode is undoubtedly the diffuse scattering from the roughness features, its dependence on R_{RMS}

should be similar to that seen with the Mie theory calculations. Indeed, as with the incoherent power curves, the curve shape in Fig. 7.6 matches the curve shape in Fig. 7.7.

The percentage of reflected power that is carried by scattered power can be calculated by adding the incoherent and Floquet mode powers and dividing by the total reflected power from the FDTD results. This value for the two systems under study is reported in the plot in Fig. 7.8. As expected, the percentage of the power that is carried by scattered light is extremely small. In the worst case, it is about 4.5% of the total reflected power. This is not surprising in light of the results of chapter 6, which suggested that the total amount of scattered power in these systems was low. However, it is surprising in consideration of the actual amount of architectural deviation from perfection that these structures exhibit (see Fig. 4.5).

Nevertheless, examination of the worst case scenario reveals that the radius of the scatterers rarely exceeds 7% of the incident wavelength. Consider the case where the

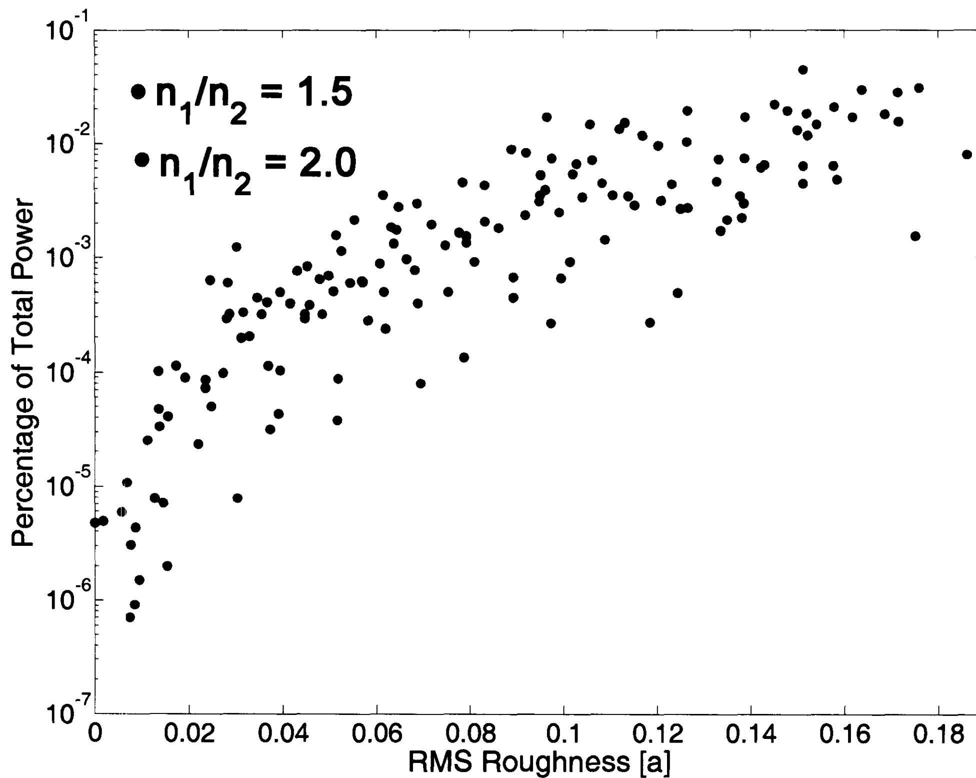

Figure 7.8 The percentage of reflected power that is carried by scattered light (incoherent plus Floquet mode) for the n_1=2.25, n_2=1.5 and n_1=3.0, n_2=1.5 systems. In the worst case, only 4.5% of the reflected power is carried by scattered light.

roughness is so large that the high index layers (which are the thinner layers in the quarter-wave stacks) actually become discontinuous. This results in a structure which looks more like rows of individual cylindrical high index scatterers in a matrix of low index material than a multilayer stack. For such a structure, the scatterer diameter is now equal to the entire width of the high index layer in a quarter wave stack (Eq. 4.5). The incident wavelength will be equal to the vacuum wavelength divided by the value of the low refractive index. So the ratio of the scatterer radius to the incident wavelength is

$$\frac{r_s}{\lambda_i} = \frac{\frac{1}{2}\frac{an_2}{(n_1+n_2)}}{\lambda_0 / n_2} = \frac{1}{8(n_1/n_2)}, \tag{7.7}$$

where Eqs. 4.7 and 4.8 were utilized to substitute out a/λ_0.

So in this worst case structure, the ratio of the scatterer radius to the incident wavelength is actually inversely proportional to the index contrast. Therefore, in reality, this value will be the largest for the lowest index contrast structures. But the intensity of the scattered power rapidly decreases as the index contrast decreases (see Fig 2.11), counteracting the effect from this larger scatterer size. For the highest index contrast structures tested here (n_1/n_2=2.0), the above value equals only 6.25%. Thus, despite the large structural deviations, the size of the scatterer relative to the incident wavelength remains small. The amount of integrated back-scattering from a scatterer this size is only 3×10^{-3} for an incident intensity of 1.0. With this realization, it is clear why the main role of the roughness features is to grade the index profile of the interfaces rather than diffusely scatter the incoming light.

7.4 Conclusions

The results of the previous chapter implied that the amount of incoherent power in the reflection from roughened structures was extremely small. This was confirmed by extracting the amount of scattered power directly from the FDTD data. The scattered power included the incoherent power as well as the power carried by the propagating Floquet mode. Since the Floquet modes were just artifacts of the periodic boundary conditions used in the simulation, their power was considered to be power that would have otherwise been contained in the incoherent field. The highest percentage of the

reflected power that was carried by the scattered field was 4.5%. This was true even for the highest index contrast structure tested (n_1/n_2=2.0). A close examination of the worst case scenario structure revealed that the scatterer size rarely exceeds 7% of the incident wavelength. This explains the extremely small amount of scattered power despite the large structural changes in the highest R_{RMS} structures.

Now that a physical understanding of what is occurring in the structures has been achieved, more studies can be done using the FDTD simulation technique on other relevant problems in photonic crystals. This will allow the validity of the homogenization approximation to be tested under these other conditions as well. The first problem that will be addressed is simply an extension of the problem investigated in chapter 4. Again, structures that have interfacial roughness will be simulated, but now the effect of this roughness on the entire normal incidence bandgap will be determined. The results of these simulations will be presented in the next chapter.

Chapter 8: Effect of Interfacial Roughness on the Normal Incidence Band Gap

Chapters 5 through 7 presented several studies that were done in an attempt to gain a physical understanding of the results seen in chapter 4. It was found that the roughened structures presented in chapter 4 could be represented accurately with the homogenization approximation. More studies can now be done using the FDTD simulation technique to investigate whether or not this approximation is still valid for other relevant problems in photonic crystals. The problem that will be addressed in this chapter is simply an extension of the problem investigated in chapter 4. The same type of structural imperfection, interfacial roughness, will be simulated. However, the effect of this roughness on the reflectivity of the entire normal incidence bandgap, not just the

reflectivity at the center of the gap, will be investigated. This is an important issue because many devices that use 1DPCs, for example band-pass filters, utilize their reflectivity behavior across the entire bandgap.

Again, because of their wide-spread use, the photonic crystal configuration used in these studies was the quarter-wave stack, with the high index layer as the top layer. In fact, the structures used in this study were the exact same structures used in the chapter 4 study. The only difference is that the wavelength used in these simulations was different from the wavelength given by Eq. 4.8. Thus, the characteristic parameter (R_{RMS}), the generation of the structures, and the simulation and analysis method pertaining to this study are given by the explanation of those same aspects presented in chapter 4.

As mentioned in chapter 4, Eq. 4.8 can be used to scale all other wavelengths to appropriate nodal magnitudes. For example, if the bandgap for a given structure is known to span between λ_l and λ_h in some spatial units (i.e. nanometers), then the nodal magnitudes corresponding to those wavelengths (λ_{l0} and λ_{h0}) can be calculated from Eq. 4.8 if the quarter-wave tuned wavelength λ_c is known in the same spatial units. This is done by a simple unit conversion:

$$\lambda_{l0} = \frac{\lambda_l}{\lambda_c}\lambda_0 = \frac{\lambda_l}{\lambda_c}\frac{4n_y}{num_bilayers}\left(\frac{n_1 n_2}{n_1 + n_2}\right). \tag{8.1}$$

λ_{h0} would be found in a similar manner.

This method was used to calculate the appropriate nodal wavelengths for this study. The spatial wavelengths corresponding to the edges of the bandgap were found by using a 1D transfer matrix calculation to plot the normal incidence bandgap for the perfect structures in arbitrary spatial units. These spatial wavelengths were then converted to nodal magnitudes using Eq. 8.1. In addition, several wavelengths within the bandgap, which were also converted with Eq. 8.1, were chosen for the study. On average, twenty separate wavelengths spanning the bandgap were simulated for each structure at four different roughness values.

8.1 FDTD Reflectivity Results

Approximately 400 FDTD simulations were done in order to determine the effect of interfacial roughness on the full normal incidence bandgap of several different 1D

photonic crystal configurations. The reflectivities (calculated with Eq. 4.9) from a TE-polarized normal incidence plane wave impinging on the roughened quarter-wave stacks were obtained. For comparison, these reflectivities were then plotted on top of the normal incidence reflectance spectrum for the corresponding perfect structure. The reflectance data was also fit with a polynomial expression in order to better observe any trends resulting from the simulations.

The simulated reflectance spectra corresponding to several 4-bilayer systems are shown in Fig. 8.1. Each point on the plots corresponds to the calculated reflectivity results obtained from a single simulation. On the other hand, the curves shown are the fits to the reflectivity data described above, which represent the resulting band structure at each roughness value.

As expected from the results of chapter 4, Fig. 8.1 shows that the reflectivity decreases dramatically with increasing roughness across the entire normal incidence bandgap for all the structures tested. However, the magnitude of this decrease is not the same for all wavelengths. The blue end of the bandgap (smaller wavelengths) experiences a much larger change in reflectivity than the red end (larger wavelengths). This results in a narrowing and red-shifting of the normal incidence bandgap with increasing RMS roughness. Although this effect is seen in all the structures presented in Fig. 8.1, the lowest index contrast structure (n_1/n_2=1.25) appears to be more sensitive to this red-shifting. This is illustrated by the fact that the red-shifting is already evident in the lowest index contrast structure at the smallest R_{RMS} value tested (~0.035a), whereas the same roughness value in the other structures produces no such effect.

Fig. 8.2, which plots the percent change in reflectivity from the perfect structure across the bandgap (Δr, Eq. 4.10), shows this more clearly. Due to the steep slope of the reflectivity at the edges of the bandgap, the Δr value in this region becomes very large. Because of this, the region where the perfect bandgap is within 10% of its maximum value (i.e. where the bandgap reflectance is reasonably flat) is highlighted in the plots. Outside of this region, the edges of the bandgap begin to effect the Δr value of the structure. So the below analysis focuses on the behavior of the reflectivity change within this shaded region.

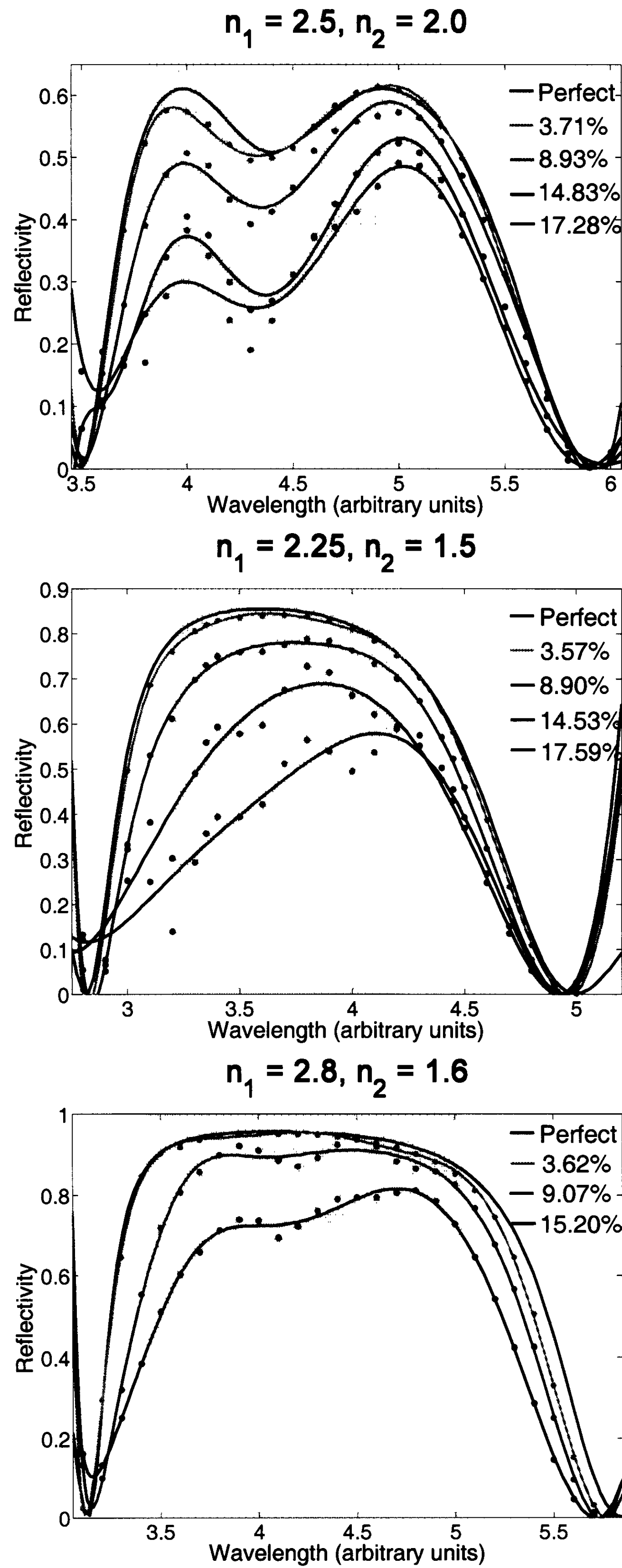

Figure 8.1 The simulated normal incidence reflectance spectra corresponding to several 4-bilayer systems. In all systems, a narrowing and red-shifting of the normal incidence bandgap is apparent.

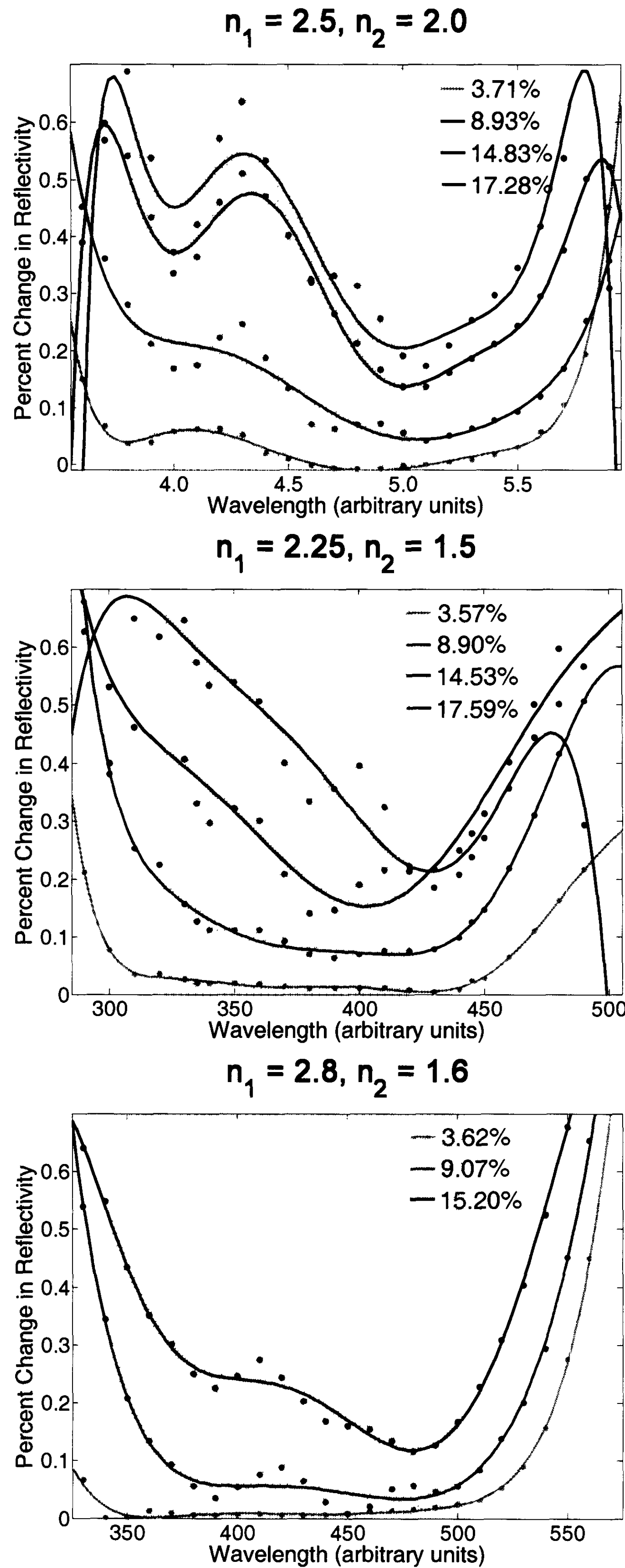

Figure 8.2 The percent change in reflectivity (Δr) across the entire normal incidence bandgap for several 4-bilayer systems. The shading indicates the region where the reflectivity of the bandgap is within 10% of its maximum value. Again, the red-shift is apparent in all systems.

Again, Fig. 8.2 shows that all simulated systems experience a decrease in the percent change in reflectivity as the wavelength increases. However, the lowest index contrast structure shows evidence of this red-shifting at even the smallest R_{RMS} value. This same roughness produces only a uniform change in the reflectivity across the shaded region in the higher index contrast structures. Notice also that the magnitude of the reflectivity change is larger overall in the lowest index contrast structure, and decreases as the index contrast increases. This is consistent with the results in chapter 4, which showed that the higher index contrast structures were more tolerant to interfacial roughness.

The reason why the lower index contrast structure appears to be more sensitive to the red-shifting can be explained with one of the conclusions that was made from the results of chapter 5. There, it was seen that the higher index contrast structures had a lower change in their reflectivity despite the fact that they experienced a larger structural modification. The conclusion was that the higher index contrast structures were more tolerant to structural changes than the low index contrast systems. Thus, again here, the higher index contrast systems appear to be more forgiving of structural imperfections, causing the red-shifting to be indiscernible at low roughness values.

As with the chapter 4 study, additional simulations were done to investigate the effect of increasing the number of bilayers in the structure. Fig. 8.3 shows the reflectance spectra for several n_1/n_2=1.5 systems with differing bilayer numbers. Again, a red-shifting is observed in all the systems. However, unlike the previous study, there does not appear to be one system that is more sensitive to this red-shifting than another. This can be seen more clearly with the plots in Fig. 8.4. Like the plots in Fig. 8.2, this figure shows the percent change in reflectivity (Δr) for the n_1/n_2=1.5 systems. Notice that the lowest R_{RMS} value shows no signs of the red-shift for any of the systems. However, the trend of the reflectivity change is again consistent with the results of chapter 4 – the system with more bilayers experiences a lower percent change in the reflectivity overall.

8.2 Homogenization Approximation Reflectivity Results

The reason why a red-shift in the normal incidence bandgap occurs at all could be explained easily using scattering theory. As was demonstrated in chapter 2, the

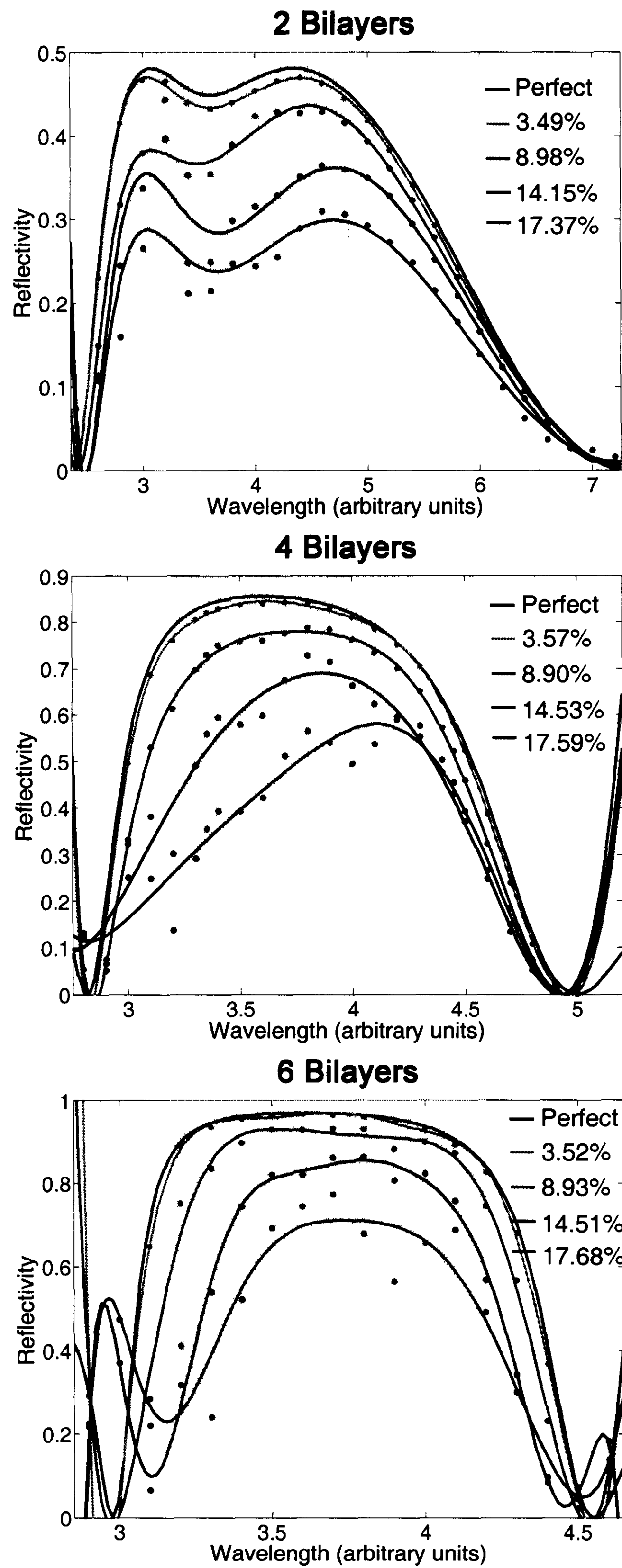

Figure 8.3 The simulated normal incidence reflectance spectra corresponding to several bilayer systems with n_1=2.25 and n_2=1.5. Again, a narrowing and red-shifting of the bandgap is evident in all systems.

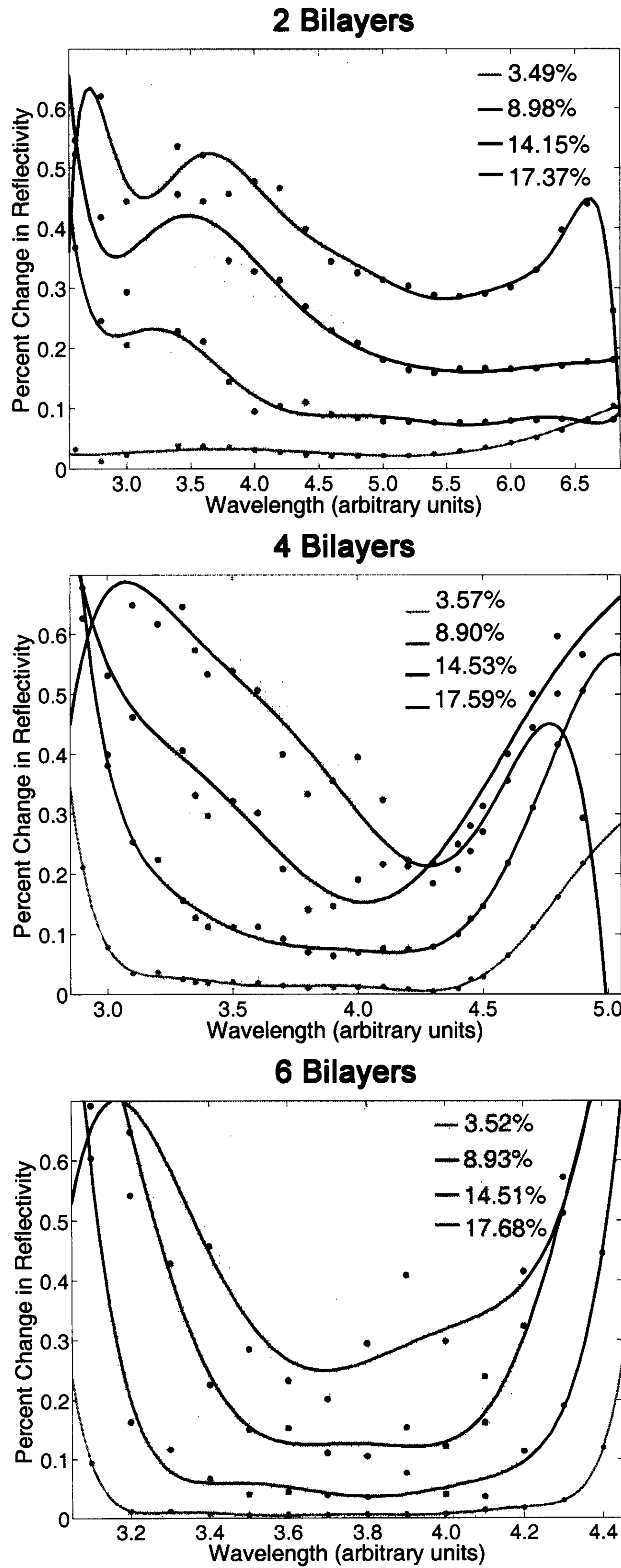

Figure 8.4 The percent change in reflectivity (Δr) across the entire normal incidence bandgap for several bilayer systems with n_1=2.25 and n_2=1.5.

magnitude of scattering increases as the incident wavelength decreases. Thus, if the decrease in reflectivity from these structures was largely due to diffuse scattering losses, then the blue end of the bandgap would show a larger reflectivity change.

However, chapters 6 and 7 showed that the amount of diffuse scattering in these systems is extremely small. Instead, the main source of the reflectivity loss is actually the graded index profile at the interfaces within the structure. This was demonstrated through the success of the homogenization approximation to accurately predict the change in reflectivity given by the FDTD calculations in chapter 4. In order to determine if this physical picture is still valid at wavelengths other than λ_0, the homogenization approximation needs to be applied to this study as well. This only requires changing the incident wavelength in the transfer matrix calculations of the approximated structures.

The results of the homogenization approximation applied to the 4-bilayer structures presented above are shown in Figs. 8.5 and 8.6. The points on each plot correspond to the calculated reflectivity from the approximated structures. The curves are polynomial fits of this data that represent the band structure at each roughness value. A comparison between these figures and Figs. 8.1 and 8.2 reveals that the homogenization approximation also matches the FDTD calculations across the entire normal incidence bandgap. Specifically, it reproduces the red-shifting seen with the FDTD data, and moreover, it accurately predicts the increased sensitivity of the low index contrast structure to the red-shifting. The validity of the homogenization approximation in this regime is further supported with the comparison of Figs. 8.7 and 8.8 with Figs. 8.3 and 8.4. Again, the red-shifting behavior is clearly predicted and the magnitude of the reflectivity change matches well with the FDTD calculations.

It is interesting that the homogenization approximation can capture this red-shifting behavior seen with the FDTD results. The reason for this is that the length over which the interfaces are diffuse compared to the incident wavelength is larger for bluer light than for redder light. So the interfaces actually appear sharper to longer wavelengths than to shorter ones. This causes the deviate structure to “look” more like the perfect structure to redder parts of the spectrum. Thus, the red end of the bandgap shows a smaller decrease in the reflectivity than the blue end, resulting in a red-shift.

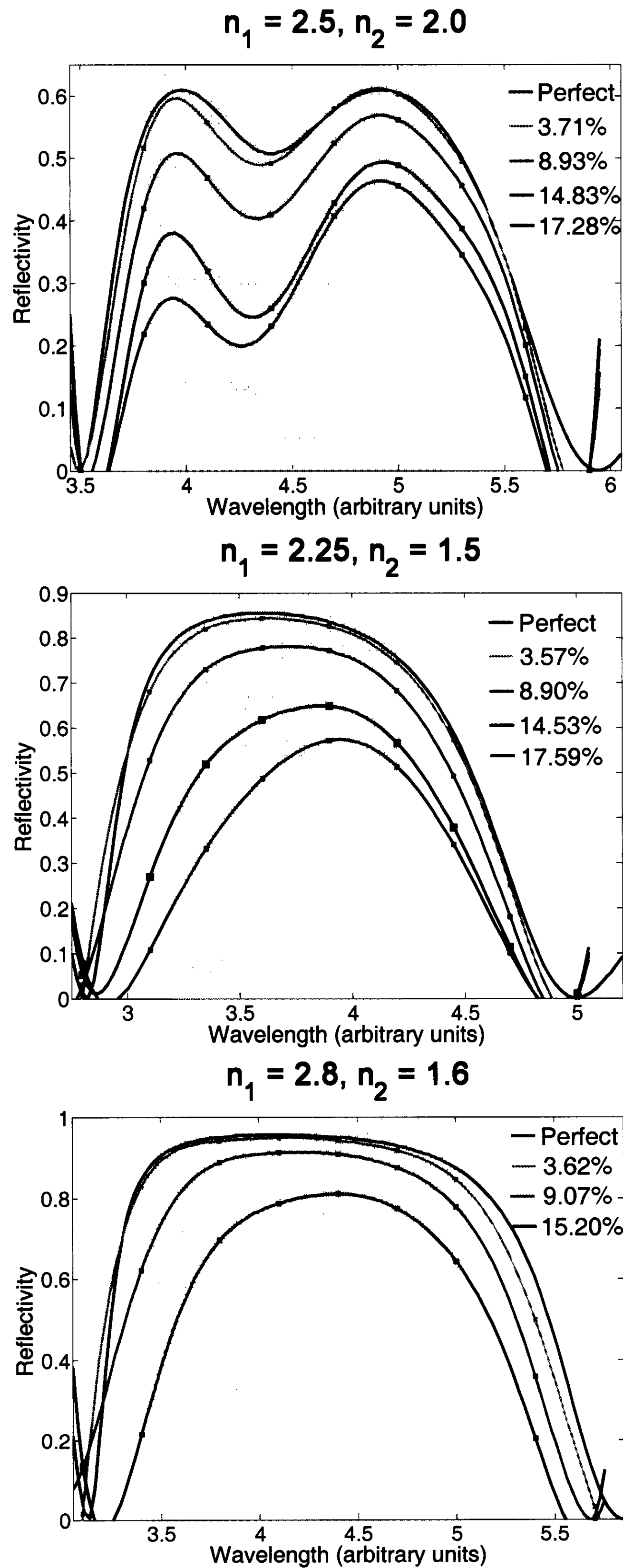

Figure 8.5 The results of the homogenization approximation applied to the 4-bilayer structures presented in Fig. 8.1. Comparison of the two figures shows that the homogenization approximation is in good agreement with the FDTD results.

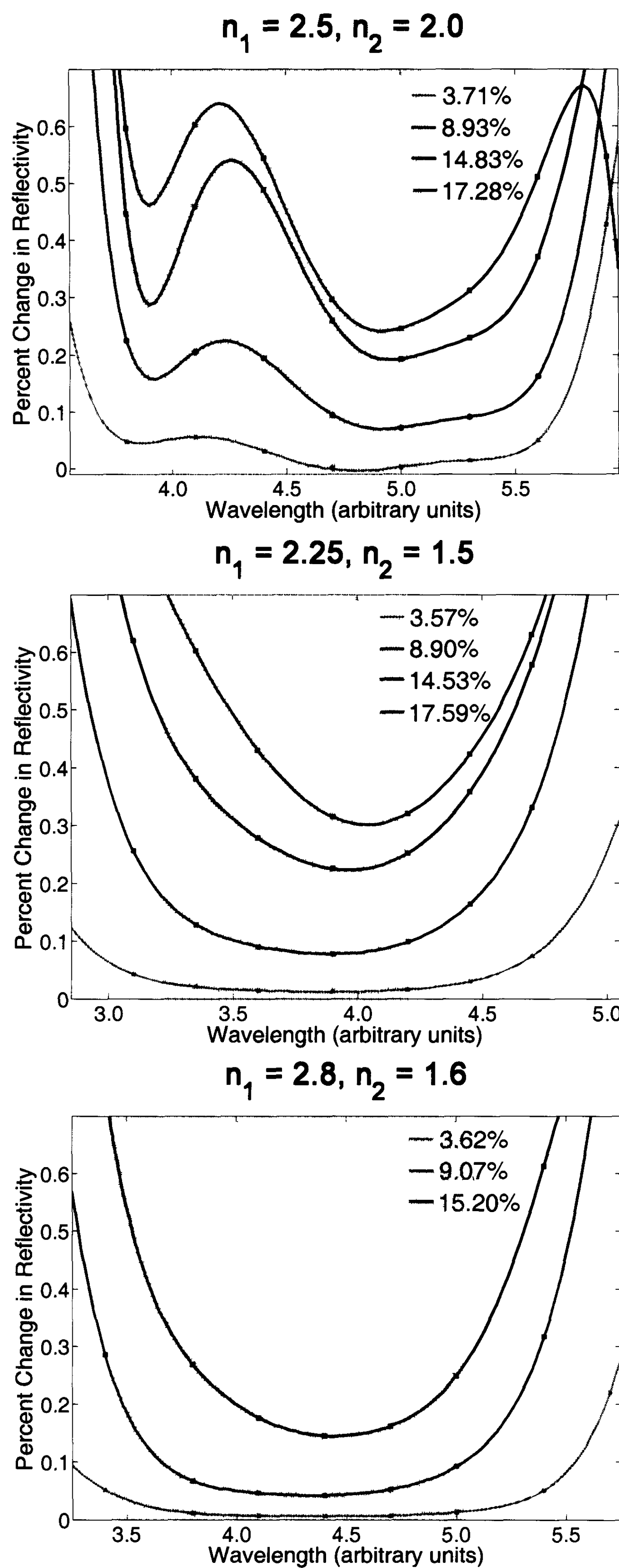

Figure 8.6 The results of the homogenization approximation applied to the 4-bilayer structures presented in Fig. 8.2.

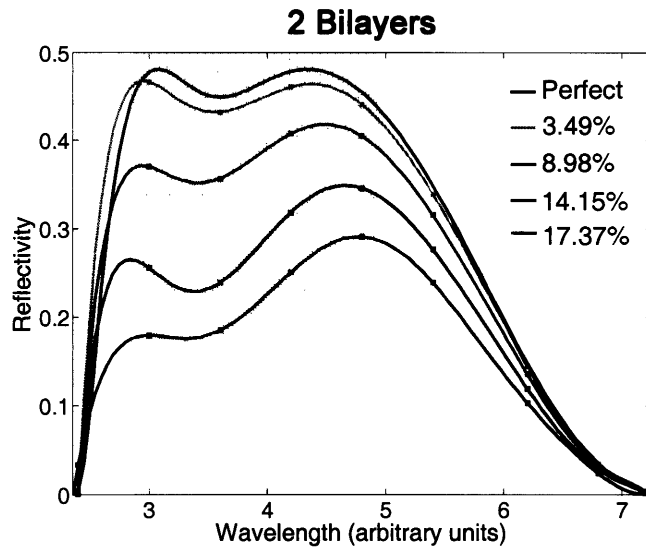

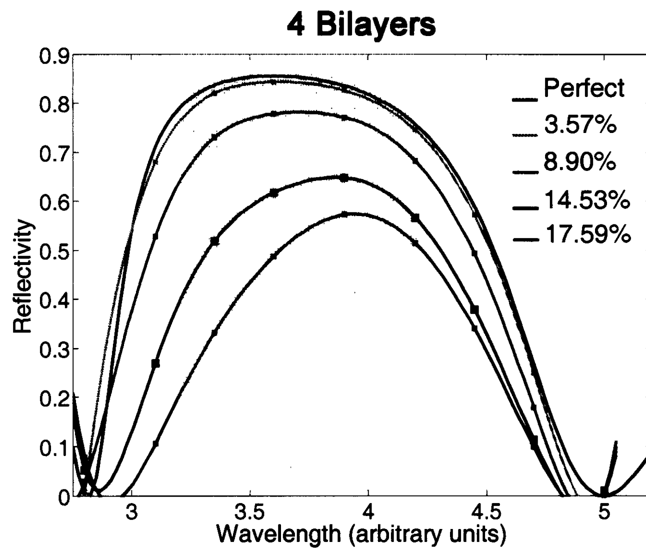

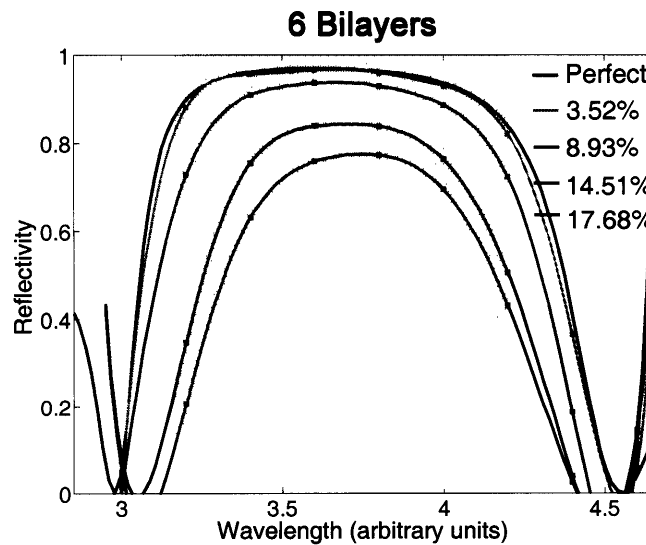

Figure 8.7 The results of the homogenization approximation applied to the bilayer systems shown in Fig. 8.3. Again, comparison of the two figures shows that the homogenization approximation is in good agreement with the FDTD results.

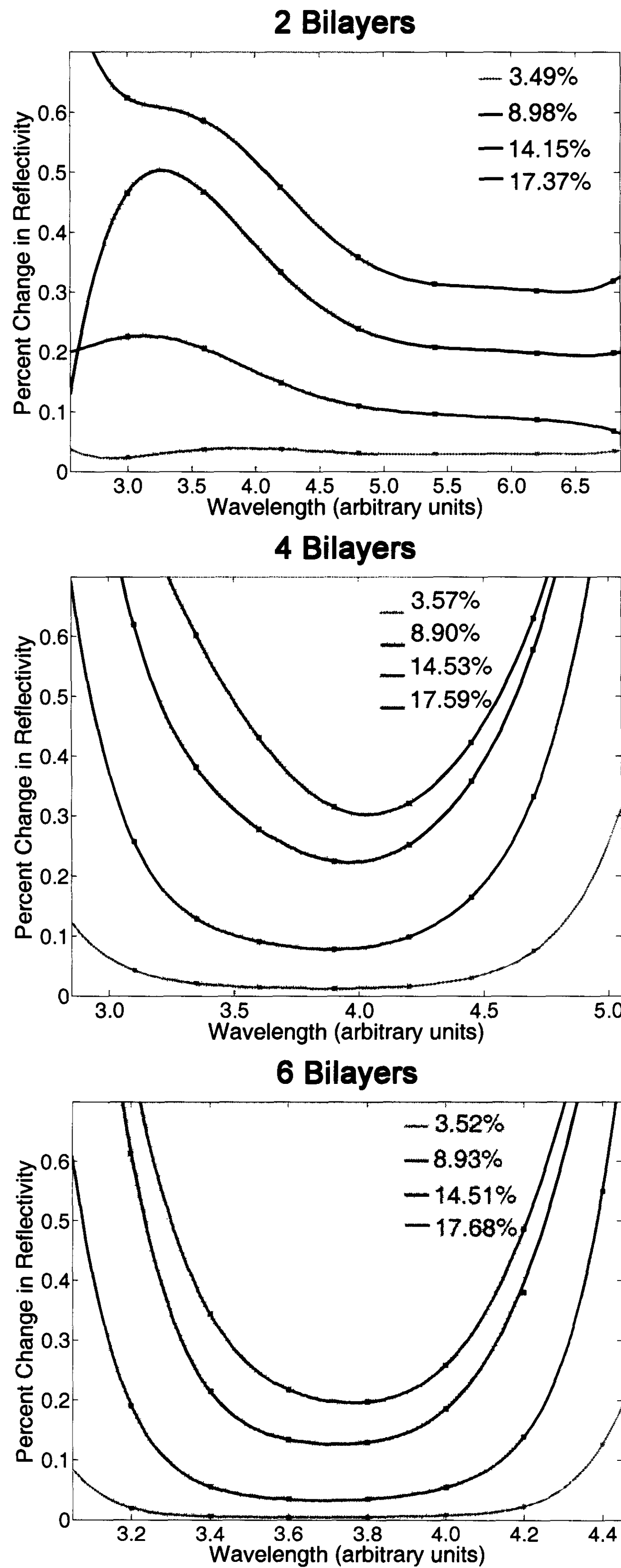

Figure 8.8 The results of the homogenization approximation applied to the bilayer structures presented in Fig. 8.4.

8.3 Conclusions

Several 2D FDTD simulations were done in order to determine the effect of interfacial roughness on the normal incidence bandgap. Many 1D photonic crystal configurations were tested, with systematic variations in the index contrast and number of bilayers. In all systems tested, a narrowing and red-shifting of the normal incidence bandgap was observed. Furthermore, the lowest index contrast system exhibited a higher sensitivity to the red-shifting. This can be explained by the fact that lower index contrast structures are less tolerant to structural changes than higher index contrast system, as was concluded from the study done in chapter 5.

Although the red-shifting observed in the reflectance spectra could be explained using scattering theory, the results from chapters 6 and 7 revealed that the amount of diffuse scattering in these systems is extremely small. Thus, the homogenization approximation was applied to this study in order to determine if it could also reproduce the red-shifting. The results of these calculations revealed that the homogenization approximation could be used to accurately predict the reflectance behavior in this study as well. Thus, it is valid approximation of the structures tested here for all wavelengths spanning the normal incidence bandgap.

In the next chapter, the validity of the homogenization approximation will be tested on another type of structural imperfection: surface scratches. The simulated structures for this study are very similar to those tested in this chapter. The one major difference is that there is only roughness present on the top surface of the structure, representing scratches on the surface of the crystal. The addition of protective coatings will also be explored to determine design conditions that will optimize device tolerance to scratches. Finally, the FDTD results will be compared to the results of the homogenization approximation to determine its validity for these structures.

Chapter 9: Surface Scratches on 1D Photonic Crystals

The unique optical properties of photonic crystals make them desirable for incorporation into a variety of devices. Due to an increasing demand for instruments that are operable in remote areas ("in-field-use" instruments), these devices are progressively being intended for use in uncontrolled environments. In such situations, these devices may be subject to abuse and subsequent damage due to the harsh conditions. Additionally, some devices, such as biosensors, may require the photonic crystal to be subject to a flow field in order to increase the throughput of the device and sample a greater volume of material. Since the sample material that is being pushed past the device will likely be contaminated with a variety of foreign objects, there is a high potential for the photonic crystal to be damaged by these objects. Furthermore, if the

photonic crystal is put in contact with incompatible chemicals, then it may experience etching or pitting on the exposed surface of the device.

Thus, the effect of such damage on the desirable optical properties of photonic crystals should be investigated. One type of damage that is relevant to the above situations is the introduction of surface scratches on the top layer of 1D photonic crystals. The effect of this particular structural modification is explored in the following chapter. As in the previous chapters, a 2D FDTD code was used to determine the change in reflectivity of the photonic crystal due to the surface scratches. Again, the simulations involved quarter-wave stacks with a TE polarized normal incidence plane wave. Studies were done at both the quarter-wave tuned wavelength and other wavelengths spanning the entire normal incidence bandgap. Both periodic and absorbing boundary conditions were used to simulate infinitely long structures that had a finite number of bilayers. The reflectivity of the structures was found using Eq. 4.9, and the corresponding percent change in reflectivity from the perfect structure was calculated with Eq. 4.10. Each stack was arranged so that the top layer was the higher index material, and all simulations were done on free-standing crystals – the surrounding medium on both sides of the crystals is vacuum (dielectric constant 1.0). These simulations were run in conjunction with simulations of equivalent photonic crystal configurations topped with protective coatings of various refractive indices. This was done in order to explore the effect of these coatings and determine design parameters to optimize device tolerance to surface scratches.

Due to the success of the homogenization approximation in the previous studies, this approximation was also applied to this study in order to determine its predictive capability for this type of structural imperfection. As before, the FDTD results were compared to the results of the homogenization approximation in order to determine its validity for these structures.

9.1 Surface Scratch Parameter

The characteristic parameter defined for the simulated structures in this study is very similar to the RMS roughness parameter defined for the interfacial roughness

problems in chapters 4 and 8. For this study, the characteristic parameter is the RMS scratch depth:

$$R_{RMS} \equiv \left(\frac{1}{n_{nodes}} \sum_{1}^{n_{nodes}} (y_i - y_0)^2 \right)^{1/2} . \tag{9.1}$$

Note the similarity between Eq. 9.1 and Eq. 4.1. The only difference in the definitions of the RMS roughness and the RMS scratch depth is that y_0 in the above equation is the maximum interface height rather than the average interface position. This is because all of the surface scratches in the simulated structures are directed into the surface of the crystal. Again, the scratch depth was normalized to the characteristic periodicity of the quarter-wave stacks, given by Eq. 4.3. Thus, all the results of these calculations are scalable based on the spatial magnitude of this parameter for a given fabricated device.

9.2 Generation of the Scratched Structures

The scratched structures were generated with a modified version of the same C++ code used to generate the roughened structures in chapter 4. Again, a quarter-wave stack with no surface scratches was created first, and the top interface nodes of the structure were then displaced by a random amplitude. Because the effect of protective coatings was also investigated with this study, the code was augmented with the ability to add a surface coating to the crystal with a specified (input) refractive index and thickness.

The nodal thicknesses of the layers in the perfect quarter-wave stack were calculated as described in chapter 4. Again, a two-dimensional array was then created to hold the refractive index information of the structure. The refractive index values corresponding to the perfect structure were written into the array, along with the refractive index of the coating layer at the input thickness. Ambient buffer layers were also created above and below the structure with refractive index values of 1.0.

The scratches on the top surface of the structure were created using the same algorithm as that described in chapter 4 for the creation of the roughness features. The only difference, as mentioned above, was that all displacements were directed into the structure, so there was no need for a random angle to determine the direction of the displacement. Additionally, the algorithm used to maintain the average position of the

interface at the quarter-wave thickness condition was abandoned because this constraint was no longer necessary.

The RMS scratch depth was calculated according to Eq. 9.1 from the displacement list generated with the displacement algorithm. The refractive index array was written to an output file, which was then used as an input into the FDTD code. The nodal magnitude of the incident wave was also input into the FDTD simulation. As in chapter 4, all simulations were done with the quarter-wave tuned wavelength, so Eq. 4.8 could also be used to calculate the nodal magnitude of the incident wavelength for these simulations.

In order to properly compare the reflectivity changes between the coated and uncoated structures, it was desired that the absolute reflectivity of the structures would not change with the addition of the coatings. In general, the addition of a top surface coating to a photonic crystal will alter its absolute reflectivity, even if the coating has a perfectly flat surface. However, careful tailoring of the thickness of the coating can allow one to avoid this reflectivity change at a specific wavelength. If the thickness of the material equals a multiple of a half wavelength, then it will resonantly transmit light with that wavelength. This is called the resonant transmission thickness:

$$t_{rt,\lambda} = \frac{n\lambda}{2n_c}. \tag{9.2}$$

Note that this thickness will only resonantly transmit the wavelength to which it is tuned. All other wavelengths, except for harmonics of the fundamental wavelength, will experience some amount of reflection off the coating. Thus, if a resonant transmission coating that is tuned to a particular wavelength is added to the top of a quarter-wave stack, then the reflectivity of the stack at that wavelength will not change. Hence, the thicknesses chosen for the protective coatings in this study corresponded to resonant transmission thicknesses at the quarter-wave tuned wavelength. Furthermore, in order to minimize computational run time, the smallest resonant transmission thickness (n=1 in Eq. 9.2) was used. Combining Eq. 9.2 with Eq. 4.8, the value of the coating thickness for each photonic crystal system tested was

$$t_{rt,\lambda_0} = \frac{2n_y}{n_c(num_bilayers)}\left(\frac{n_1 n_2}{n_1 + n_2}\right). \tag{9.3}$$

This analysis assumed that there was no absorption present in the coating material. If absorption is present, then there will be power lost when any amount of the material is put on top of the structure. However, this loss can be minimized by choosing low loss materials for the coating and using the smallest thickness acceptable to still retain the protective utility of the coating.

9.3 FDTD Reflectivity Results

Approximately 500 simulations at various conditions were done in order to determine the effect of surface scratches on the optical properties of 1D photonic crystals. Quarter-wave stack configurations with and without protective scratch coatings were simulated in order to determine the optimal design conditions that minimize the effects of these imperfections. The reflectivity changes for several 4-bilayer quarter-wave stacks with different constituent refractive index values are shown in Fig. 9.1. Each stack configuration was tested with a variety of coatings that had refractive indices ranging from 1.5 to 2.5. Equivalent configurations with no protective coating were also tested for comparison.

The results of these simulations show that the addition of a protective coating does affect the tolerance of the structure to scratches. Moreover, every system tested reveals that the ratio between the refractive index of the coating (n_c) and the refractive index of the top layer (n_1) determines the overall effect of the coating. If n_c/n_1 is less than one, then the coating has a beneficial effect, increasing the tolerance of the structure to surface scratches. Furthermore, the coating becomes more beneficial as this ratio decreases. However, if n_c/n_1 is greater than one, then the coating has a negative impact on the tolerance of the crystal, actually exacerbating the effect of the scratches.

This trend is apparent in all of the systems presented in Fig. 9.1. For the n_1=2.5, n_2=2.0 system, all coatings that have refractive index values less than 2.5 result in a structure that is more robust than the configuration without any coating at all. Additionally, as the coating refractive index decreases, the structure's tolerance to the scratches increases. It is interesting to note that a coating with the same refractive index as the top layer actually slightly decreases the tolerance of the structure. Thus, it would not be beneficial to make a protective coating for a device by simply increasing the

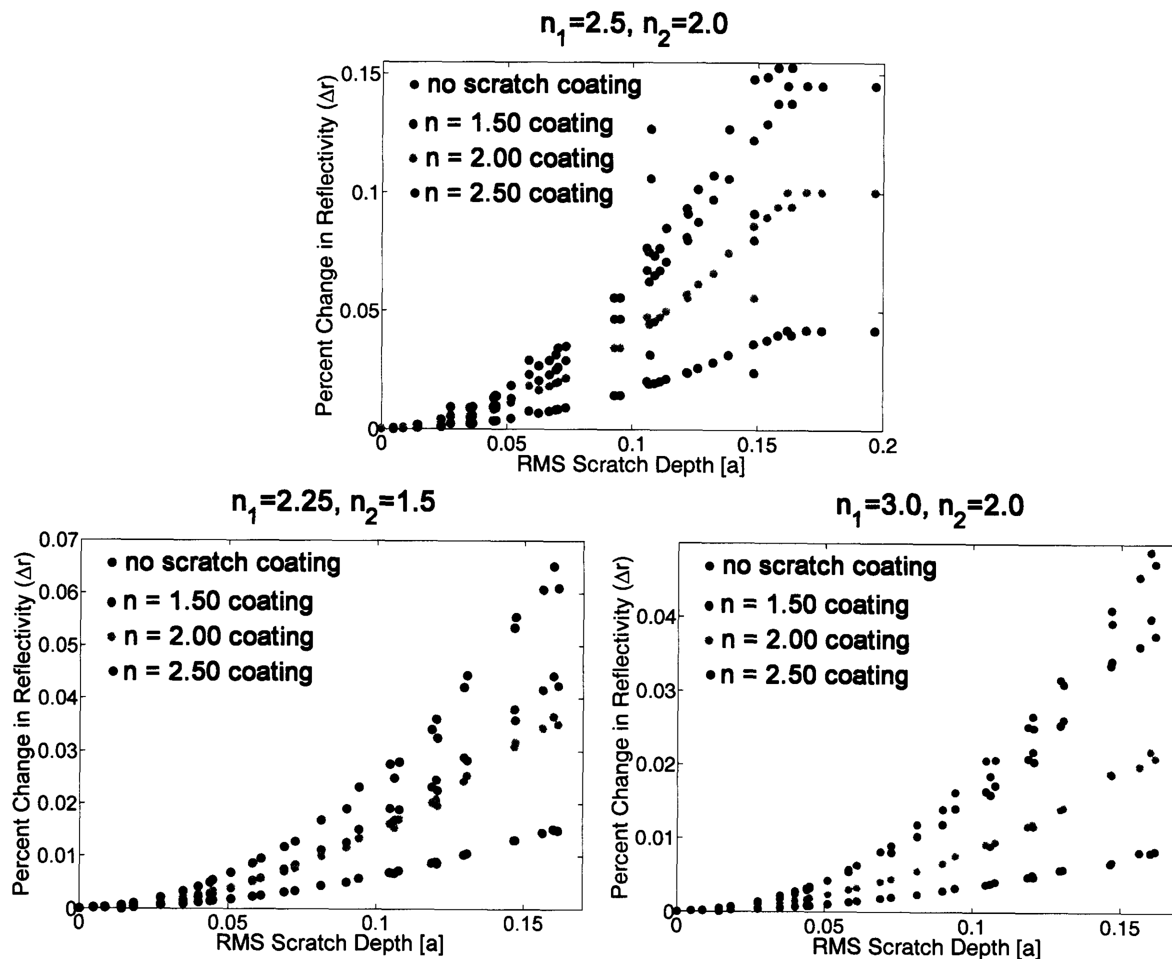

Figure 9.1 The percent change in reflectivity (Δr) for several 4-bilayer quarter-wave stacks with different constituent refractive index values. In addition to structures without protective coatings, structures with coatings were also tested in all of the systems. The coatings had refractive index values of 1.5, 2.0, and 2.5.

thickness of the top layer of the structure. However, it would be beneficial to put an additional low index (n_2) layer on top of the structure that was a half-wave thickness instead of a quarter-wave thickness to act as a protective coating.

The other two plots in Fig. 9.1 reveal another curious aspect of this study. For two structures that have the same index contrast (both have n_1/n_2=1.5), identical coatings on each structure can have dramatically different effects. This is illustrated by the fact that the n_c=2.5 coating results in a very different behavior from each of the two structures. For the n_1=3.0, n_2=2.0 structure, this coating increases the tolerance of the crystal. However, the same coating on the n_1=2.25, n_2=1.5 structure decreases its tolerance. Furthermore, the n_c=1.5 coating has a more beneficial effect on the n_1=3.0,

n_2=2.0 structure than the n_1=2.25, n_2=1.5 structure. So the role of the protective coating is not determined by the index contrast, but instead by the actual value of the high refractive index.

Note, however, that the results for the structures without protective coatings are still consistent with the results from the previous chapters. Both n_1/n_2=1.5 structures experience similar reflectivity changes, while the lower index contrast structure (n_1/n_2=1.25) experiences a much larger change in the reflectivity for the same RMS scratch depth values. Thus, the effect of surface scratches can be minimized through the use of photonic crystals that have a high index contrast (preferably with a high average index so the top layer has a high refractive index value) combined with a coating which has a very low value for its refractive index.

Also note that the reflectivity changes involved with these defects are much smaller than those resulting from the interfacial roughness defects. This is because there is only roughness on the top interface of the structure, rather than all the interfaces. Still, this reflectivity change can reach up to 15% in the case of the lowest index contrast structure without the aid of a protective scratch coating.

Even though the protective coatings used above do not affect the absolute reflectivity of the structures (without scratches) at the quarter-wave tuned wavelength, they do impact the reflectivity at other wavelengths. This is illustrated by the plots in Fig. 9.2. The top plot shows the normal incidence bandgap for an uncoated 4-bilayer quarter-wave stack with n_1=2.25 and n_2=1.5. On the other hand, the bottom plot shows the normal incidence bandgap for an equivalent quarter-wave stack configuration that has an n_c=1.5 protective coating (beneficial coating). Notice that the reflectivity at the quarter-wave tuned wavelength (3.6 in this case) is the same in both plots. However, the reflectivities at other wavelengths differ. With the addition of the coating, the bandgap narrows and the reflectivity at the edges of the bandgap do not fall completely to zero.

With this alteration of the bandgap in mind, several simulations were done to investigate the effect of scratches on the entire normal incidence bandgap for structures with and without coatings. The results of these simulations for the same structures presented in Fig. 9.2 are shown in Figs. 9.3 and 9.4. As in chapter 8, a narrowing and red-shifting of the bandgap is observed with increasing RMS scratch depth for both

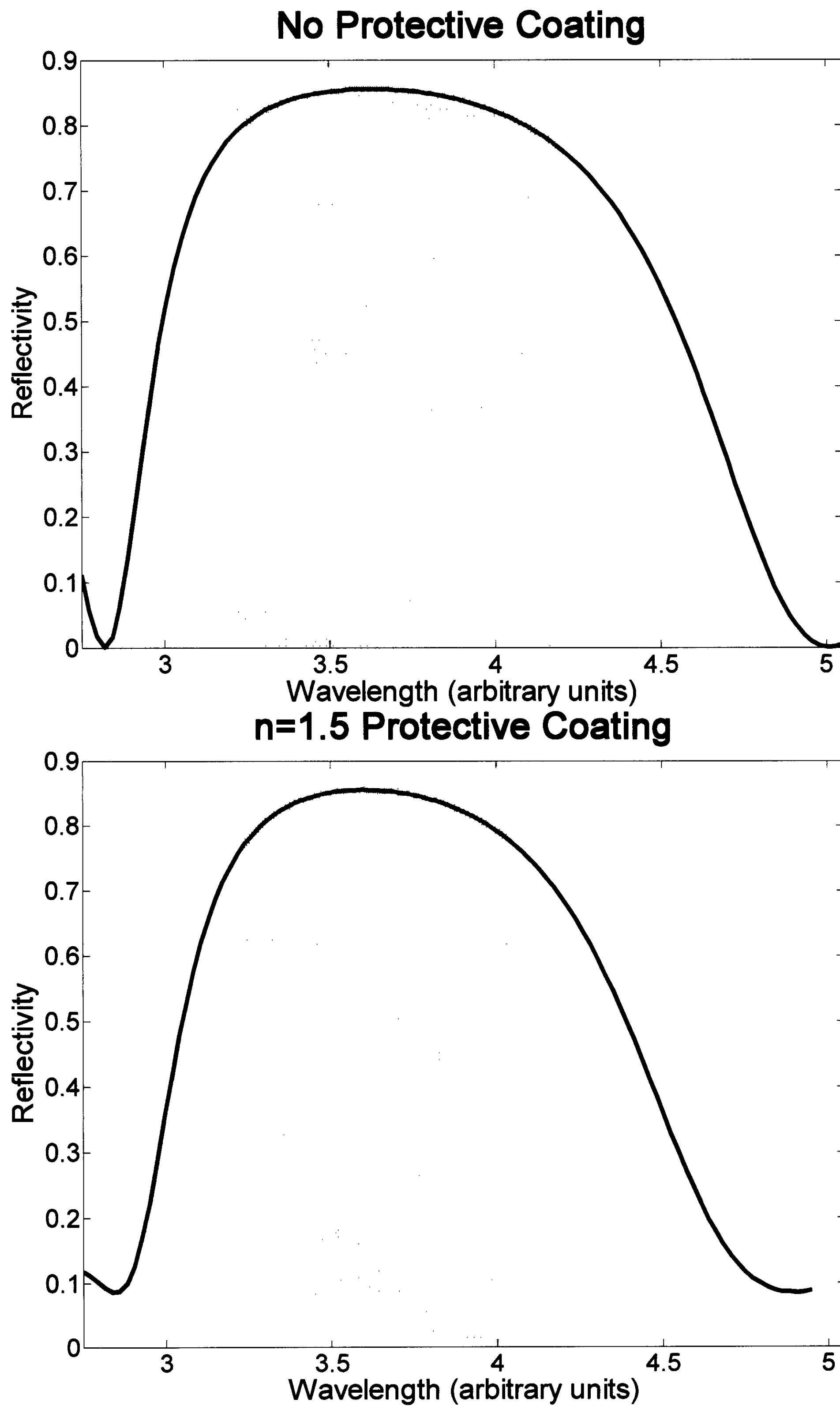

Figure 9.2 The normal incidence bandgap for a unscratched 4-bilayer n_1=2.25, n_2=1.5 structure with (top) and without (bottom) a protective coating. The coating used for the bottom structure had a refractive index of 1.5 (beneficial coating).

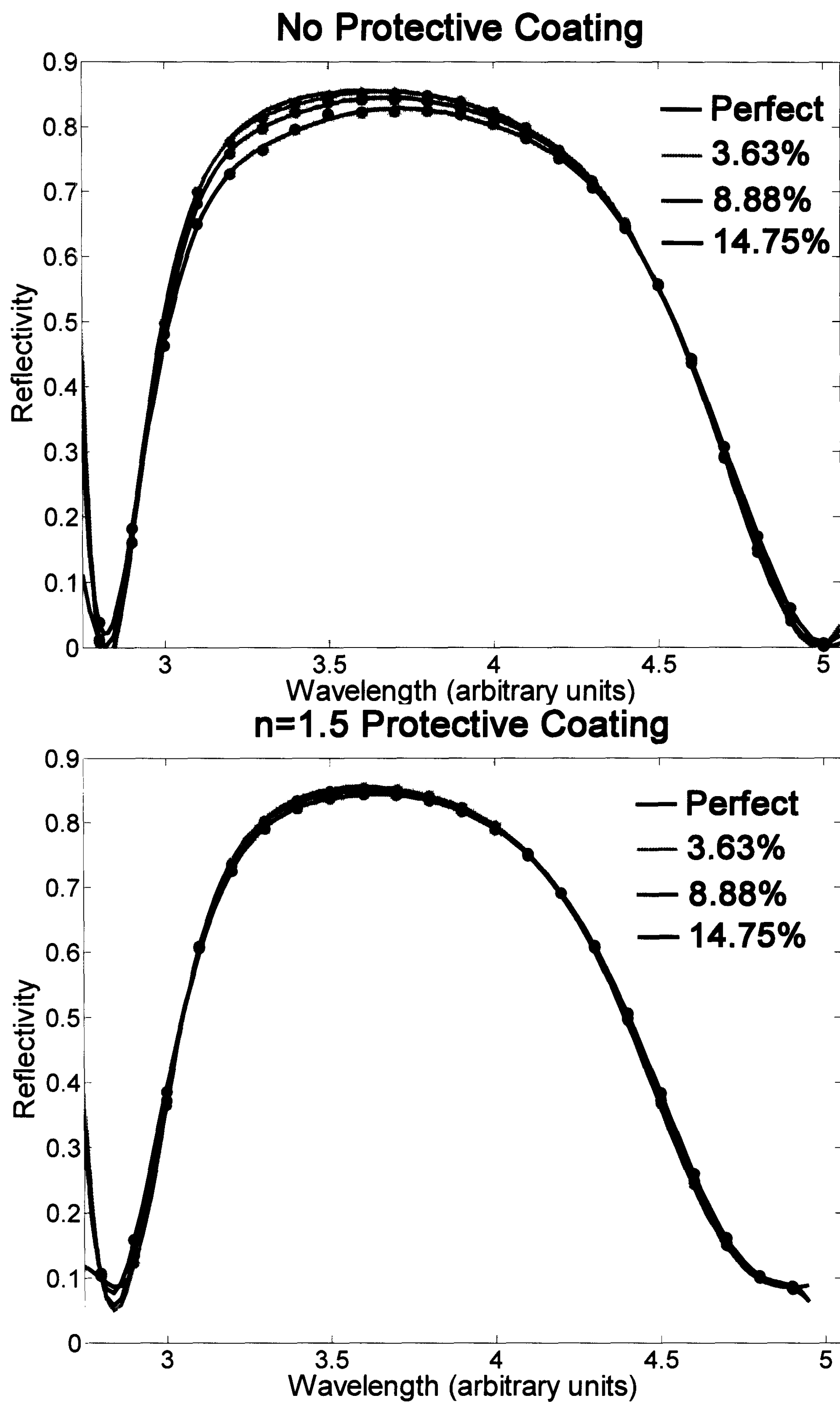

Figure 9.3 The effect of surface scratches on the normal incidence bandgap for two 4-bilayer n_1=2.25, n_2=1.5 structures. The top structure has no protective coating, while the bottom structure has an n_c=1.5 coating (beneficial coating).

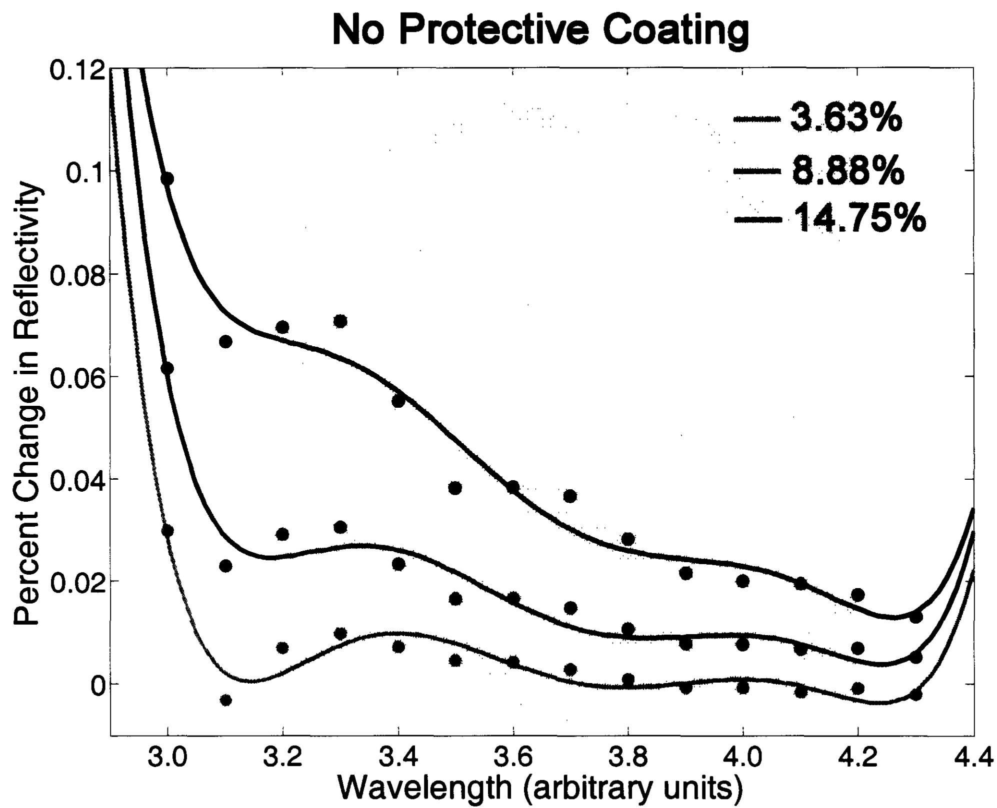

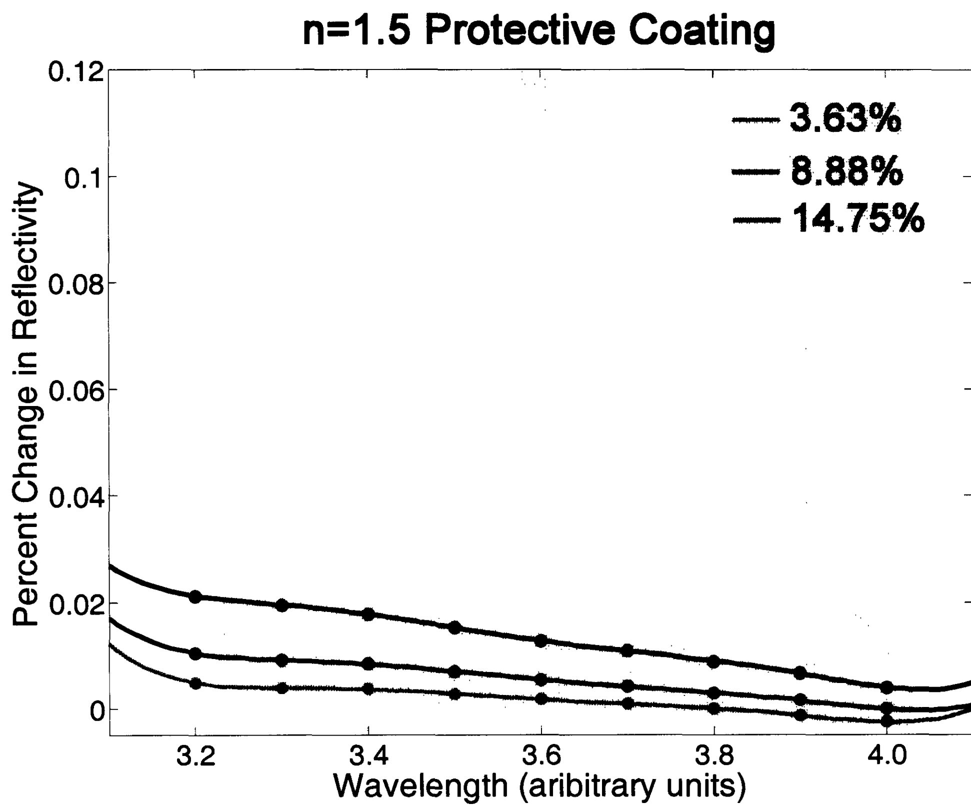

Figure 9.4 Percent change in reflectivity (Δr) for two 4-bilayer structures with n_1=2.25 and n_2=1.5. The top structure has no protective coating, while the bottom structure has an n_c=1.5 coating (beneficial coating).

structures. However, this effect is much more apparent in the structure without the scratch coating. Fig. 9.4 indicates that the percent change in reflectivity reaches about 7% for the uncoated structures, while it only reaches about 2% for the coated structure. Thus, the addition of an $n_c/n_1 < 1.0$ coating actually increases the tolerance of the quarter-wave stack over the entire normal incidence bandgap. However, as mentioned above, the absolute reflectivity of the coated structure is altered by the presence of the coating. Therefore, if the application for which the device is intended can tolerate the bandgap changes associated with the added coating, then it is more beneficial to use a coated structure across the entire normal incidence bandgap.

9.4 Homogenization Approximation Reflectivity Results

From chapters 5 and 8, the homogenization approximation was shown to have predictive capabilities for the reflectivity changes associated with interfacial roughness. Because of this, the homogenization approximation was also applied to the scratched structures tested in this study. These results are shown in Figs. 9.5 and 9.6. As before, the homogenization approximation matches the FDTD results extremely well, even for the coated structures. As Fig. 9.6 shows, it captures the red-shifting of the normal incidence bandgap and correctly predicts that the coated structure is more robust over the entire normal incidence bandgap. Thus, again, the homogenization approximation appears to be valid for the scratch depths tested here ($\sim 0.17a$). However, unlike the interfacial roughness study, real scratches on photonic crystal devices could be much larger than the ones tested here. Thus, for much deeper scratches with much larger pitches (RMS wavelengths, Eq. 4.2), the homogenization approximation may no longer hold. More simulations need to be done to determine where this approximation begins to break down.

9.5 Conclusions

Several FDTD simulations were done to determine the effect of surface scratches on the optical properties of 1D photonic crystals. The reflectivity changes of quarter-wave stacks with various protective coatings were calculated and compared to the reflectivity results from equivalent structures without coatings. The thickness of these

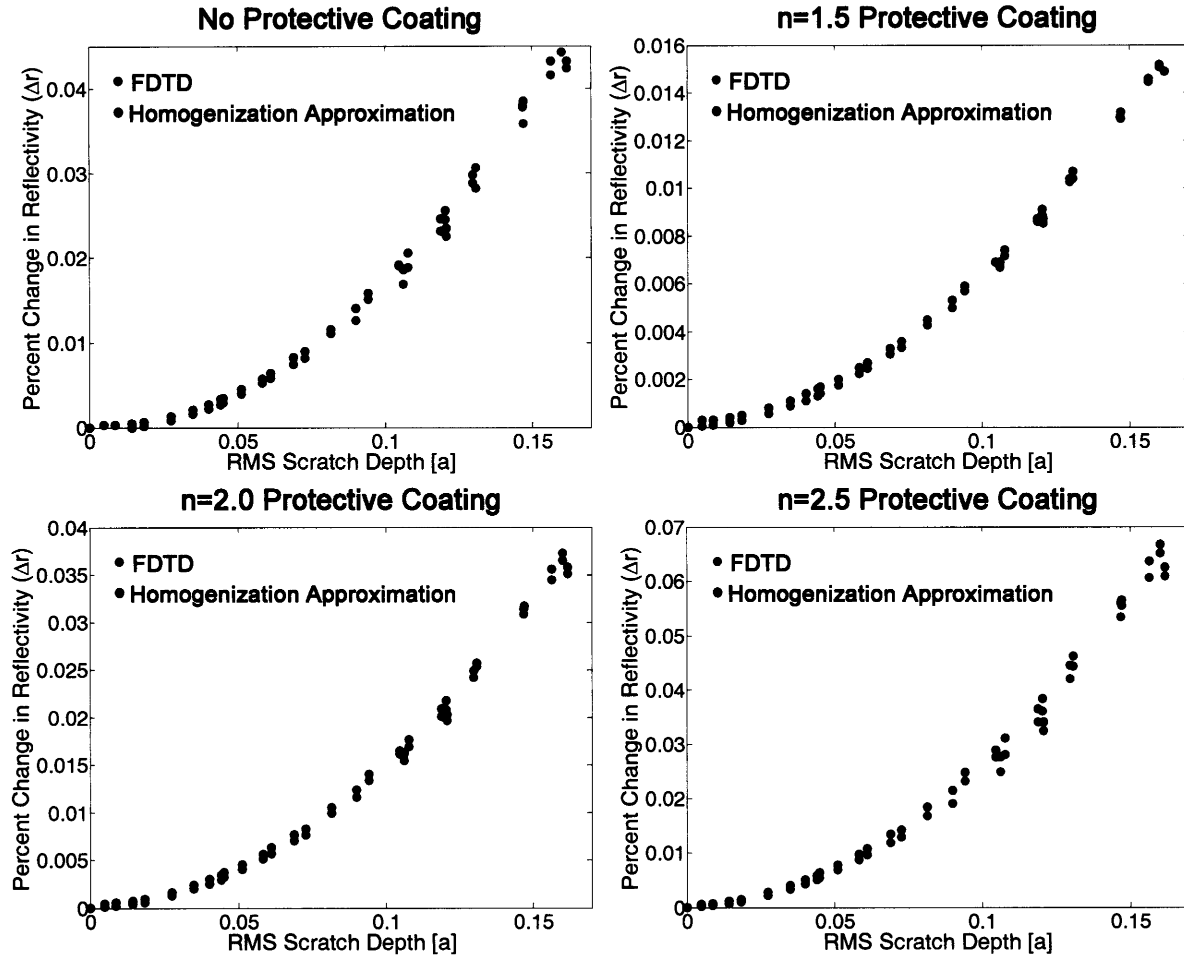

Figure 9.5 The results of the homogenization approximation for the 4-bilayer n_1=2.25, n_2=1.5 structures presented in Fig. 9.1. As with the other studies, the homogenization approximation correctly predicts the FDTD results for the scratched structures.

coatings corresponded to the resonant transmission thickness for the quarter-wave tuned wavelength of each structure. This was done in order to prevent the absolute reflectivity at the quarter-wave tuned wavelength from changing when coatings of different refractive indices were added to each structure.

The FDTD simulations revealed that the utility of the coatings is determined by the value of the coating's refractive index (n_c) relative to the refractive index of the top layer of the crystal (n_1). The addition of a protective coating with $n_c/n_1 < 1.0$ results in a structure that is more robust over the entire normal incidence bandgap than an uncoated structure. Furthermore, a lower value of n_c/n_1 always results in a structure that has a higher tolerance to surface scratches. On the other hand, a structure with $n_c/n_1 > 1.0$ is actually less tolerant to surface scratches than an uncoated structure. Additionally, a

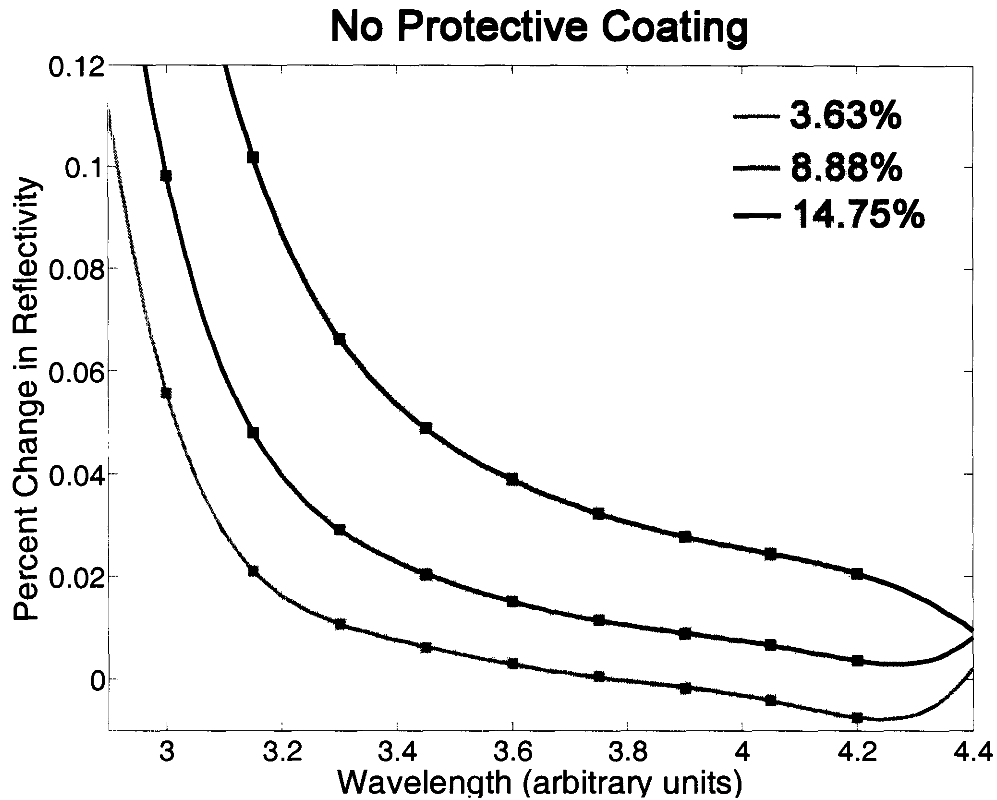

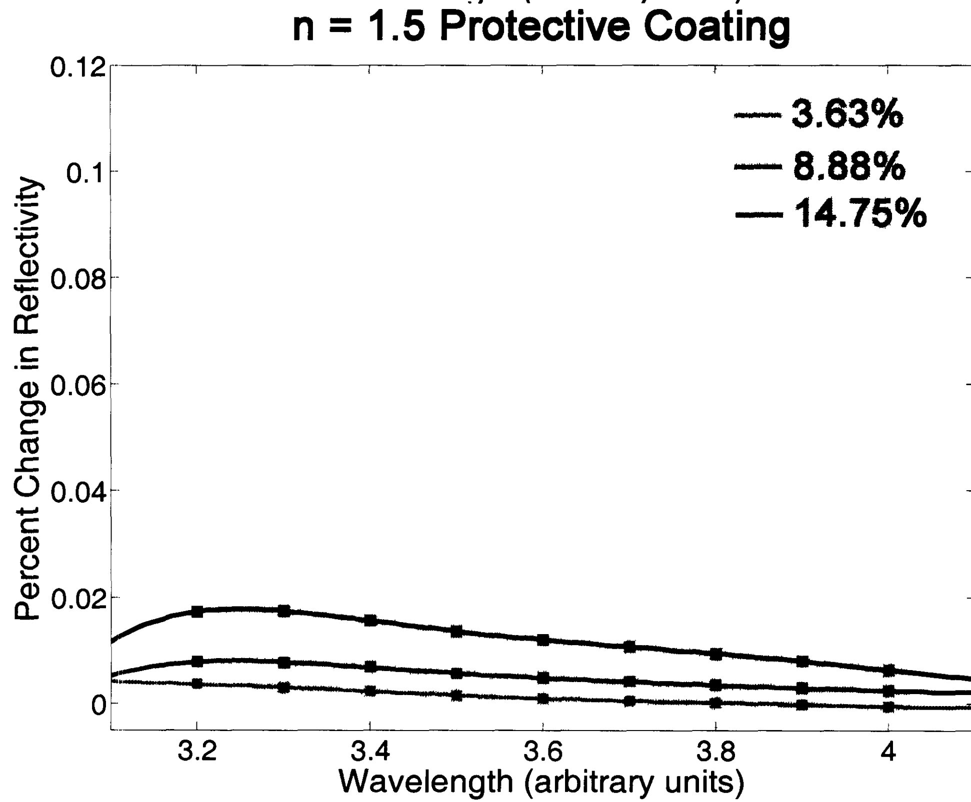

Figure 9.6 The homogenization approximation results for the 4-bilayer, n_1=2.25, n_2=1.5 systems across the entire normal incidence bandgap. The benefit of an $n_c/n_1 < 1.0$ coating is correctly predicted with the approximation.

structure with $n_c = n_1$ is slightly worse than an uncoated structure, revealing that it would not be beneficial to make a protective coating by simply increasing the thickness of the top layer.

The magnitude of the reflectivity change follows the trend seen in the previous studies of the interfacial roughness. Specifically, a higher index contrast structure will have a lower percent change in reflectivity due to scratches than a lower index contrast structure. Combined with the above results, this means that the effects of surface scratches can be minimized by using a high index contrast structure (preferably with a high average index so the top layer has a high refractive index value) with an $n_c/n_1 << 1.0$ protective coating.

Although the absolute reflectivity at the quarter-wave tuned wavelength does not change with the addition of a coating, the reflectivity at other wavelengths does. For an $n_c/n_1 < 1.0$ coating, the normal incidence bandgap narrows and does not reach zero at the edges. Nonetheless, the addition of the coating will increase the tolerance of the structure across the entire normal incidence bandgap. Therefore, if the device can allow for such bandgap alterations, it is beneficial to add the $n_c/n_1 < 1.0$ coating to the structure for increased device tolerance across the entire normal incidence bandgap.

As expected, the results of the homogenization approximation for these structures were in good agreement with the FDTD calculations. Thus, the homogenization approximation is valid for the range of RMS scratch depths tested here (up to about $0.17a$). However, unlike the interfacial roughness study, the scratch depths used in this study do not fully encompass the scratch depth values that could be found in real systems. Thus, more simulations should be done to determine when the homogenization approximation can no longer be applied accurately to these systems.

Up until now, all of the simulations done in this thesis have been used to explore the effect of structural imperfections on 1D photonic crystals. However, in the next chapter, the FDTD code will be used to explore structural imperfections in 2D photonic crystals. Specifically, the problem that will be investigated is acircular pores in 2D hexagonal photonic crystals, which is a very relevant issue in current research. The same analysis used to characterize the tolerance of a 1D photonic crystal to structural

imperfections will be used to characterize the tolerance of 2D photonic crystals. Thus, the full capability of the 2D FDTD code will be explored.

Chapter 10: Acircular Pores in 2D Photonic Crystals

As with 1D photonic crystals, the technologically useful properties of 2D photonic crystals are based on theoretical calculations performed on perfect structures. However, fabricated 2D photonic crystals can have a variety of imperfections. One such imperfection that is especially relevant to current research is acircular pores in 2D hexagonal photonic crystals. This particular imperfection is manifested in electrochemically fabricated 2D self-assembling systems, such as porous alumina, porous silicon, and porous indium phosphide. These systems are currently being researched for 2D photonic crystal applications because they can be fabricated on a large scale very quickly and cheaply due to their self-assembling nature.

Porous alumina is created by anodizing aluminum in a dilute acidic solution to create a porous oxide surface film [O'Sullivan (1970)]. The pores in the film form

cylindrical columns with axes oriented perpendicular to the plane of the film. Furthermore, under the right conditions, these pores will self-assemble into an ordered hexagonal structure. The periodic array of pores creates a photonic bandgap in the plane of the pores (i.e. in the plane of the film) [Nielsch (2002), Mikulskas (2001)]. The period and size of the pores scale linearly with the applied voltage, allowing one to tailor the structure to a desired central bandgap frequency. When the anodization conditions are carefully controlled, evenly spaced pores with almost perfect circular cross sections can be created. This is illustrated by the structure in the left micrograph in Fig. 10.1. However, poor control over the fabrication process can lead to porous arrays that are highly disordered. As shown in the right micrograph in Fig. 10.1, the pores in these structures can have cross-sections that deviate significantly from circularity. This particular structure was created on a large-scale manufacturing level by a company interested in using the porous alumina as a filter membrane rather than a photonic crystal [Whatman (2005)]. Therefore, they were not interested in maintaining careful control over the anodization process because they did not require the pores to form a periodic array without imperfections.

As mentioned in chapter 4, porous silicon is made by anodizing silicon in a hydrofluoric acid solution to create etched pores in its surface. As with the porous alumina, the porous silicon pores are cylindrical with axes oriented perpendicular to the surface of the silicon. Additionally, the pores self-assemble into a hexagonal array and their period and size can be controlled by the amount of current that is passed during the

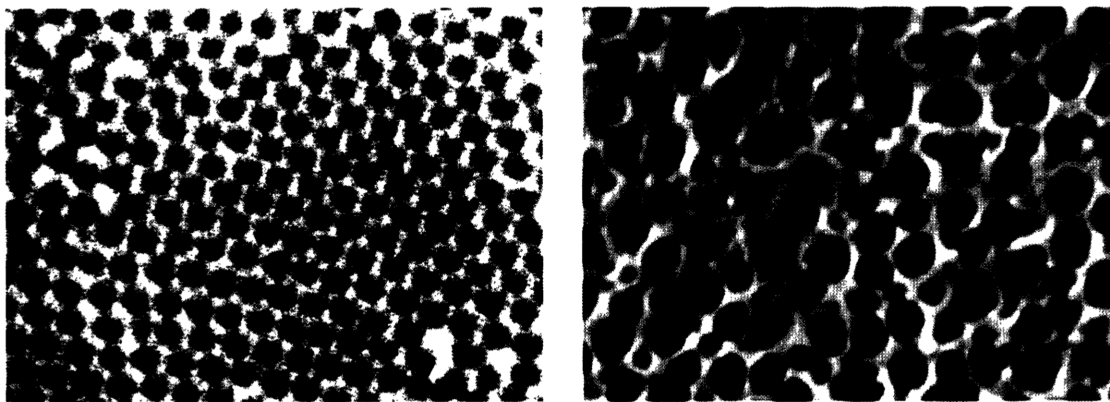

Figure 10.1 Two micrographs of porous alumina. The structure in the left micrograph was produced under controlled anodization conditions, while the structure on the right was fabricated with poor control over the anodization process.

anodization process. This makes porous silicon, like porous alumina, very desirable for 2D photonic crystal applications [Schilling (2001)]. However, poor control over the anodization conditions can again lead to acircular pores. Fig. 10.2 shows a micrograph of porous indium phosphide, which is made in a similar manner to porous silicon [Carstensen (2005), Christopherson (2005)]. Although this structure does not deviate from its ideal as much as the porous alumina in Fig. 10.1, some amount of porous acircularity is still evident in the structure.

The following chapter will present the results of several 2D FDTD simulations that were done to study the optical effect of porous acircularity in 2D photonic crystals. The specific systems that were investigated in this study correspond to the two systems mentioned above: porous alumina and porous silicon. Thus, the simulated 2D photonic crystal structures consisted of hexagonally arranged pores (refractive index n_p=1.0) in a higher index matrix (refractive index n_m). Furthermore, the arrangement of the lattice for all structures was such that the incident wave vector corresponded to the M-point in the irreducible Brillouin zone (see chapter 2). This is illustrated in Fig. 10.3. As detailed below, the incident wavelength and mean radius of the pores were chosen to correspond to the center of the bandgap of each structure. As with the 1D photonic crystal simulations, all structures in this study were free-standing crystals – the surrounding medium on both sides of the crystals is vacuum (dielectric constant 1.0). Again, both periodic and absorbing boundary conditions were used to simulate infinitely long structures that had a finite number of pore rows. The reflectivity of the structures was

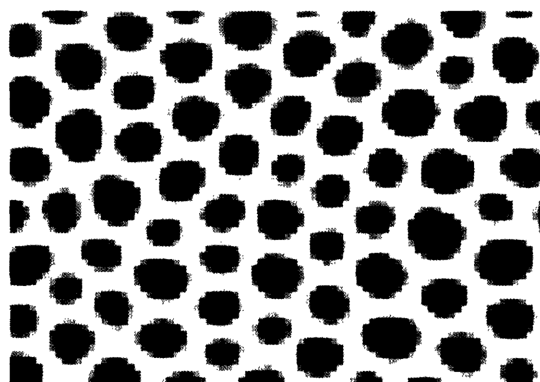

Figure 10.2 A micrograph of porous indium phosphide [Carstensen (2005), Christophersen (2005), reprinted with permission]. Although this structure does not deviate from its ideal as much as the porous alumina in Fig. 10.1, some amount of pore acircularity is still evident.

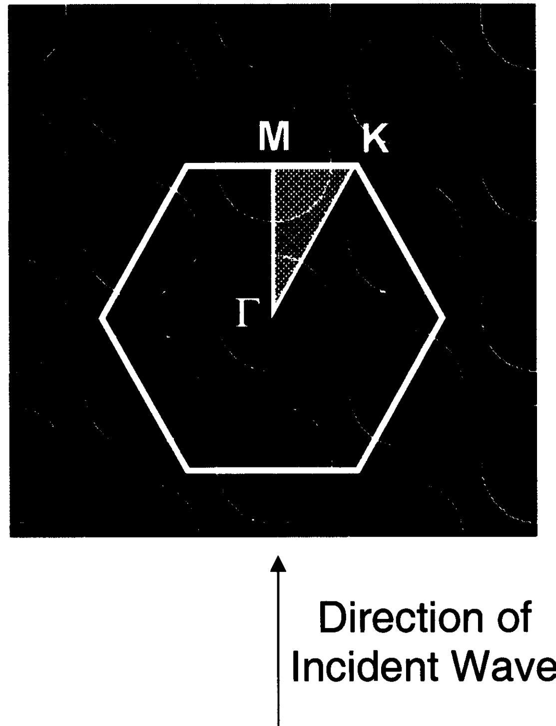

Figure 10.3 Schematic of the hexagonal lattice used in the simulations. The Brillouin zone, with the irreducible section shaded, is also shown superimposed on the lattice. The direction of the incident wave vector is coincident with the M-point of the irreducible Brillouin zone.

found using Eq. 4.9, and the corresponding percent change in reflectivity from the perfect structure was calculated with Eq. 4.10.

10.1 Determination of Simulation Conditions

Unlike 1D photonic crystals, the structural conditions that maximize the primary bandgap in 2D photonic crystals must be determined using simulation. Forunately, because this can be done using perfect infinite structures, a simulation technique that is much faster than FDTD can be used. The specific technique employed to establish the optimal 2D architecture for the systems tested here was the frequency domain method (see chapter 3). A freeware frequency domain code called MIT Photonic-Bands (MPB) was used to map out the primary bandgaps of porous alumina and porous silicon as a function of pore radius [Johnson (2001), Johnson (2005)]. These maps are shown in Fig. 10.4. Because alumina has such a low refractive index ($n \approx 1.7$), the porous alumina structure only has a complete gap for the TE polarization. However, porous silicon has a

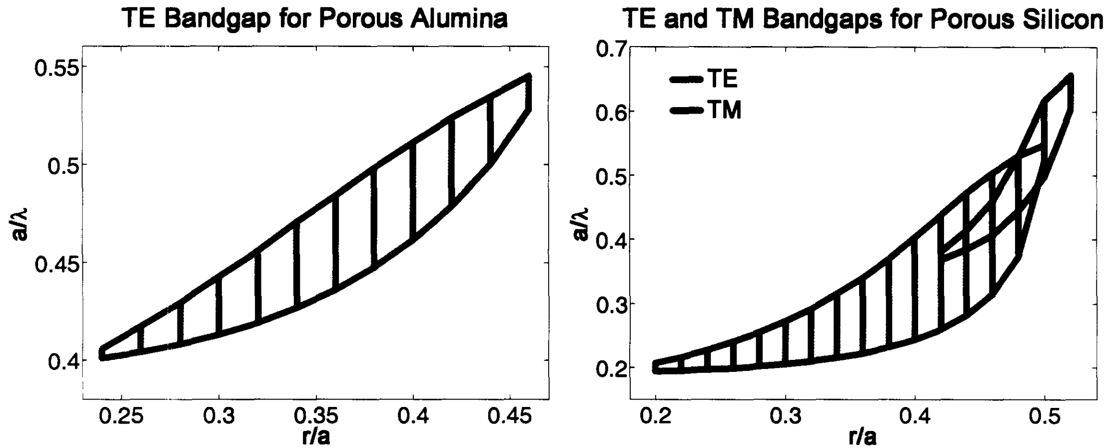

Figure 10.4 The TE bandgap in porous alumina, and the TE and TM bandgaps in porous silicon are shown as a function of the pore radius (r) normalized to the center-to-center distance between pores (a). These maps were calculated for the perfect structures using the MPB frequency domain code [Johnson (2001), Johnson (2005)].

large enough constituent refractive index ($n \approx 3.5$) that a bandgap for both the TE and TM polarizations opens up. Thus, in the region where these bandgaps overlap, a 2D omnidirectional bandgap exists.

The conditions used for the FDTD simulations were chosen to be close to the center of the maximized TE bandgap for the porous alumina, and the maximized omnidirectional bandgap for the porous silicon. This was done by resolving the radius where the bandgap had a maximum width, and then determining the wavelength that corresponded to the center of the bandgap at that optimal radius. For the porous alumina, this corresponded to a radius of $0.38a$ and a wavelength of $2.12a$ ($a/\lambda = 0.4725$), where a is the center-to-center distance between pores. For the porous silicon, the optimal radius was $0.48a$ and the corresponding wavelength was $2.05a$ ($a/\lambda = 0.4872$). Again, because all lengths used in the simulations were normalized to the characteristic periodicity of the crystal a, the results are scalable to any size structure.

10.2 Porous Acircularity Parameter

The imperfect 2D structures were characterized by their RMS acircularity, illustrated in Fig. 10.5. This is defined as the RMS radius of curvature deviation from the mean radius of the pore r_0:

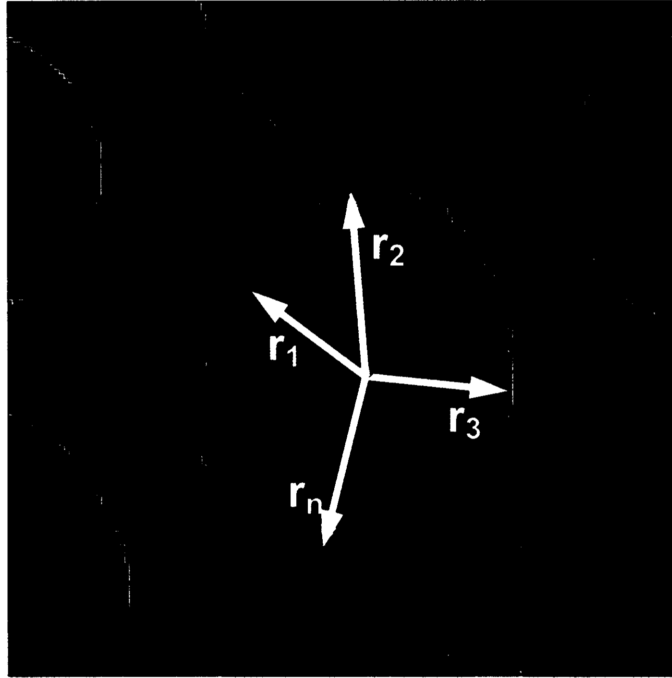

Figure 10.5 Schematic illustrating the range of curvature radii that characterize an acircular pore. The RMS acircularity (A_{RMS}) is defined as the RMS radius of curvature deviation from the mean radius of the pore r_0.

$$A_{RMS} = \left[\frac{1}{n_{circ}} \sum_{1}^{n_{circ}} \left(r_i / r_0 - 1 \right)^2 \right]^{1/2} . \tag{10.1}$$

Note that this definition causes the RMS acircularity to be given as a percentage of the mean radius of the pore rather than the periodicity of the crystal a. This was done so that the magnitude of the radial deviation was matched with the pore size. If the deviations were normalized to the periodicity of the crystals instead, then a given deviation would result in a much more severe change for small pores than for larger ones.

10.3 Generation of the Acircular Structures

The acircular structures were generated with a C++ code similar to the one used to generate the roughened structures in chapter 4. Again, the total number of nodes in the simulation domain (n_x), the index of refraction of the matrix material (all pores had n_p=1.0), as well as the number of rows and the number of columns of pores in the structure were given as input into the code. Note that the total number of columns had to

be odd in order to maintain the periodic boundary conditions. Unlike the 1D structure code, the number of nodes in the y direction (n_y) was constrained by the values of the above inputs. This is because the layout of the hexagonal lattice is required to have certain proportions: for a given pore, the nearest neighbor pores in all directions must be equidistant away. Thus, from the input values above, the number of nodes in the y direction is given by

$$n_y = \frac{n_x}{\sqrt{3}}\left(\frac{num_rows - 1}{num_columns - 1}\right). \tag{10.2}$$

This and the above input values were then used to calculate the center positions of the pores corresponding to a hexagonal lattice, shown in Fig. 10.6. For a pore in the ith column and jth row, the x coordinate of the pore center is given by

$$x_c^{i,j} = n_x\left(\frac{i - 1}{num_columns - 1}\right). \tag{10.3}$$

The y coordinate of the pore center is based on whether the corresponding column index of the pore is even or odd. For even columns, the y center position is

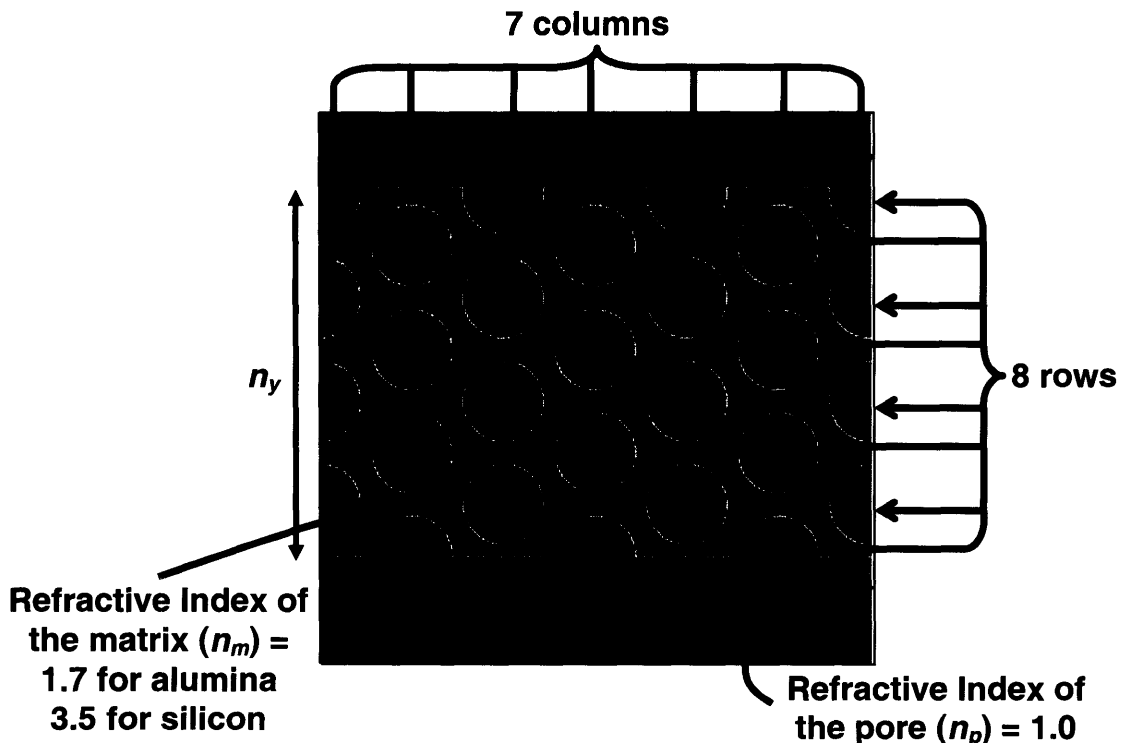

Figure 10.6 Schematic of the simulated hexagonal lattice illustrating the relevant parameters.

$$y_{c,o}^{i,j} = n_y \left(\frac{j-1}{num_rows - 1} \right), \tag{10.4}$$

while for odd columns, the y center position needs to include an offset to create a hexagonal lattice rather than a square lattice:

$$y_{c,e}^{i,j} = n_y \left(\frac{j-2}{num_rows - 1} \right) + \frac{n_y}{num_rows - 1}. \tag{10.5}$$

Values for the mean radius of the structure r_0, corresponding to the optimal radius from the frequency domain calculation, and the maximum allowable deviation of the radius were also given as inputs. These values were converted from percentages of a to number of nodes, using the calculated value of a:

$$a = \frac{2n_y}{num_rows - 1}. \tag{10.6}$$

Each pore in the simulation was assigned a value for its particular mean radius based on the above input values. This was done in order to get a range of pore sizes around the mean pore size for the structure. Each pore's mean radius was found by multiplying a Gaussian deviate times the maximum radial displacement, and subsequently adding that value to the structure's mean radius. Gaussian deviate values greater than three standard deviations away from the center were thrown out in order to avoid outliers.

After each pore's particular mean radius was determined, the pores were made acircular by generating a list of radial deviation values for each pore. The members in each list corresponded to the nodes on the circumference of each pore. Since the radius of each pore needed to vary smoothly, Gaussian functions were used to determine the radial deviation along each pore's circumference. Between three and seven Gaussian functions, centered at random positions within the lists, were chosen for each pore. A random number between plus and minus half the maximum radial deviation was chosen for the height of each Gaussian. The standard deviation was determined by a random number between 5% and 10% of the total pore circumference. These values were used because they produced structures that best represented the actual imperfect structures (Figs. 10.1 and 10.2).

The list of radial deviations was used to offset the mean radius of each pore. This was done by simply adding the mean radius of each pore to the values in the corresponding deviation list, resulting in a list of the total radii of curvature for each pore. The value of the structure's mean radius was then subtracted from all of the values in these lists, creating a list of the radii differences from the mean. The values in this difference list were then summed. If the summed value was not equal to zero, then the structure's mean radius was no longer the input value. In order to remedy this, one nodal displacement was added or subtracted from each value in the total radii lists until the summed differences were zero.

The total radii lists were then used to write the pores into a 2D array that held the index of refraction information of the structure. This array was initially filled with the index of refraction of the matrix material. The center of each pore in the array, which is given by the calculated positions above, was located. The index of refraction of the pores (1.0) was then written into the array at each angle around the circumference, from the pore center out to the value of the radius in the total radius list. Buffer layers with refractive index values of 1.0 (corresponding to air or vacuum) were written into the array above and below the structure as well.

The RMS acircularity was then calculated from the difference between the radii lists and the mean radius of the structure using Eq. 10.1. The refractive index array was written to an output file, which was then used as an input into the FDTD code. The nodal magnitude of the incident wave was also input into the FDTD simulation. This was calculated by combining Eq. 10.6 with the optimal wavelength found from the frequency domain calculation.

10.4 Simulation Equilibration

The FDTD code for the 1D calculations in chapter 4 was verified by comparing the reflectivity results of a perfect structure with a 1D transfer matrix calculation of the same structure. Unfortunately, the same method can not be used to verify the results of these simulations. This is because there is no other independent computational technique that provides reflectance information for 2D finite structures. The frequency domain code used above only provides information on the frequency position of the eigenmodes

for an infinite structure. However, because the same FDTD code has been shown to be accurate for the 1D structures, it is reasonable to assume that it will also be accurate for 2D structures. Moreover, the code can be further verified by checking that it reaches an equilibrium value after a certain number of time steps. This will also determine the amount of time the code needs to run before the reflectivity can be accurately calculated with Eq. 4.9.

The results of this equilibration run for both the 8 row and 12 rows structures tested are shown in Fig. 10.7. In both cases, the calculated reflectivity does reach a steady state value after about 20,000 simulation steps. Because of this, the total number of simulation steps used for both systems was 25,000 steps. The pink region in Fig. 10.7 represents the simulation steps over which the time-averaging was done for Eq. 4.9. This corresponds to an averaging of 16 full cycles of the reflected wave.

10.5 Porous Alumina Reflectivity Results

A total of 60 FDTD simulations were run to determine the percent change in reflectivity due to acircularity in the porous alumina system. The reflectivity change, calculated with Eq. 4.10, from structures with both 8 and 12 rows of pores is shown in Fig. 10.8. The plot also shows example structures corresponding to the most extreme structural deviations tested in this study. As detailed above, these simulations were run at the optimal conditions determined with the frequency domain calculations of the perfect infinite structure. For porous alumina, the optimal conditions were established to be: r_0/a=0.38, a/λ=0.4725. Only the TE polarization was tested because porous alumina only displays a bandgap for that polarization.

Again, the simulation results reveal that there is a strong dependence of the percent change in reflectivity on the structural deviation parameter, A_{RMS} in this case. The reflectivity change reaches almost 50% for the 8 row structure at an RMS acircularity of $0.22r_0$. Furthermore, the curve shape appears to be linear with an x-intercept offset corresponding to the number of rows in the structure. As with the 1D simulations, this study reveals that a larger number of periods in the structure (i.e. a larger number of rows) will make it more robust to structural deviations. These complementary

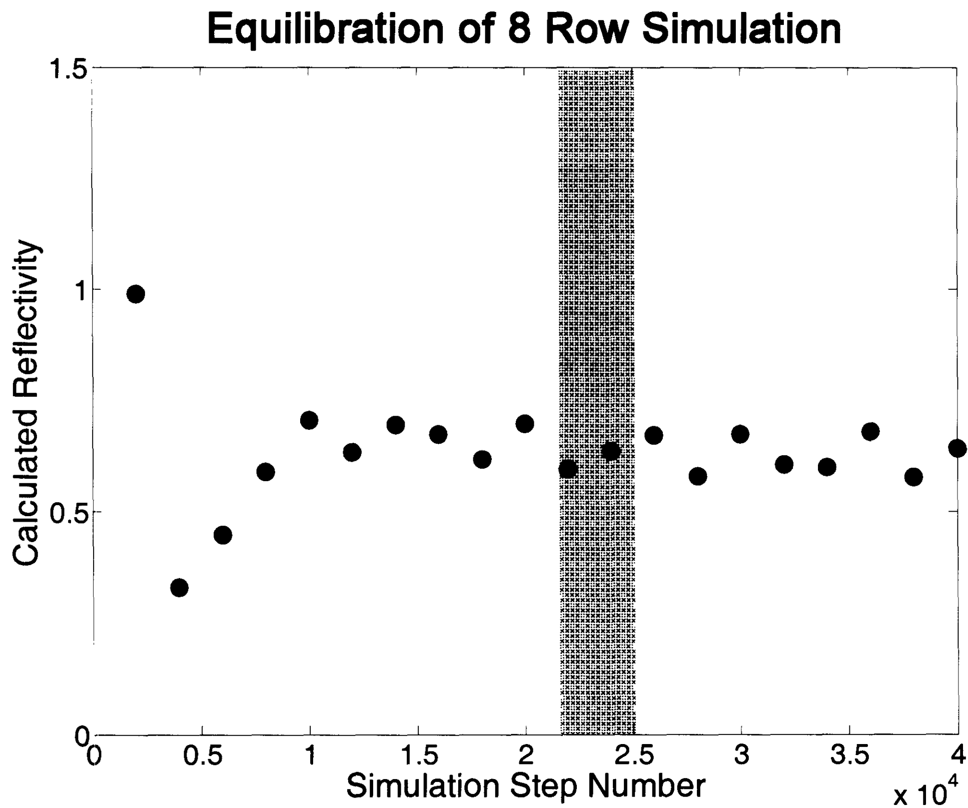

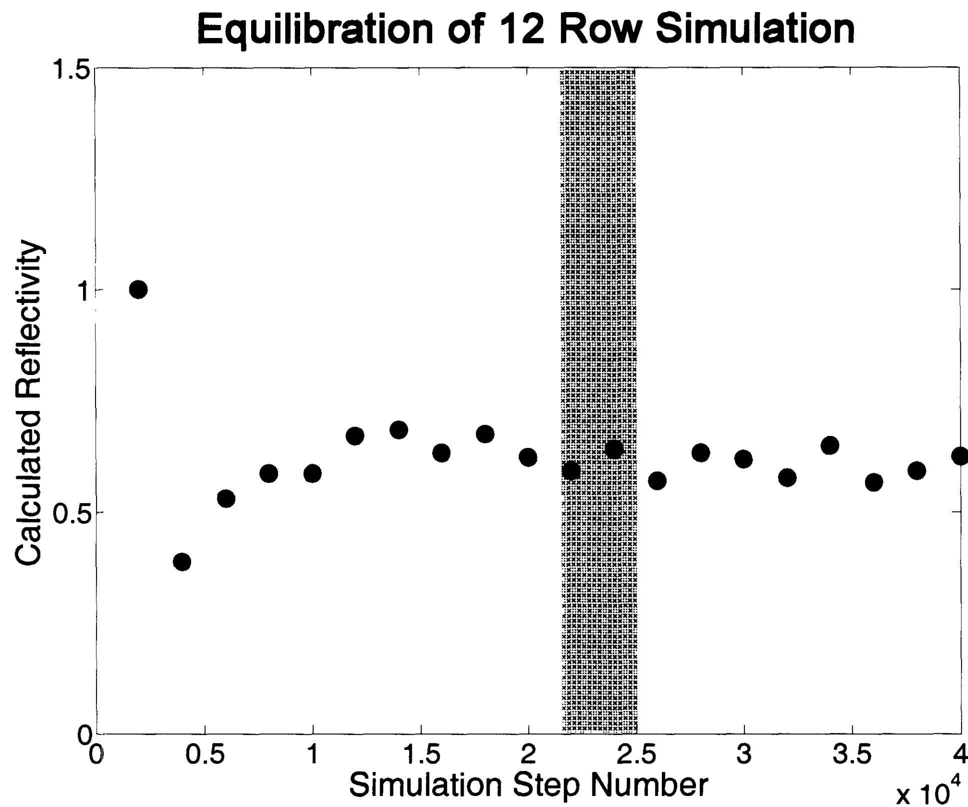

Figure 10.7 Results of the equilibration run for both the 8 row and 12 row structures. The initial large transient behavior is gone by about the 20,000th step in both cases. The shaded region indicated the time steps over which the time-averaging was done in the reflectivity calculation.

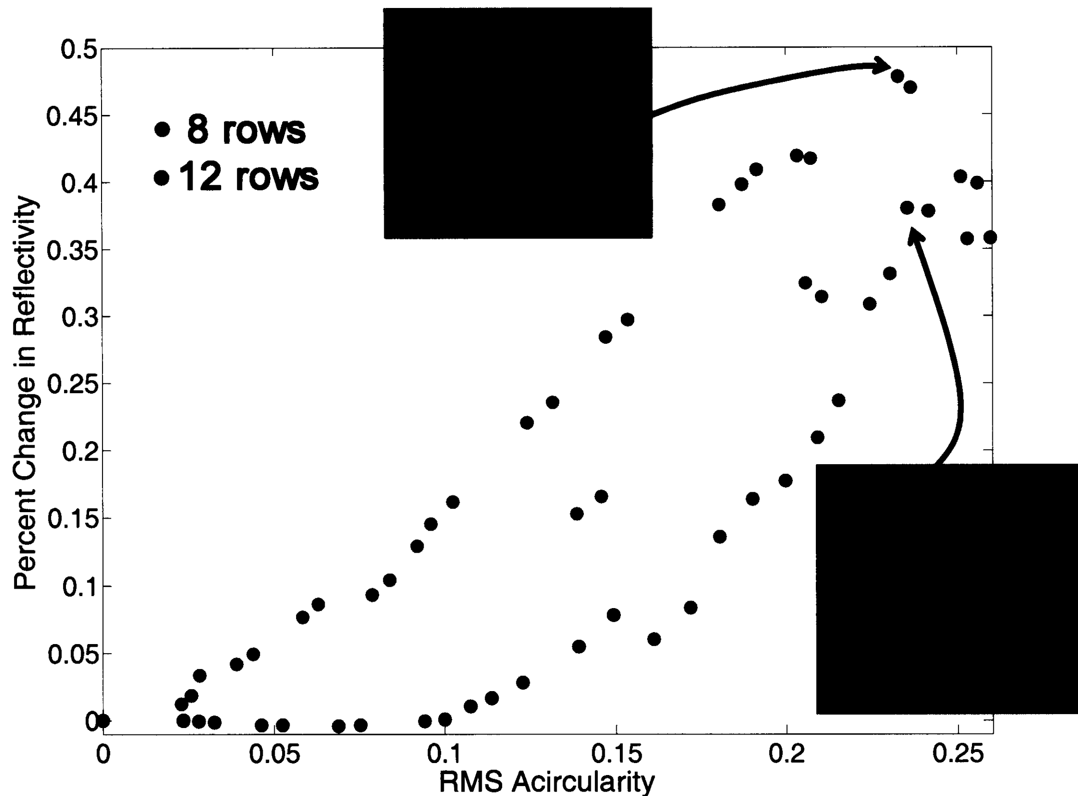

Figure 10.8 The percent change in the TE polarized reflectivity (Δr) for 8 and 12 row structures of porous alumina. Also shown are two example structures corresponding to the most extreme structural deviations tested in this study.

results suggest that this may be a general trend that can also be applied to structures with many other types of structural imperfections.

10.6 Porous Silicon Reflectivity Results

Equivalent FDTD simulations were run on the porous silicon system. This time, both the TE and TM polarizations were simulated due to the presence of an omnidirectional bandgap in this system. The reflectivity results of these 120 simulations are shown in Figs. 10.9 and 10.10, along with several example structures corresponding to specific simulation points on the plots. Again, the simulation conditions used here were determined by the frequency domain calculations of the perfect infinite structure. These were established to be: r_0/a=0.48, a/λ=0.4872.

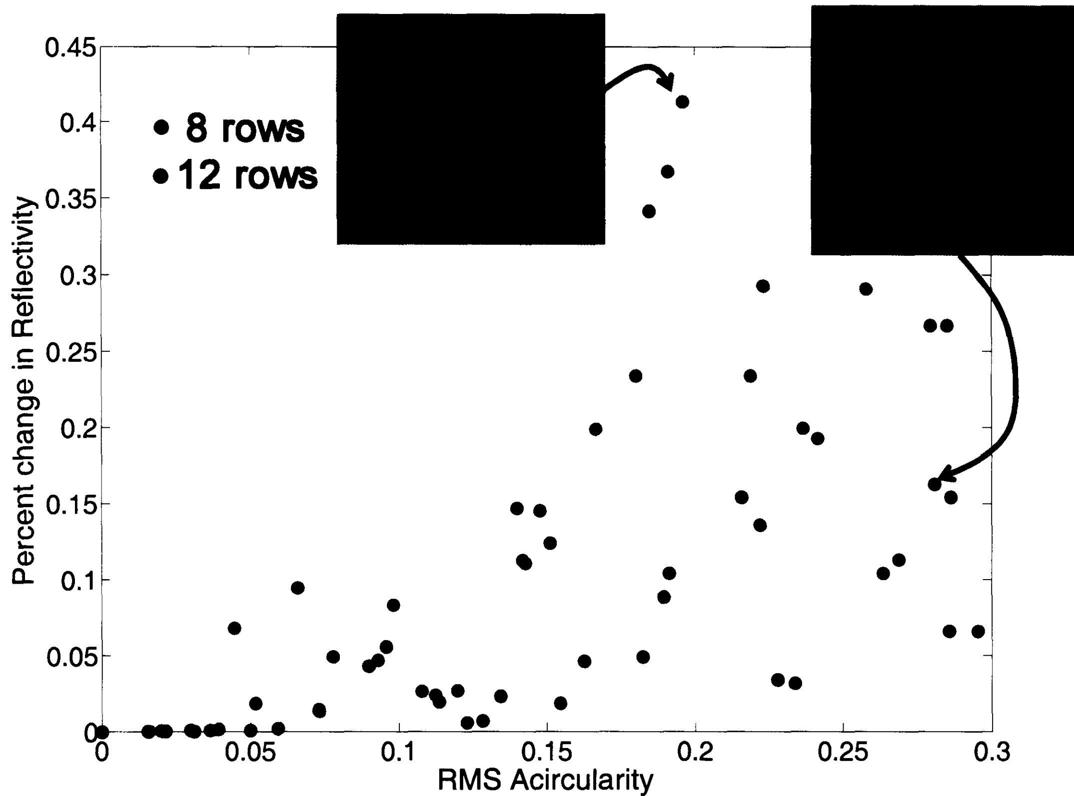

Figure 10.9 The percent change in the TM polarized reflectivity (Δr) for 8 and 12 row structures of porous silicon. Again, two example structures are shown that corresponding to the most extreme structural deviations tested in this study. The architectural deviations in these structures are much more severe than those in the porous alumina study.

Unlike the porous alumina system, the results from these calculations are very sporadic after an A_{RMS} value around $0.05r_0$. The reason for this is clear once the morphology of these particular deviate structures is explored. The r_0/a value of these structures is quite high: 0.48. At an r_0/a value of 0.5, the pores will begin to touch and overlap each other. Therefore, the perfect structure in this system has pores that are already very close to overlapping. So a small deviation in the radius is all that is needed to produce a structure that has a significant amount of overlapping pores. The A_{RMS} value at which this would occur can be approximated by calculating the RMS deviation that would cause the pores to touch:

$$A_{RMS}^{c} = \frac{0.5 - r_0/a}{r_0/a}. \tag{10.7}$$

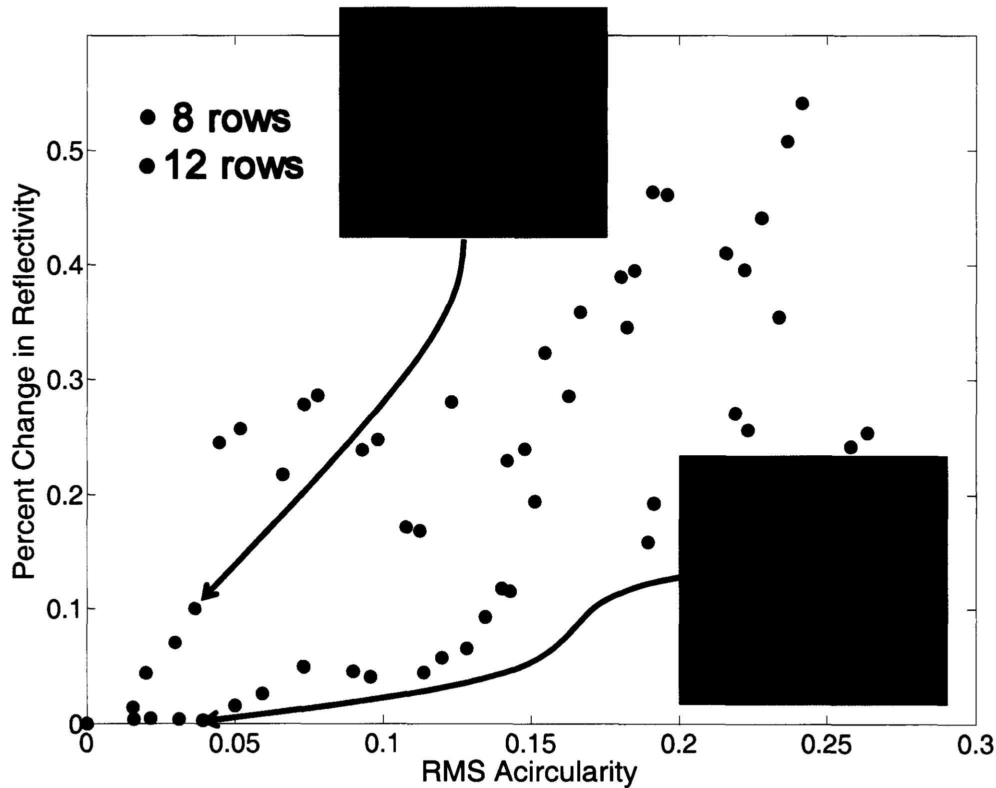

Figure 10.10 The percent change in the TE polarized reflectivity (Δr) for 8 and 12 row structures of porous silicon. Two example structures with much lower A_{RMS} values are shown for comparison with those in Figs. 10.8 and 10.9.

For the porous alumina structure, this critical RMS acircularity value is 0.32. However, for the porous silicon system, the value becomes only 0.04. The consequence of this difference can be clearly seen through comparison of the example structures in Figs. 10.8, and 10.9 and 10.10. After the pores begin to significantly overlap eachother, the morphology of the structure itself drastically changes. The structure transitions from being a series of pores in a matrix to a mix of pores and discrete misshapen rods in air. The remaining structure is made up of the negative spaces left behind in between the overlapping pores. Furthermore, once the pores begin to overlap, the measure of acircularity in Eq. 10.1 no longer accurately characterizes the structure.

Therefore, in order to get meaningful results for the porous silicon system, another series of calculations was done focusing on the A_{RMS} region below $0.04r_0$. The results of these calculations, along with some corresponding structures, are shown in Figs. 10.11 and 10.12. These results are clearly much better behaved than the results in

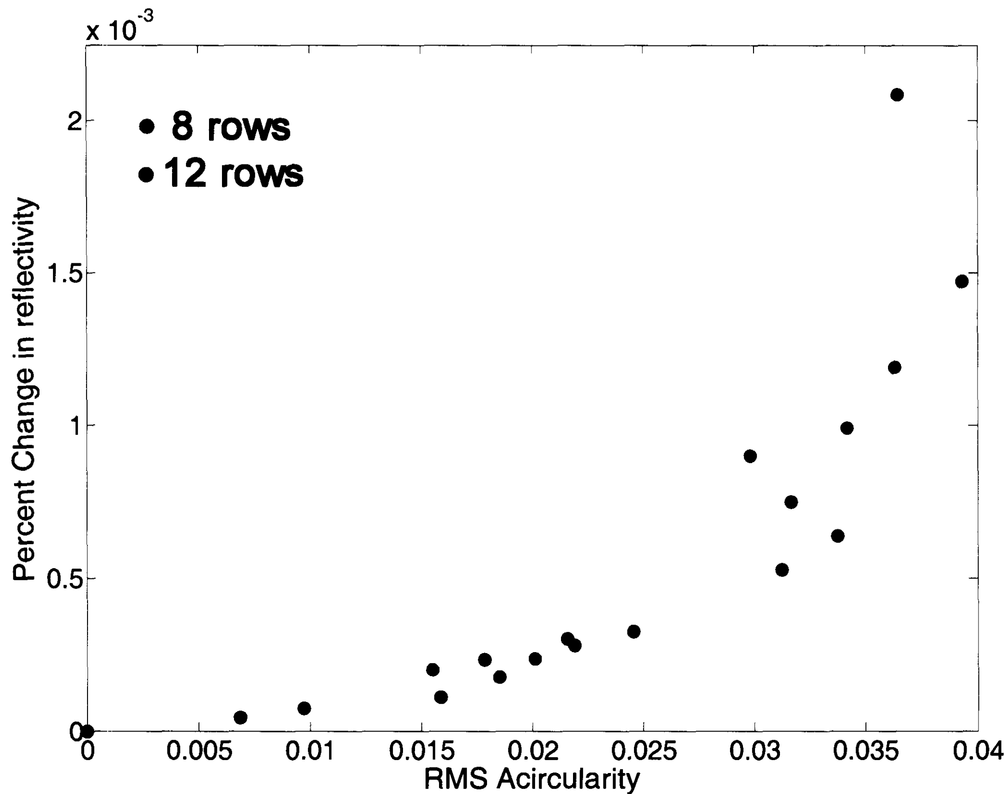

Figure 10.11 The percent change in the TM polarized reflectivity from the porous silicon system for A_{RMS} values less than $0.04r_0$.

Figs. 10.9 and 10.10. Furthermore, these calculations reveal that there is a distinct difference between the TE and TM polarization behavior. The TE polarization shows the same trend in the number of rows that the porous alumina calculations revealed: more rows produce a more robust structure. However, no such trend is seen with the TM polarization results. Furthermore, the magnitude of the reflectivity change in the 8 row structure is much smaller for the TM polarization than for the TE polarization.

Although these results may seem puzzling, they can be explained with one simple concept that was actually concluded from the results in chapter 5. For the 8 row structure, the magnitude of the absolute reflectivity for the TM polarization is larger than the absolute reflectivity for the TE polarization. Thus, the results above are consistent with the idea that the magnitude of the absolute reflectivity of a photonic crystal system is an indication of how tolerant it will be to structural changes. Thus, any modification to the structure that will increase the absolute reflectivity of the perfect analogue (i.e. increasing the index contrast, increasing the number of periods, etc.) will correspondingly

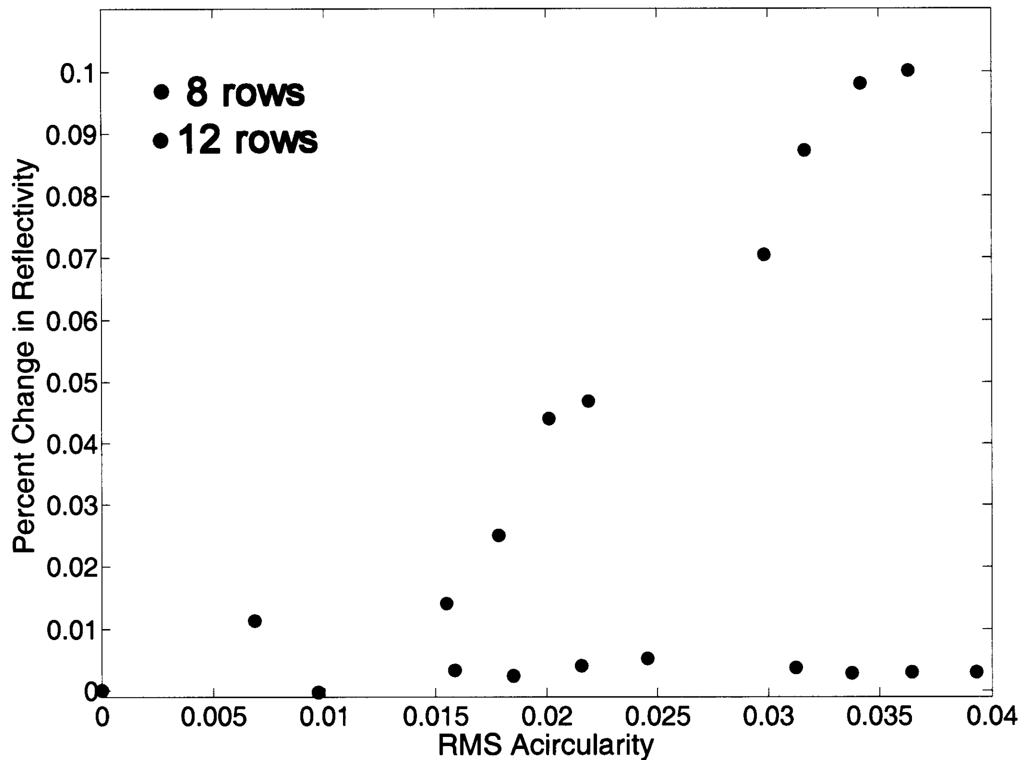

Figure 10.12 The percent change in the TE polarized reflectivity from the porous silicon system for A_{RMS} values less than $0.04r_0$.

increase the structure's tolerance to structural imperfections. This conclusion is supported by all of the results presented in this thesis.

10.7 Conclusions

Several 2D FDTD simulations were done to investigate the effect of acircular pores on the reflectivity of 2D hexagonal photonic crystals. Two specific systems were examined: porous alumina and porous silicon. The exact simulation conditions used for these systems were chosen to be near the center of the maximized photonic bandgap of the corresponding perfect infinite structures. These conditions were determined through frequency domain calculations using the MPB freeware code [Johnson (2001), Johsnon (2005)]. Like the 1D results presented in chapter 4, the porous alumina simulations revealed that a larger number of periods in the structure made it more tolerant to structural imperfections.

However, the equivalent simulations for the porous silicon produced sporadic results. This is because the mean radius that was used in the simulations corresponded to a structure where the pores were very close to overlapping, even in the perfect structure. Thus, just a small radial deviation ($>0.04r_0$) caused significant overlap of the pores and correspondingly resulted in a critical morphological shift of the structure. More simulations were done to focus on smaller radial deviations that would avoid this severe morphological change. The results of these simulations were much better behaved, revealing clear trends in the data. Like the porous alumina results, the porous silicon TE polarization simulations showed an increase in robustness for a structure with more pore rows. However, the TM polarization results did not show any difference between the 8 row and 12 row structures. Furthermore, the reflectivity change for the TE polarization was much larger than for the TM polarization in the 8 row structure. However, there is one important difference between the TE and TM reflectivities of the perfect 8 row porous silicon structure. The magnitude of the reflectivity is lower for TE polarized light than for TM polarized light.

Thus, the trends seen in this chapter are consistent with the trends from all the previous chapters. The absolute reflectivity of the perfect representation of a structure is an indication of how tolerant the structure will be to structural imperfection. Therefore, any change that is made to the structure that would increase the absolute reflectivity of the perfect analogue would correspondingly make the structure more tolerant to imperfections. This conclusion is supported by all of the results presented in this thesis.

Chapter 11: Experimental Corroboration

A quick review of the literature reveals that there are many researchers currently working on 1D photonic crystal systems with rough interfaces. For example, a search of the words “porous”, “silicon”, and “1D” produces 34 results between the years 2000 and 2005. Granted, not all of these publications pertain to 1D photonic crystals. However, this still reveals the amount of research currently probing just porous silicon’s potential as a 1D photonic crystal technology.

The results of these and other articles from assorted other search queries (see Table 11.1) were extensively scrutinized. Unfortunately, for various reasons, no article was found that could be used to quantitatively compare the results of actual experiments to the computational findings in this thesis. Often, the RMS roughness of the structure would not be reported, and therefore the roughness would have to be ascertained from

Table 11.1 Relevant results of various literature searches for rough 1D photonic crystals.

Search: "porous" "silicon" "1D", 2000-2005 → 34 results	
Golovan, et al. (2000)	No micrograph.
Reece, et al. (2004)	Does not report the absolute index values.
Haurylau, et al. (2004)	Does not provide the absolute index values, only index contrast.
Ghulinyan, et al. (2003)	Shows a poor and incomplete micrograph.
Agarwal, et al. (2003)	Never gives exact structure.
Golovan, et al. (2004)	Does not show structures or reflectance spectra.
Search: "porous" "silicon" "photonic", 2000-2005 → 34 results	
Reece, et al. (2002)	Very poor image of crystal (unusable).
Weiss, et al. (2005)	Gives an incomplete micrograph.
Xu, et al. (2003)	Gives reflectance and transmittance in arbitrary units, no micrographs.
Ohno, et al. (2001)	Does not show any measured reflectivity.
Dolgova, et al. (2001)	No micrographs.
Oton, et al. (2003)	No micrographs.
Nava, et al. (2003)	No micrographs.
Meade, et al. (2004)	Reflectivities are relative, no micrographs.
Kordas, et al. (2004)	Gives incomplete micrograph.
Jain, et al. (2001)	No relevant data or micrographs.
Petrov, et al. (2003)	No micrographs.
Crisan, et al. (2002)	No reflectance spectra.
Search: "porous" "silicon" "photonic", 1995-1999 → 15 results	
Setzu, et al. (1998)	No micrograph.
Pavesi (1996)	No micrographs.
Search: Amra (1994) citings → 45 results	
Gatto, et al. (2002)	Provides an incomplete micrograph, does not give the refractive index values.
Xiong, et al. (1997)	Never gives reflectance spectra or roughness.
Amra (1994)	Never gives roughness.
Amra, et al. (1997)	Never gives roughness or micrograph.
Ruppe, et al. (1996)	No reflectivity data given.
Lysenko, et al. (2001)	No reflectivity data given.
Ferre-Borrull, et al. (2000)	Actually measured amount of scattering from quarter-wave stack - got about 8×10^{-4} for about $0.02a$ RMS roughness.
Jokobs, et al. (1998)	Reports scattering of about 10^{-3} for a quarter-wave stack with 24 bilayers with a RMS roughness of about $0.015a$.

any micrographs provided in the publication. This could be done by converting the micrograph into a refractive index file using a simple Matlab script. This refractive index file would represent the exact microstructure in the micrograph. Thus, it would be equivalent to the refractive index output files representing the roughened structures used in the FDTD simulations (see chapter 4). Since the homogenization approximation was shown to give the same results as the FDTD simulations (see chapter 6), this approximation could also be applied to the refractive index file from the micrographs to calculate their alleged reflectivity.

Out of the publications that provided micrographs of their structures, all of the images were either very poor quality or incomplete (did not show the entire structure), as indicated in Table 11.1. Although this latter issue could be accommodated for simple multilayer structures, the structures involved in these studies were often complicated, containing defect cavities or multiple periodicities. Thus, another means of experimentally corroborating the predictions in this thesis had to be found.

11.1 Calculated Reflectance Spectra for Two Rough Structures

I contacted Vincent Kuei-Sen Hsiao at the University of Buffalo, who works on tunable photonic crystals through liquid crystal incorporation. These structures are known to have extremely rough interfaces (See Fig. 4.1). He provided me with a full micrograph of one of his structures, shown in Fig. 11.1, along with its reflectance spectrum, shown in Fig. 11.2.

This micrograph was converted into a refractive index file in the manner mentioned above. This was done using the Matlab function `imread`, which converts a

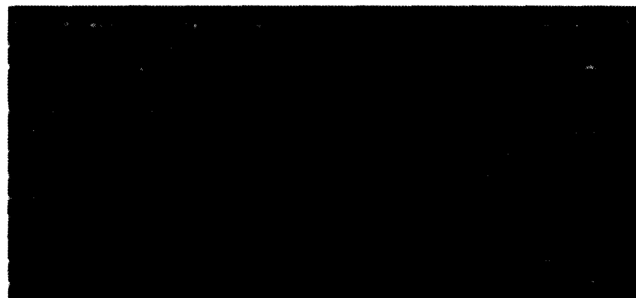

Figure 11.1 One of the "real-world" roughened structures analyzed with the homogenization approximation [Hsiao (2005), reprinted with permission].

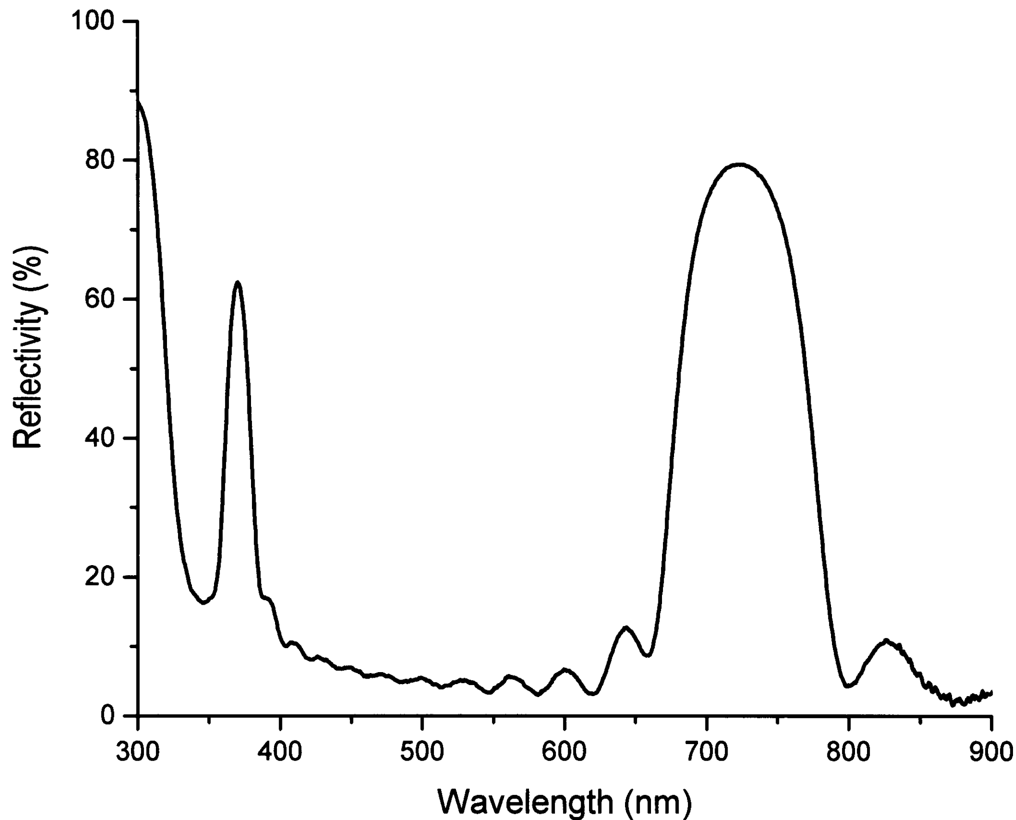

Figure 11.2 Experimental reflectance spectrum for the structure shown in Fig. 11.1 [Hsiao (2005), reprinted with permission].

black and white image into an array. The number of array entries is equal to the number of pixels in the images. The members of the array each have a value between 0 and 256 corresponding to the shade of gray of the equivalent image pixel. Thus, for an image of a multilayer structure, this array can then be converted into refractive index information by changing all the "white" entries (> 128) to one constituent index and all the "black" entries (< 128) to the other constituent index. Once the refractive index array for the micrograph was determined, the averaged index profile for the structure (see chapter 6) was obtained for use in the homogenization approximation calculations.

Unfortunately, the exact value of the low refractive index in this specific structure was unknown. This is because the low index layers were composed of a mixture of air pores and polymer (n~1.52). The low index value was selected to align the calculated reflectivity peak with the experimental one. Due to inaccurate measurements of the layer

thickness, the periodicity of the structure (in pixel units) was obtained by taking the Fast Fourier Transform of the average index profile. The periodicity was combined with the refractive index information to scale the reflectivity results of the homogenization approximation from wavelength units of pixels to nanometers for comparison with the experimental reflectance spectrum. Fig. 11.3 shows the results of these calculations for the structure presented in Fig.11.1. Comparison with Fig. 11.2 reveals a favorable match between the homogenization approximation results and the experimental results. The increase in reflectivity on the far right of the plot in Fig. 11.2 is most likely due to the fact that those wavelengths are near the edge of the spectrometer's spectral range. Therefore, this feature is not reproduced in Fig. 11.3. Furthermore, the calculated secondary reflectance peak around 360nm is too high compared to the same peak in the experimental data. This is again most likely due to the proximity of this peak to the edge of the spectrometer's viable range.

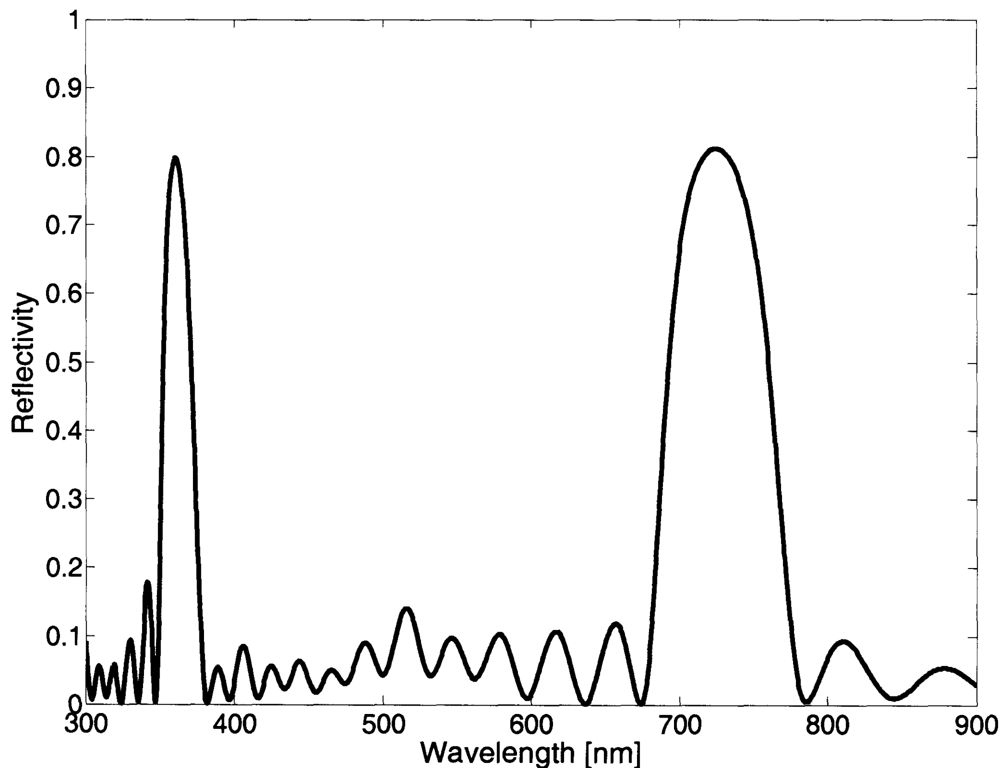

Figure 11.3 Results of the homogenization approximation applied to the structure shown in Fig. 11.1.

A comparison of the absolute values of the calculated and experimental reflectivities is difficult due to variations in experimental conditions. For example, the experimental reflectivity depends on the quality of the reflectivity reference that is used. Absolute reflectance measurements can avoid this complication, but require a complex experimental setup, which was not used by the Buffalo group. However, the favorable correspondance of the shape of the reflectivity peak is significant, because it depends on the specific microstructure of the photonic crystal.

In addition to the micrograph shown in Fig. 11.1, K. Hsiao also provided the micrograph of another structure, shown in Fig. 11.4, along with its corresponding reflectance spectrum, shown in Fig. 11.5. This structure corresponds to a three-color filter. Thus, its architecture consists of three distinct periodicities to produce bandgaps at three different wavelengths. Although this is clear from the reflectance spectrum, the different periodicities are not apparent to the eye in the micrograph. Also, it is clear in the micrograph that the roughness in this structure is large because individual layers are discontinuous.

The same procedure as that described above was also applied to this structure. These results are shown in Fig. 11.6. Again, the calculated peak shapes match the experimental ones well, except for the left-most peak. This peak has a broader width, which is probably due to the sampling area from the micrograph. The left-most

Figure 11.4 The second roughened structure analyzed with the homogenization approximation [Hsiao (2005), reprinted with permission]. Although it is not apparent to the eye, there are three periodicities built into the structure.

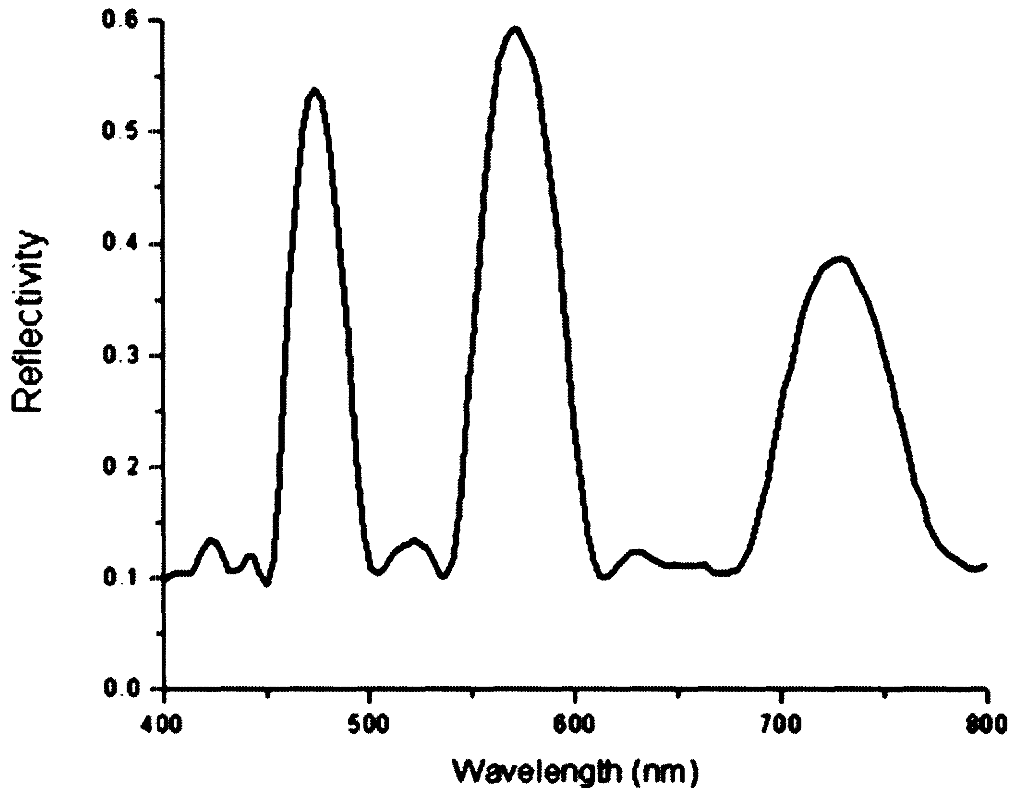

Figure 11.5 Experimental reflectance spectrum for the structure shown in Fig. 11.4 [Hsiao (2005), reprinted with permission]. Notice the three distinct reflectivity peaks.

peak corresponds to the longest periodicity in the microstructure. Thus, more sampling area is required to accurately represent this periodicity. In addition to the comparable peak shapes, the relative magnitudes of the peaks also approximate the experimental data. Furthermore, despite the complexity of the structure, the results of homogenization theory applied to a single micrograph of this structure correspond extremely well in reproducing relative peak positions. This again supports the applicability of homogenization theory to roughened photonic crystals.

11.2 Proposed Experiments

Although the above calculations support the validity of the predictions presented in this thesis, further confirmation of the predicted absolute reflectivity and scattered powers requires more specially designed experiments. The preparation, measurements, and analysis required in these experiments are detailed below.

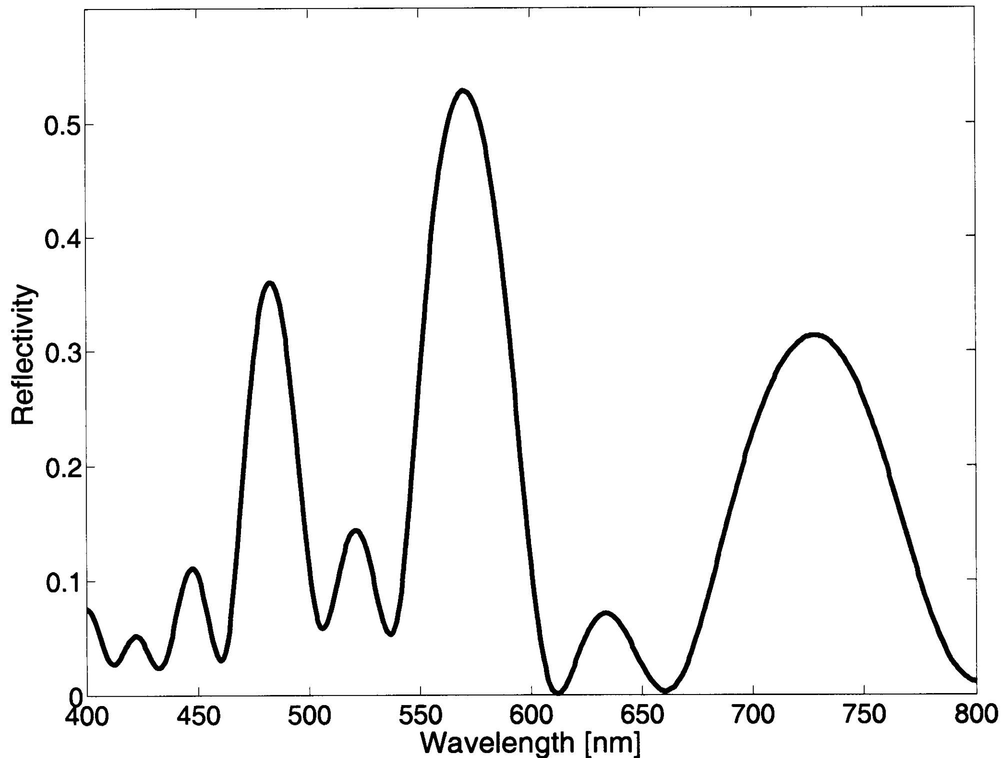

Figure 11.6 Results of the homogenization approximation applied to the structure shown in Fig. 11.4. Again, note the three distinct reflectivity peaks.

Produce a structure with rough interfaces. While many approaches are available to produce photonic crystals, a large roughness is desired to confirm the theoretical predicitions. Such a structure can be obtained in a variety of ways:

1. 3D Printing: Ideally, one would want to control the roughness scale and architecture of the structures. 3D printing allows one to design a structure on computer and then "print" it out layer by layer [Arptech (2005)]. This could not be used for photonic crystals that are tuned to the visible or even infrared regime because the resolution of a single layer is about 0.3mm. However, rough terahertz or microwave structures may be able to be produced using this technique. The materials that are compatible with 3D printing are limited and their optical properties are not well known in this wavelength regime. Therefore, this option requires extensive experimental investigation before a viable rough structure could even be made.

2. Precision machining (CNC milling): Computer controlled mills are able to produce features on surfaces as small as 10μm [Denford (2005)]. Therefore, one could use this technique to create a roughened quarter-wave stack. This would be done by depositing a layer of material, milling it, and then depositing another layer on top of that, etc. However, there are a few issues with using this technique. Again, the materials that can be machined are limited to plastics and metals. Thus, since the minimum feature size rules out the visible and near infrared regimes, extensive investigation of the optical properties of these materials in the terahertz and microwave regimes would again be needed.
3. Lapping films: Instead of trying to rigidly control the actual roughness profile, one could simply use lapping paper to physically roughen a deposited surface. The advantage of this technique is that lapping paper roughnesses range from 0.1μm to several μm [Pace (2005)]. Therefore, rough structures tuned to the visible or near infrared wavelengths, where the optical properties of many materials are already known, could be used.
4. Polyelectrolyte multilayers: Research done by T. Wang, R. Cohen, and M. Rubner suggests that the interfacial roughness of 1D photonic crystals can be controlled through tuning nanoparticle synthesis in polyelectrolyte multilayers [Wang (2002)]. Although there is a limited materials selection, these structures can be easily produced in the near infrared regime. However, the only way to characterize the roughness of these structures is to use electron microscopy to examine a cross-section of the sample after it is made.
5. Poor deposition or electroplating: As evidenced by the example structures presented in this work (See Figs. 4.1 and 4.2), interfacial roughness can be induced by simply having poor control over the fabrication process. Thus, roughened multilayer structures can be produced by using traditional deposition techniques.
6. Sol-gel processing: Sol-gel techniques could be used to spin-coat various rough layers onto substrates. The roughness of these layers could be somewhat controlled by varying the aging time of the sol-gel solution, the

volume fraction of the sol-gel components, or the heat treatment. However, the exact dependence of these variables on the roughness of the film is currently unknown. Therefore, a systematic study of the effect of these parameters on the film quality would need to be done first.

All of these techniques require subsequent characterization of the roughened structure because the processing of higher layers may affect the roughness of lower ones. Furthermore, the roughness parameter values need to be determined to ensure that they fall within the ranges tested in this study (i.e. $R_{RMS} < 0.2a$, $W_{RMS} < 1.0a$). Thus, the structures need to be cross-sectioned (i.e. with ultramicrotoming, or other techniques that would not significantly disturb the microstructure) and viewed using electron microscopy to ensure that the roughness has not changed significantly. Moreover, this will also allow a micrograph of the structure to be produced that can be later used to compare the calculated prediction to the experimental results. Alternatively, AFM measurements can be conducted between the deposition of each layer to measure the RMS roughness. However, these measurements should be conducted only if subsequent deposition will not disturb the underlying layer roughness. For example, with sol-gel processes, AFM measurements must be conducted after any heat treatments.

Besides ascertaining the deposited film roughness, the use of amorphous materials would be preferable since polycrystallites could cause bulk scattering independent of the interfacial roughness scattering. Dust should also be minimized to prevent large defects on the interfaces, which would cause the roughness scales in the fabricated structures to be much larger than those tested in this thesis. Finally, with many deposition techniques, large roughness levels may result in correlated roughness between layers. As the homogenization theory results do not explicitly account for correlated roughnesses, it may be necessary to minimize such effects in the experimental structures.

Measure the reflectivity and off-angle scattering. The reflectivity of the sample can be measured with a spectrometer in the appropriate spectral range. These devices are available in both the visible/infrared regimes as well as the terahertz regime. The reference used for this measurement, however, must be carefully calibrated so that the absolute reflectivity can be compared to the calculated numbers. Ideally, an absolute reflectivity measurement would be conducted.

Off-angle scattering measurements require a more complex optical setup than reflectivity measurements. One apparatus that could be used for this measurement is an integrating sphere. This is a device that captures all the light that is scattered from a sample at once. Unfortunately, there are no integrating spheres that have been made to work in the terahertz or microwave regimes. For these wavelengths, another (inferior) setup is required. Such a setup, called a scatterometer, is detailed in Deumie, et al. (1996). This utilizes a detector that is attached to a goniometer. Unfortunately, this setup can only measure scattering in one plane around the photonic crystal. But it can at least provide an order-of-magnitude estimate of the amount of scattering from the roughened structures.

Compare the experimental and calculated results. The micrograph obtained to characterize the roughness of the sample can be converted into a refractive index file as described above. The homogenization approximation can then be applied to this representation of the structure to calculate the alleged reflectivity of the sample. The results can then be compared to the absolute reflectivity obtained with the spectrometer. The prediction for the amount of scattered power, however, would require either estimation based on the results already obtained for various structures, or more FDTD calculations. In any event, if the homogenization approximation is able to reproduce the reflectance spectra obtained with the spectrometer, then the amount of scattered power is most likely extremely small (see chapter 6).

Chapter 12: Conclusions and Future Work

This thesis presented the results of several FDTD simulations designed to systematically study the effect of structural imperfections in 1D and 2D photonic crystals. The specific imperfections investigated were: interfacial roughness in 1D photonic crystals (normal incidence, full bandgap), surface scratches in 1D photonic crystals (normal incidence, full bandgap), and acircular pores in 2D photonic crystals (M-point). Several important results were uncovered concerning the quantitative effects of these imperfections on various photonic crystal configurations.

For the interfacial roughness study, it was found that certain roughened structures can experience more than a 50% change in reflectivity for roughness scales on the order of 20% of the characteristic periodicity of the crystal at the quarter-wave tuned wavelength. Although this is not too surprising, it is curious that this reflectivity change can be substantially reduced to 15% by increasing the refractive index contrast of the structure from 1.25 to 2.0. Increasing the number of bilayers can also be used to increase

a crystal's tolerance to interfacial roughness at the center bandgap wavelength. A 2-bilayer structure with an index contrast of 1.5 will have over a 50% reflectivity change at roughness scales around 20% of the periodicity, while a 6-bilayer structure with the same index contrast will have only a 30% reflectivity change at an equivalent roughness. Furthermore, the RMS distance between roughness features (up to 100% of the structure's periodicity), as well as the average refractive index of the structure, appear to play no role in determining the change in reflectivity due to interfacial roughness.

These results are counter-intuitive to the trends that would be predicted by a simple scattering theory analysis. However, a more rigorous application of scattering theory to the specific roughened structures tested in this thesis reveals trends that are consistent with the FDTD results. Unfortunately, these results also show that the amount of scattering in these structures is too small to explain the large change in reflectivity observed with the FDTD simulations.

Thus, another mechanism was sought to explain the marked reflectivity changes from the roughened photonic crystals. Two approximations that are commonly used to study the coherent reflectivity from single rough interfaces were applied to the systems studied here with multiple interfaces. One of these approximations, the homogenization approximation, produced results that matched the FDTD data very accurately. This provided physical insight into the mechanism that causes the reflectivity decrease in roughened structures: the roughness features act to grade the refractive index profile of the interfaces in the photonic crystal. These graded interfaces allow more light to pass through the structure, decreasing its reflectivity. The length over which the interfaces in the approximated structure are graded depends on the RMS roughness scale in the actual structure. Larger roughness scales produce more diffuse interfaces, which in turn further increases the transmissivity (decreases the reflectivity) of the structure.

However, the homogenization approximation only predicts the amount of coherent reflectivity, while the FDTD calculations include both the incoherent and coherent portions of the power. Thus, the success of this approximation implied that the amount of incoherent reflected power from these structures was extremely small. This was verified by directly extracting the amount of incoherent power from the FDTD data. In the worst case, the amount of incoherent power was only about 4.5% of the total

reflected power from the structure. This explains why the homogenization approximation can be accurately applied to the roughened structures tested here. Note, however, that this only includes roughened structures where the RMS roughness is less than about 20% of the crystal periodicity and the RMS distance between roughness features is less than 100% of the crystal periodicity. Nevertheless, this range of parameters represents the roughness scales that typically occur in most imperfect photonic crystals.

Furthermore, the fact that the homogenization approximation is valid for the structures tested here is also significant because the homogenization approximation is much faster and easier to apply to a real structure than the FDTD simulations. For example, a curve consisting of 40 data points would take a few days to calculate with the FDTD code. However, the same curve would be generated in a few minutes using the homogenization approximation.

With this understanding, the homogenization approximation was tested on the entire normal incidence bandgap of the roughened structures. The FDTD results showed a narrowing and red-shifting of the bandgap with increasing roughness scales. Furthermore, the low index contrast structure appeared to be more sensitive to this red-shifting effect. As with the other simulations, the homogenization approximation was able to correctly predict the behavior observed in the FDTD results. Thus, it was determined that the homogenization approximation could be accurately applied to the entire normal incidence bandgap of roughened structures.

Next, the problem of surface scratches on 1D photonic crystals was investigated. As expected, the amount of reflectivity change was much smaller than the interfacial roughness study because these structures only had roughness on the top interface. Still a reflectivity decrease of almost 15% was observed in low index contrast structures for roughness scales around 15% of the photonic crystal periodicity. However, it was observed that this reflectivity change could be mitigated by adding a protective coating to the top of the photonic crystal. As long as the protective coating had a refractive index less than the top layer in the crystal, the coating acted to make the structure more tolerant to scratches. However, if the protective coating index was higher than the top layer index, the structure would become less tolerant to surface scratches. Furthermore, this

result was found to be true for the entire normal incidence bandgap. As expected, the homogenization approximation was able to accurately reproduce these trends as well.

The problem of pore acircularity in 2D hexagonal photonic crystal structures was the last imperfection explored in this study. Two "real-world" systems, porous alumina and porous silicon, were tested. For the porous alumina, a percent change in reflectivity of almost 50% was observed for an RMS acircularity of about 25% of the mean pore radius. As with the 1D structures, this reflectivity change could be mitigated by increasing the number of periods in the crystal from 8 rows of pores to 12 rows. In the porous silicon system, the reflectivity decreases were smaller, although the RMS acircularities that could be properly tested were limited to less than 4% of the mean pore radius. Despite this, these results revealed a trend that is consistent with all of the other simulation results in this thesis: the absolute reflectivity of a structure is an indication of how tolerant a photonic crystal will be to structural imperfections. Thus, any structural change that can be made to the crystal to increase its absolute reflectivity (i.e. increasing the number of periods, increasing the index contrast, etc.) will also increase its tolerance to structural imperfections.

Finally, the concepts put forth in this thesis were verified for two experimental structures with interfacial roughness. The measured reflectance spectra from the structures were compared to spectra calculated using the homogenization approximation. The results were in very good agreement. Additionally, more rigorous experiments were proposed to further verify the validity of the homogenization approximation for roughened 1D photonic crystals.

This work provides a comprehensive basis for future studies on imperfect photonic crystals. For 1D structures, other angles besides normal incidence conditions should be tested and compared to the homogenization approximation results to determine if this approximation is still valid for oblique incidence angles. Furthermore, more roughness scales should be tested to determine when the homogenization approximation can no longer be accurately applied to roughened/scratched structures even at normal incidence. This is especially relevant for scratched crystals because actual scratch scales may differ significantly from those tested in this study. As for the 2D structures, more reflectivity tests at other incidence conditions should be done to see if there is a variation

in the reflectivity response. Furthermore, other structural imperfections, such as deviation of the pore center positions from the hexagonal lattice spacing, should also be explored. These methods could be applied to 3D imperfect systems as well. Finally, rigorous experimental studies can be done to determine the validity of the computational findings.

In summary, the studies presented in this thesis have contributed to the field of photonic crystals in the following ways:

1. Quantified the effect of interfacial roughness on the optical properties of 1D photonic crystals for the full normal incidence bandgap.
2. Identified structural property requirements for optimizing tolerance to interfacial roughness.
3. Showed that the homogenization approximation for analyzing reflection from single rough surfaces can be applied with little error to 1D photonic crystal structures (for RMS roughnesses < 20% of the crystal periodicity, RMS wavelengths < 100% of the crystal periodicity, refractive index contrasts < 2.0, and bilayers < 6).
4. Obtained values for the scattered power from roughened structures and showed that the trends and magnitudes are roughly consistent with Mie theory predictions.
5. Demonstrated that TE and TM polarizations produce equivalent results for the roughened structures tested (see point 3 above for parameter constraints), allowing the results herein to be applied to full 3D rough interfaces.
6. Quantified the effect of surface scratches on the optical properties of 1D photonic crystals (with and without protective coatings) at normal incidence.
7. Identified design requirements for optimizing device tolerance to surface scratches.
8. Demonstrated the utility of protective coatings for providing higher structural tolerance to surface scratches over the entire normal incidence bandgap.
9. Quantified the effect of pore acircularity on the optical properties of 2D photonic crystals at the M-point.

10. Demonstrated that the same analysis as above can be used to determine the decrease in reflectivity from imperfect 2D photonic crystals.
11. Experimentally verified the use of the homogenization approximation to predict the reflectance spectrum from roughened photonic crystals (see point 3 above for parameter constraints).

Appendix A: Code for the Simulation of Actual Roughened Structures

The Matlab code used in chapter 11 to apply the homogenization approximation to black and white micrographs of actual structures is provided here. The transfer matrix part of the code was written by Garry Maskaly [Maskaly (2001)], and is reproduced here with his permission. There are a few requirements for the applicable micrographs: (1) the layers must be oriented horizontally with the bottom interface being the first one in the stack, (2) the different materials in the structure (i.e. the layers) should be distinguishable by their shade of gray, and (3) the higher index material should correspond to the darker shade of gray. In addition, the contrast of the image should be as large as possible so there is less error in assigning refractive indices to each pixel in the image. However, if the image has poor contrast, the code can still handle the image. A remedy was devised that utilizes white and black thresholds. Any number below the white threshold is taken to be a white pixel. Similarly, any number above the black threshold is taken to be a black pixel. For the numbers in between the two thresholds, an average is taken between

the high and low indices of the structure. These thresholds can be adjusted on the command line in order to optimize the computed fit to the experimental reflectance spectrum.

There are a series of script files that all need to be loaded into the same directory along with the image file. A subfolder called 'results' should be included in this directory as well. This folder holds all the results of each run in a file called 'test'. The code can be run at any angle, and if only one wavelength is input, the code also computes the energy density in the approximated structure at that wavelength.

Function: `imgscript`

This is the main function. So one only needs to call this function in order to calculate the homogenization results for the micrograph. This function calls all the other functions.

```
function
[lambda,r]=imgscript(nh,nl,ns,angle,TETM,minwave,maxwave,resolution,bth
reshold,wthreshold,pixres,imagefile,extension);

%function
[lambda,r]=imgscript(nh,nl,ns,angle,TETM,minwave,maxwave,resolution,bth
reshold,wthreshold,pixres,imagefile,extension);
%
%nh = high refractive index
%nl = low refractive index
%ns = substrate refractive index
%angle = angle of incidence in degrees
%TETM = 'TE' or 'TM' for the polarization of the incident light
%maxwave = maximum wavelength on the plot
%minwave = minimum wavelength on the plot
%resolution = number of points to calculate between maxwave and minwave
%wthreshold = white threshold (between 0 and 256)
%bthreshold = black threshold (between 0 and 256, <= wthreshold)
%pixres = number of pixels per unit wavelength (i.e. pixels/nm or um)
%imagefile = the name of the image file in single quotes
%extension = the extension of the image file (i.e. 'JPEG', 'GIF')
%
%NOTE: If using a GIF image, you must either reverse the high and low
%index inputs (i.e. nh = low index and nl = high index) or take the
%negative of the image. GIF format uses the opposite convention of all
%other formats when assigning numerical values to black and white
%pixels.


%Calculate the step width corresponding to the input resolution
step=(minwave - maxwave)/resolution;
lambda=[minwave:step:maxwave];
```

```
%Convert wavelengths from spatial units to pixels
minpixlambda=minwave*pixres;
maxpixlambda=maxwave*pixres;

%Calculate the smoothed index profile with the Smoothindex function
[stepindex,stepwidth]=Smoothindex(nh,nl,ns,bthreshold,wthreshold,imagef
ile,extension);

%Calculate the reflectivity for the smoothed index profile
r=stepbands(stepindex,stepwidth,minpixlambda,maxpixlambda,resolution,an
gle,TETM,'test',pixres);
```

Function: `Smoothindex`

This function converts the image file into a digital refractive index file. It outputs a plot of the corresponding refractive index file that can be used as a check by the user to make sure the refractive index information correctly represents to input structure. This function also takes the refractive index file and calculates the smoothed refractive index profile and corresponding multilayer structure for it. It then outputs the refractive index (`stepindex`) and thickness (`stepwidth`) of the approximated structure.

```
function
[stepindex,stepwidth]=Smoothindex(nh,nl,ns,bthreshold,wthreshold,imagef
ile,extension);

%function
[stepindex,stepwidth]=Smoothindex(nh,nl,ns,bthreshold,wthreshold,imagef
ile,extension);
%
%nh is the high index in the structure
%nl is the low index in the structure
%ns is the index of the substrate
%wthreshold is the white threshold (between 0 and 256)
%bthreshold is the black threshold (between 0 and 256, <= wthreshold)
%pixres is the number of pixels per unit wavelength (i.e. pixels/nm)
%imagefile is the the name of the image file in single quotes
%extension is the the extension of the image file (i.e. 'JPEG', 'GIF')
%
%NOTE: If using a GIF image, you must either reverse the high and low
%index inputs (i.e. nh = low index and nl = high index) or take the
%negative of the image. GIF format uses the opposite convention of all
%other formats when assigning numerical values to black and white
%pixels.


%Read in the image file
A=imread(imagefile,extension);

%Convert the image to refractive indices based on the thresholds
```

```
for ix=1:1:size(A,1)
    for iy=1:1:size(A,2)
        if (double(A(ix,iy)) >= wthreshold)
            buffstruct(size(A,1)+1-ix,iy)=nl;
        elseif (double(A(ix,iy)) <= bthreshold)
            buffstruct(size(A,1)+1-ix,iy)=nh;
        else
            buffstruct(size(A,1)+1-ix,iy)=nh-((double(A(ix,iy))-
bthreshold)/(wthreshold-bthreshold))*(nh-nl);
        end;
    end;
end;

%These lines let you view what the refractive index array looks like
figure;
surf(buffstruct);
view(2);
shading interp;
colorbar vert;
title('Refractive index file for structure','fontsize',20);
xlabel('Pixels parallel to layers','fontsize',18);
ylabel('Pixels perpendicular to layers','fontsize',18);
axis([1,size(A,2),1,size(A,1)]);
set(gca,'fontsize',16);

%Calculate the dielectric constant from the refractive index array and
%average
index=buffstruct;
eps = index.*index;

smoothedeps = mean(eps');
smoothedindex = smoothedeps.^0.5;

%These lines allow you to view the smoothed structure in a 3D plot
%rather than a 2D plot
%for ix=1:1:size(index,2)
%    for iy=1:1:size(index,1)
%        zsurf(ix,iy)=smoothedindex(iy);
%    end;
%end;

%Calculate the discrete layers that approximate the smoothed index
%profile
baseindex = 1;
counter = 1;
counter2 = 2;
counter3 = 0;
stepindex(1) = 1;
stepwidth(1) = 0;
flag = 0;

for ix=1:1:(size(index,1)-1)
    if (smoothedindex(ix) == 1)
        baseindex = 1;
        if (flag == 0)
            counter3 = counter3 + 1;
```

```
        end
    else
        flag = 1;
        nextindex = smoothedindex(ix);
        if ((nextindex == nh) && (smoothedindex(ix+1) ~= nh))
            stepindex(counter2) = nh;
            stepwidth(counter2) = counter;
            counter2 = counter2 + 1;
            counter = 1;
            baseindex = nextindex;
        elseif ((nextindex == nl) && (smoothedindex(ix+1) ~= nl))
            stepindex(counter2) = nl;
            stepwidth(counter2) = counter;
            counter2 = counter2 + 1;
            counter = 1;
            baseindex = nextindex;
        elseif (abs(nextindex - baseindex) >= 0.005)
            stepindex(counter2) = (baseindex+nextindex)/2;
            stepwidth(counter2) = counter;
            counter2 = counter2 + 1;
            counter = 1;
            baseindex = nextindex;
        else
            counter = counter + 1;
        end;
    end;
end;


stepindex(counter2) = ns;
stepwidth(counter2) = 0;

%These lines allow you to plot the stepped profile
%counter4 = counter3 + 1;
%counter5 = counter4;
%
%for iy=1:1:length(stepindex)
%    for iy2 = 1:1:stepwidth(iy)
%        plotindex(counter4) = stepindex(iy);
%        plotwidth(counter4) = counter3 + iy2;
%        for ix=1:1:450
%            zstep(ix,counter4)=plotindex(counter4);
%        end;
%        counter4 = counter4 + 1;
%    end;
%    counter3 = counter3 + stepwidth(iy);
%end;
%
%for ix=counter3:1:size(index,1)
%    plotindex(ix)=1;
%    plotwidth(ix)=ix;
%    for iy=1:1:450
%        zstep(iy,ix)=1;
%    end;
%end;
%figure;
```

```
%plot(plotwidth,plotindex,'r-');
%hold on;
%for ix=1:1:length(stepindex)
%    plot([counter5, counter5], [0, stepindex(ix)], 'k-');
%    hold on;
%    plot([counter5, stepwidth(ix)+counter5], [stepindex(ix),
stepindex(ix)], 'k-');
%    hold on;
%    counter5 = counter5 + stepwidth(ix);
%end;

%These lines allow you to plot the smoothed index profile
%figure;
%plot([1:1:size(index,1)],smoothedindex,'b-');
%hold on;

%These lines allow you to plot the stepped index on a 3D plot
%figure;
%surf(zstep');
%view(2);
%shading interp;

clear index;
```

Function: `stepbands`

This function calls a transfer matrix code to calculate the reflectivity for each wavelength step within the desired range. It also stores all the output information (reflectivity, transmissivity, absorption, and wavelength) into a file prefixed by 'test' in the /results subdirectory. If only one wavelength is specified, it calls a function that calculates and plots the energy density in the structure at that wavelength. Otherwise, it calls a function that plots the reflectivity vs. wavelength results.

```
function
r=stepbands(stepindex,stepwidth,xmin,xmax,xsteps,angle,TETM,storename,p
ixres);

%function
r=stepbands(stepindex,stepwidth,xmin,xmax,xsteps,angle,TETM,storename,p
ixres);
%
%stepindex = a column vector with the refractive indices of each layer
%in the structure, starting with the top layer.  The first layer and
%last layer correspond to the incident and transmitting medium,
%respectively.
%
%stepwidth = a column vector with the thicknesses of each layer in the
%structure, starting with the top layer.  The thicknesses should be
%given in the same units as the wavelength(s).  The first layer and
%layer layer are both semi-infinite, so their thicknesses should be
```

```
%input as 0.
%
%xmin = minimum wavlength
%xmax = maximum wavelength
%xsteps = number of data points to calculate between xmin and xmax
%angle = angle of incidence in degrees
%TETM = 'TE' or 'TM' for the polarization of the incident light
%
%storename = name of file in single quotes where the output data will
%be stored (in the /results directory)
%
%pixres = the number of pixels per unit wavelength (i.e. pixels/nm)


%Determine accuracy of input data
errorflag=0;
if ((TETM~='TE')&(TETM~='TM'))
    disp('Error, neither TE or TM was entered for TETM.')
    errorflag=1;
elseif (angle>90)|(angle<0)
    disp('Error, angle out of range.')
    errorflag=1;
end

if errorflag==1
    return
end

%Convert input to useable numbers
if angle==90
    angle=89.999;
end

if TETM=='TE'
    TETM=0;
else
    TETM=1;
end

%Create the wavelength range matrix
if xsteps==1;
    xrange=xmin;
else
    for counter=1:1:xsteps
        xrange(counter)=xmin+(counter-1)*(xmax-xmin)/(xsteps-1);
    end
end

%If the ranges were input backwards, correct it
if (xrange(1)>xrange(length(xrange)))
    for x=length(xrange):-1:1
        xrange2(length(xrange)-x+1)=xrange(x);
    end
    xrange=xrange2;
end
```

```
%Create the angle range matrix (2 components consisting of the angle
%and the polarization)
anglerange=[angle,TETM];

%Reassign the refractive index and layer width information
materialsfile = stepindex;
layers = stepwidth;

%For each wavelength to calculate, read in the refractive index profile
for counter=1:1:size(materialsfile')
        n(counter,xsteps)=(materialsfile(counter));
        n(counter,:)=(materialsfile(counter));
end

%Ensure that the width of the first and last layers are 0
%(semi-infinite ambient layers)
layers(1)=0;
layers(length(layers))=0;
warn=0;

%If only one wavelength is input, then calculate the energy
%distribution in the structure, and just output the reflectivity to the
%screen (single number)
if xsteps==1
   r=stepenergydist(xrange(1),anglerange(1),anglerange(2),layers,n)
   return
end

%Calculate the reflectivity, transmissivity, and absorption at each
%wavelength for the structure.
for x=1:1:length(xrange)
    if anglerange(2)==0
        [r(x),t(x),a(x),e(x),ang(x),warn]=bandTE(xrange(x), n(:,x),
anglerange(1), layers, warn);
    else
        [r(x),t(x),a(x),e(x),ang(x),warn]=bandTM(xrange(x), n(:,x),
anglerange(1), layers, warn);
    end
end

ang=real(ang);

%Display message if r+t>=1 (i.e. no absorption and/or gain present)
if warn==1
   disp(['Rounding errors have occurred or there is no absorption in
',storename,'.']);
   disp(['Zero absorption was assumed in those regions.']);
end

%Write output to storename file in /results subdirectory.
fid=fopen(['results/',storename,'r'],'w+');
fwrite(fid,r,'real*8');
fclose(fid);
fid=fopen(['results/',storename,'a'],'w+');
```

```
fwrite(fid,a,'real*8');
fclose(fid);
fid=fopen(['results/',storename,'t'],'w+');
fwrite(fid,t,'real*8');
fclose(fid);
fid=fopen(['results/',storename,'e'],'w+');
fwrite(fid,e,'real*8');
fclose(fid);
fid=fopen(['results/',storename,'ang'],'w+');
fwrite(fid,ang,'real*8');
fclose(fid);
fid=fopen(['results/',storename,'lamb'],'w+');
fwrite(fid,xrange,'real*8');
fclose(fid);

%Plot reflectivity results
plotTETMfunc(storename,pixres)
```

Function: `stepenergydist`

This function calls a transfer matrix code that calculates the reflectivity as well as the field amplitudes inside each layer in the input structure. It then uses that information to calculate the energy density inside the structure. Finally, it plots the energy density as well as the interface positions of the layers in the structure as a reference.

```
function [r,EE2,spacing]=stepenergydist(lambda,angle,TM,layers,n)

%function [r,EE2,spacing]=stepenergydist(lambda,angle,TM,layers,n)
%
%lambda = the incident wavelength
%angle = the incident angle in degrees
%TM = 0 for TE polarization
%    = 1 for TM polarization
%
%layers = a column vector with the thicknesses of each layer in the
%structure, starting with the top layer.  The thicknesses should be
%given in the same units as the wavelength(s).  The first layer and
%layer layer are both semi-infinite, so their thicknesses should be
%input as 0.
%
%n = a row vector with the refractive indices of each layer in the
%structure, starting with the top layer.  The first layer and last
%layer correspond to the incident and transmitting medium,
%respectively.
%
%The output is the reflectivity, the energy density, and the depth into
%the structure


%Initialize variables and define constants
hold off
resolution=50;
```

```
warn=0;
c=3*10^8;
e0=8.85418781762*10^-12;

%Use Transfer Matrix code to calculate the reflectivity and the wave
%amplitudes in each layer
if TM==0
   [r,A,B,warn]=energyTE(lambda, n, layers, angle, warn);
else
   [r,A,B,warn]=energyTM(lambda, n, layers, angle, warn);
end

%Initialize variables and define k vector of incident wave (ko) to find
%kx
EE2 = 0;
spacing(1) = 0;
E2(1)=A(2)+B(2);

ko=2*pi*n(1)/(lambda);
omega=c*ko;
kx=ko*sin(angle);
thickness=sum(layers);

%Calculate the electric field amplitude within each layer of the
%structure
for counter=2:1:length(layers)-1
      k=ko*n(counter);
      kz=sqrt(k^2-kx^2);
      layerstep=layers(counter)/resolution;
      counter2=0;
      offset=spacing((counter-2)*resolution+1);
      for z=0:layerstep:layers(counter)
          counter2=counter2+1;
          spacing((counter-2)*resolution+counter2+1)=spacing((counter-
2)*resolution+counter2)+layerstep;
          if TM==0
              E2((counter-2)*resolution+counter2+1)=A(counter)*exp(-
i*kz*(z-(layers(counter))))+B(counter)*exp(i*kz*(z-(layers(counter))));
          else
              coeff1=kz/(omega*(n(counter)^2)*e0);
              coeff2=-kx/(omega*(n(counter)^2)*e0);
              term1=coeff1*(A(counter)*exp(-i*kz*(z-
(layers(counter))))-B(counter)*exp(i*kz*(z-(layers(counter)))));
              term2=coeff2*(A(counter)*exp(-i*kz*(z-
(layers(counter))))+B(counter)*exp(i*kz*(z-(layers(counter)))));
              E2((counter-
2)*resolution+counter2+1)=sqrt(term1^2+term2^2)/376.730313462;
          end
      end
end

%Calculate the energy density from the electric field amplitude
EE2=E2.*conj(E2);

%Plot the energy density and the interfaces of the layers in the
%structure (as a reference)
```

```
figure
hold on;
layerst(1)=0;
for counter=1:1:length(layers)
   layerst(counter+1)=layerst(counter) + layers(counter);

plot([layerst(counter+1),layerst(counter+1)],[max(EE2)/4,0],'color',[0.
75,0.75,0.75]);
end
hold on;
plot(spacing,EE2,'linewidth',2.0);
axis([0 spacing(length(spacing)) 0 1.1*max(EE2)]);
title('Calculated Energy Density','fontsize',20);
xlabel('Depth into structure [pixels]','fontsize',18);
ylabel('Energy','fontsize',18);
set(gca,'fontsize',16);
disp('Light gray lines on energy plot indicate positions of interfaces
between layers in structure.');

%Display message if r+t>=1 (i.e. no absorption and/or gain present)
if warn==1
   disp('Rounding errors have occurred.  Zero absorption was assumed in
those regions.');
end
hold off;
```

Function: `energyTE`

This function calculates the reflectivity and field amplitudes in a multilayer structure using the transfer matrix technique for a TE polarized wave.

```
function [r,A,B,warn]=energyTE(lambda,n,layers,angle,warn);

%function [r,A,B,warn]=energyTE(lambda,n,layers,angle,warn);
%
%lambda = incident wavelength
%
%n = a vector with the refractive indices of each layer in the
%structure, starting with the top layer.  The first layer and last
%layer correspond to the incident and transmitting medium,
%respectively.
%
%angle = incident angle in degrees
%
%layers = a vector with the thicknesses of each layer in the structure,
%starting with the top layer.  The thicknesses should be given in the
%same units as the wavelength(s).  The first layer and layer layer are
%both semi-infinite, so their thicknesses should be input as 0.
%
%warn = warning flag (default is 0)


%Initialize variables
```

```
numoflayers=length(layers);
totalthick=sum(layers);

%Convert angle to radians
angle=angle*pi/180;

%Define k vector of incident wave and calculate kx, kt, kz, etc.
ko=2*pi*n(1)/(lambda);
kx=ko*sin(angle);
kt=ko*n(2);
kiz=sqrt(ko^2-kx^2);
ktz=sqrt(kt^2-kx^2);

%Define pti (change of variables) and Rti
pti=kiz/ktz;  %TE Wave
Rti=(1-pti)/(1+pti);

%Calculate and propagate transfer matrices based on refractive indices
%and thicknesses of layers
if numoflayers>2
    for x=2:1:numoflayers-1
        ki=ko*n(x-1);
        kt=ko*n(x);
        kiz=sqrt(ki^2-kx^2);
        ktz=sqrt(kt^2-kx^2);
        pti=kiz/ktz;  %TE Wave
        Rti=(1-pti)/(1+pti);
        if exist('V')
            V=(.5*(1+pti)*[exp(-i*ktz*layers(x)), Rti*exp(-
i*ktz*layers(x));Rti*exp(i*ktz*layers(x)),exp(i*ktz*(layers(x)))])*V;
        else
            V=(.5*(1+pti)*[exp(-i*ktz*layers(x)), Rti*exp(-
i*ktz*layers(x));Rti*exp(i*ktz*layers(x)),exp(i*ktz*(layers(x)))]);
        end
    end
end

%Calculate transfer matrix corresponding to the final layer
ki=ko*n(numoflayers-1);
kt=ko*n(numoflayers);
kiz=sqrt(ki^2-kx^2);
ktz=sqrt(kt^2-kx^2);
pti=kiz/ktz;  %TE Wave
Rti=(1-pti)/(1+pti);
if exist('V')
    V=(.5*(1+pti)*[exp(i*ktz*totalthick),
Rti*exp(i*ktz*totalthick);Rti*exp(-i*ktz*totalthick),exp(-
i*ktz*totalthick)])*V;
else
    V=(.5*(1+pti)*[exp(i*ktz*totalthick),
Rti*exp(i*ktz*totalthick);Rti*exp(-i*ktz*totalthick),exp(-
i*ktz*totalthick)]);
end

%Calculate R and T from transfer matrix
R=-V(3)/V(1);
```

```
T=-(V(3)/V(1))*V(2)+V(4);

%Calculate reflectivity
r=abs(R)^2

%Calculate transmissivity and absorption
ki=ko*n(1);
kt=ko*n(numoflayers);
kiz=sqrt(ki^2-kx^2);
ktz=sqrt(kt^2-kx^2);
pit=ktz/kiz;  %TE Wave
if r+pit*abs(T)^2>1.000 %If r+t > 1.000 (rounding errors, etc.)
   warn=1;
   t=1-r;
   a=0;
   e=1;
   angTE=atan(imag(R)/real(R))*180/pi;
else
    t=pit*abs(T)^2
    t=real(t);
    a=1-r-t;
    a=real(a);
    e=0;
    angTE=atan(imag(R)/real(R))*180/pi;
end

%Calculate phase shift of reflected wave
if R~=0
    Phase_Shift_Degrees=atan(imag(R)/real(R))*180/pi
end

%Calculate the field amplitudes in each layer
A(1)=R;
B(1)=1;
kx=ko*sin(angle);
kt=ko*n(2);
kiz=sqrt(ko^2-kx^2);
ktz=sqrt(kt^2-kx^2);
pti=kiz/ktz;  %TE Wave
Rti=(1-pti)/(1+pti);
if numoflayers>2
    for x=2:1:numoflayers-1
        ki=ko*n(x-1);
        kt=ko*n(x);
        kiz=sqrt(ki^2-kx^2);
        ktz=sqrt(kt^2-kx^2);
        pti=kiz/ktz;  %TE Wave
        Rti=(1-pti)/(1+pti);
        V=(.5*(1+pti)*[exp(-i*ktz*layers(x)), Rti*exp(-
i*ktz*layers(x));Rti*exp(i*ktz*layers(x)),exp(i*ktz*(layers(x)))]);
        AB=V*[A(x-1);B(x-1)];
        A(x)=AB(1);
        B(x)=AB(2);
    end
end
```

```
%Calculate the field amplitude in the transmitting region
ki=ko*n(numoflayers-1);
kt=ko*n(numoflayers);
kiz=sqrt(ki^2-kx^2);
ktz=sqrt(kt^2-kx^2);
pti=kiz/ktz;  %TE Wave
Rti=(1-pti)/(1+pti);
V=(.5*(1+pti)*[exp(i*ktz*totalthick),
Rti*exp(i*ktz*totalthick);Rti*exp(-i*ktz*totalthick),exp(-
i*ktz*totalthick)]);
AB=V*[A(numoflayers-1);B(numoflayers-1)];
A(numoflayers)=AB(1);
B(numoflayers)=AB(2);
```

Function: `energyTM`

This function calculates the reflectivity and field amplitudes in a multilayer structure using the transfer matrix technique for a TM polarized wave.

```
function [r,A,B,warn]=energyTM(lambda,n,layers,angle,warn);

%function [r,A,B,warn]=energyTM(lambda,n,angle,layers,warn);
%
%lambda = incident wavelength
%
%n = a vector with the refractive indices of each layer in the
%structure, starting with the top layer.  The first layer and last
%layer correspond to the incident and transmitting medium,
%respectively.
%
%angle = incident angle in degrees
%
%layers = a vector with the thicknesses of each layer in the structure,
%starting with the top layer.  The thicknesses should be given in the
%same units as the wavelength(s).  The first layer and layer layer are
%both semi-infinite, so their thicknesses should be input as 0.
%
%warn = warning flag (default is 0)


%Initialize variables
numoflayers=length(layers);
totalthick=sum(layers);

%Convert angle to radians
angle=angle*pi/180;

%Define k vector of incident wave and calculate kx, kt, kz, etc.
ko=2*pi*n(1)/(lambda);
kx=ko*sin(angle);
kt=ko*n(2);
kiz=sqrt(ko^2-kx^2);
ktz=sqrt(kt^2-kx^2);
```

```
%Define pti (change of variables) and Rti
pti=(kiz*n(2)^2)/(ktz*n(1)^2);  %TM Wave
Rti=(1-pti)/(1+pti);

%Calculate and propagate transfer matrices based on refractive indices
%and thicknesses of layers
if numoflayers>2
    for x=2:1:numoflayers-1
        ki=ko*n(x-1);
        kt=ko*n(x);
        kiz=sqrt(ki^2-kx^2);
        ktz=sqrt(kt^2-kx^2);
        pti=(kiz*n(x)^2)/(ktz*n(x-1)^2); %TM Wave
        Rti=(1-pti)/(1+pti);
        if exist('V')
            V=(.5*(1+pti)*[exp(-i*ktz*layers(x)), Rti*exp(-
i*ktz*layers(x));Rti*exp(i*ktz*layers(x)),exp(i*ktz*(layers(x)))])*V;
        else
            V=(.5*(1+pti)*[exp(-i*ktz*layers(x)), Rti*exp(-
i*ktz*layers(x));Rti*exp(i*ktz*layers(x)),exp(i*ktz*(layers(x)))]);
        end
    end
end

%Calculate transfer matrix corresponding to the final layer
ki=ko*n(numoflayers-1);
kt=ko*n(numoflayers);
kiz=sqrt(ki^2-kx^2);
ktz=sqrt(kt^2-kx^2);
pti=(kiz*n(numoflayers)^2)/(ktz*n(numoflayers-1)^2);  %TM Wave
Rti=(1-pti)/(1+pti);
if exist('V')
    V=(.5*(1+pti)*[exp(i*ktz*totalthick),
Rti*exp(i*ktz*totalthick);Rti*exp(-i*ktz*totalthick),exp(-
i*ktz*totalthick)])*V;
else
    V=(.5*(1+pti)*[exp(i*ktz*totalthick),
Rti*exp(i*ktz*totalthick);Rti*exp(-i*ktz*totalthick),exp(-
i*ktz*totalthick)]);
end

%Calculate R and T from transfer matrix
R=-V(3)/V(1);
T=-(V(3)/V(1))*V(2)+V(4);

%Calculate reflectivity
r=abs(R)^2;

%Calculate transmissivity and absorption
ki=ko*n(1);
kt=ko*n(numoflayers);
kiz=sqrt(ki^2-kx^2);
ktz=sqrt(kt^2-kx^2);
pit=(n(1)^2)*ktz/(kiz*n(numoflayers)^2);  %TM Wave
if r+pit*abs(T)^2>1.000 %If r+t > 1.000 (rounding errors, etc.)
```

```
    warn=1;
    t=1-r;
    a=0;
    e=1;
    angTM=atan(imag(R)/real(R))*180/pi;
else
     t=pit*abs(T)^2
     t=real(t);
     a=1-r-t;
     a=real(a);
     e=0;
     angTM=atan(imag(R)/real(R))*180/pi;
end

%Calculate phase shift of reflected wave
if R~=0
     Phase_Shift_Degrees=atan(imag(R)/real(R))*180/pi
end

%Calculate the field amplitudes in each layer
A(1)=R;
B(1)=1;
kx=ko*sin(angle);
kt=ko*n(2);
kiz=sqrt(ko^2-kx^2);
ktz=sqrt(kt^2-kx^2);
pti=(kiz*n(2)^2)/(ktz*n(1)^2);  %TM Wave
Rti=(1-pti)/(1+pti);
if numoflayers>2
     for x=2:1:numoflayers-1
          ki=ko*n(x-1);
          kt=ko*n(x);
          kiz=sqrt(ki^2-kx^2);
          ktz=sqrt(kt^2-kx^2);
          pti=(kiz*n(x)^2)/(ktz*n(x-1)^2); %TM Wave
          Rti=(1-pti)/(1+pti);
          V=(.5*(1+pti)*[exp(-i*ktz*layers(x)), Rti*exp(-
i*ktz*layers(x));Rti*exp(i*ktz*layers(x)),exp(i*ktz*(layers(x)))]);
          AB=V*[A(x-1);B(x-1)];
          A(x)=AB(1);
          B(x)=AB(2);
     end
end

%Calculate the field amplitude in the transmitting region
ki=ko*n(numoflayers-1);
kt=ko*n(numoflayers);
kiz=sqrt(ki^2-kx^2);
ktz=sqrt(kt^2-kx^2);
pti=(kiz*n(numoflayers)^2)/(ktz*n(numoflayers-1)^2);  %TM Wave
Rti=(1-pti)/(1+pti);
V=(.5*(1+pti)*[exp(i*ktz*totalthick),
Rti*exp(i*ktz*totalthick);Rti*exp(-i*ktz*totalthick),exp(-
i*ktz*totalthick)]);
AB=V*[A(x);B(x)];
A(numoflayers)=AB(1);
```

```
B(numoflayers)=AB(2);
```

Function: `bandTE`

This function uses the transfer matrix technique to calculate the reflectivity and transmissivity for a TE polarized wave incident on an arbitrary multilayer structure.

```
function [r,t,a,e,angTE,warn]=bandTE(lambda,n,angle,layers,warn);

%function [r,t,a,e,angTE,warn]=bandTE(lambda,n,angle,layers,warn);
%
%lambda = incident wavelength
%
%n = a vector with the refractive indices of each layer in the
%structure, starting with the top layer.  The first layer and last
%layer correspond to the incident and transmitting medium,
%respectively.
%
%angle = incident angle in degrees
%
%layers = a vector with the thicknesses of each layer in the structure,
%starting with the top layer.  The thicknesses should be given in the
%same units as the wavelength(s).  The first layer and layer layer are
%both semi-infinite, so their thicknesses should be input as 0.
%
%warn = warning flag (default is 0)


%Initialize variables
numoflayers=length(layers);
totalthick=sum(layers);

%Convert angle to radians
angle=angle*pi/180;

%Define k vector of incident wave and calculate kx, kt, kz, etc.
ko=2*pi*n(1)/(lambda);
kx=ko*sin(angle);
kt=ko*n(2)/n(1);
kiz=sqrt(ko^2-kx^2);
ktz=sqrt(kt^2-kx^2);

%Define pti (change of variables) and Rti
pti=kiz/ktz;  %TE Wave
Rti=(1-pti)/(1+pti);

%Calculate and propagate transfer matrices based on refractive indices
%and thicknesses of layers
if numoflayers>2
    for x=2:1:numoflayers-1
        ki=ko*n(x-1)/n(1);
        kt=ko*n(x)/n(1);
        kiz=sqrt(ki^2-kx^2);
```

```
        ktz=sqrt(kt^2-kx^2);
        pti=kiz/ktz;  %TE Wave
        Rti=(1-pti)/(1+pti);
        if exist('V')
            V=(.5*(1+pti)*[exp(-i*ktz*layers(x)), Rti*exp(-
i*ktz*layers(x));Rti*exp(i*ktz*layers(x)),exp(i*ktz*(layers(x)))])*V;
        else
            V=(.5*(1+pti)*[exp(-i*ktz*layers(x)), Rti*exp(-
i*ktz*layers(x));Rti*exp(i*ktz*layers(x)),exp(i*ktz*(layers(x)))]);
        end
    end
end

%Calculate transfer matrix corresponding to the final layer
ki=ko*n(numoflayers-1)/n(1);
kt=ko*n(numoflayers)/n(1);
kiz=sqrt(ki^2-kx^2);
ktz=sqrt(kt^2-kx^2);
pti=kiz/ktz;  %TE Wave
Rti=(1-pti)/(1+pti);
if exist('V')
    V=(.5*(1+pti)*[exp(i*ktz*totalthick),
Rti*exp(i*ktz*totalthick);Rti*exp(-i*ktz*totalthick),exp(-
i*ktz*totalthick)])*V;
else
    V=(.5*(1+pti)*[exp(i*ktz*totalthick),
Rti*exp(i*ktz*totalthick);Rti*exp(-i*ktz*totalthick),exp(-
i*ktz*totalthick)]);
end

%Calculate R and T from transfer matrix
R=-V(3)/V(1);
T=-(V(3)/V(1))*V(2)+V(4);

%Calculate reflectivity
r=abs(R)^2;

%Calculate transmissivity and absorption
ki=ko*n(1);
kt=ko*n(numoflayers);
kiz=sqrt(ki^2-kx^2);
ktz=sqrt(kt^2-kx^2);
pit=ktz/kiz;  %TE Wave
if r+pit*abs(T)^2>1.000 %If r+t > 1.000 (rounding errors, etc.)
   warn=1;
   t=1-r;
   a=0;
   e=1;
   angTE=atan(imag(R)/real(R))*180/pi;
else
    t=pit*abs(T)^2;
    t=real(t);
    a=1-r-t;
    a=real(a);
    e=0;
    angTE=atan(imag(R)/real(R))*180/pi;
```

```
end
```

Function: `bandTM`

This function uses the transfer matrix technique to calculate the reflectivity and transmissivity for a TM polarized wave incident on an arbitrary multilayer structure.

```
function [r,t,a,e,angTM,warn]=bandTM(lambda,n,angle,layers,warn);

%function [r,t,a,e,angTM,warn]=bandTM(lambda,n,angle,layers,warn);
%
%lambda = incident wavelength
%
%n = a vector with the refractive indices of each layer in the
%structure, starting with the top layer.  The first layer and last
%layer correspond to the incident and transmitting medium,
%respectively.
%
%angle = incident angle in degrees
%
%layers = a vector with the thicknesses of each layer in the structure,
%starting with the top layer.  The thicknesses should be given in the
%same units as the wavelength(s).  The first layer and layer layer are
%both semi-infinite, so their thicknesses should be input as 0.
%
%warn = warning flag (default is 0)


%Initialize variables
numoflayers=length(layers);
totalthick=sum(layers);

%Convert angle to radians
angle=angle*pi/180;

%Define k vector of incident wave and calculate kx, kt, kz, etc.
ko=2*pi*n(1)/(lambda);
kx=ko*sin(angle);
kt=ko*n(2)/n(1);
kiz=sqrt(ko^2-kx^2);
ktz=sqrt(kt^2-kx^2);

%Define pti (change of variables) and Rti
pti=(kiz*n(2)^2)/(ktz*n(1)^2);  %TM Wave
Rti=(1-pti)/(1+pti);

%Calculate and propagate transfer matrices based on refractive indices
%and thicknesses of layers
if numoflayers>2
    for x=2:1:numoflayers-1
        ki=ko*n(x-1)/n(1);
        kt=ko*n(x)/n(1);
        kiz=sqrt(ki^2-kx^2);
```

```
        ktz=sqrt(kt^2-kx^2);
        pti=(kiz*n(x)^2)/(ktz*n(x-1)^2);  %TM Wave
        Rti=(1-pti)/(1+pti);
        if exist('V')
            V=(.5*(1+pti)*[exp(-i*ktz*layers(x)), Rti*exp(-
i*ktz*layers(x));Rti*exp(i*ktz*layers(x)),exp(i*ktz*(layers(x)))])*V;
        else
            V=(.5*(1+pti)*[exp(-i*ktz*layers(x)), Rti*exp(-
i*ktz*layers(x));Rti*exp(i*ktz*layers(x)),exp(i*ktz*(layers(x)))]);
        end
    end
end

%Calculate transfer matrix corresponding to the final layer
ki=ko*n(numoflayers-1)/n(1);
kt=ko*n(numoflayers)/n(1);
kiz=sqrt(ki^2-kx^2);
ktz=sqrt(kt^2-kx^2);
pti=(kiz*n(numoflayers)^2)/(ktz*n(numoflayers-1)^2);  %TM Wave
Rti=(1-pti)/(1+pti);
if exist('V')
    V=(.5*(1+pti)*[exp(i*ktz*totalthick),
Rti*exp(i*ktz*totalthick);Rti*exp(-i*ktz*totalthick),exp(-
i*ktz*totalthick)])*V;
else
    V=(.5*(1+pti)*[exp(i*ktz*totalthick),
Rti*exp(i*ktz*totalthick);Rti*exp(-i*ktz*totalthick),exp(-
i*ktz*totalthick)]);
end

%Calculate R and T from transfer matrix
R=-V(3)/V(1);
T=-(V(3)/V(1))*V(2)+V(4);

%Calculate reflectivity
r=abs(R)^2;

%Calculate transmissivity and absorption
ki=ko*n(1);
kt=ko*n(numoflayers);
kiz=sqrt(ki^2-kx^2);
ktz=sqrt(kt^2-kx^2);
pit=(n(1)^2)*ktz/(kiz*n(numoflayers)^2);  %TM Wave
if r+pit*abs(T)^2>1.000 %If r+t > 1.000 (rounding errors, etc.)
   warn=1;
   t=1-r;
   a=0;
   e=1;
   angTM=atan(imag(R)/real(R))*180/pi;
else
    t=pit*abs(T)^2;
    t=real(t);
    a=1-r-t;
    a=real(a);
    e=0;
    angTM=atan(imag(R)/real(R))*180/pi;
```

```
end
```

Function: `plotTETMfunc`

This function looks up the data stored in a specified file storename in the /results subdirectory and plots it.

```
function plotTETMfunc(storename,pixres)

%function plotTETMfunc(storename,pixres)
%
%storename = name of file in single quotes where the output data is
%stored (in the /results directory)
%
%pixres = number of pixels per unit wavelength (i.e. pixels/nm or um)


%Read out the results corresponding to storename
fid=fopen(['results/',storename,'lamb'],'r+');
Wavelength=fread(fid,'real*8');
fclose(fid);
fid=fopen(['results/',storename,'r'],'r+');
Reflect=fread(fid,'real*8');
fclose(fid);
fid=fopen(['results/',storename,'ang'],'r+');
Ang=fread(fid,'real*8');
fclose(fid);

%Plot the reflectivity data
figure;
hold on;
plot(Wavelength./pixres,Reflect,'linewidth',2.0)
xlabel('Wavelength','fontsize',18);
ylabel('Reflectivity','fontsize',18);
title('Calculated Reflection','fontsize',20);
axis([Wavelength(1)/pixres, Wavelength(length(Wavelength))/pixres, 0,
1])
set(gca,'fontsize',16);
```

Bibliography

1. Alexanian, N.J., et al. " Three-dimensional FDTD analysis of quasi-optical arrays using Floquet boundary conditions and Berenger's PML", *IEEE Microw. Guided W.*, Vol. 6, p. 138 (1996).
2. Ampere, A.M. *Memoire presente a l'Academie royale des sciences, Annales de Chimie tome XV* (1820).
3. Amra, C. "Light scattering from multilayer optics. I. Tools of investigation", *J. Opt. Soc. Am. A*, Vol. 11, No. 1, p. 197 (1994).
4. Arptech 3DP P1500 Specifications online pamphlet: http://www.arptech.com.au/specs/3DP-P1500.pdf (viewed 02/2005).
5. Ashcroft, N.W. and N.D. Mermin. *Solid State Physics*. Holt, Rinehart and Winston, New York (1976).
6. Agarwal, V., and J.A. del Rio. "Tailoring the photonic bandgap of a porous silicon dielectric mirror", *Appl. Phys. Lett.*, Vol. 82, No. 10, p. 1512 (2003).
7. Bahzan, V. Scatlab scattering program website: http://www.scatlab.com/ (viewed 01/2005).
8. Barnett, D. Loughborough University, Matlab Mie (1997) Functions website: http://www.lboro.ac.uk/departments/el/research/photonics/matmie/mfiles.html (viewed 01/2005).
9. Bayliss, A. and E. Turkel. "Radiation boundary conditions for wave-like equations", *Commun. Pur. Appl. Math.*, Vol. 23, p.707 (1980).
10. Bayliss, A., et al. "Boundary conditions for the numerical solution of elliptic equations in exterior regions", *SIAM J. Appl. Math.*, Vol. 42, p. 430 (1982).
11. Baylard, C., et al. "Coherent reflection factor of a random rough surface: applications", *J. Opt. Soc. Am. A*, Vol. 10, p. 2637 (1993).
12. Beckmann, P. and A. Spizzichino, eds. *The Scattering of Electromagnetic Waves from Rough Surfaces*. Pergamon, Oxford (1963).
13. Bekefi, G., and A.H. Barrett. *Electromagnetic Vibrations, Waves, and Radiation*. The MIT Press, Cambridge (1990).
14. Berenger, J.P. "A perfectly matched layer for the absorption of electromagnetic waves", *J. Comput. Phys.*, Vol. 114, p. 185 (1994).
15. Bohren, C.F., and D.R. Huffman. *Absorption and Scattering of Light by Small Particles*. John Wiley & Sons, Inc., New York (1983).
16. Cangellaris, A.C., et al. "A hybrid spectral / FDTD method for the electromagnetic analysis of guided waves in periodic structures", *IEEE Microw. Guided W.*, Vol. 3, p. 375 (1993).
17. Carstensen, J. and M. Christophersen. University of Kiel, Macroporous silicon website: http://www.tf.uni-kiel.de/matwis/amat/por_model/ (viewed 02/2005).
18. Celuch-Marcysiak, M. and W.K. Gwarek. "Spatially looped algorithms for time-domain analysis of periodic structures", *IEEE T. Microw. Theory*, Vol. 43, p. 860 (1995).

19. Chan, H., et al. "Electromagnetic scattering of waves by random rough surface: a finite-difference time-domain approach", *Microw. Opt. Techn. Let.*, Vol. 4, p. 355 (1991).
20. Chigrin, D.N., et al. "Observation of total omnidirectional reflection from a one-dimensional dielectric lattice", *Appl. Phys. A – Mater.*, Vol. 68, No. 1, p. 25 (1999).
21. Christophersen, M. and J. Carstensen. University of Maryland and University of Kiel, Macroporous silicon website: http://www.macroporous-silicon.com/ (viewed 02/2005).
22. Costa, R., et al. "Bandpass resonant filters in photonic-crystal waveguides" *IEEE Photonic Tech L*, Vol. 15, No. 3, p. 401 (2003).
23. de Coulomb, C.A. Memior (1785).
24. Denford Triton Pro Product specifications website: http://www.denford.co.uk/tritonpro.htm (viewed 02/2005).
25. Deopura, M., et al. "Dielectric omnidirectional visible reflector", *Opt. Lett.*, Vol. 26, No. 15, p. 1197 (2001).
26. Deumie, C., et al. "Ellipsometry of light scattering from multilayer coatings", *Appl. Opt.*, Vol. 35, No. 28, p. 5600 (1996).
27. Elson, J.M. "Multilayer-coated optics: guided-wave coupling and scattering by means of interface random roughness", *J. Opt. Soc. Am. A*, Vol. 12, No. 4, p. 729 (1995).
28. Faraday, M. "On Electrical Decomposition", *Philosophical Transactions of the Royal Society* (1834).
29. Feynman, R.P., et al. *The Feynman Lectures on Physics*, Vol. II., Addison-Wesley, Reading (1965).
30. Fink, Y., et al. "Dielectric omnidirectional reflector", *Science*, Vol. 282, No. 5394, p. 1679 (1998).
31. French, A.P. *Vibration and Waves*. W.W. Norton & Co., New York (1971).
32. Engquist, B. and A. Majda. "Absorbing boundary conditions for the numerical simulation of waves", *Math. Comput.*, Vol. 31, p. 629 (1977).
33. Givoli, D. "Non-reflecting boundary conditions", *J.Comput. Phys.*, Vol. 94, p.1 (1991).
34. Gauss, C.F. *Allgemeine Theorie des Erdmagnetismus* (1839).
35. Gaylord, T.K., et al. "Zero-reflectivity high spatial frequency rectangular groove dielectric surface relief gratings", *Appl. Opt.*, Vol. 25, p. 4562 (1986).
36. Gerken, M., and D.A.B. Miller. "Multilayer thin-film structures with high spatial dispersion", *Appl. Opt.*, Vol.42, No.7, p.1330 (2003).
37. Grillet, C., et al. "Low loss single line photonic crystal waveguide on InP membrane", *Physica E*, Vol. 17, No. 1-4, p. 472 (2003).
38. Halpern, L. and L.N. Trefethen. "Wide-angle one-way wave equations", Numerical Analysis Report 86-5, Dept. of Mathematics, Massachusetts Institute of Technology (1986).
39. Happ, T.D., et al. "Nanofabrication of two-dimensional photonic crystal mirrors for 1.5 mu m short cavity lasers", *J. Vac. Sci. Technol. B*, Vol. 19, No. 6, p. 2775 (2001).
40. Hecht, E. *Optics*. Addison-Wesley, Reading (1987).
41. Higdon, R.L. "Absorbing boundary conditions for difference approximations to the multi-dimensional wave equation", *Math. Comput.*, Vol. 47, p.437 (1986).

42. Higdon, R.L. "Numerical absorbing boundary conditions for the wave equation", *Math. Comput.*, Vol. 49, p.65 (1987).
43. Ho, K.M., et al. "Existence of a photonic gap in periodic dielectric structures", *Phys. Rev. Lett.*, Vol. 65, No. 25, p. 3152 (1990).
44. Hsiao, K. Personal communications (2004).
45. Hunter, R.J. *Foundations of Colloid Science*. Oxford University Press, New York (2001).
46. Iga, K. "Surface-emitting laser - its birth and generation of new optoelectronics field", *IEEE J. Sel. Top. Quant.*, Vol. 6, No. 6, p. 1201 (2000).
47. Jackson, J.D. *Classical Electrodynamics*. John Wiley & Sons, Inc., New York (1999).
48. Joannopoulos, J.D., et al. *Photonic Crystals: Molding the Flow of Light*. Princeton University Press, Princeton (1995).
49. Joannopoulos, J.D., et al. "Photonic crystals: Putting a new twist on light," *Nature*, Vol. 386, p. 143 (1997).
50. John, S. "Localization of light," *Phys. Today*, p. 32 (1991).
51. Johnson, S.G. and J.D. Joannopoulos. "Block-iterative frequency-domain methods for Maxwell's equations in a planewave basis", *Opt. Express*, Vol. 8, No. 3, p. 173 (2001).
52. Johnson, S.G. Massachusetts Institute of Technology, MIT Photonic-Bands website: http://ab-initio.mit.edu/mpb/ (viewed 02/2005).
53. Jonasz, M. MJC Optical Technology, Light scattering calculator website: http://www.mjcopticaltech.com/Products/LscHomoSphHelp.htm (viewed 01/2005).
54. Kelley, P.K., et al. "Photonic bandgap structures of finite thickness: theory and experiment", *P. 1994 IEEE Antenn. Propag. Soc. Int. Symp.*, Vol. 2, p. 718 (1994).
55. Kerker, M. *The Scattering of Light and Other Electromagnetic Radiation*. Academic Press, New York (1969).
56. Kesler, M.P., et al. "Antenna design with the use of photonic bandgap materials as all-dielectric planar reflectors", *Microw. Opt. Techn. Let.*, Vol. 11, p. 169 (1996).
57. Kittel, C. *Introduction to Solid State Physics*. John Wiley & Sons, Inc., New York (1996).
58. Kong, J.A. *Electromagnetic Wave Theory*. EMW Publishing, Cambridge (2000).
59. Kunz, K.S. and R.J. Luebbers. *The Finite Difference Time Domain Method for Electromagnetics*. CRC Press, Boca Raton (1993).
60. Liao, Z.P., et al. "A transmitting boundary for transient wave analyses", *Sci. Sinica* (series A), Vol. XXVII, p. 1063 (1984).
61. Liu, Y. "Fourier analysis of numerical algorithms for the Maxwell's equations", *J. Comput. Phys.*, Vol. 124, p. 396 (1996).
62. Maskaly, G.R. Personal 1D Transfer Matrix Matlab code (2001).
63. Maskaly, K.R., et al. "Diminished normal reflectivity of one-dimensional photonic crystals due to dielectric interfacial roughness", *Opt. Lett.*, Vol. 29, No. 23 (2004).
64. Maxwell, J.C. *A Treatise on Electricity and Magnetism*. Dover Publications, New York (1954).
65. Mie, G. "Beitrage zur Optik truber Medien speziell kolloidaler Metallosungen", *Ann. Phys.*, Vol. 25, p. 377 (1908).
66. Mikulskas, I., et al. "Aluminum Oxide Photonic Crystals Grown by a New Hybrid Method" *Adv. Mater.*, Vol. 13, No. 20, p. 1574 (2001).

67. Mikulskas, I., et al. "Aluminum oxide film for 2D photonic structure: Room temperature formation" *Opt. Mater.*, Vol. 17, p. 343 (2001).
68. Miura, K. and Y. Ohtera. "Reduction of propagation and bending losses of heterostructured photonic crystal waveguides by use of a high-Delta structure" *Opt. Lett.*, Vol. 28, No. 9, p. 734 (2003).
69. Moore, T.G., et al. "Theory and application of radiation boundary operators", *IEEE T. Antenn. Propag.*, Vol. 36, p.1797 (1988).
70. Mur, G. "Absorbing boundary conditions for the finite-difference approximation of the time-domain electromagnetic field equations", *IEEE T. Electromagn. C.*, Vol. 23, p. 377 (1981).
71. Navarro, E.A., et al. "Modeling of periodic structures using the finite difference time domain method combined with the Floquet theorem", *Electron. Lett.*, Vol. 29, p. 446 (1993).
72. Nielsch, K., et al. "Self-ordering Regimes of Porous Alumina: The 10% Porosity Rule" *Nanoletters*, Vol. 2, No. 7, p. 677 (2002).
73. Noda, S., et al. "Semiconductor Three-Dimensional and Two-Dimensional Photonic Crystals and Devices", *IEEE J. Quantum Elect.*, Vol. 38, No. 7, p. 726 (2002).
74. Ogilvy, J.A. *Theory of Wave Scattering from Random Rough Surfaces*. Hilger, Bristol (1991).
75. Okoniewski, M. "Vector wave equation 2-D FDTD method for guided wave problems", *IEEE Microw. Guided W.*, Vol. 3, p. 307 (1993).
76. Omar, M.A. *Elementary Solid State Physics : Principles and Applications*. Addison-Wesley, Reading (1993).
77. O'Sullivan, J.P., and G.C. Wood. "The Morphology and Mechanism of Formation of Porous Anodic Films on Aluminum" *Proc. Roy. Soc. Lond. A*, Vol. 317, p. 511 (1970).
78. Pace Technologies Lapping Films website: http://www.fiberlap.com/ (viewed 02/2005).
79. Painter, O., et al. "Two-dimensional photonic band-gap defect mode laser" *Science*, Vol. 284, No. 5421, p. 1819 (1999).
80. Press, W.H., et al. *Numerical Recipes in C++: The Art of Scientific Computing*. Cambridge University Press, New York (2002).
81. Purcell, E.M. *Electricity and Magnetism, Vol. 2*. McGraw-Hill, Inc., New York (1985).
82. Ramahi, O.M. "The complementary operators method in FDTD simulations", *IEEE Antennas Propag.*, Vol. 39, No. 6, p. 33 (1997).
83. Ramahi, O.M. "The concurrent complementary operators method for FDTD mesh truncation", *IEEE T. Antenn. Propag.*, Vol. 46, p. 1475 (1998).
84. Russell, P.S., and T.A. Birks. "Hamiltonian optics of nonuniform photonic crystals", *J. Lightwave Technol.*; 1999; v.17, no.11, p.1982-1988.
85. Sanchez, J.A., et al. "Limits of validity of three perturbation theories of the specular scattering of light from one-dimensional randomly rough, dielectric surfaces", *J. Opt. Soc. Am. A*, Vol. 12, p. 1547 (1995).
86. Schilling, J., et al. "A model system for two-dimensional and three-dimensional photonic crystals: Macroporous silicon", *J. Opt. A - Pure Appl. Op.*, Vol. 3, No. 6, p. S121 (2001).

87. Schneider, J.B. and C.L. Wagner. "FDTD dispersion revisited: Faster-than-light propagation", *IEEE Microw. Guided W.*, Vol. 9, p. 54 (1999).
88. Sentenac, A., et al. "Study of coherent scattering from one-dimensional rough surfaces with a mean-field theory", *J. Opt. Soc. Am. A*, Vol. 15, No. 4 (1998).
89. Shifrin, K.S. *Scattering of Light in a Turbid Medium*. NASA Technical Translation, NASA TT F-477 (1951).
90. Sullivan, D.M. *Electromagnetic Simulation Using the FDTD Method.* IEEE Press, New York (2000).
91. Taflove, A., and S.C. Hagness. *Computational Electrodynamics*. Artech House, Inc., Boston (2000).
92. Temelkuran, B. et al. "Low-loss infrared dielectric material system for broadband dual-range omnidirectional reflectivity", *Opt. Lett.*, Vol. 26, No. 17, p. 1370 (2001).
93. Temelkuran, B., et al. "Wavelength-scalable hollow optical fibres with large photonic bandgaps for CO2 laser transmission", *Nature*, Vol. 420, No.6916, p. 650 (2002).
94. Tencor P-10 Profilometer Manual, Chapter 3: Theory of Operation (1996).
95. Thorsos, E. "The validity of the Kirchhoff approximation for rough surface scattering using a Gaussian roughness spectrum", *J. Accoust. Soc. Am.*, Vol. 83, p. 78 (1988).
96. Trefethen, L.N. and L. Halpern. "Well-posedness of one-way wave equations and absorbing boundary conditions", *Math. Comput.*, Vol. 47, p. 421 (1986).
97. Tropper, A.C., et al. "Vertical-external-cavity semiconductor lasers", *J. Phys. D Appl. Phys.*, Vol. 37, No. 9, p. R75 (2004).
98. Tsay, W.J. and D.M. Pozer. "Application of the FDTD technique to periodic problems in scattering and radiation", *IEEE Microw. Guided W.*, Vol. 3, p. 250 (1993).
99. Umashankar, K.R., and A. Taflove. "A novel method to analyze electromagnetic scattering of complex objects", *IEEE T. Electromagn. C.*, Vol. 24, p. 397 (1982).
100. Usievich, B.A., and V.A. Sychugov. "A narrow-band optical filter based on a corrugated one-dimensional photonic crystal" *Quantum Electron*, Vol. 32, No. 6, p. 531 (2002).
101. van de Hulst, H.C. *Light Scattering by Small Particles*. John Wiley & Sons, Inc., New York (1957).
102. Voronovich, G. *Wave Scattering from Rough Surfaces*. Springer-Verlag, Berlin (1994).
103. Wang, T.C., et al. "Metallodielectric Photonic Structures Based on Polyelectrolyte Multilayers", *Adv. Mater.*, Vol. 14, No. 21, p. 1534 (2002).
104. Watts, A.A., ed. *Commercial Opportunities for Advanced Composites*. ASTM, Philadelphia (1980).
105. Whatman International Ltd., Whatman Anopore® inorganic membranes website: http://www.whatman.com/products/?pageID=7.25.7.19 (viewed 02/2005).
106. Winn, J.N., et al. "Omnidirectional reflection from a one-dimensional photonic crystal", *Opt. Lett.*, Vol. 23, No.20, p. 1573 (1998).
107. Yablonovitch, E., "Photonic band-gap structures", *J. Opt. Soc. Am. B*, Vol. 10, p. 283 (1993).

108. Yee, K.S. "Numerical solution of initial boundary value problems involving Maxwell's equations in isotropic media", *IEEE T. Antenn. Propag.*, Vol. AP-17, p.585 (1966).
109. Yeh, P. *Optical Waves in Layered Media*. John Wiley & Sons, Inc., New York (1988).
110. Zhang, Z. and S. Satpathy. "Electromagnetic-Wave Propagation in Periodic Structures - Bloch Wave Solution of Maxwell Equations", *Phys. Rev. Lett.*, Vol. 65, No. 21, p. 2650 (1990).

Room 14-0551
77 Massachusetts Avenue
Cambridge, MA 02139
Ph: 617.253.5668 Fax: 617.253.1690
Email: docs@mit.edu
http://libraries.mit.edu/docs

DISCLAIMER OF QUALITY

Due to the condition of the original material, there are unavoidable flaws in this reproduction. We have made every effort possible to provide you with the best copy available. If you are dissatisfied with this product and find it unusable, please contact Document Services as soon as possible.

Thank you.

Some pages in the original document contain color pictures or graphics that will not scan or reproduce well.